Université
de Toulouse

THÈSE

En vue de l'obtention du

DOCTORAT DE L'UNIVERSITÉ DE TOULOUSE

Délivré par :
Institut National Polytechnique de Toulouse (INP Toulouse)

Discipline ou spécialité :
Energétique et Transferts

Présentée et soutenue par :
Mme MANQI ZHU
le mardi 5 mai 2015

Titre :

SIMULATION AUX GRANDES ECHELLES DU CRAQUAGE THERMIQUE DANS L'INDUSTRIE PETROCHIMIQUE

Ecole doctorale :
Mécanique, Energétique, Génie civil, Procédés (MEGeP)

Unité de recherche :
Centre Européen de Recherche et Formation Avancées en Calcul Scientifique (CERFACS)

Directeur(s) de Thèse :
MME BENEDICTE CUENOT
MME ELEONORE RIBER

Rapporteurs :
M. FRANCK NICOUD, UNIVERSITE MONTPELLIER 2
M. KEVIN VON GEEM, UNIVERSITE DE GENT

Membre(s) du jury :
M. LAURENT JOLY, ISAE TOULOUSE, Président
M. ANDRÉ NICOLLE, IFPEN, Membre
M. DAVID J. BROWN, TOTAL PETROCHEMICALS, Membre
Mme BENEDICTE CUENOT, CERFACS, Membre
M. PIERRE-ALEXANDRE GLAUDE, UNIVERSITE DE LORRAINE, Membre

Acknowledgements

I would like to express the deepest appreciation to my supervisors Bénédicte Cuenot and Eléonore Riber for their supervision of my PhD thesis during more than three years at CERFACS, for their support, advice, valuable comments and suggestions. They encourage me a lot, stay by my side giving me care and shelter in doing this research, share their knowledge and idea, and help in the analysis of results and in the simulations. They also give invaluable suggestions to my presentations and an endless help to finish this manuscript. Especially near the end of my thesis, the warm and serious manner of my supervisors gives me lots of encouragement, confidence and console. Without their guidance and persistent help which benefited me much, this dissertation would not have been possible.

I also want to give my grateful thanks to Thierry Poinsot, who also play an important role in this project, giving me this opportunity to work on this topic at CERFACS, and share many helpful ideas and discussions during my thesis.

I place on record, my sense of gratitude to Philippe Ricoux from TOTAL. S.A for the financial support to my PhD project, the valuable discussions and warm welcome to the meetings organized by TOTAL. In addition, a thank you to David Brown and Dominique Viennet for providing necessary data and documents, and their time for discussing in the regular meeting two times per year and for checking this manuscript.

It also gives me great pleasure in acknowledging the cooperation and support from Kevin Van Geem and his student David Van Cauwenberge at Gent University, who have provided very useful information and chemical schema used in my thesis.

I would like to thank Julien Bodart for his time and effort in conducting simulations using CharLes^X, making possible the comparison between my results and his, which becomes one section of my thesis. It is a good experience working with him during the summer in Stanford and I really appreciate his helpful discussions.

I am also very grateful to Franck Nicoud who gives me lot of advices and patience on my work concerning the numerical schemes.

It's my privilege to thank the seniors, engineers at CERFACS: Olivier Vermorel, Gabriel Staffelbach, Jérôme Dombard, Laurent Gicquel, for their competent experience and providing me necessary help and valuable suggestions during my research pursuit.

I am indebted to my friendly colleagues who support me much on my life and work at CERFACS: Matthias Kraushaar, Patricia Sierra-Sanchez, Benedetta Giulia Franzelli, Antoine Dauptain, Geoffroy Chaussonnet who I have meet during my internships at CERFACS in 2009 and 2010, give me genuine help and warm welcome in the beginning of thesis; my co-office Lucas Esclapez for his consistent help of any problems and helpful discussions on my thesis topic; Antony Misdariis, Corentin Lapeyre, Michaël Bauerheim, Raphael Mari, Dorian Lahbib for their valuable advices for time to time and the joyful lunch time with them; Gaofeng Wang, Pierre Quillatre, Rémy Fransen, Clément Durochat, Adrien Bonhomme and Thomas Livebardon, for providing helpful information and help analyzing the results; Thomas Jaravel and Anne Felden for their help and suggestions about the use of Cantera. I am also very happy to be colleagues with Luis Miguel Segui Troth, Jérôme de Laborderie, David Barre, Abdulla Ghani, Franchine Ni, Sandrine Berger, Francis Shum-Kivan, César Becerril, Damien Paulhiac. I could not list all but they all make me a beautiful memeory.

I'd like also thank Isabelle D'Ast, Gérard Dejean, Fabrice Fleury, Patrick Laporte and other CSG people for their helpful technical support.

Another thank you to Séverine Toulouse for her providing the necessary reading materials needed in my accomplishment of this study; Marie Labadens, Nicole Boutet for taking care of me all the time, and for the help in printing this manuscript; Michèle Campassens, Chantal Nasri, Lydia Otero and other ADM people for their help and amity during my life at CERFACS.

Finally I remain indebted to my friends Yi Gao, Le Cui, Yali Meng for their help preparing the day of my defense. Thanks to all of my friends (Wenjie, Qingxiao, Yue, Yihui, Xiaoxuan, Long...) and my parents for their love, moral support and remarkable encouragement.

I would like to thank all the people helping me, encouraging me, taking care of me during my whole PhD thesis, where ever they are, where ever I am.

Abstract

To improve the efficiency of thermal-cracking processes, and to reduce the coking phenomena due to high wall temperature, the use of ribbed tubes is an interesting technique as it allows better mixing and heat transfer. However it also induces significant increase in pressure loss. The complexity of the turbulent flow, the chemical system, and the chemistry-turbulence interaction makes it difficult to estimate a priori the real loss of ribbed tubes in terms of selectivity. Experiments combining turbulence, heat transfer and chemistry are very rare in laboratories and too costly at the industrial scale. In this work, Wall-Resolved Large Eddy Simulation (WRLES) is used to study non-reacting and reacting flows in both smooth and ribbed tubes, to show the impact of the ribs on turbulence and chemistry. Simulations were performed with the code AVBP, which solves the compressible Navier-Stokes equations for turbulent flows, using reduced chemistry scheme of ethane and butane cracking for reacting cases.

Special effort was devoted to the wall flow, which is analyzed in detail and compared for both geometries, providing useful information for further development of roughness-type wall models. The impact of grid resolution and numerical scheme is also discussed, to find the best trade-off between computational cost and accuracy for industrial application. Results investigate and analyze the turbulent flow structures, as well as the effect of heat transfer efficiency and mixing on the chemical process in both smooth and ribbed tubes. Pressure loss, heat transfer and chemical conversion are finally compared.

Keywords: Large Eddy Simulation, turbulent reacting flow, roughness, helically ribbed tubes, heat transfer, thermal cracking process

Résumé

Pour améliorer l'efficacité des procédés thermiques de craquages et réduire les phénomènes de cokage liés à la température de paroi trop élevée, l'utilisation de tubes nervurés est une technique potentiellement car elle permet d'améliorer le mélange et d'augmenter les transferts de chaleur. Cependant, la perte de charge est significativement augmentée. En raison de la complexité de l'écoulement turbulent, du système chimique et du couplage turbulence-chimie, il est difficile d'estimer a priori la perte réelle en termes de sélectivité des tubes nervurés. Les expériences représentatives de laboratoire combinant turbulence, transferts de chaleur et chimie sont très rares et trop coûteuses à l'échelle industrielle. Dans ce travail, l'approche simulation aux grandes échelles résolue à la paroi (WRLES) est utilisée pour étudier écoulement non-réactif puis réactif dans des tubes à la fois lisses et nervurés, pour quantifier leur impact sur la turbulence et sur la chimie. Le code AVBP, qui résout les équations de Navier-Stokes compressibles pour les écoulements turbulents, est utilisé avec des schémas chimique réduites du craquage de l'éthane puis du butane.

L'écoulement à la paroi est analysé en détail et comparé pour les deux géométries, fournissant des informations utiles pour le développement ultérieur de modèles de parois pour ce type de rugosité. L'impact de la résolution du maillage et du schéma numérique est également discuté, pour trouver le meilleur compromis entre coût et précision de calcul pour une application industrielle. L'impact des structures d'écoulement turbulent ainsi que leurs effets sur le transfert thermique et le mélange sur les réactions chimique sont étudiés à la fois pour les tubes lisses et les tubes nervurés. Perte de pression, transfert de chaleur et conversion chimique sont finalement comparés.

Mots clés: Simulation aux grandes échelles, écoulement turbulent réactif, rugosité, tubes en hélices nervurées, transfert thermique, craquage

Contents

List of Figures

List of Tables

Chapter 1

Introduction

Contents

1.1 Industrial context

The hydrocarbon processing industry (HPI) and chemical processing industry (CPI) cover all aspects of producing petroleum-based products, including refining of petroleum (a picture of an oil refinery in Fig. 1.1.1), manufacturing of chemical and petrochemicals from petroleum feedstocks, processing of gases, and production of synthetic fuels [1]. These industries take raw materials such as crude oil, natural gas and convert them into usable products, including the gasoline, diesel, fuels and precursor materials for the generation of plastics that go into many products, from clothing to plastic bottles, of our daily life, illustrated on Fig. 1.1.2. A critical factor to all these process is heat as chemical conversion is most efficient in narrow temperature ranges.

A majority of operations in the HPI occur in petroleum refining. The major petroleum refining processes are categorised as: 1) topping (the separation of crude oil), 2) thermal and catalytic cracking, 3) combination/rearrangement of hydrocarbon, 4) treating and 5) specialty product manufacturing [3]. Most of them require a fired heater, as illustrated on Fig. 1.1.3, showing typical exterior and interior structures. In such systems, the flow inside the tubes is heated from outside by the flames of the burners (Fig. 1.1.3b). The major heat transfer processes include radiation and convection: in the radiation section, heat transfer occurs between the flame and process tubes through thermal radiation; in the

Figure 1.1.1: Total Refining & Chemicals, Usine de Gonfreville l'Orcher. source: TOTAL

convection section, hot gases through flowing through a network of tubes generate external convective heat transfer, while the inner tube flow generates internal convective heat transfer, as illustrated in Fig. 1.1.3c.

As one of the major petroleum refining processes, the objective of the cracking process is to produce ethylene C_2H_4, which is the largest volume building block for many petrochemicals. Ethylene can be produced via a myriad of different processes, such as catalytic pyrolysis and hydropyrolysis processes [7], fluidized bed cracking, paraffin dehydrogenation, and oxydehydrogenation [8]. The present work mainly concerns thermal cracking. During the thermal cracking processes, steam-cracking furnaces produce ethylene by heating hydrocarbons such as ethane C_2H_6, propane C_3H_8, butane C_4H_{10}, naphtha, or gas oils to very high temperatures in the presence of steam [1], leading to the the thermal decomposition of large molecules into lighter ones. Thermodynamic equilibrium favors the formation of olefins only at high temperature and low pressure. Typical reactor coil outlet temperatures are in the range of 788-885°C (1061-1158 K), and the pressure is 1.7-2.4 bar. The hydrocarbon partial pressure is lowered by the presence of the dilution steam. Moreover, a high selectivity is achieved by operating with a very short residence time, typically 0.1-0.5 s.

The reactions during cracking processes are highly endothermic. As the residence time in the process tube is very short, a high heat flux is required to maintain the temperature at a level sufficient for the reactions to occur. As a consequence, heat transfer enhancement techniques always play an important role in the exchanger system optimization. Artificial roughness in the inner surface of tubes is one passive method of heat transfer enhancement which, in contrast to active methods, does not require a direct application of external power. Different kinds of artificial roughness are widely used in various industrial applications. In the next section, a classification of the different artificial roughness of tubes is introduced.

Figure 1.1.2: Some of the petrochemical products in daily life [2]

1.2 Classification of artificial roughness

The cross section of heat exchanger ducts are of different forms, either rectangular (channels) or circular (tubes). As our subject is to study the heat exchanger tubes in a radiation zone of the pyrolysis furnace (i.e. thermal cracking furnace) for the thermal cracking processes (as shown in Fig. 1.2.1), only tubular geometries are discussed.

1.2.1 One/two/three dimensional roughness

Some examples of different families of artificial roughness are introduced in this section. As a big family of the artificial roughness, tubes with twisted tape inserts as illustrated in Fig.1.2.2 and other variations are widely investigated and reviewed in Kumar et al.(2012) [9]. A part from this family, Vicente et al.(2002) [10] presented two types of artificial roughness: 1) two-dimensional roughness includes transverse and helical ribs, helically corrugated and wire coil inserts; 2) three-dimensional roughness includes sand-grain roughness, attached particle roughness, "cross-rifled" roughness and helically dimples. Note that Withers (1980) [11] classified that sand-grain roughness (Fig. 1.2.3) as one-dimensional, because it is characterized by only one parameter: the roughness height "e" according to Nikuradse's experiments [12].

The 3D helically dimpled roughness is illustrated in Fig. 1.2.4: the height of the roughness e, the pitch between two parallel series of obstacles p and the distance between two neighbor obstacles l compose the three dimensions which influence the behavior of roughness.

In the same way, 2D roughness is described with two parameters, ribs height "e" and pitch "p" as indicated in Fig. 1.2.5, that affect the performance. This study will mainly focus on 2D roughness.

Some illustrations of different 2D roughness types are given in Fig. 1.2.5.

Saha [18] indicated that the rib (Fig.1.2.5a and b) is built into the inner wall of tubes,

(a) Exterior. Source from [4].

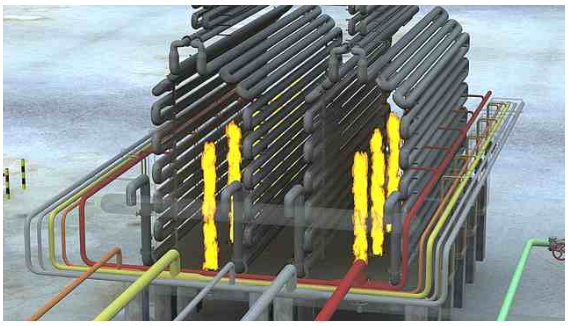

(b) Interior. Source from [5].

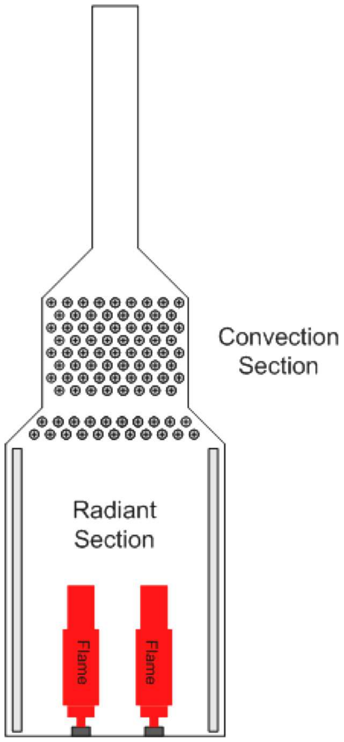

(c) Schematic. Source from [6]

Figure 1.1.3: Typical fired heater.

whereas the wire-coil inserts (Fig.1.2.5d) are wall-attached. Corrugated tubes (Fig.1.2.5c) are characterized by a rough outer surface, contrary to others tubes having a smooth outer surface. The different manufacturing technique may lead to different shapes. Garcia et al. (2012) ([13]) found that, in the petrochemical industry, the use of mechanically deformed tubes (like the corrugated tubes and dimpled tubes) is not allowed for safety reasons due to the risk of being broken, however, the use of wire coils does not cause any problem.

1.2.2 D-type and K-type

Perry et al.(1969) [19] studied the turbulent boundary layer over a transversally ribbed wall and proposed to distinguish two types of 2D roughness: K-type and D-type, "K" representing the roughness height (in this report "e" will be used as the symbol of the roughness height according to some more recent papers) and "D" the outer scales like boundary-layer thickness, pipe diameter, or channel height. Tani (1987) [20] suggested that, for regularly spaced ribs, a demarcation between K-type and D-type roughness might be made at the pitch to height ratio $p/e = 4$, where p is the pitch between the roughness elements [21]:

- For D-type, roughness is typified by closely spaced ribs with $p/e < 4$. The ribs are so closely spaced that stable vortices are set up in the grooves, eddy shedding from the roughness elements into the outer flow is negligible, and the outer flow is relatively undisturbed by the roughness elements. The roughness performance (e.g., its impacts on the friction factor) is independent of the size of roughness.

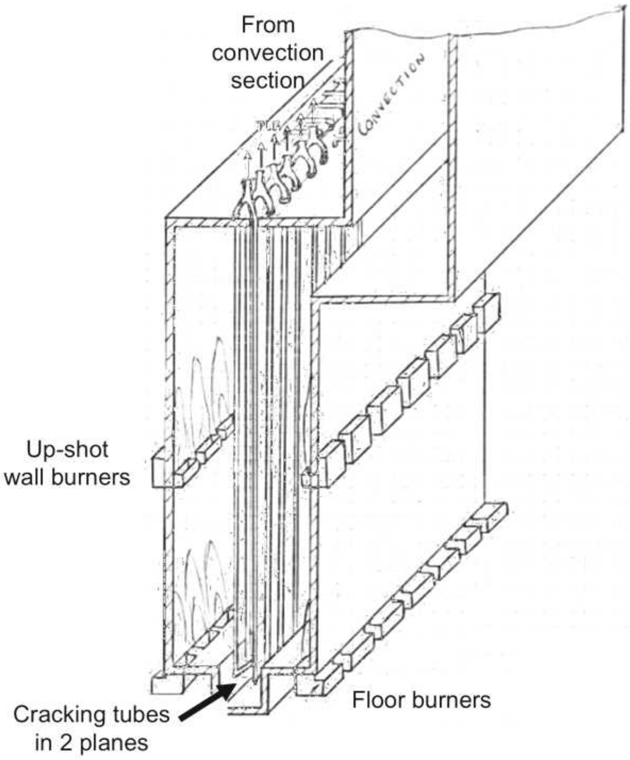

Figure 1.2.1: Cracking tubes (vertical, in two planes) in the radiation zone of the pyrolysis furnace. Source: Total Petrochemicals

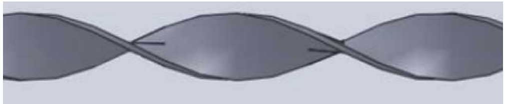

Figure 1.2.2: Twisted tape inserts [9]

- For K-type roughness, typified by sparsely spaced transverse ribs, with $p/e > 4$, eddies with length scale of the order of the roughness height are shed from the roughness elements and penetrate into the bulk flow toward the pipe or channel center (or boundary layer edge). The roughness performance depends on the size of the roughness elements.

In the present study, only K-type 2D roughness is considered.

1.3 The Mixing Element Radiant Tube technology in steam-cracking process

In a thermal cracking furnace (Fig. 1.2.1), the cracking tubes are usually 10 meters long. The Reynolds number of the turbulent flow inside the tubes ranges from 10^4 to 10^5, and the residence time is typically 0.1-0.5 s. As mentioned in section 1.1, the steam-cracking process is favored at high temperature. At the same time, high tube skin temperature, typically between 1000-1125°C (1273-1398 K) [1], promots undesired but inevitable formation and deposit of coke (carbon) on the inner wall of the tubes. If the coke layer in the tubes becomes

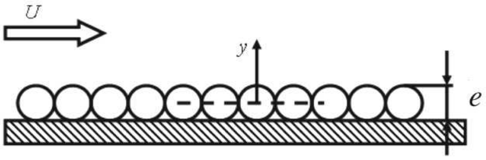

Figure 1.2.3: Illustration of the “sand-grain” roughness.

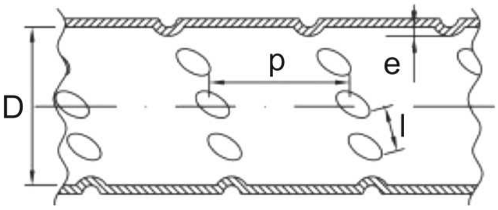

Figure 1.2.4: Dimpled tube [13]: 3D roughness

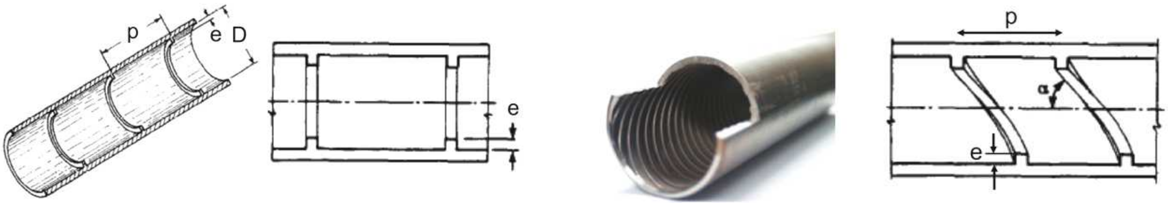

(a) Transverse ribs [14]

(b) Helical ribs [15]

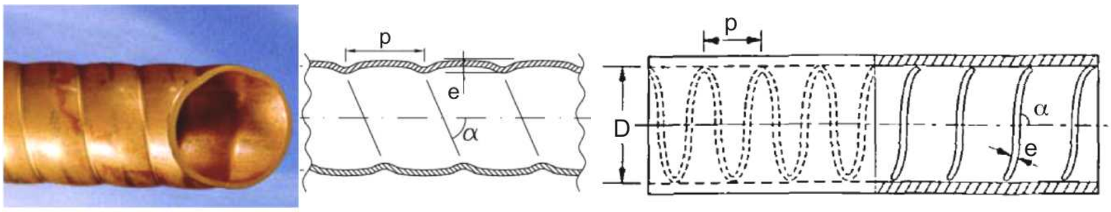

(c) Helically corrugated [16]

(d) Wire coil insert [17]

Figure 1.2.5: Different types of 2D roughness

thicker, the pressure loss and the wall temperature both increase, due to the increase of the wall friction and the reduction of the heat transfer, then the problem gets worse. When either the pressure drop limit or the tube skin temperature limit is reached, the tubes must be decoked. This is a long and uneasy operation, requiring to stop the production, i.e., having a high cost. For this reason, coking phenomena must be avoided as much as possible. For these reasons, heat transfer enhancement techniques is required, which increase the heat transfer efficiency and can reduce the skin temperature. However, note that these techniques often induce increased pressure losses.

Many technologies are developed in order to improve the performance of steam-cracking tubes. Helically ribbed tubes are widely studied and many patents on this technology are submitted. Fig. 1.3.1 shows examples of helically ribbed tubes of the Mixing Element Radiant Tube (MERT) family technology [22–26], developed by KUBOTA [27] to be used in tubular pyrolysis furnaces. According to the previous classification, the “normal MERT” [23] (Fig. 1.3.1a) is a 2D roughness type because of the continuous helically ribs on the inner

(a) Normal MERT (b) Slit-MERT (Below) & X-MERT (Upper)

Figure 1.3.1: Helically ribbed steam cracking tube MERT [27]

surface, while the “slit-MERT” & “X-MERT” (Fig. 1.3.1b) is kind of 3D roughness type as the ribs are non-continuous.

MERT tubes have clear advantages in thermal cracking processes: thanks to enhanced mixing, the wall heat transfer efficiency is improved and the flow in the tube is more homogeneous in both temperature and composition. As a consequence, the temperature of the tube’s skin decreases and coke deposit is reduced [27]. Another result is the improved operating efficiency of the chemical process. Fig. 1.3.2 shows that the heat transfer is around 1.5 times higher than that in a smooth tube in the same condition, while the pressure loss is 3-4 times higher.

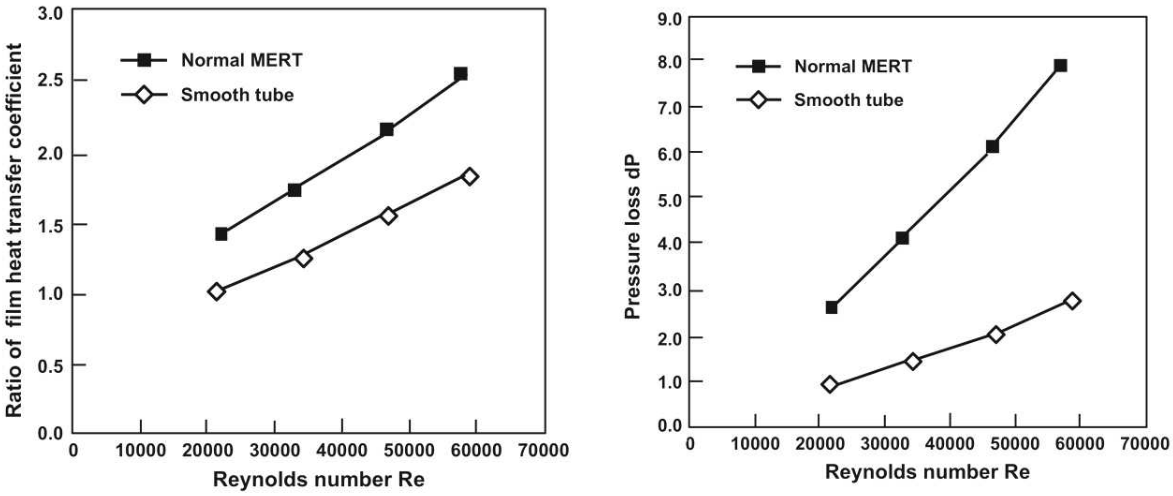

(a) Heat transfer vs Reynolds number (b) Pressure loss vs Reynolds number

Figure 1.3.2: Heat transfer (a) and pressure loss (b) measurements in the normal MERT tube compared with a smooth tube [24]

The performance of MERT technology could be optimized by changing the ribs arrangement, the ribs height, the ribs pitch, etc. This requires an understanding of the physical phenomena of turbulent flows in ribbed tubes, and to reveal the impact of ribs.

1.4 Aims of the work

To achieve heat enhancement while avoiding increased pressure loss and reducing coking phenomena, the main objective of the present work is the understanding of helically ribbed tubes flow dynamics and impact on the chemical process. This requires to face scientific issues as wall flows in tubes, heat transfer in turbulent flows, and interaction of cracking chemistry with turbulence.

Many experimental and numerical research studies have been devoted to the turbulent flow in smooth tubes and wall models have been established, that lead to a correct calculation of both the wall friction and heat flux. The situation is much different for ribbed tubes. Experiments lead to very different results, with no clear conclusions about the nature of the wall flow. Moreover, the experimental instrumentation cost limits the measurements.

For these reasons, numerical simulation appears as an interesting tool to investigate turbulent flows in ribbed tubes. Examples of numerical simulations of ribbed tubes, especially of helically ribbed tubes, are much scarce in the literature. In the present work, the turbulent flow and heat transfer in a ribbed tube is investigated by use of high-fidelity numerical simulation, with the following objectives:

- to understand the dynamic properties of the turbulent wall flow in ribbed tubes,
- to understand heat transfer phenomena of the turbulent wall flow in ribbed tubes,
- to understand the impact of ribs on the petrochemical process for the optimization of the cracking tube,
- to apply numerical simulation to a real industrial system and demonstrate the feasibility and added-value of such simulations.

1.5 Outline

- **Part I: Chapter 2**
  The study begins with a literature survey. Experiments are reviewed, showing the dominant geometric parameters of ribbed tubes and their effect on the flow properties. Some semi-experimental correlation formula for calculating the friction factor and Nusselt number (which characterize the heat transfer properties) in the different tubes are also presented.

- **Part II: Chapters 3 to 5**
  To understand the physics of ribbed tube flows, academic cases are first considered in this part. Both smooth and ribbed tubes are simulated in non-reacting, either non-heated (Chapter 3) or heated (Chapter 4) conditions. Special effort is devoted to the wall flow, which is analyzed in detail and compared for both geometries. The impact of grid resolution and numerical scheme is also discussed, to find the best trade-off between computational cost and accuracy for the industrial application.

  In Chapter 5, a mixture of ethane C_2H_4 and steam (H_2O) is injected and reacts to produce ethylene. The effect of heat transfer efficiency and turbulence on the chemical process, which is of high interest to the petrochemical industry, is reproduced and analyzed.

- **Part III: Chapter 6**
  In this third part, the methodology developed in Part II is applied to evaluate the efficiency in terms of chemical conversion of a real industrial case, which constitutes the final objective of the work. Both smooth and ribbed tubes with inner diameter of 38 mm, are simulated using the real heat flux and pressure drop applied in the industrial process. The flow is a mixture of butane C_4H_{10} and steam (H_2O) producing ethylene.

- **Part IV: Chapter 7**
  The manuscript ends with conclusions and perspectives of this project.

Chapter 2

Turbulent flows in smooth and rough tubes

Contents

Most flows in nature, in daily life and in industry are turbulent. In real life, and in contrast to free shear flows, most turbulent flows are bounded by one or more solid surfaces. The solid surface plays a key role in external flows such as the flow around aircraft or ships' hull, the atmospheric boundary layer, or the flow of rivers [28]. Internal flows in complex geometries are often encountered in industrial systems, and can be first studied in simpler configurations such as channels or pipes. The research on wall flows over smooth surfaces has been very intense for many years [29–43]. However, flows are rarely bounded by smooth surfaces in nature, or in industrial systems, where wall roughness is often used to improve performances. Nevertheless, much less progress on flow over rough surfaces has been achieved due to its complexity, and this topic is still a current scientific challenge.

This chapter begins with a general description of turbulent wall flows and some definitions. Next, a literature survey of experimental and numerical studies for both smooth and rough walls/channels/tubes is made, reporting theoretical/semi-experimental correlation formula for the friction factor and the Nusselt number. As the present work targets reacting flow applications, the coupling of chemistry with turbulence is finally presented.

2.1 Turbulent wall flows

The presence of walls leads to the development of dynamic and thermal boundary layers. These flow structures are very different from the bulk turbulent flow, while they however impact greatly, and require specific modeling. Three of the simplest academic wall flows are channel flow, pipe flow and flow over a flat-plate, either laminar or turbulent. The near-wall behavior in these flows is very similar, and has been extensively studied throughout the history of turbulent flow studies [28].

2.1.1 Governing equations of compressible reacting flows

The governing equations of compressible reacting flows, are here written in the form of mass, species, momentum and total-non-chemical-energy conservation laws:

$$\frac{\partial \rho}{\partial t} + \frac{\partial (\rho u_i)}{\partial x_i} = 0, \tag{2.1.1}$$

$$\frac{\partial (\rho Y_k)}{\partial t} + \frac{\partial (\rho (u_i + V_{k,i}) Y_k}{\partial x_i} = \dot{\omega}_k, \tag{2.1.2}$$

$$\frac{\partial (\rho u_i)}{\partial t} + \frac{\partial (\rho u_i u_j)}{\partial x_j} = -\frac{\partial P}{\partial x_i} + \frac{\partial \tau_{ij}}{\partial x_j} + \rho \sum_{k=1}^{N} Y_k f_{k,j}, \tag{2.1.3}$$

$$\rho \frac{DE}{Dt} = -\frac{\partial q_i}{\partial x_i} + \frac{\partial}{\partial x_j}(\tau_{ij} u_i) - \frac{\partial}{\partial x_i}(P u_i) + \dot{\omega}_T + \dot{\mathcal{Q}} + \rho \sum_{k=1}^{N} Y_k f_{k,i}(u_i + V_{k,i}) \tag{2.1.4}$$

These equations [44] are written in Cartesian coordinates and using the conventional Einstein notation. In Eq. 2.1.1, x_i and u_i are the ith coordinate and velocity component, ρ is the density; in Eq. 2.1.2, Y_k is the mass fraction of the kth species, $V_{k,i}$ is the i-component of the diffusion velocity V_k of species k and $\dot{\omega}_k$ its reaction rate. A necessary condition is that $\sum_{k=1}^{N} Y_k V_{k,i} = 0$ for the reason of total mass conservation. In Eq. 2.1.3, P is the pressure, $f_{k,j}$ is the volume force acting on species k in direction j, τ_{ij} the viscous stress tensor:

$$\tau_{ij} = -\frac{2}{3}\mu \frac{\partial u_k}{\partial x_k}\delta_{ij} + \mu \left(\frac{\partial u_i}{\partial x_j} + \frac{\partial u_j}{\partial x_i} \right), \tag{2.1.5}$$

where μ (kg/(m·s)) is the dynamic viscosity of the fluid ($\mu = \rho\nu$, where ν is the kinematic viscosity), and δ_{ij} is the Kronecker symbol.

In Eq. 2.1.4, $E = e_s + (1/2)u_i u_i$ is the total non-chemical energy, sum of sensible energy e_s and kinetic energy $(1/2)u_i u_i$, $q_i = -\lambda \partial T/\partial x_i$ (defined with thermal conductivity λ (W/(m·K)) and temperature T, according to Fourier's law [45]) is energy flux, $\dot{\omega}_T$ is the heat released by reactions, $\dot{\mathcal{Q}}$ is other heat source term (due for example to an electric spark, a laser or a radiative flux), and $\rho \sum_{k=1}^{N} Y_k f_{k,i}(u_i + V_{k,i})$ is the power produced by volume forces f_k on species k.

2.1.2 Dimensionless parameters

This section introduces two classical dimensionless numbers for describing flow dynamics and thermal conduction.

Reynolds number

In fluid mechanics, the Reynolds number is used to characterize the possible transition to turbulence and similar flow patterns in different flow situations. It was introduced by George Gabriel Stokes in 1851 [46], then named after Osborne Reynolds, who popularized its use in 1883 [47,48]. The Reynolds number is defined as the ratio of inertial forces to viscous forces and consequently quantifies the relative importance of these two types of forces [49]:

$$\mathrm{Re} = \frac{LU_b}{\nu}, \tag{2.1.6}$$

where L is a characteristic length (m) which refers to the inner diameter of the tube when the pipe flow is examined for example. $\nu = \mu/\rho$ is the kinematic viscosity (m^2/s) and U_b is the bulk flow velocity (m/s):

$$U_b = \frac{\int_V \rho U dV}{\int_V \rho dV}, \tag{2.1.7}$$

where $U = (U_i)$ is the flow velocity and V is the inner volume of the tubes.

The turbulent flow corresponds to dominant inertial forces while the laminar flow corresponds to dominant viscosity forces. In pipe flows, turbulence develops typically when $\mathrm{Re} > 4000$, while the flow stays completely laminar until $\mathrm{Re} < 2100$ [50].

Prandtl number

The Prandtl number is named after Ludwig Prandtl, defined as the ratio of momentum diffusivity (kinematic viscosity) to thermal diffusivity:

$$\mathrm{Pr} = \frac{\nu}{\alpha}, \tag{2.1.8}$$

where thermal diffusivity is $\alpha = \lambda/(\rho C_p)$ with heat capacity C_p.

Note that the Prandtl number contains no length scale and depends only on the fluid proprties. $\mathrm{Pr} \ll 1$ means that thermal diffusivity dominates while $\mathrm{Pr} \gg 1$ means momentum diffusely dominates. In this study, Pr is always taken at the value of air (at standard temperature ~ 300 K) at 0.71.

2.1.3 Turbulence modeling

In CFD, three main approaches, namely Direct Numerical Simulation (DNS), Large Eddy Simulation (LES) and Reynolds Averaged Navier-Stockes (RANS), may be used to solve the flow equations. The three approaches consider different fluid scales and lead to different computational cost and modeling. They are often described in terms of energy spectrum, as illustrated on Fig. 2.1.1 [51].

DNS

In DNS, all scales of turbulence are resolved, as illustrated on Fig. 2.1.1. As a consequence, a very fine mesh is required to describe the Kolmogorov dissipation scale, while the computational domain must be sufficiently large to represent the large scales of the flow. The total grid points number required to perform a DNS of a 3D homogeneous isotropic turbulence (HIT) is then proportional to the ratio of the largest to the smallest scale, and some estimations can be found in Pope (2000) [28]. For DNS of turbulent boundary layers, the required number of grid points is estimated as $\mathrm{Re}^{9/4}$ by Rogallo & Moin (1984) [52], and $\mathrm{Re}^{37/14}$ by

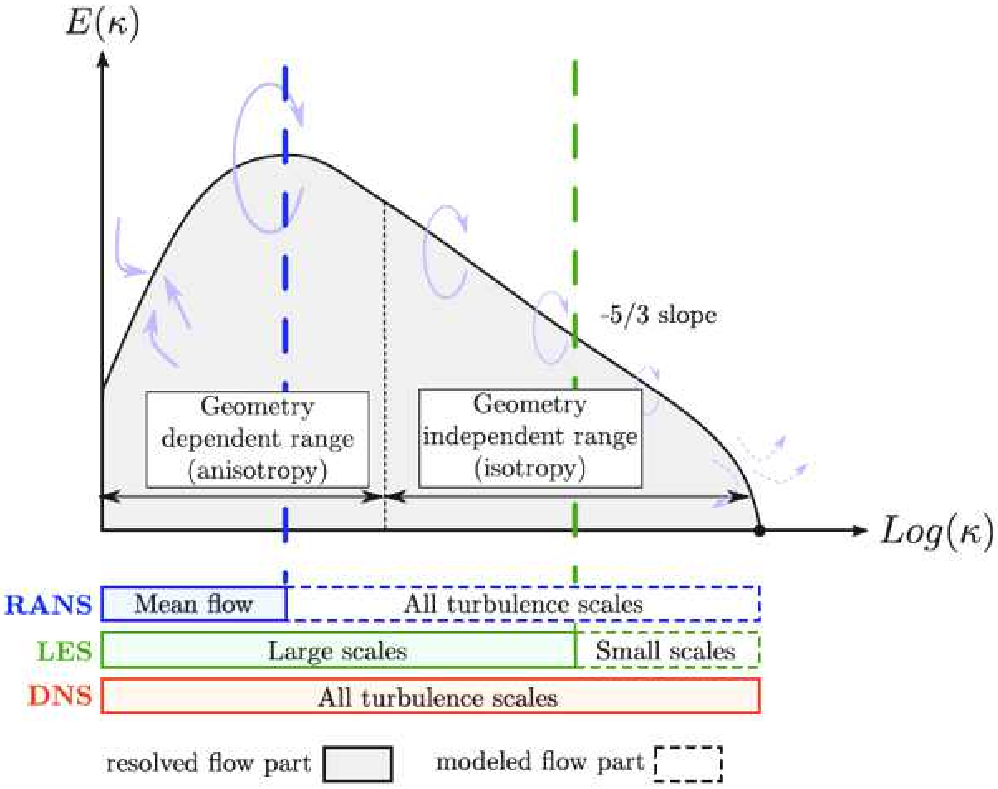

Figure 2.1.1: RANS, LES and DNS in the turbulent energy spectrum [51].

Choi & Moin (2012) [53]. A review of DNS of turbulent flow studies may be found in Moin & Mahesh (1998) [54].

DNS, mainly as a research tool, is usually limited to simple geometries, in view of understanding fundamental processes and mechanisms. In the present work, DNS will be used to fully resolve the flow around ribs and provide reference data for modeling. Due to the high CPU cost, DNS cannot be used by engineers in an industrial context.

RANS

In contrast to the DNS, RANS only solves statistically-averaged flow quantities and all turbulent scales are modeled (Fig. 2.1.1). The Reynolds average of a quantity is noted as:

$$\phi = \overline{\phi} + \phi', \tag{2.1.9}$$

where ϕ' is the fluctuating component. Usually, in reacting flows with high density changes, the RANS approach is based on Favre-averaged quantities [55], as:

$$\phi = \langle \phi \rangle + \phi'', \tag{2.1.10}$$

where the Favre averaged component is defined by [44, 51]:

$$\langle \phi \rangle = \frac{\overline{\rho \phi}}{\overline{\rho}}, \tag{2.1.11}$$

The fluctuating part ϕ'' satisfies:

$$\overline{\rho\phi''} = 0 \tag{2.1.12}$$

Substituting Eq. 2.1.10 into the flow equations (Eq. 2.1.4) and averaging, the following equations are obtained [44, 51]:

$$\frac{\partial \overline{\rho}}{\partial t} + \frac{\partial(\overline{\rho}\langle u_i\rangle)}{\partial x_i} = 0, \tag{2.1.13}$$

$$\frac{\partial(\overline{\rho}\langle Y_k\rangle)}{\partial t} + \frac{\partial(\overline{\rho}\langle u_i\rangle\langle Y_k\rangle)}{\partial x_i} = -\frac{\partial(\overline{V_{k,i}Y_k} + \overline{\rho}\langle u_i''Y_k''\rangle)}{\partial x_i} + \overline{\dot{\omega}_k}, \tag{2.1.14}$$

$$\frac{\partial(\overline{\rho}\langle u_i\rangle)}{\partial t} + \frac{\partial(\overline{\rho}\langle u_i\rangle\langle u_j\rangle + \overline{P}\delta_{ij} - \overline{\tau_{ji}} - \overline{\tau_{ji}}^t)}{\partial x_j} = \overline{\rho}\langle f_i\rangle, \tag{2.1.15}$$

$$\frac{\partial(\overline{\rho}\langle E\rangle)}{\partial t} + \frac{\partial(\overline{\rho}\langle u_j\rangle\langle E\rangle + \langle u_i\rangle\overline{P} + \overline{q_j} + \overline{q_j}^t - \langle u_i\rangle(\overline{\tau_{ij} - \tau_{ij}^t}))}{\partial x_j} = \overline{\rho}\langle u_j f_j\rangle, \tag{2.1.16}$$

where the unknowns to be modeled are the turbulent Reynolds stress tensor $\overline{\tau_{ij}}^t = -\overline{\rho}\langle u_i''u_j''\rangle$, the turbulent species flux $\overline{\rho}\langle u_i''Y_k''\rangle$ and the turbulent heat flux $\overline{q_j}^t = -C_p\overline{\rho}\langle u_j''T''\rangle$. The turbulent Reynolds stress tensor is described in a similar expression as for τ_{ij} (Eq. 2.1.5) [44]:

$$\overline{\tau_{ij}}^t = -\frac{2}{3}\mu_t\frac{\partial\langle u_k\rangle}{\partial x_k}\delta_{ij} + \mu_t\left(\frac{\partial\langle u_i\rangle}{\partial x_j} + \frac{\partial\langle u_j\rangle}{\partial x_i}\right) - \frac{2}{3}\overline{\rho}k, \tag{2.1.17}$$

introducing the turbulent dynamic viscosity μ_t ($\mu_t = \overline{\rho}\nu_t$, where ν_t is the turbulent kinematic viscosity) and the turbulent kinetic energy (TKE) k:

$$k = \frac{1}{2}\sum_{k=1}^{3}\langle u_k''u_k''\rangle \tag{2.1.18}$$

To evaluate the turbulent viscosity μ_t, multiple approaches have been proposed of various complexity [44]: zero-equation models (e.g., Prandtl mixing length model), one-equation models (e.g., Prandtl-Kolmogorov) and two-equations model ($k-\epsilon$).

The turbulent species flux is closed using a classical gradient assumption [44]:

$$\overline{\rho}\langle u_i''Y_k''\rangle = -\frac{\mu_t}{Sc_{kt}}\frac{\partial\langle Y_k\rangle}{\partial x_i} \tag{2.1.19}$$

where Sc_{kt} is the turbulent Schmidt number for species k.

The turbulent heat flux $\overline{q_j}^t$ is modeled using a turbulent thermal conductivity $\lambda_t = \nu_t\overline{C_p}/\mathrm{Pr}_t$ with the Prandtl number Pr_t [51]:

$$\overline{q_j}^t = -\lambda_t\frac{\partial\langle T\rangle}{\partial x_j} \tag{2.1.20}$$

RANS leads to very low computational cost, and it is widely used in industry [56, 57]. However, RANS has several drawbacks which limit its capabilities. First, RANS does not lead to physical flow solutions but gives only its first moments. Second, as RANS also models the largest scales, it cannot be fully predictive in complex geometries unless it has been calibrated against experiments. Finally, RANS models are mostly derived for steady flows and transient phenomena are difficult to capture.

LES

The present work is performed by means of Large Eddy Simulation (LES). As an intermediate technique between RANS and DNS, LES is increasingly used in the investigation of turbulent flows as an optimized trade-off between computational cost and accuracy. It relies on the filtering of the flow equations in spectral space or in physical space [44], so that the most energetic part of the flow is directly resolved while the smallest scales (lowest energy) are modeled. The assumption behind this method is that all turbulent length scales can be divided into two parts, as illustrated on Fig. 2.1.1 [51]:

- a high energy anisotropic large scales range, above the filter length scale,
- a low energy and dissipative isotropic small scale range, below the filter length scale.

In practice, the filter is simply the grid, and the small, modeled scales are the sub-grid scale (SGS), i.e., smaller than the cell size. LES of compressible flow also uses the Favre filtering is introduced as [44]:

$$\overline{\rho}\widetilde{\phi}(x1, x2, x3) = \overline{\rho}\widetilde{\phi}(\mathbf{x}) = \int \rho\phi(\mathbf{x}')F(\mathbf{x}-\mathbf{x}')d\mathbf{x}' \tag{2.1.21}$$

where F is the LES filter. Filtering flow equations leads to similar forms as RANS (Eq. 2.1.16), except the turbulent Reynolds stress $\overline{\rho}(\widetilde{u_i u_j} - \widetilde{u_i}\widetilde{u_j})$, the species fluxes $\overline{\rho}(\widetilde{u_i Y_k} - \widetilde{u_i}\widetilde{Y_k})$ and heat fluxes $\overline{\rho}(\widetilde{u_i T} - \widetilde{u_i}\widetilde{T})$ instead of $\overline{\rho}\langle u_i'' u_j''\rangle$, $\overline{\rho}\langle u_i'' Y_k''\rangle$ and $\overline{\rho}\langle u_i'' T''\rangle$:

$$\frac{\partial \overline{\rho}}{\partial t} + \frac{\partial(\overline{\rho}\widetilde{u_i})}{\partial x_i} = 0, \tag{2.1.22}$$

$$\frac{\partial(\overline{\rho}\widetilde{Y_k})}{\partial t} + \frac{\partial(\overline{\rho}\widetilde{u_i}\widetilde{Y_k})}{\partial x_i} = -\frac{\partial(\overline{V_{k,i}Y_k} + \overline{\rho}(\widetilde{u_i Y_k} - \widetilde{u_i}\widetilde{Y_k}))}{\partial x_i} + \overline{\dot{\omega}_k}, \tag{2.1.23}$$

$$\frac{\partial(\overline{\rho}\widetilde{u_i})}{\partial t} + \frac{\partial(\overline{\rho}\widetilde{u_i}\widetilde{u_j} + \overline{P}\delta_{ij} - \overline{\tau_{ji}} + \overline{\rho}(\widetilde{u_i u_j} - \widetilde{u_i}\widetilde{u_j}))}{\partial x_j} = \overline{\rho}\widetilde{f_i}, \tag{2.1.24}$$

$$\frac{\partial(\overline{\rho}\widetilde{E})}{\partial t} + \frac{\partial(\overline{\rho}\widetilde{u_j}\widetilde{E} + \widetilde{u_i}\overline{P} + \overline{q_j} - C_p\overline{\rho}(\widetilde{u_i T} - \widetilde{u_i}\widetilde{T}) - \widetilde{u_i}(\overline{\tau_{ij} - \tau_{ij}^t}))}{\partial x_j} = \overline{\rho}\widetilde{u_j f_j}, \tag{2.1.25}$$

The Reynolds stress $\mathcal{T}_{ij} = \overline{\rho}(\widetilde{u_i u_j} - \widetilde{u_i}\widetilde{u_j})$ requires a SGS model, e.g., Smagorinsky model, scale similarity model, Germano dynamic model, etc [44].

LES is usually more accurate than RANS because the small scales that are modeled tend to be more isotropic and homogeneous than the large ones, and thus more amenable to universal modeling [58]. Compared with DNS, LES does not suffer from the same strict resolution requirements of DNS, leading to a moderate computational cost, so it has the capability to handle complex geometries with unstructured, multi-element meshes, hence making LES potential tool for industry. Some reviews of LES can be found in the articles by Mason (1994) [59], Lesieur & Métais (1996) [60], Piomelli (1999) [61], and Meneveau & Katz (2000) [62].

2.1.4 Boundary layer

The aerodynamic boundary layer was first studied and defined by Ludwig Prandtl (1904) [63]. The fluid flow field bounded by surfaces having a zero velocity on the surface is divided into two areas: in the boundary layer, closest to the wall, the effects of viscosity are significant; in the outer layer, the effects of viscosity can be neglected. The concept of the boundary layer has since then become very important, helping the understanding and the modeling of wall flows. Lots of discussions on boundary layers have been published, e.g., Sakiadis (1961) [64], Lighthill (1963) [65], Kader (1981) [37], Robinson (1991) [66] and Schlichting (2000) [67], and books about turbulent flows, as the book of Pope (2000) [28], always make this topic as a separate section.

The dynamic boundary layer is typically investigated with flows over a semi-infinite flat plate. The flow transits from laminar to turbulent when the limit Reynolds number is reached, and the velocity boundary layer in the flow develops, as shown in Fig. 2.1.2.

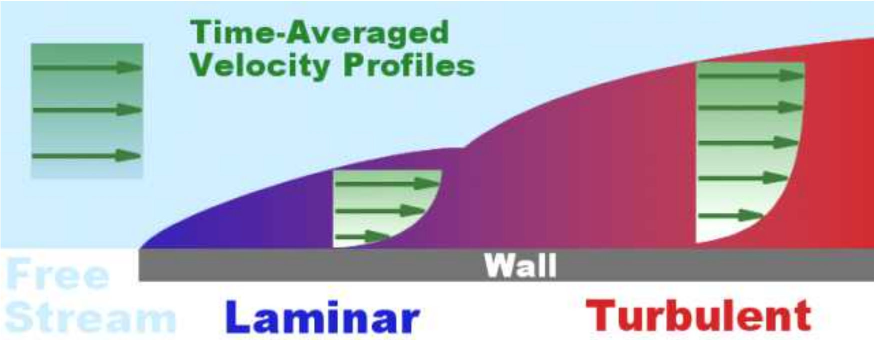

Figure 2.1.2: Boundary layer, showing transition from laminar to turbulent condition. Source: courtesy of Symscape [68].

The thickness of the dynamic boundary layer δ_{th} is usually defined as the distance from the wall at which the velocity is 99% of the freestream velocity. For flows over a semi-infinite flat plate or an open channel, the boundary layer thickness is based on $U = 99\% U_\infty$, where U_∞ is the freestream velocity at infinity. For the pipe or channel flows, the centerline velocity U_c is used to define δ_{th}.

When the surface temperature is not equal to the bulk flow temperature, a thermal boundary layer also develops. The thermal boundary layer shows a similar shape as the dynamic boundary layer when the Prandtl number is equal to 1 in laminar flows, thanks to the similarity in the momentum and energy balance, according to Blasius similarity solution [69]. If $\mathrm{Pr} > 1$, the thermal boundary layer is thinner than the velocity one, while if $\mathrm{Pr} < 1$, the thermal boundary layer is thicker.

In a fully developed turbulent wall flow, the profile of temperature established from the wall temperature to the stream temperature, leads to a constant wall heat flux. Like for laminar flow, the similarity between the temperature and velocity behaviors in the wall region has been extensively studied [70–73]. In particular, the definition of the non-dimensional temperature Θ (Eq. 2.1.26) is used to define the thickness of the thermal boundary layer δ_T

in a similar way as δ_{th}, as the distance from the wall at which $\Theta = 99\%$ [74].

$$\Theta = \frac{T_w - T}{T_w - T_{ref}}, \tag{2.1.26}$$

where T_w is the wall temperature and T_{ref} is chosen differently depending on the application case, e.g., freestream temperature at infinity T_∞ for a plate flow or centerline temperature T_c for channel or pipe flows [75].

2.1.5 Dimensionless quantities

This section gives the definition of some basic dimensionless quantities for wall flows.

Dimensionless velocity

To simplify the description of physical phenomena in wall flows, a two-dimensional domain is considered, where the streamwise direction and the wall-normal direction are noted x (velocity u) and y (velocity v), as illustrated in Fig. 2.1.3. The total shear stress in a turbulent wall flow is the sum of the viscous stress $\rho\nu(\partial\bar{u}/\partial y)$ and the Reynolds stress $-\rho\overline{u'v'}$:

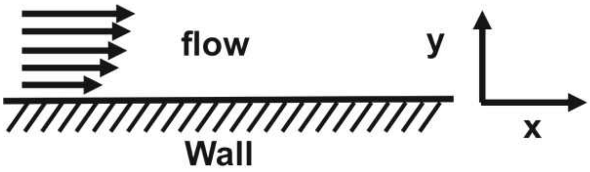

Figure 2.1.3: An illustration of the 2D domain of wall flow.

$$\tau = \rho\nu\frac{\partial\bar{u}}{\partial y} - \rho\overline{u'v'}, \tag{2.1.27}$$

where the operator $\bar{\cdot}$ indicates the time-averaged (mean) value, and u' and v' are the fluctuation velocities, using notations in Eq. 2.1.9. The boundary condition at the wall $u = 0$ dictates that all Reynolds stresses are zero, consequently the wall shear stress reduces to the viscous contribution:

$$\tau_w \equiv \rho\nu\left(\frac{\partial\bar{u}}{\partial y}\right)_w \equiv \rho\nu\left(\frac{\partial\bar{u}}{\partial y}\right)_{y=0} \tag{2.1.28}$$

The viscosity ν and the wall shear stress τ_w are evidently important in the study of wall flows. From these parameters, the friction velocity u_τ, the friction Reynolds number Re_τ based on the boundary layer thickness, the dimensionless velocity u^+ and the dimensionless distance from the wall y^+ are defined as:

$$u_\tau \equiv \sqrt{\frac{\tau_w}{\rho}}, \tag{2.1.29}$$

$$\mathrm{Re}_\tau \equiv \frac{u_\tau \delta_{th}}{\nu}, \tag{2.1.30}$$

$$u^+ \equiv \frac{u}{u_\tau}, \tag{2.1.31}$$

$$y^+ \equiv \frac{u_\tau y}{\nu} \tag{2.1.32}$$

Dimensionless temperature

Similarly, the friction temperature T_τ is defined [43]:

$$T_\tau = \frac{q_w}{\rho C_p u_\tau}, \tag{2.1.33}$$

where q_w is the wall heat flux $q_w = -\lambda(\partial T/\partial y)_w$. Replacing q_w with its expression leads to [76]:

$$T_\tau = -\frac{\alpha}{u_\tau}\left(\frac{\partial T}{\partial y}\right)_w \tag{2.1.34}$$

The temperature difference $T_w - T$ is then normalized by the friction temperature T_τ:

$$\Theta^+ = \frac{T_w - T}{T_\tau} \tag{2.1.35}$$

2.1.6 Flow regions in the turbulent boundary layer

Velocity

The wall distance y^+ in Eq. 2.1.32 has the form of a local Reynolds number, thus its magnitude can be viewed as the relative importance of viscous and inertial processes, and may be used to define the different regions in the boundary layer, summarized in Table 2.1.1.

Region	Location	Defining property
Viscous sublayer	$y^+ < 5$	The Reynolds shear stress is negligible compared with the viscous stress.
Logarithmic region	$y^+ > 30$	The velocity profile follows a logarithmic law.
Buffer layer	$5 < y^+ < 30$	The region between the viscous sublayer and the logarithmic region.

Table 2.1.1: Wall regions and their defining properties [28].

- For small y^+, the viscous sublayer is a region of dominant viscous processes. In this region the velocity profile follows linear evolution $u^+ = y^+$.

- For layer $y^+ > 30$, the mean velocity is proportional to the logarithm of the distance from wall [29]:

  $$u^+ = \frac{1}{\kappa} \log y^+ + C^+, \tag{2.1.36}$$

  where κ is the Von Karman constant and C^+ is also a constant, found to be from experiments $\kappa \sim 0.41$ and $C^+ \sim 5.0$ for smooth wall.

- For $5 < y^+ < 30$, is the buffer layer, connecting the two above regions.

Fig. 2.1.4 illustrates the various regions and the shape of the velocity curve in the boundary layer.

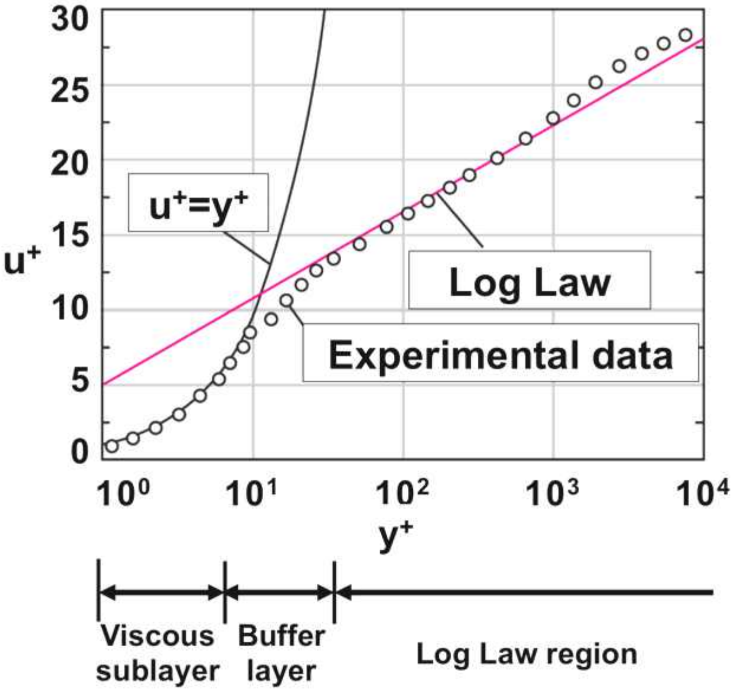

Figure 2.1.4: Wall flow structure in a fully developed turbulent flow in a pipe [77]

Temperature

Similar to the velocity, the profiles of mean temperature in turbulent wall flow can be interpreted by plotting the dimensionless temperature Θ^+ (Eq. 2.1.35) *vs* y^+, which also features a linear zone and a logarithmic zone.

The temperature profile is Prandtl number dependent, as shown in Fig. 2.1.5 [43]. Note that the y axis in the two figures is set differently to facilitate the visualization. Considering the non-dimensional temperature normalized by the friction temperature Θ^+, the linear part of wall law for temperature profile follows [37]:

$$\Theta^+ = Pr\ y^+, \tag{2.1.37}$$

while the logarithmic region becomes smaller with decreasing Pr. thus unlike the dynamic boundary layer, no classification of various wall regions is defined with the values of y^+. The

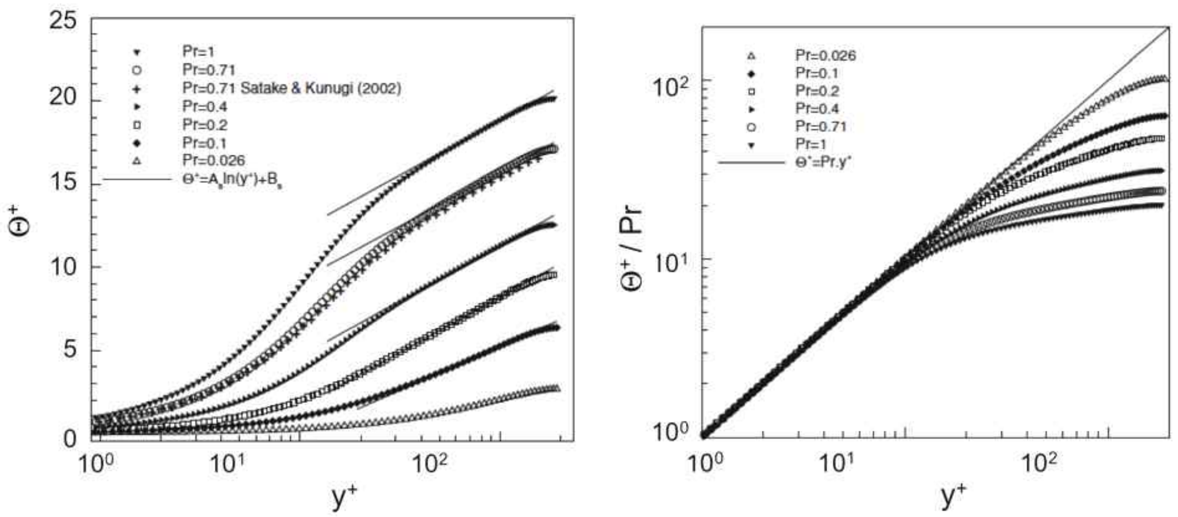

Figure 2.1.5: Mean temperature profiles in wall units for turbulent pipe flows: Pr dependence effect [43].

logarithmic law reads [37]:

$$\Theta^+ = \frac{1}{\kappa_\Theta} \log y^+ + \beta_\Theta, \tag{2.1.38}$$

where the values of constants κ_Θ and β_Θ are Pr dependent. For a flow with Pr=0.71 (close to the present work), the linear

For higher Prandtl number (Pr > 0.2), κ_Θ exhibits a plateau at 0.347 according to Redjem-Saad et al. (2007) [43], which agrees well with Piller's results (2005) for Pr=0.71 ($\kappa_\Theta = 0.34$) [42] but is smaller than the DNS prediction by Kawamura et al. (1999) [78] ($\kappa_\Theta \sim 0.4$), and the one proposed by Kays in his book for Pr=0.7 and 5.9 ($\kappa_\Theta \sim 0.45$) [75]. On the other hand, β_Θ is more affected by Prandtl number. Redjem-Saad et al. (2007) [43] reported that β_Θ is equal to 2 for Pr=0.71, while another form for β_Θ was proposed by Kays [75]:

$$\beta_\Theta = 13.39\text{Pr}^{2/3} - 5.66 \tag{2.1.39}$$

For a wall flow with Pr=0.71 (as in the present work), the linear wall region of the thermal boundary layer is $y^+ < 30$ while the logarithmic region is $y^+ > 90$.

2.1.7 Mean axial velocity profiles

The turbulent pipe flow is here taken as an example to show the axial velocity profiles across the tube section. In contrary to the fully developed laminar pipe flow, whose axial velocity profile is demonstrated by analysis to be parabolic, the mean velocity profile in a turbulent pipe flow is more complex and based on both analysis and experimental measurements. A typical streamwise velocity profile for fully developed turbulent pipe flow is given in Fig. 2.1.6 [77]. A sharp drop near the pipe wall is observed and the different layers as presented in Table 2.1.1 are indicated.

Numerous empirical velocity profiles exist for turbulent pipe flow, among which, the

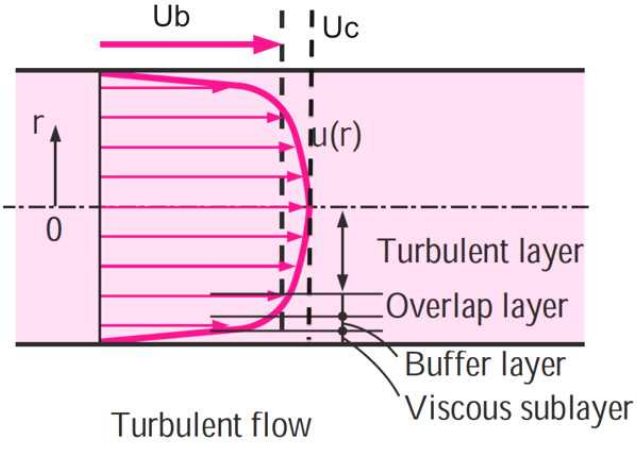

Figure 2.1.6: Typical streamwise velocity profile of fully developed turbulent pipe flow [77].

simplest and the best known is the power-law velocity profile expressed as:

$$\frac{U}{U_c} = \left(1 - \frac{r}{R}\right)^{1/n} \tag{2.1.40}$$

where U_c is the centerline velocity and the exponent n is a constant increasing with Reynolds number. The value 7 for n generally approximates many flows in practice [67,77]. Fig. 2.1.7 shows the various power-law velocity profiles for $n = 6, 8, 10$, comparing with the fully developed laminar flow. The turbulent velocity profile is flatter than laminar one and its flatness increases with increasing n, i.e., increasing Reynolds number. This agrees well with the experimental measurements of fully developed turbulent pipe flow (Re=50 000 and 500 000) by Laufer (1954) [34] and the numerical results of fully developed turbulent channel flow (Re=5600 and Re=13750) by Kim et al. (1987) [28,38]. Note that the power law profile fails to give zero slope at the centerline and cannot be used to calculate the streamwise

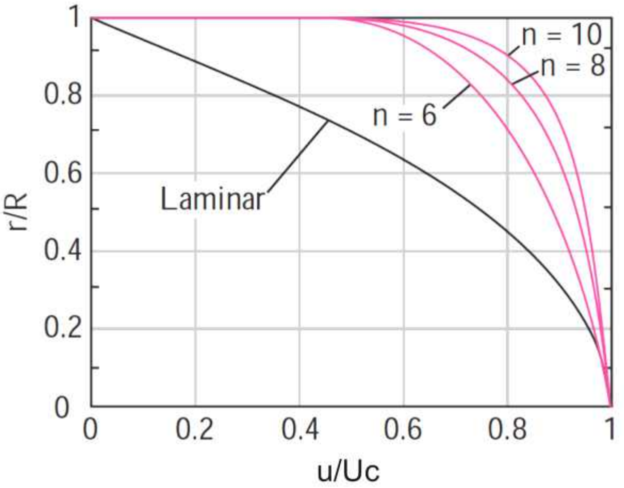

Figure 2.1.7: Various power-law velocity profiles for different exponents n, comparing with the fully developed laminar flow [77]

shear stress which is radially linear from the center to the wall in the time-averaged field of turbulent pipe flow, but these discrepancy only concerns a small portion of the flow, and the power law is still a good approximation [77].

2.1.8 Turbulence intensity

Velocity

Turbulence intensity can be measured from the velocity fluctuations u'_i, used to compute the turbulence kinetic energy (TKE) (Eq. 2.1.18). The dimensionless TKE k^* is normalized with the friction velocity:

$$k^* = \frac{k}{u_\tau^2} \tag{2.1.41}$$

The root-mean-square (RMS) of velocity fluctuations $u'_{i,rms} = \sqrt{\overline{(u'_i)^2}}$ is also normalized by u_τ:

$$u'^{+}_{i,rms} = u'_{i,rms}/u_\tau \tag{2.1.42}$$

Statistics obtained from the experimental data by Laufer (1954) [34] of a fully developed pipe flow at Reynolds number 50 000 are shown in Fig. 2.1.8, which plots the dimensionless

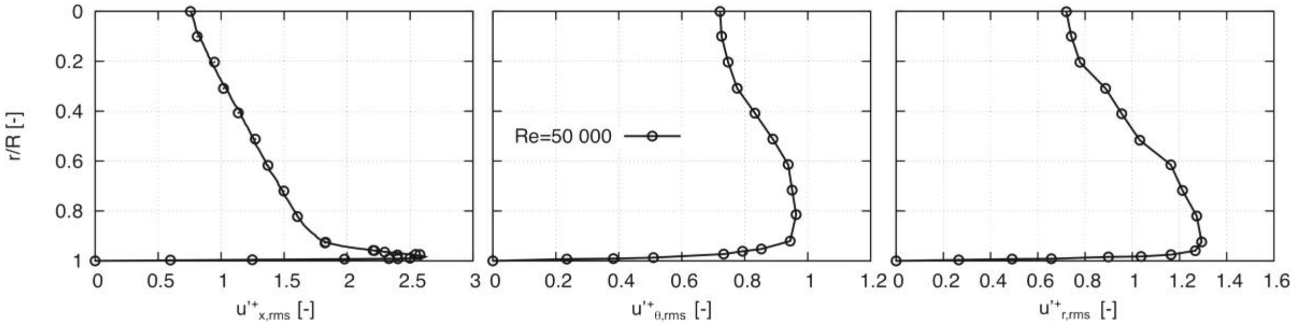

Figure 2.1.8: Dimensionless RMS of velocity fluctuations $u'^{+}_{x,rms}$, $u'^{+}_{\theta,rms}$ and $u'^{+}_{r,rms}$ versus the dimensionless radius r/R for fully developed turbulent pipe flow [34]

RMS of velocity fluctuations in cylinder coordinates $u'^{+}_{x,rms}$, $u'^{+}_{\theta,rms}$ and $u'^{+}_{r,rms}$ along the dimensionless radius r/R ($r/R = 0$ indicates the centerline and $r/R = 1$ represents the pipe wall). The axial velocity fluctuation is the strongest and the peak value is about twice the two others. The peak value appears close to the wall at $r/R = 0.998$ for $u'^{+}_{x,rms}$, while around $r/R = 0.9$ for $u'^{+}_{\theta,rms}$ and $u'^{+}_{r,rms}$. Very similar results were observed in DNS results of a turbulent pipe flow at Reynolds number around 7000 by Eggels et al. (1994) [39], except that the peak values of the velocity fluctuations, which are Reynolds number dependent [41], were lower than the ones observed in [34].

Temperature

The dimensionless temperature fluctuation is defined as:

$$\Theta'^{+}_{rms} = \frac{T'_{rms}}{T_\tau} \tag{2.1.43}$$

where $T'_{rms} = \sqrt{\overline{(T')^2}}$ is the RMS of the temperature fluctuation T'.

Redjem et al. (2007) [43] conducted DNS of turbulent pipe flow at Re=5500 and gave in Fig. 2.1.9 the effect of Prandtl number to the temperature fluctuation, showing increasing temperature fluctuation with increasing Pr, and comparing with DNS results by Satake & Kunugi (2002) [79] and Kawamura et al. (1998) [78]. The peak appears between $10 < y^+ < 70$ and comes closer to the wall with increasing Pr.

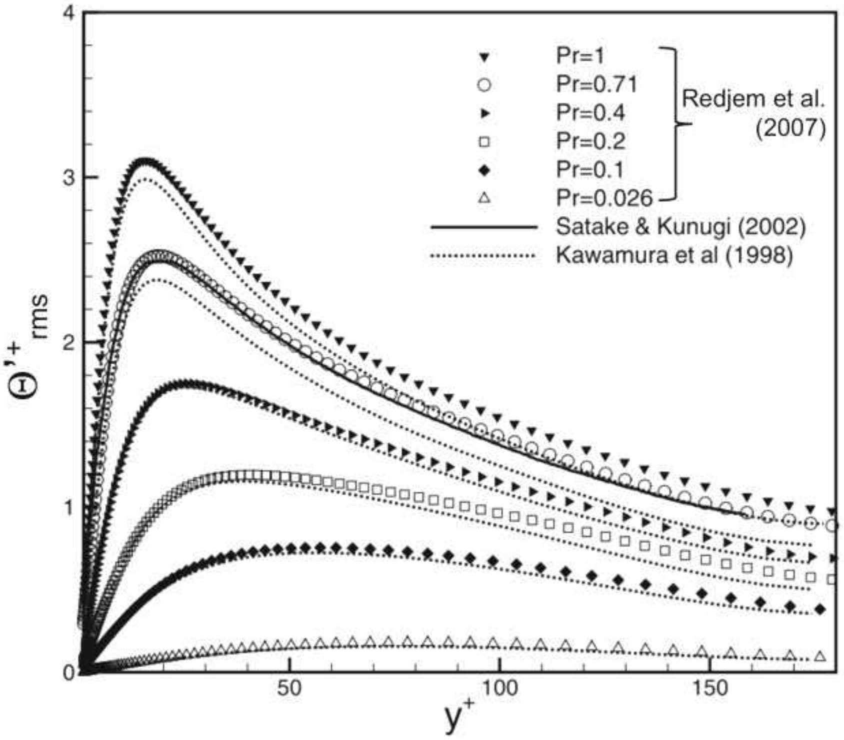

Figure 2.1.9: Dimensionless temperature fluctuation of turbulent pipe flows: Pr dependence effect [43].

2.1.9 Friction factor

The wall shear stress τ_w (Eq. 2.1.28) normalized by a reference kinetic energy is called the fanning friction factor (noted as f), named after John Thomas Fanning (1837-1911). It is defined:

$$f = \frac{\tau_w}{\frac{1}{2}\rho_{ref}U_{ref}^2} \tag{2.1.44}$$

The choice of the reference variables ρ_{ref} and U_{ref} depends on the configuration and conditions. In this study, bulk values will be used, with the bulk density (Eq. 2.1.45) and bulk velocity (Eq. 2.1.7) defined as:

$$\rho_b = \frac{1}{V}\int_V \rho dV \tag{2.1.45}$$

Note that this formula defines the Fanning friction factor f, which is by definition one-fourth of the Darcy friction factor f_D. Of the two, the Fanning friction factor is the more commonly used by chemical engineers and those following the British convention. In this report, all friction factors are Fanning friction factors.

Considering the balance of mean forces, the flow in a channel/tube is driven by pressure drop, i.e., pressure loss between the inflow and outflow. The pressure loss is deduced from Eq. 2.1.3 in its stationary ensemble-averaged form, integrated over the pipe volume V in steady conditions, leading:

$$\frac{\partial \overline{P}}{\partial x} = \frac{\int_S \tau_w \mathrm{d}S}{V}, \tag{2.1.46}$$

where S is the inner surface of the channel/pipe. For a channel flow, Eq. 2.1.46 can be simplified as:

$$\frac{\partial \overline{P}}{\partial x} = -\frac{\tau_w}{\delta}, \tag{2.1.47}$$

where δ is the half height of the channel. In a circular pipe flow, a similar expression is obtained:

$$\frac{\partial \overline{P}}{\partial x} = -\frac{4\tau_w}{D}, \tag{2.1.48}$$

where D is the inner pipe diameter.

Therefore, the global friction factor can be related to the pressure loss in a circular pipe:

$$f_g = \frac{\partial P}{\partial x}\frac{D}{2\rho_b U_b^2} \tag{2.1.49}$$

2.1.10 Wall heat transfer

Heat transfer coefficient

Convective heat transfer in fluids is a combination of advection and conduction of heat. On no-slip walls, as the flow velocity on wall is zero, no advection occurs and there is only conductive heat transfer between solid surfaces and flows. This conductive heat transfer is the main heat transfer mode in tubes heated by flames in a furnace in many chemical processes (when radiation can be neglected). To describe this kind of heat transfer, the heat transfer coefficient h is defined as the ratio between the wall heat flux q_w and the thermodynamic driving force:

$$\mathrm{h} = \frac{q_w}{\Delta T} = \frac{q_w}{T_w - T_{ref}}, \tag{2.1.50}$$

where the reference temperature T_{ref} is often chosen as the bulk temperature of the fluid:

$$T_b = \frac{\int_V \overline{\rho u T}\mathrm{d}V}{\int \overline{\rho u}\mathrm{d}V} \tag{2.1.51}$$

As the temperature and the heat flux at the fluid/solid interface are equal in the fluid and the solid, the heat transfer coefficient h in Eq. 2.1.50 for the fluid at the wall may be rewritten as:

$$\mathrm{h} = \frac{-\lambda\left(\dfrac{\partial T}{\partial n}\right)_w}{\Delta T} \tag{2.1.52}$$

with n representing the wall normal.

Nusselt Number

Nusselt number, Named after Wilhelm Nusselt, is a dimensionless number defined with the heat transfer coefficient h and thermal conductivity λ:

$$\mathrm{Nu} = \frac{hL}{\lambda}, \tag{2.1.53}$$

where L is a characteristic length, usually taken as the inner diameter D of tubes for pipe flows.

Using Eq. 2.1.52 for h, the Nusselt number may be written as:

$$\mathrm{Nu} = -\left(\frac{\partial T}{\partial n}\right)_w \left(\frac{L}{\Delta T}\right) \tag{2.1.54}$$

As a consequence, for a given geometry and the same ΔT, Nu is proportional to the temperature gradient at the wall.

The Nusselt number is a measure of the efficiency of the heat transfer, and more precisely of the impact of convection on the wall heating or cooling. As turbulence increases mixing, for a flow with imposed wall temperature, the heat flux at the wall is established more rapidly and it leads to larger Nusselt number.

In the present work, the Nusselt number in tubes is obtained from the formula:

$$\mathrm{Nu} = \frac{q_w D}{\lambda(T_w - T_b)} \tag{2.1.55}$$

where λ is calculated from Eq. 2.1.8, knowing the Prandtl number, kinematic viscosity ν, mass density ρ and the heat capacity C_p of the fluid. The global Nusselt number Nu_g is defined with the averaged wall flux $q_{w,g}$ over the surface of the tube instead of the local wall flux q_w:

$$q_{w,g} = \frac{\int_S q_w \mathrm{d}S}{S} \tag{2.1.56}$$

Note that, contrary to the wall shear stress τ_w which stays constant along the tube, the heat flux q_w may vary depending on the thermal treatment applied to the tube, justifying the definition of a local and a global Nusselt number.

Stanton Number

As a complement, the Stanton number, St or C_H, named after Thomas Edward Stanton (1865-1931), is also introduced. It is a dimensionless number that measures the ratio of heat transferred into a fluid to its thermal capacity. It is used to characterize heat transfer in forced convection flows:

$$\mathrm{St} = \frac{h}{C_p \rho_b U_b}, \tag{2.1.57}$$

The Stanton, Nusselt, Reynolds, and Prandlt numbers are linked through the relation:

$$\mathrm{St} = \frac{Nu}{Re \cdot Pr} \tag{2.1.58}$$

2.2 Correlations for the friction factor and Nusselt number in smooth tubes

Many theoretical, semi-theoretical or experimental correlations for the friction factor and Nusselt number exist. For pipe flows, flows with constant physical properties have been firstly studied, then, correlations with variable physical properties have been proposed for the application to industrial heat-exchange systems which often operate under conditions of high heat load, thus considerable variation of physical properties of liquids or gases [35].

To carry out the analysis, the following assumptions are made [35]:

- the effect of mass forces is small in comparison with the effect of viscous and inertial forces.
- flows far from the inlet of the tube are investigated, thus the change in the axial component of mass velocity along the tube axis is small.

Oonly correlations for turbulent flow are discussed in this section.

2.2.1 Friction factor

The friction factor f_g depends on the parameters of the pipe and the velocity of the flow, but it is known with high accuracy within certain flow regimes. It may be evaluated for given conditions by the use of various empirical or theoretical relations, or it may be obtained from published charts. These charts are often referred to as Moody diagrams [32] (see Fig. 2.2.1), after L. F. Moody, and hence the factor itself is sometimes called the Moody friction factor. The Moody diagram is divided into two regions: laminar and turbulent (between these two regions, in the “transition region”, the flow behaviors are more difficult to capture). For a rough pipe, the friction factor can be read by knowing the “relative roughness” (on the right side of the diagram, this parameter was mostly used in the early research about rough pipe flows, which will be introduced in section 2.4.1.)

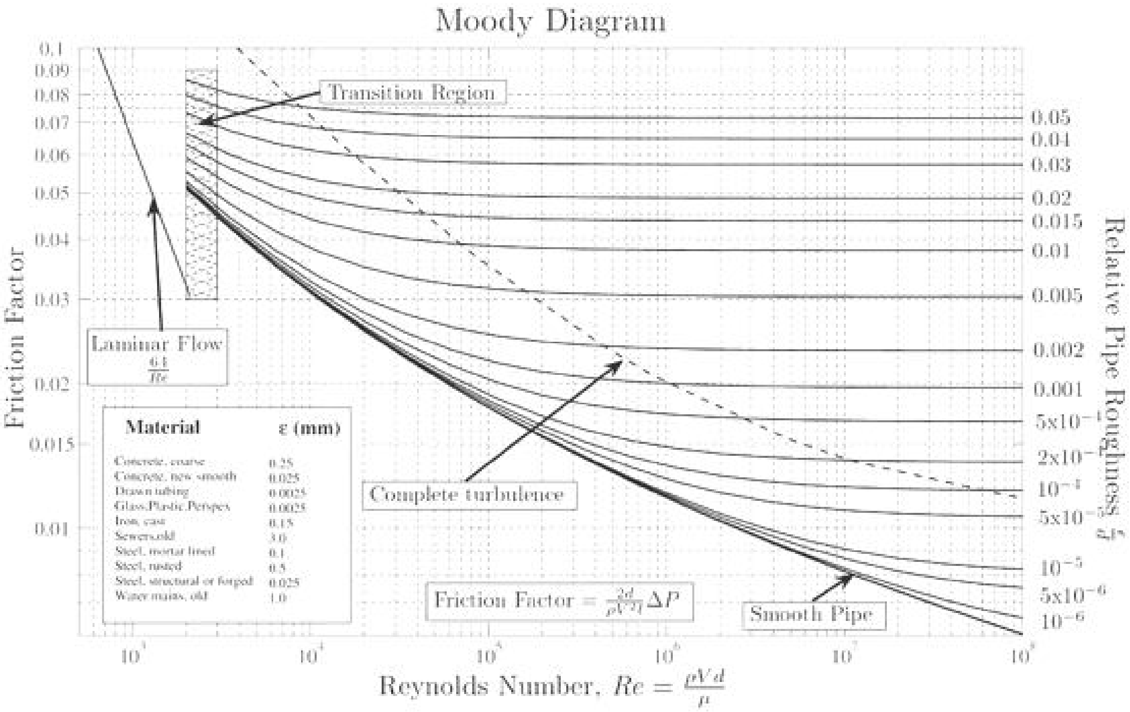

Figure 2.2.1: Moody diagram - friction factor *vs* Reynolds number [32].

The friction factor f_g can also be obtained from correlation formula. The classical Kármán-Nikuradse equation was obtained semi-experimentally by Kármán (1934) [75, 80]:

$$\frac{1}{\sqrt{f_g/2}} = 2.46 \ln \mathrm{Re}\sqrt{f_g/2} + 0.30 \tag{2.2.1}$$

As this equation is an implicit one, and not very handy to use, Kays gave a commonly employed empirical equation that closely fits the Kármán-Nikuradse equation over the range $3 \times 10^4 < \mathrm{Re} < 10^6$:

$$f_g = 0.046\mathrm{Re}^{-0.2} \tag{2.2.2}$$

Another formula was given by Petukhov [35] in 1963:

$$f_g = \frac{1}{(1.58 \ln \mathrm{Re} - 3.28)^2} \quad \text{for} \quad 10^4 < \mathrm{Re} < 5 \times 10^6 \tag{2.2.3}$$

One of the most wildly used correlations was proposed by Blasius in 1913 [69] (among several), and is called the Blasius friction factor. Assuming a one-seventh power-law velocity profile [40], Blasius obtained [81]:

$$f_g = 0.079\mathrm{Re}^{-0.25} \tag{2.2.4}$$

It is used as a reference in the present work.

2.2.2 Nusselt number

Contrary to the friction factor which is related only to the Reynolds number, the Nusselt number depends on both the Reynolds number and the Prandtl number. The impact of Prandtl number has been widely studied experimentally and numerically [43, 78, 82]. By using an analogy between friction and heat transfer, Kays [75] proposed a semi-experimental formula for the global Nusselt number (the formula of Stanton number can also be found in his book):

$$\mathrm{Nu}_g = \frac{\mathrm{Re}\mathrm{Pr}(f_g/2)}{0.88 + 13.39(\mathrm{Pr}^{2/3} - 0.78)\sqrt{f_g/2}}, \tag{2.2.5}$$

for a circular tube with Prandtl numbers in the range 0.6-6.0.

By replacing the friction factor f_g in Eq. 2.2.2, the formula becomes:

$$\mathrm{Nu}_g = \frac{0.023\mathrm{Re}^{0.8}\mathrm{Pr}}{0.88 + 2.03(\mathrm{Pr}^{2/3} - 0.78)\mathrm{Re}^{-0.1}}, \tag{2.2.6}$$

Similarly, Petukhov [35] proposed in 1963:

$$\mathrm{Nu}_g = \frac{\mathrm{Re}\mathrm{Pr}(f_g/2)}{1.07 + 12.7(\mathrm{Pr}^{2/3} - 1)\sqrt{f_g/2}}, \tag{2.2.7}$$

with f_g in Eq. 2.2.3.

This correlation was later modified by Gnielinski [83] in 1976, using experimental data in a Reynolds number range from 2300 to 10 000:

$$\mathrm{Nu}_g = \frac{(\mathrm{Re} - 1000)\mathrm{Pr}(f_g/2)}{1 + 12.7(\mathrm{Pr}^{2/3} - 1)\sqrt{f_g/2}}, \tag{2.2.8}$$

Kays [75] reported in his book that this formula was in fact in the valid Reynolds number range [2300, 5×10^6] and Prandtl number range [0.5, 2000].

Kays also indicated that, in the Prandtl number range [0.5, 1.0], Eq. 2.2.6 can be approximated quite well by [75]:

$$\mathrm{Nu}_g = 0.022\mathrm{Re}^{0.8}\mathrm{Pr}^{0.5} \tag{2.2.9}$$

This expression is very close to the most widely used “Dittus-Boelter correlation” for a heating case:

$$\mathrm{Nu}_g = 0.023\mathrm{Re}^{0.8}\mathrm{Pr}^{0.4} \tag{2.2.10}$$

Expression 2.2.10 is a little different from the original “Dittus-Boelter correlation” in the paper of Dittus & Boelter (1930) [84], and the history of correlations of the type $\mathrm{Nu}_g = A\mathrm{Re}^B\mathrm{Pr}^C$, where A, B, C are constants, can be found in Winterton (1998) [85]. Dittus & Boelter (1930) [84] summarized all the available data (from McAdams & Frost (1922, 1924) [86, 87], and Morris & Whitman (1928) [88]) [40], and averaged them to get the correlations. By converting all the variables in Dittus & Boelter (1930) [84] to basic SI unit, Winterton (1988) [85] found the original Dittus-Boelter correlations to be:

$$\mathrm{Nu}_g = \begin{cases} 0.0241\mathrm{Re}^{0.8}\mathrm{Pr}^{0.4} & \text{for heating} \\ 0.0264\mathrm{Re}^{0.8}\mathrm{Pr}^{0.3} & \text{for cooling} \end{cases} \tag{2.2.11}$$

which agree well with Kays [75].

2.2.3 Correlations for flows having variable properties

According to Kays [75], for liquids where the viscosity variation is responsible for most of the effect, excellent approximations can be obtained from:

$$\frac{f_{g,v}}{f_{g,c}} = \left(\frac{\mu_w}{\mu_b}\right)^m \tag{2.2.12}$$

$$\frac{\mathrm{Nu}_{g,v}}{\mathrm{Nu}_{g,c}} = \frac{\mathrm{St}_v}{\mathrm{St}_c} = \left(\frac{\mu_w}{\mu_b}\right)^n \tag{2.2.13}$$

where index v means the estimation value for variable properties flows (non-isothermal flows), index c indicates constant properties flows (isothermal flows), and μ_w and μ_b are the dynamic viscosities respectively at the wall temperature and the bulk temperature. Sieder and Tate (1936) [89] proposed $m = n = 0.14$.

On the other hand, as the viscosity, thermal conductivity, and density of gases depend on the temperature, and as this dependence is similar for different gases, the temperature-dependent-property effects can be correlated by:

$$\frac{f_{g,v}}{f_{g,c}} = \left(\frac{T_w}{T_f}\right)^m, \tag{2.2.14}$$

$$\frac{\mathrm{Nu}_{g,v}}{\mathrm{Nu}_{g,c}} = \frac{\mathrm{St}_v}{\mathrm{St}_c} = \left(\frac{T_w}{T_f}\right)^n, \tag{2.2.15}$$

where T_f is the mean calorimetric temperature of the fluid in the section of the tube [75], which can be considered as T_b in the present work.

The indices m and n in Eq. 2.2.15 and 2.2.15 are discussed below.

Index m for the friction factor

Petukhov (1963) [35] considered the results for air and hydrogen at high temperature load. By tracing the relation between $f_{g,v}$ and $f_{g,c}$ in function of Reynolds number, he noted that the ratio m is strongly dependent on the Reynolds number, and proposed:

$$m = \begin{cases} -0.6 + 3.3/(\mathrm{Re}\sqrt{f_{b,c}/32})^{1/2} & \text{for heating,} \\ -0.6 + 0.6/(\mathrm{Re}\sqrt{f_{b,c}/32})^{1/8} & \text{for cooling} \end{cases}$$

When Re varies from 14×10^3 to 10^6, the value of m varies from -0.44 to -0.58 for heating and from -0.32 to -0.42 for cooling. m can also be taken as constant and equal to -0.52 for heating and equal to -0.38 for cooling, giving an error of less than 7% and 4% respectively [35].

Moreover, Petukhov compared his correlation with the experimental results from Il'in [90] and found good agreement for heating condition but not for cooling condition.

On the other hand, Kays [75] proposed m =-0.1.

Index n for the Nusselt number

Petukhov [35] noted that index n for the Nusselt number in Eq. 2.2.15 also depends on Reynolds number, but in contrast to the friction factor, this dependence is not strong. So he proposed a constant value for n: for the air and hydrogen flow in the Reynolds number range $[1.4\ 10^4, 10^6]$, $n = -0.5$ for heating and $n = -1/3$ for cooling.

Kays [75] also proposed n values for $T_w/T_b < 1$ and $T_w/T_b > 5$, while Sleicher & Rouse (1975) [91] gave n for $1 < T_w/T_b < 5$ [92]:

$$n = \begin{cases} 0, & T_w/T_b < 1 \\ -\left[\log_{10}\left(\frac{T_w}{T_b}\right)\right]^{1/4} + 0.3, & 1 < T_w/T_b < 5 \\ -0.5 & T_w/T_b > 5 \end{cases} \tag{2.2.16}$$

2.3 Turbulent flow over ribbed walls: review of experiments

In this section, the turbulent flow over rough wall is discussed. Many experiments have been conducted to investigate global quantities like the global friction factor and Nusselt number for different kinds of rough tubes/channels flows, and various correlation formula for friction factor and Nusselt number are proposed in the literature. However, the flow structures or the velocity/temperature fields of fully developed turbulent flow in a ribbed tube are rarely experimentally measured due to measurement difficulties. Only Nourmohammadi et al. [93] performed experimental investigations of fully developed turbulent flow in regularly ribbed tubes (i.e., tubes with repeated or transversal ribs) and gave streamwise velocity and shear stress profiles at different axial locations. More literature may be found about ribbed channels or plates, where particle image velocimetry (PIV) [94–99], microphone array and split-fiber film [100] were used to measure the velocity and wall-pressure, as well as real-time holographic interferometry [101], Liquid Crystal Thermometry (LCT) [95] or infrared thermography (IRT) [102] to measure the heat transfer.

Since the turbulent flow over ribbed channels/plates is qualitatively representative of most kind of ribbed walls, this section makes a short review of such flows to give a preliminary impression of what could be expected in ribbed tubes. Despite that the turbulent boundary layers over a ribbed plate or a ribbed channel show some discrepancy due to the different outer boundary condition [97], this discrepancy will be ignored in the present review.

2.3.1 Turbulent flow structure over ribbed walls

Because of the presence of ribs on the wall, separation of the turbulent flow occurs behind the obstacle where recirculation flow patterns appear, as shown in Fig. 2.3.1, and reattachment

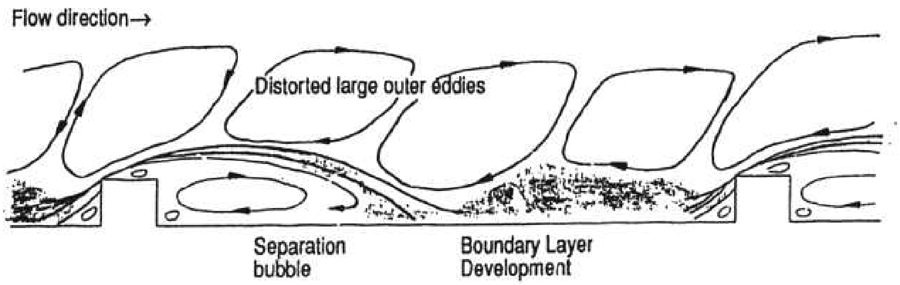

Figure 2.3.1: Illustration of turbulent flow structure with the separation and reattachment mechanisms in a ribbed channel [103].

location depends on the rib pitch. If the turbulent flow is not fully developed, different flow patterns are observed along the channel: reattachment occurs earlier after the last rib than the first rib [104]. This phenomenon is not in considered in the present work, where only fully developed turbulent flows are studied.

The impact of the rib pitch on reattachment is observed in Fig. 2.3.2 as proposed by Webb et al. (1971) [14]. When the pitch tends to infinity, the reattachment distance tends

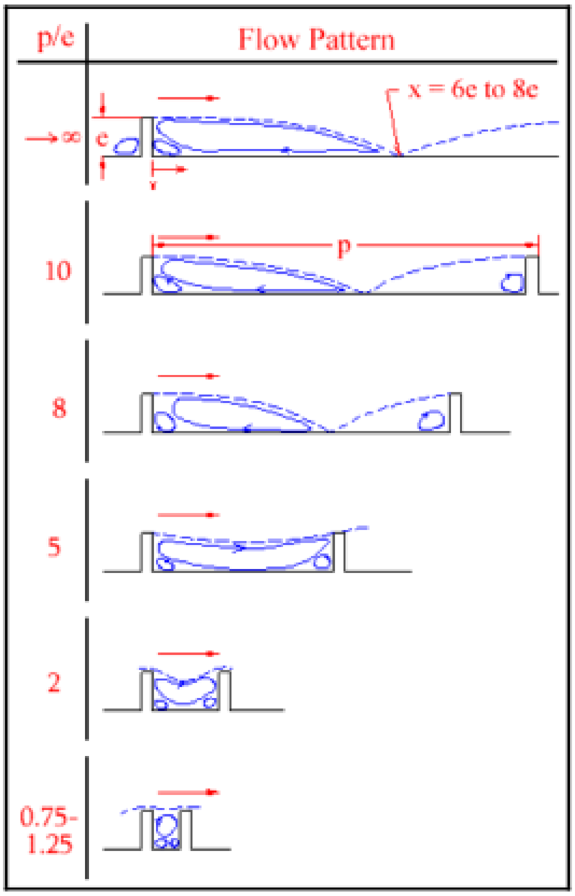

Figure 2.3.2: Recirculation flow patterns over transverse ribs as a function of rib pitch in a ribbed channel [14, 105].

to stay in the range $6e$ to $8e$ where e is the rib height. This agrees with Mantle (1966) [106]'s observation of a constant reattachment length in this case at $8.5e$. Liu et al. (2008) [100]

measured a reattachment length of $9.75e$ for a turbulent flow over a plate with only one rib.

With the decreasing of the rib pitch (Webb et al. (1971) [14] proposed the range $5 < p/e < 10$), the reattachment appears earlier. Mantle (1966) [106] reported that the reattachment length decreases from 8.5 to 4 as p/e decreases from 28 to 12 [107]. Aliaga et al. (1994) observed similar results (reattachment length between $3e$ and $4e$ for p/e=12) [108], and Islam et al. (2002) [109] demonstrated a reattachment length approximately $4e$ for $p/e = 10$ and 20.

Finally reattachment disappears when p/e is below 5. This limit p/e was found to be 6.6 by Mantle (1966) [106], and the experimental results of Aliaga et al. (1994) [108] confirmed no reattachment for $p/e = 5$. Tsikata & Tachie (2013) [99] recently tested three ribbed channel flows with $p/e = 2, 4, 8$ respectively, showing reattachment only for $p/e = 8$. This coincides with the classification of K-type ($p/e > 4$) and D-type ($p/e < 4$) roughness, also mentioned by Jimenez (2004) [110].

2.3.2 Mean velocity profiles in ribbed channels

Unlike the velocity profiles in smooth tubes where the profiles do not evolve, in the rough tube, velocity profiles vary significantly between two consecutive ribs. Still, for a fully developed turbulent flow, all patterns between two consecutive ribs behave the same. This pattern, stretched in Fig. 2.3.3, may be discretized in segments of length $1e$, where e is the rib height.

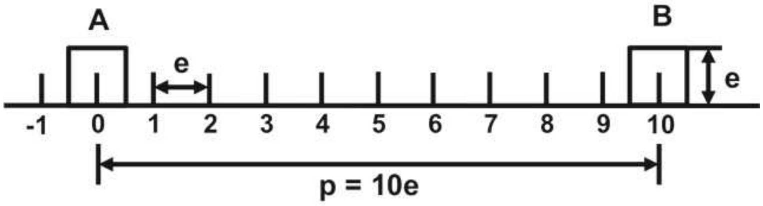

Figure 2.3.3: Numerotation of successive locations between two ribs A and B, with distances expressed in rib height e unit.

All measurements of the mean velocity profiles in regularly transverse-ribbed channels give very similar results, in Liou et al. (1993) [101], Casarsa et al. (2002) [95], Palikaras et al. (2003) [94], Lee et al. (2008) [111], Wang et al. (2010) [98], and Tsikata & Tachie (2013) [99]. Fig. 2.3.4 shows the mean streamwise velocity field with streamlines, measured by Tsikata & Tachie (2013) [99]. Mean streamwise velocity profiles normalized by the bulk velocity, at different locations in a ribbed channel by Labbé (2013) [112] are illustrated in Fig. 2.3.5. From Fig. 2.3.4 and Fig. 2.3.5, the following phenomena are observed: first, a flow acceleration on rib top appears; second, the recirculation zones appear in front (a small one) and behind the ribs (a larger one), the latter ending at a distance $x = 3e$ to $4e$ away from the rib center, where reattachment occurs, which agrees well with the reattachment length reported by other authors mentioned in section 2.3.1.

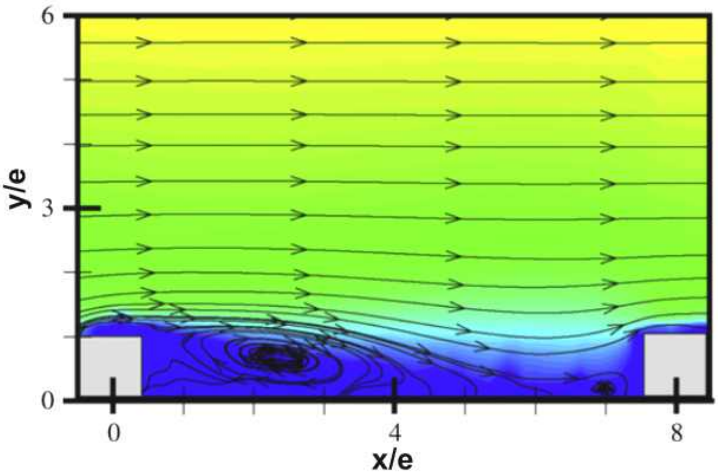

Figure 2.3.4: Mean streamwise velocity field with the streamlines in ribbed channel where $p/e = 8$ [99].

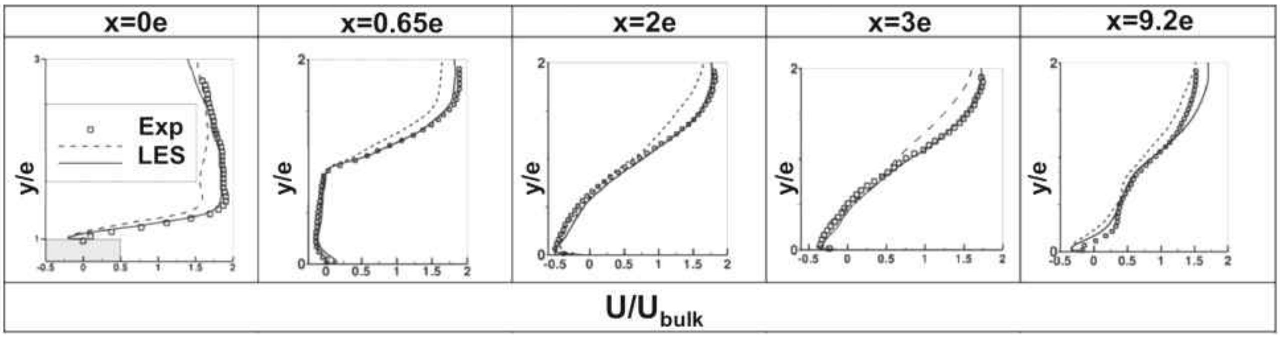

Figure 2.3.5: Mean normalized streamwise velocity profiles at different locations in a ribbed channel where $p/e = 10$ (experimental results: symbols) [95]. LES results are also plotted with lines [112].

Comparison with the smooth tube

The streamwise velocity profile in ribbed and smooth channels are compared in the work by Tsikata and Tachie (2013) [99] as shown in Fig. 2.3.6, where the smooth tube data taken from DNS of Moser et al. (1999) [41] and the experimental data of the ribbed channel is validated by DNS of Leonardi et al. (2004) [113] and of Nagano et al. (2004) [114]. The distance from the wall is normalized with each boundary layer thickness δ_{th} (but the location where the δ_{th} is measured in the ribbed channel is not mentioned by Tsikata and Tachie (2013) [99]), thicker on ribbed wall than on smooth wall, and even thicker with increasing rib pitch ($p/e = 2, 4, 8$ are investigated in [99]). The mean steamwise velocities are all normalized with the maximum streamwise mean velocity value U_m, which are the same in the ribbed and smooth channel. As the channel has a diverging form, two different regions, in the parallel section and diverging section respectively, are chosen to plot the profiles. The impact of ribs is observed in Fig. 2.3.6 where only the case $p/e = 8$ is shown. Within the boundary layer, the velocity increases rapidly away from the smooth wall, but much more slowly over the ribbed wall. Similar effects are observed at the two locations, the difference being due to the diverging shape.

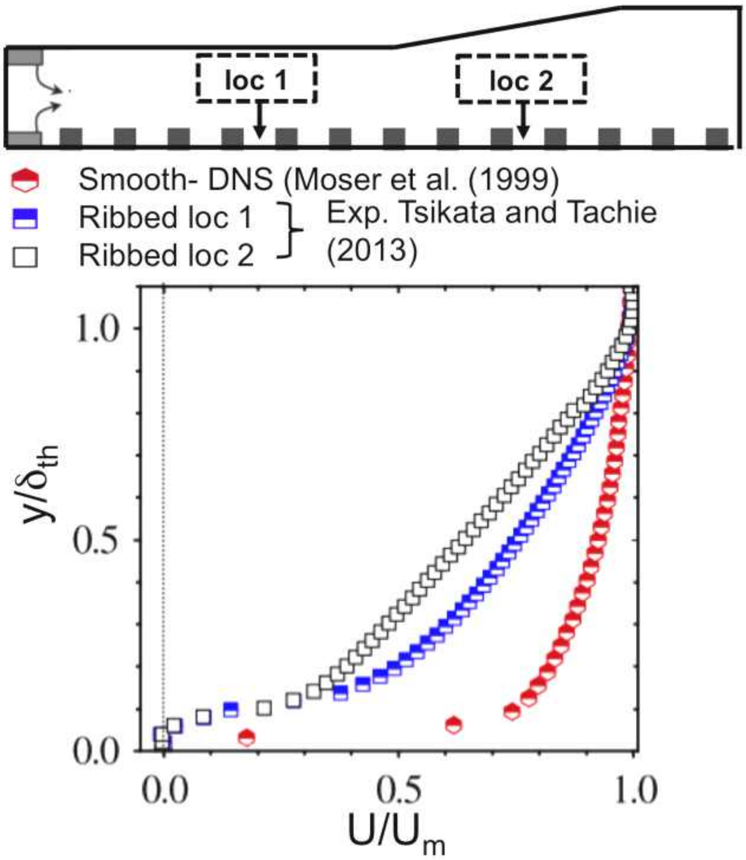

Figure 2.3.6: Mean streamwise velocity profiles over smooth and ribbed walls, normalized by the mixed outer velocity [99].

When plotted in wall units, the profiles show a global velocity shift $\Delta U^+ = 9.86$ [99,115] in the ribbed channel compared to the smooth wall, as shown in Fig. 2.3.7. Agelinchaab and

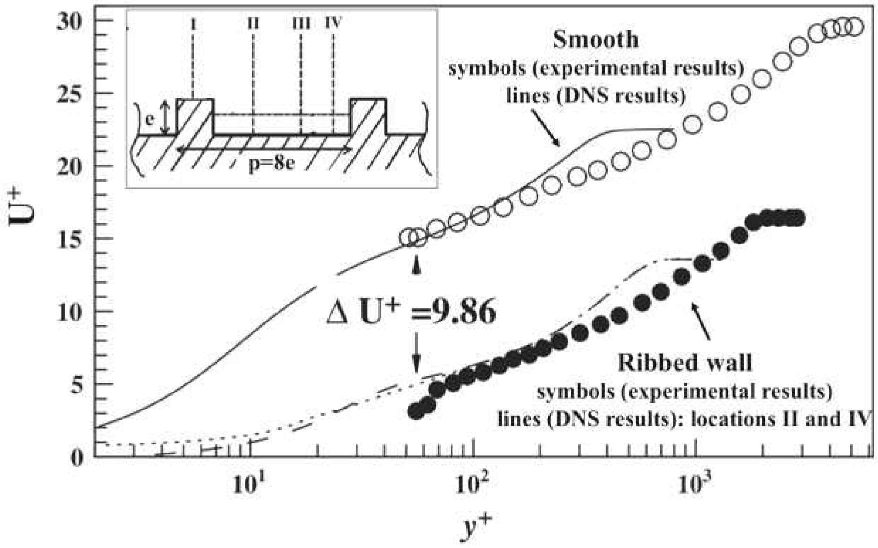

Figure 2.3.7: Mean streamwise velocity profiles in wall units for two locations II and IV between ribs (black symbols), comparing with the experimental data of smooth wall (white symbols) [115], and DNS results are also plotted in lines [111].

Tachie (2006) [116] found similar results over hemispherical ribs in open channel flow, and observed that with increasing p/e (2, 4 and 8 in their experiments), the shift ΔU^+ increases.

2.3.3 Velocity fluctuations in ribbed channel

Measurements of velocity fluctuations were also reported in previous literature. The profiles of the RMS of axial and normal velocity fluctuations u'_{rms} and v'_{rms} (using the same notation as in Fig. 2.1.3) normalized by the bulk velocity U_b (note that they are not normalized by the friction velocity u_τ), at different locations in the ribbed channel, is illustrated in Fig. 2.3.8 by Labbé (2013) [112]. The profiles are disturbed by the recirculation zone near the wall, and the peaks appear at a different distance from the wall for the different locations. Casarsa et al. (2002) [95] and Labbé (2013) [112] mentioned that the maximum value decreases with the axial distance, but this was not observed by other authors. Note that, fluctuations v'_{rms} are weaker than u'_{rms}.

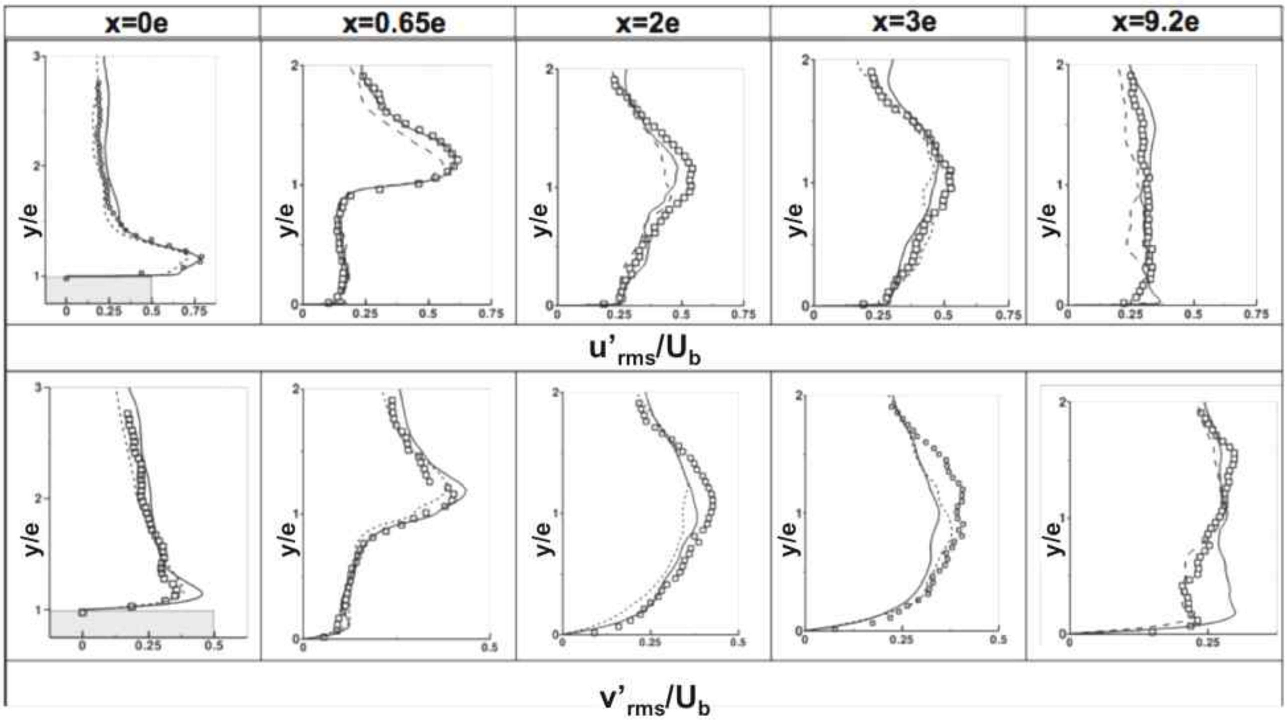

Figure 2.3.8: Profiles of the mean velocity fluctuations u'_{rms} and v'_{rms} normalized by the bulk velocity U_b, at different locations in a ribbed channel where $p/e = 10$ (experimental results: symbols) [95]. LES results are also plotted in lines for two locations [112].

Comparison with the smooth tube

The comparison of velocity fluctuations with smooth channels was also done by Tsikata and Tachie (2013) [99], as shown in Fig. 2.3.9. The Reynolds normal stress u'^2_{rms}/U^2_m defined with the RMS of the axial fluctuation velocity u'_{rms} and the mixed outer velocity U_m is investigated, and the distance from the wall is normalized with half of the channel height δ. Profiles are plotted at two locations, as introduced in Fig. 2.3.6. The peak appears closer to the wall in the smooth channel, while it moves towards the center in ribbed channel, and

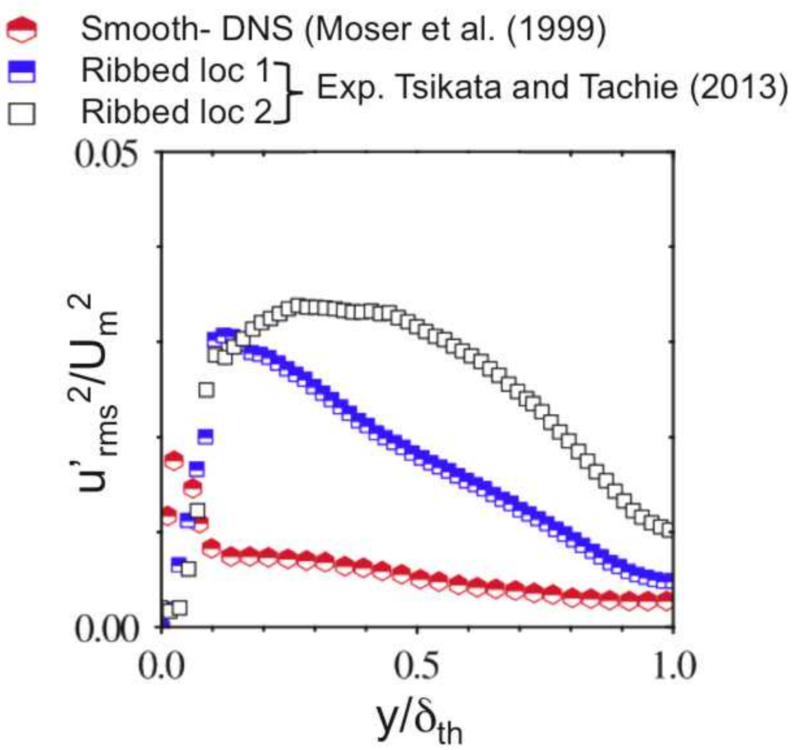

Figure 2.3.9: Streamwise Reynolds normal stress over the smooth and ribbed walls [99].

ribs induce stronger fluctuations. The difference between the two locations in the ribbed channel is due to the diverging shape of the tested channel.

2.3.4 Temperature profiles in ribbed channel

Only Liou et al. (1993) [101] reported experimental results of temperature profiles using real-time holographic interferometry. Profiles of instantaneous dimensionless temperature Θ^+ (Eq. 2.1.35) are plotted in Fig. 2.3.10 for three locations (no time-averaged results are reported). The wall distance is normalized with the channel height h. The upper wall of the channel ($y/h = 1$) is an adiabatic smooth wall, while the temperature of the bottom ribbed wall ($y/h = 1$) T_w is higher than the upper smooth wall temperature. Higher dimensionless temperature Θ^+ (thus lower temperature) is observed with further distance x/e, and at location $x/e = 2.5$, the thermal boundary layer is thicker due to the recirculation zone. On rib top $x/e = 0$ and on $x/e = 5.5$, the temperature gradient at the ribbed wall is stronger, leading to a higher heat flux.

2.3.5 Distribution of local friction coefficient over ribbed wall

The local friction coefficient, usually noted as C_f, defined differently from Eq. 2.1.44:

$$C_f = \frac{\vec{\tau}(x)}{\frac{1}{2}\rho_{ref} U_{ref}^2} \tag{2.3.1}$$

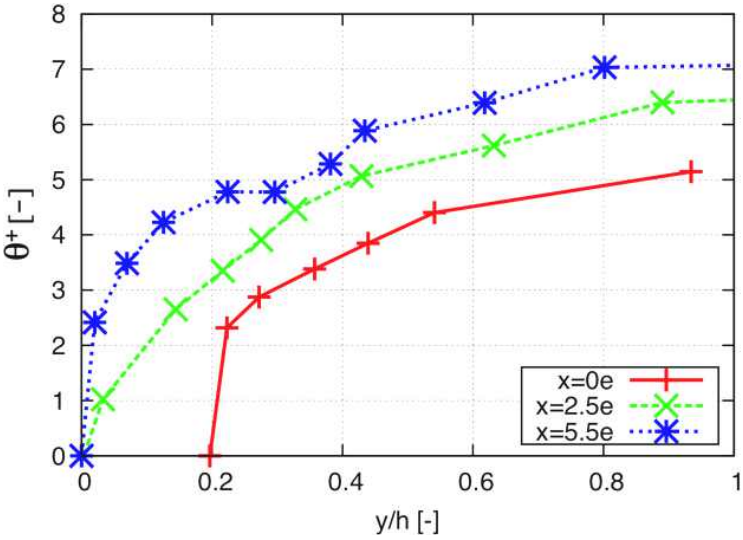

Figure 2.3.10: Dimensionless temperature profiles in ribbed channel ($p/e = 7.2$) [101].

where $\vec{\tau}(x)$ is the axial component of the stress vector (see Appendix B). In contrary to the smooth wall, where the friction factor is the same all along the wall for a fully developed turbulent channel/tube flow, on a ribbed wall, C_f changes at different locations, and has a negative value in the recirculation zone. A view of the distribution of the local friction coefficient over a ribbed wall is given in Fig. 2.3.11 by Lee et al. (2008) [97], and a comparisons

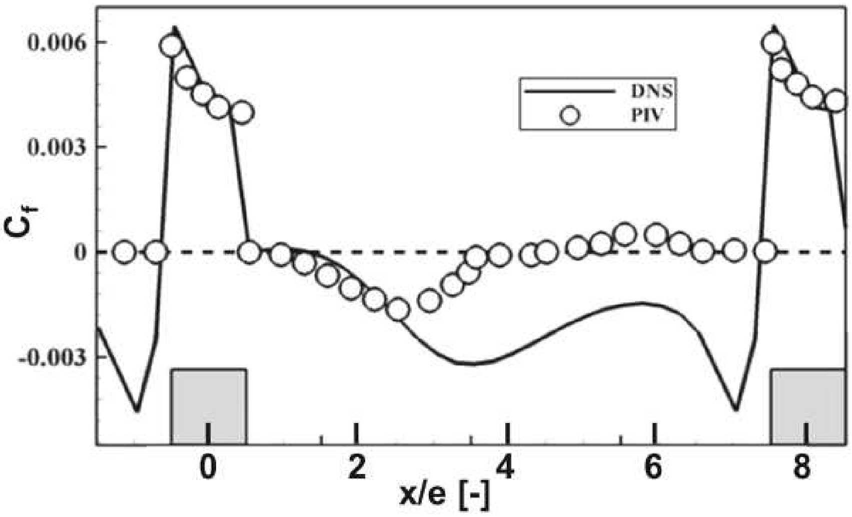

Figure 2.3.11: Distribution of local friction factor over ribbed wall ($p/e = 8$) [97].

with DNS results by Lee & Sung (2007) [117] is also shown. Maximum value is observed on top of the ribs and negative value is found in the recirculation zone. DNS results give negative values in the whole region between the two ribs, which seems not usual. Lee et al. (2008) [97] attributed the discrepancy between results of PIV and DNS to the limited spatial resolution of PIV along the wall-normal direction.

2.3.6 Distribution of local Nusselt number over ribbed wall

Similar to the friction coefficient, the Nusselt number also locally varies along a ribbed wall. The heat transfer over a ribbed wall was measured experimentally by Liou et al. (1993) [101], Aliaga et al. (1994) [108], Lorenz et al. (1995) [102] and Cakan (2000) [118]. As shown in Fig. 2.3.12 [101] (note that the surface of the rib is unfolded along the axial axis, marking A, B and C for three corners), the Nusselt number (normalized by the Nusselt number on a smooth wall Nu_s) reaches a maximum value around the leading edge of the ribs, then decreases on top of the ribs till the trailing edge. The minimum value is located at the back side of the rib-wall conjunction, and then the Nu number increases again, reaching a relative maximum value when reattachment occurs, and finally decreases till the next upstream rib-wall conjunction. The maximum Nusselt is found up to 4 times higher than on a smooth wall.

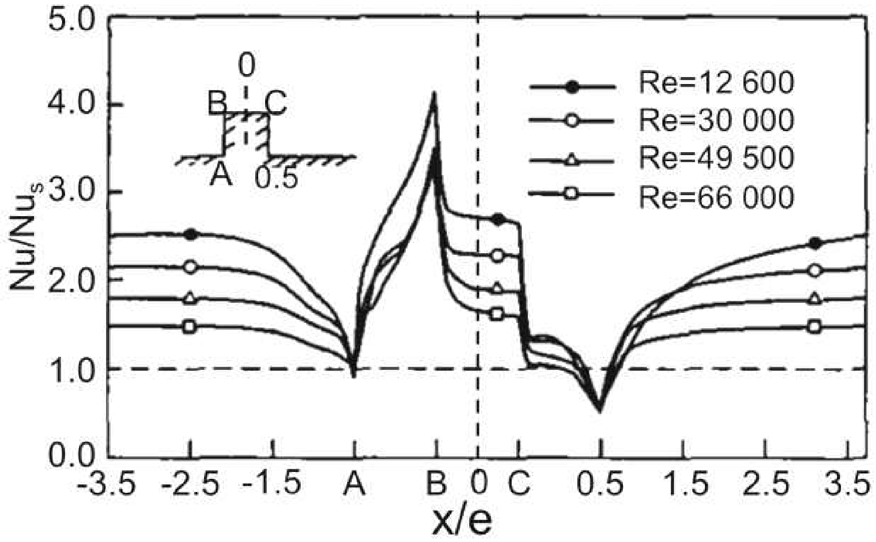

Figure 2.3.12: Distribution of Nusselt number over ribbed wall ($p/e = 7.2$) [101].

2.4 Correlations for the friction factor and Nusselt number in rough tubes

Though details of turbulent flow in rough tubes are difficult to find, many global measurements in rough tubes have been done in past years. Correlations have then been proposed for the global friction factor and Nusselt number, taking into account geometrical parameters of the roughness.

R. Von Mises (1914) [12, 119] introduced the "relative roughness" $2e/D$, where D is the diameter, to observe all of the then-known data from the viewpoint of similarity. For 2D roughness, T. E. Stanton (1911) [120] proved the similarity of flow though rough pipes, by varying the pitch p and depth e of the roughness. So the rough pipes who have the same proportions p/D and e/D can be seen as "similar". For multi-started helically ribbed tubes, the helix angle α is another factor. Moreover, the shape of the rib will also have an impact.

Table 2.4.1 lists several main studies on rough tubes, with various roughness type, ribs shapes, geometrical parameters (using the concept of the similarity), and various Reynolds number range for different flows. According to the classification of “k-type” and “d-type” roughness by Perry et al. (1969) [19] (section 1.2.2), most data are obtained for “k-type” roughness, as shown in Fig.2.4.1.

Year	Author	Roughness type [Ribs shape]	e/D range [p/D range]	Test fluid	Re range [Pr range]
1971	Webb et al. [14]	Transverse ribs [Square]	0.01-0.04 [0.1-0.8]	Heated air water n-butyl alcohol	6000 - 100 000 [0.71 - 37.6]
1980	Gee & Webb [15]	Helical ribs Multi-started [Square]	0.01 [0.15]	Heated air	6000 - 65 000 [0.7]
1983	Sethumadhavan & Rao [17]	Helical ribs Single-started (Wire coil inserted) [Circle]	0.089-0.236 [0.621-3.055]	Water 50% Glycerol	4000 - 100 000 [5.2 - 32]
1991	Zhang et al. [121]	Helical ribs Single-started [Circle, rectangular]	0.037-0.177 [0.355-4.616]	Air	6000 - 100 000 [0.7]
1996	Ravigururajan & Bergles [122]	Transverse/helical ribs Single/multi-started [Square, circle, semi-circle, triangle]	0.023-0.047 [0.434-1.120]	Heated water Air	5000 - 60 000 [0.66 - 37.6]
2004	Vicente & García [16]	Helical ribs Single-started (Spirally corrugated)	0.02-0.06 [0.6-1.2]	Water Ethylene glycol	2 000 - 90 000 [2.5 - 100]
2005	García et al. [123]	Helical ribs Single-started (Wire coil inserted) [Circle]	0.07-0.10 [1.17-2.68]	Water Water-propylene glycol	80 - 90 000 [2.8 - 160]
2010	Saha et al. [18]	Helical ribs Single-started (Wire coil inserted) [Circle]	0.044-0.074 [0.220-1.470]	Air	40 000 - 100 000 4×10^7 - 3×10^9 [0.7]

Table 2.4.1: Summary of experimental studies of ribbed pipes

2.4.1 Pressure drop in rough tubes

Roughness enhances the pressure drop due to the increase of the wall friction.

J. Nikuradse (1950) [12] studied the flow in sand-grain rough tube (Fig. 1.2.3) in 1933, with the relative roughness e/R at values 0.067, 0.0327, 0.0167, 0.0079 and 0.00397 (R/e =15, 30.6, 60, 126 and 252 in his paper). He found that increasing e/R increases the friction factor, and he defined the quantity R_f with the friction factor and the relative roughness:

$$R_f = \frac{1}{\sqrt{4 f_g}} - 2\log\left(\frac{R}{e}\right), \tag{2.4.1}$$

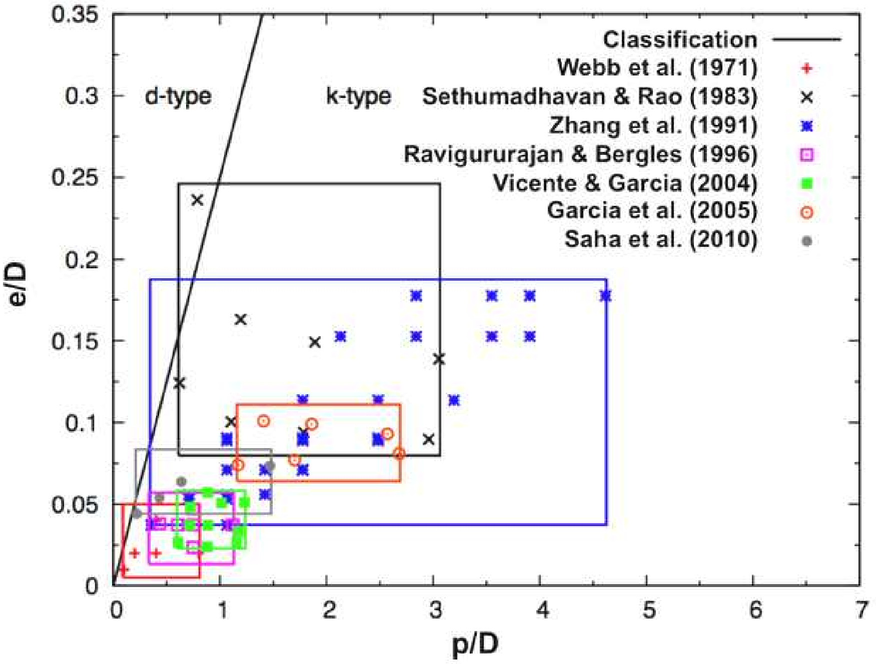

Figure 2.4.1: Geometrical parameters range of some investigators.

He also introduce another dimensionless term, the roughness Reynolds number e^+:

$$e^+ = \frac{u_\tau e}{\nu} = \left(\frac{\mathrm{Re}\sqrt{4f_g}}{4\sqrt{2}}\right) / \left(\frac{R}{e}\right) = \left(\frac{e}{D}\right)\mathrm{Re}\sqrt{\frac{f_g}{2}}, \tag{2.4.2}$$

$$\log e^+ = \log(\mathrm{Re}\sqrt{4f_g}/4\sqrt{2}) - \log\left(R/e\right) \tag{2.4.3}$$

By plotting R_f against $\log e^+$, as shown in Fig.2.4.2, he found that in region where $\log e^+ \leq 0.55$ (Re<2500, thus the flow is laminar), R_f behaves similarly as in a smooth pipe. Then a transition region appears from $\log e^+ = 0.55$ to $\log e^+ = 1.83$, and finally for

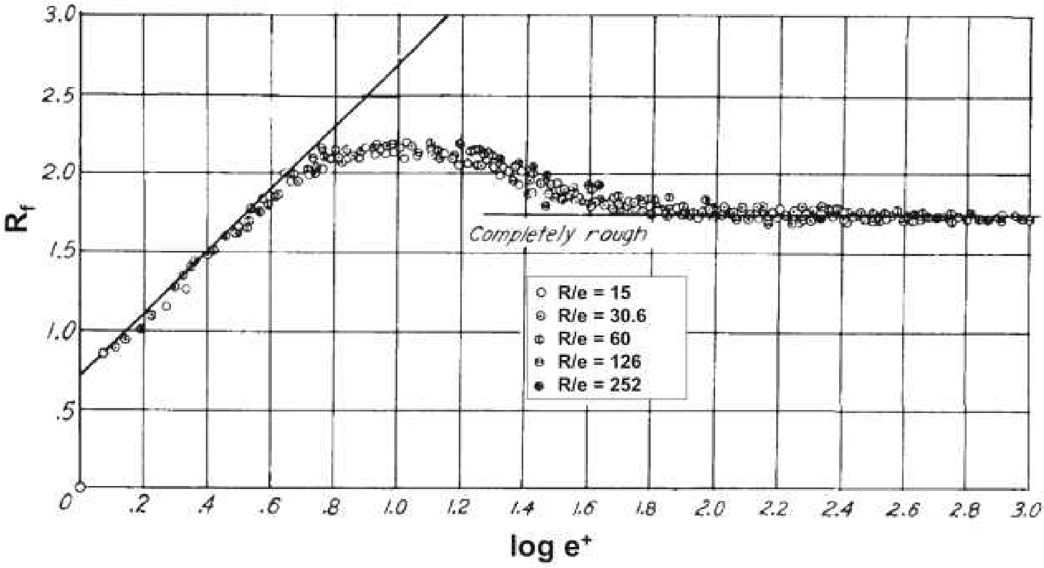

Figure 2.4.2: Relation between R_f and e^+ [12].

$\log e^+ > 1.83$, R_f is no longer dependent on $\log e^+$ and tends to a constant. He proposed the following correlations [12]:

$$R_f = \begin{cases} 0.8 + 2\log e^+, & 0 \le \log e^+ \le 0.55 \\ 1.18 + 1.13\log e^+, & 0.55 < \log e^+ \le 0.85 \\ 2.14, & 0.85 < \log e^+ \le 1.15 \\ 2.81 - 0.588\log e^+, & 1.15 < \log e^+ \le 1.83 \\ 1.74 & 1.83 < \log e^+ \end{cases} \tag{2.4.4}$$

Nikuradse also defined a dimensionless term R^+ from the velocity U and found its relation with the global friction factor [12] in the case of sand-grain roughness:

$$\begin{aligned} R^+ &= \frac{U}{u_\tau} - 5.75\log\left(\frac{y}{e}\right) \\ &= \sqrt{\frac{2}{f_g}} + 2.5\ln\left(\frac{2e}{D}\right) + 3.75, \end{aligned} \tag{2.4.5}$$

where y is the distance from the wall in the tube. Based on R^+ (Eq. 2.4.5), Webb et al. (1971) [14] plotted his own experimental results of tubes with transversally repeated ribs (Fig.1.2.5a), using R^+ *vs* e^+ (Eq. 2.4.3) to observe the effect of parameter p/e. He found that increasing p/e decreases the friction factor, and by plotting $R^+_{pe} = R^+\ (p/e)^{-0.53}$ *vs* e^+, as shown in Fig.2.4.3, the data could be correlated as:

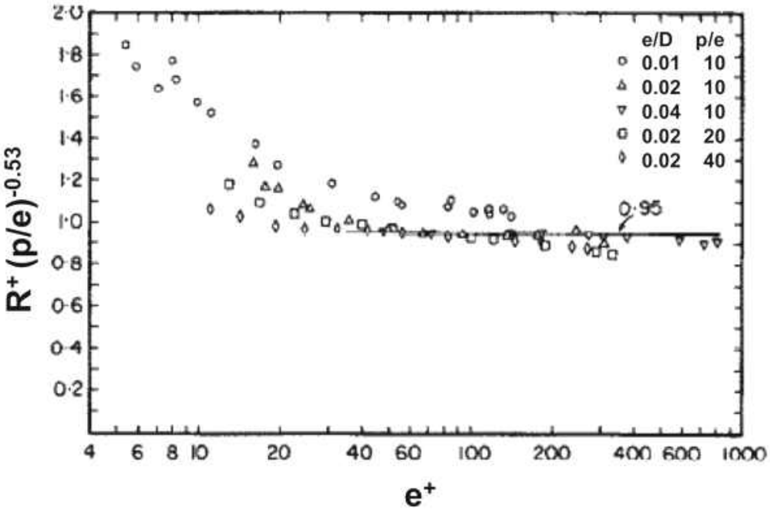

Figure 2.4.3: Friction correlation for transversal ribbed tubes by Webb et al. [14].

$$R^+_{pe} = 0.95, \quad \text{for} \quad e^+ > 35 \tag{2.4.6}$$

In this way, knowing the geometrical parameters $(e/D, p/e)$ and assuming a e^+, the friction factor f_g can be calculated from R^+ and finally the Reynolds number Re can be recomputed with $\mathrm{Re} = e^+\sqrt{(2/f_g)/(e/D)}$. He also noticed that Nikuradse's correlation calculate well the friction factor for turbulent flow in transversally ribbed tubes having $p/e = 10$.

Several years later, Gee & Webb (1980) [15] tested the effect of helix angle of helically ribbed tubes having $p/e = 15$. The helical rib was multi-started (Fig.2.4.4a), so that there is no relation between p and α as in the single-started rib (Fig.2.4.4b) when α and p/D are related by $\tan\alpha = D/2p$.

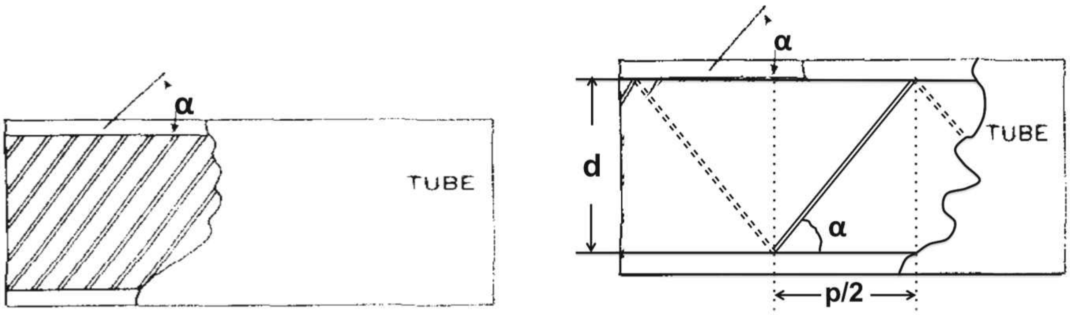

(a) Multi-started helically ribbed tube [15]. (b) Single-started helically ribbed tube.

Figure 2.4.4: Multi-started and single-started helically ribbed tube.

Data was correlated by plotting $R^+_\alpha = R^+ \, (\alpha/50)^{0.16}$ against e^+, as shown in Fig.2.4.5. Increasing the helix angle increases the friction factor. No correlation formula was proposed but data can be read directly from the figure. Gee & Webb (1980) [15] indicated that this correlation may be combined with the results in Webb et al. (1971) [14] for a range of p/e, but the accuracy cannot be ensured.

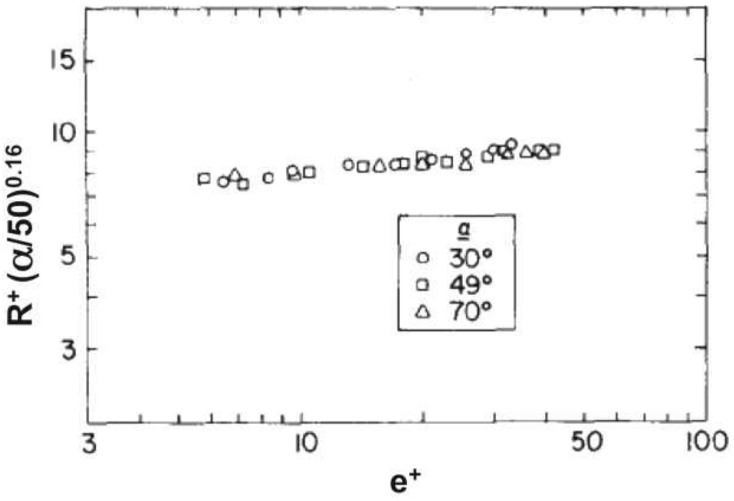

Figure 2.4.5: Friction correlations for multi-started helically ribbed tubes having $p/e = 15$ with different helix angles [15].

W. Nakayama et al. (1983) [124] also developed friction factor correlations based on R^+

in multi-started helical ribbed tubes, using p/e and classifying the data by helix angle:

$$R^+ = \begin{cases} 5.02(e^+)^{0.15}\left(\dfrac{\alpha}{45^\circ}\right)^{-0.16}\left(\dfrac{p}{e}\sin\alpha\right)^{0.1} & \alpha \leq 45^\circ, \\ 5.14(e^+)^{0.12}\left(\dfrac{\alpha}{45^\circ}\right)^{-0.8}\left(\dfrac{p}{e}\sin\alpha\right)^{0.1} & 45^\circ < \alpha < 60^\circ, \\ 4.5 + 5.63\ 10^{-4}\left(\dfrac{p}{e}\right)^{2.59}\ln e^+ & \alpha \geq 60^\circ \end{cases} \tag{2.4.7}$$

Sethumadhavan & Rao (1983) [17] correlated their data for single-started helical-wire-coil-inserted tubes. The helical-wire-coil-inserted tubes are helically ribbed tubes with ribs having a circular shape. As mentioned before, the pitch to diameter ratio p/D and the helix angle α are related (Fig. 2.4.4b). Sethumadhavan & Rao plotted $R^+_{\tan\alpha} = R^+\ (\tan\alpha)^{0.18}$ against e^+, as illustrated on Fig.2.4.6, and obtained the expression:

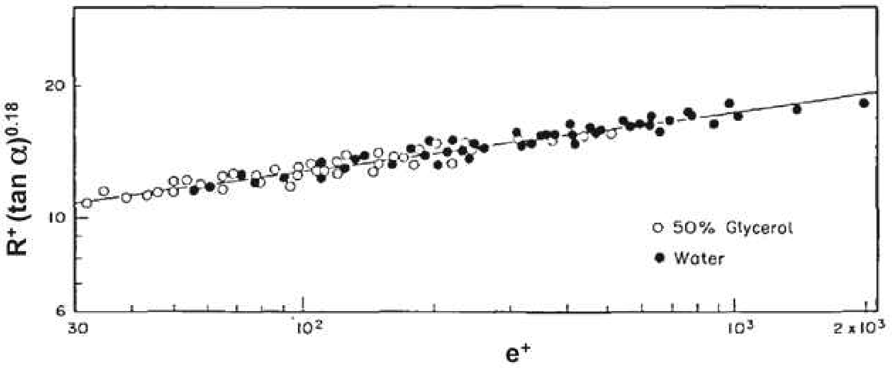

Figure 2.4.6: Friction correlation for flow in helical-wire-coil-inserted tubes by Sethumadhavan & Rao [17].

$$R^+ \cdot (\tan\alpha)^{0.18} = 7.0(e^+)^{0.13} \tag{2.4.8}$$

Li et al. (1982) [125] took experiments with water turbulent flow in the Reynolds number range 10^4 to 8×10^4 in helical-ridging tubes (helical-corrugated tube) and correlated the data by using the least-square method:

$$R^+ = 0.995\left(\frac{e}{D}\right)^{-0.156}\left(\frac{p}{e}\right)^{0.465}\left(\frac{\alpha}{90}\right)^{0.484}\exp\left(\frac{(\ln \mathrm{Re} - 9.62)^2}{1000\,(p/e)^{-1.38}}\right) \tag{2.4.9}$$

However, as the definition of R^+ in Eq. 2.4.5 came from Niskuradse's analysis and experimental data for sand-grain rough tubes, which may not be the optimum values for helical-ridging tubes (and other 2D roughness type), Li et al. (1982) [125] used the nonlinear parameter estimation to refine the correlation and obtained:

$$\sqrt{\frac{2}{f_g}} = 3.42\ln\frac{D}{2e} - 4.64 + 1.25\left(\frac{e}{D}\right)^{-0.057}\left(\frac{p}{e}\right)^{0.5}\left(\frac{\alpha}{90}\right)^{1.14}\exp\left(\frac{(\ln \mathrm{Re} - 9.62)^2}{1000\,(p/e)^{-1.38}}\right) \tag{2.4.10}$$

This correlation predicted most of their data with relative errors below ś10%. It has not anymore much relation with Nikuradse's semi-experimental correlation, where theoretical analysis and experimental results were combined, but has became a fully empirical correlation.

In 1990's, most investigators abandoned Nikuradse's correlation and developed experimental correlations in the form of $f_g = f(e/D, p/D, \mathrm{Re})$. Zhang et al.(1991) [121] gave a general expression of the friction factor as follows:

$$f_g = A \cdot \left(\frac{e}{D}\right)^B \cdot \left(\frac{p}{D}\right)^C \cdot (\ln \mathrm{Re})^D, \tag{2.4.11}$$

with A, B, C and D being equal to 1.29, 0.769, -0.707, -1.079 respectively.

Ravigururajan & Bergles (1996) [122] correlated many existing experimental results, plus their own, and proposed a correlation in the form of:

$$f_g = f_{b,s}(\mathrm{Re}) \left(1 + \left(29.1\mathrm{Re}^A \left(\frac{e}{D}\right)^B \left(\frac{p}{D}\right)^C \left(\frac{tan^{-1}(2D/p)}{90}\right)^D\right)^{15/16}\right)^{16/15} \tag{2.4.12}$$

where $f_{b,s}(Re)$ is the friction factor in a smooth tube of same Re according to Blasius correlation (Eq. 2.2.4), and A, B, C and D are all functions of p/D, e/D, or Re:

$$A(p/D) = 0.67 - 0.06\left(\frac{p}{D}\right) - 0.49\,\frac{\arctan(2D/p)}{\pi/2}, \tag{2.4.13}$$

$$B(p/D) = 1.37 - 0.157\left(\frac{p}{D}\right), \tag{2.4.14}$$

$$C(p/D, \mathrm{Re}) = -1.66\;10^{-6}\;\mathrm{Re} - 0.33\,\frac{\arctan(2D/p)}{\pi/2}, \tag{2.4.15}$$

$$D(p/D, \mathrm{Re}) = 4.59 + 4.11\;10^{-6}\;\mathrm{Re} - 0.15\left(\frac{p}{D}\right). \tag{2.4.16}$$

After year 2000, Vicente & García (2004) [16], Garcia et al. (2005) [123] and Saha et al. (2010) [18] correlated the friction factor for different types of roughness in the same form:

$$f_g = A \cdot \left(\frac{e}{D}\right)^B \cdot \left(\frac{p}{D}\right)^C \cdot \mathrm{Re}^D, \tag{2.4.17}$$

where all coefficients are constant, as given in Table 2.4.2. It indicates that the friction factor, thus the pressure loss, in the rough pipe increases with increasing e/D and decreasing p/D in their testing range of $(e/D, p/D)$.

Author	A	B	C	D
Vicente & García [16]	1.47	0.91	-0.54	-0.16
García et al. [123]	1.44	0.95	-1.21	-0.217
Saha et al. [18]	0.165	0.0782	-0.253	-0.273

Table 2.4.2: Constant coefficients of Eq. 2.4.17 proposed by different investigators.

Fig. 2.4.7 plots the above semi-experimental formula for the friction coefficient against Reynolds number, applied to the ribbed tube considered in the present work (next chapter). Results are very much dispersed, and although they all exhibit the same trend, they do

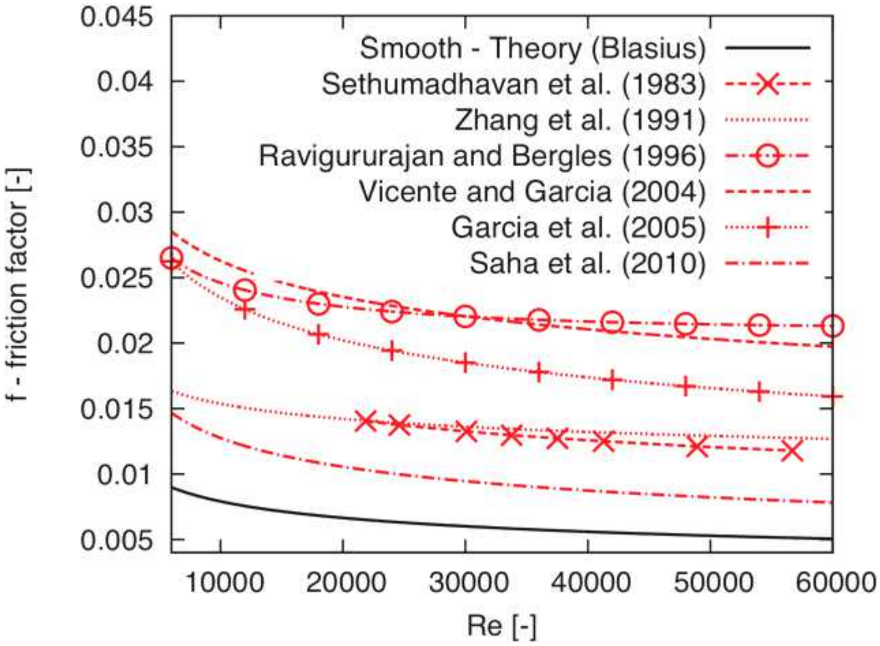

Figure 2.4.7: Global friction factor correlations versus Reynolds number according to published experimental works for the ribbed tube considered in the present work

not allow a quantitative evaluation of pressure loss. This confirms that existing experimental correlations can not be used as is to estimate the pressure loss in ribbed pipe. As a consequence, accurate simulations and/or dedicated experiments are necessary.

2.4.2 Heat transfer in rough tubes

In 1963, Dipprey & Sabersky [126] developed a heat transfer similarity law, which is complementary to Nikuradse's friction similarity law for sand-grain rough tubes. Their model is based on the heat/momentum transfer analogy applied to a two-region flow model: a viscous wall region which is affected more by roughness and a turbulent outer region which is insensitive to roughness. The data of the Stanton number for constant Pr are correlated in the form G_0^+ [126]:

$$G_0^+ = \frac{f_g/(2\,\mathrm{St}) - 1}{\sqrt{(f_g/2)}} + R^+, \tag{2.4.18}$$

where R^+ is the dimensionless term defined in Eq. 2.4.5 for the friction factor correlation. A power law correlation $G^+ = G_0^+\mathrm{Pr}^n$ can be used to account for the Prandtl number dependency. In 1971, Webb et al. [14] extended it to transverse-rib roughness. They conducted experiments by applying a heat flux matching the local heat-transfer coefficient distribution, so that the local temperature difference (between the wall and the bulk fluid temperature) did not vary more than 1 percent along the distance between the ribs. According to their results, they replaced the R^+ in G_0^+ (Eq. 2.4.18) by R_{pe}^+, leading to:

$$G_{0,pe}^+ = \frac{f_g/(2\,\mathrm{St}) - 1}{\sqrt{(f_g/2)}} + R_{pe}^+, \tag{2.4.19}$$

In addition, a cross-plot of $G^+_{pe} = G^+_{0,pe}\mathrm{Pr}^n$ *vs* Pr showed $G^+_{pe} \propto \mathrm{Pr}^{0.57}$. The final correlation in the form of G^+_{pe} *vs* e^+ is shown in Fig. 2.4.8, using a base 10 logarithmic scale for the x/y-axis, demonstrating a linear dependance for $e^+ > 25$

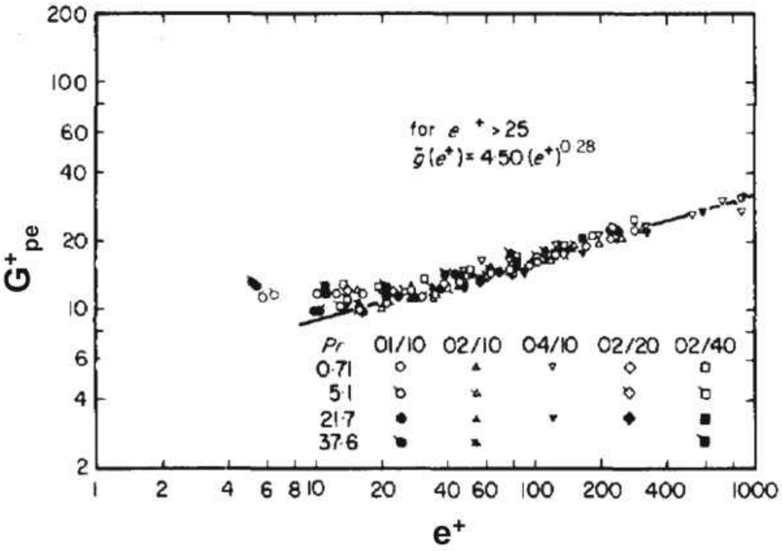

Figure 2.4.8: Heat transfer correlation for transversal ribbed tubes by Webb et al. [14]

In 1980, heat transfer investigations with multi-started helically ribbed tubes were conducted by Gee & Webb [15]. In their experiments, air was heated by 8-12 K. The helix angles were introduced into the correlation:

$$G^+_{0,\alpha} = \left(\frac{f_g/(2\,\mathrm{St}) - 1}{\sqrt{(f_b/2)}} + R^+_\alpha\right)\left(\frac{\alpha}{50^\circ}\right)^j, \tag{2.4.20}$$

$$\text{where} \tag{2.4.21}$$

$$\begin{aligned} j &= 0.37 \quad \text{for} \quad \alpha < 50^\circ \\ j &= -0.16 \quad \text{for} \quad \alpha > 50^\circ \end{aligned}$$

$G^+_{0,\alpha}$ *vs* e^+ for the air flow data (only one Prandlt number $Pr = 0.71$) are shown in Fig. 2.4.9.

Later in 1982, Sethumadhavan & Rao [17] conducted experiments about turbulent flow and heat transfer in helical-wire-coil-inserted tubes. The studies were carried out for water and 50% glycerol inside the tube placed in a heat exchanger using hot water (as the heating medium) at a constant temperature. The temperature of the exchanger fluids at inlet and outlet, and also of the metal walls, were obtained from digital temperature indicator. They reported that G^+ is a strong function of the fluid Prandtl number, and proposed:

$$G^+_{\tan\alpha} = G^+_0(\tan\alpha)^{0.18}\mathrm{Pr}^{-0.55} = 8.6(e^+)^{0.13} \tag{2.4.22}$$

Similarly to what happened with friction factor correlations, from the 1990's, most correlations turned to entirely empirical formula, and correlations for Nusselt number were developed in the form of Nu(Re, Pr, e/D, p/D).

Zhang et al. (1991) [121] experimentally measured the Nusselt number by heating air

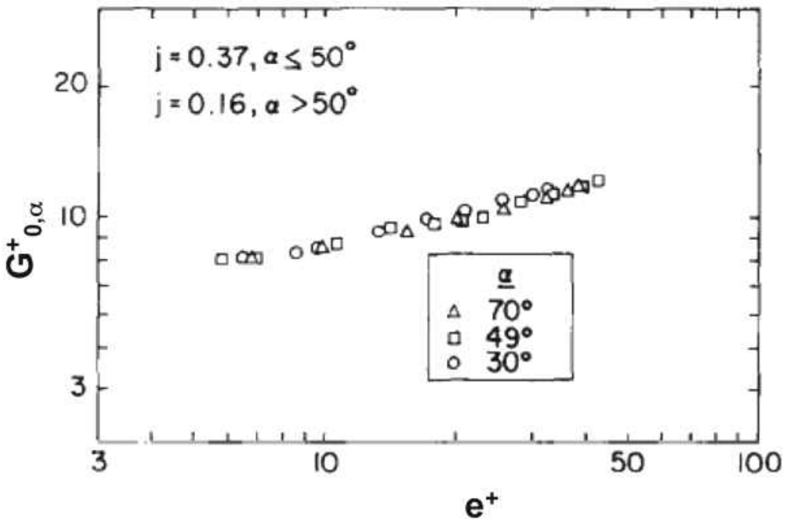

Figure 2.4.9: Heat transfer correlation data for helically ribbed tubes by Gee et al. [15].

flow at 200 ± 5°C in spiral coil inserted tubes, and proposed:

$$\mathrm{Nu}_g = A\left(\frac{e}{D}\right)^B\left(\frac{p}{D}\right)^C \mathrm{Re}^D, \tag{2.4.23}$$

where A, B, C, D are equal to 0.253, 0.378. -0.171, 0.716 respectively.

Ravigururajan & Bergles (1996) [122] gave another Nusselt number correlation:

$$\mathrm{Nu}_g = \mathrm{Nu}_{g,s}\left(1+\left(2.64\mathrm{Re}^{0.036}\left(\frac{e}{D}\right)^{0.212}\left(\frac{p}{D}\right)^{-0.21}\left(\frac{tan^{-1}(2D/p)}{90}\right)^{0.29}(\mathrm{Pr})^{0.024}\right)^7\right)^{1/7} \tag{2.4.24}$$

where $\mathrm{Nu}_{g,s}$ is the Nusselt number in smooth tube (Eq. 2.2.7) proposed by Petukhov and Popov [35].

Vicent et al. (2004) [16] carried out studies under constant heat flux conditions for corrugated tubes by using water at 40 and 65°C and ethylene glycol at 40, 55 and 70°C. Nusselt numbers were determined from measurements on a section located in fully turbulent region. The correlation of Nusselt number reads:

$$\mathrm{Nu}_g = 0.403(e/D)^{0.53}(p/D)^{-0.29}(\mathrm{Re}-1500)^{0.74}\mathrm{Pr}^{0.44}. \tag{2.4.25}$$

Garcia et al. (2005) [123] tested wire coil inserted tubes and proposed:

$$\mathrm{Nu}_g = 0.303(e/D)^{0.12}(p/D)^{-0.377}\mathrm{Re}^{0.72}\mathrm{Pr}^{0.37}. \tag{2.4.26}$$

Finally, Saha (2010) [18] also proposed a correlation of the Nusselt number for wire-coil inserted tubes for $\mathrm{Re} > 4\times10^7$:

$$\mathrm{Nu}_g = 0.1856(e/D)^{0.1392}(2D/p)^{0.317}\mathrm{Re}^{0.538}\mathrm{Pr}^{0.356}(\mu_b/\mu_w)^{0.14}, \tag{2.4.27}$$

where the impact of the variable properties is induced via the ratio $(\mu_b/\mu_w)^{0.14}$, as proposed by Sieder and Tate (1936) [89] for liquid flows. Note that Vicent et al. (2004) [16] and Garcia et al. (2005) [123] corrected their Nusselt number measurement by $(\mu_b/\mu_w)^{0.14}$ before developing the correlations.

Fig. 2.4.10 plots the above formula for the Nusselt number in ribbed tubes against Reynolds numbers, applied to the ribbed tube considered in the present work (see next chapter). Similar results are observed from the formula of Zhang et al. (1991) [121], Ravigururajan & Bergles (1996) [122], and Vicent et al. (2004) [16], while much higher Nusselt number is predicted by Garcia et al. (2005) [123]. This confirms again the necessity to conduct accurate simulations and/or dedicated experiments.

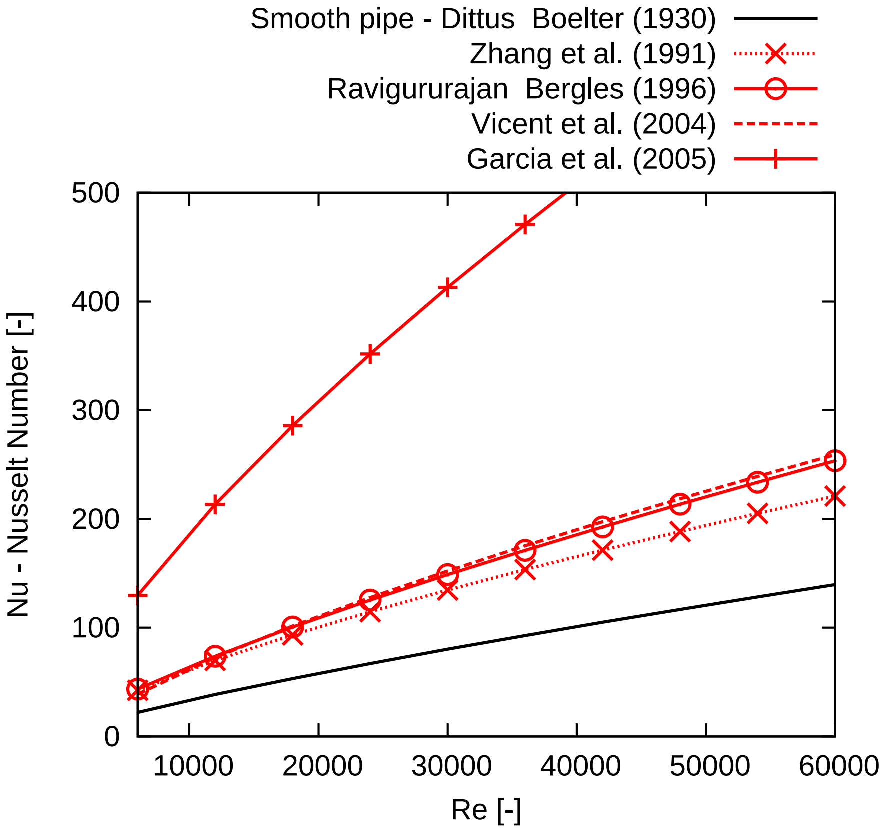

Figure 2.4.10: Global Nusselt number correlations versus Reynolds number according to published experimental works for the ribbed tube of present work

2.4.3 Performance of rough tubes

The artificial roughness's performance is evaluated, considering the impact on heat transfer compared to the impact on friction.

Gee & Webb (1980) [15] studied the performance of multi-started helically ribbed tubes in heat exchangers applications by looking at the ratio $\mathrm{St}/\mathrm{St}_s$ where St_s is the Stanton number in a smooth tube, Fig. 2.4.11. The increase of $\mathrm{St}/\mathrm{St}_s$ reaches its maximum at around $e^+ = 20$, so this value is recommended for optimum design. Second, by tracing the efficiency index $\eta = (\mathrm{St}/\mathrm{St}_s)/(f_g/f_{g,s})$, as shown in Fig. 2.4.12, the helix angle $\alpha = 49°$ gives the best performance. As a consequence, once the operating Re required for a design

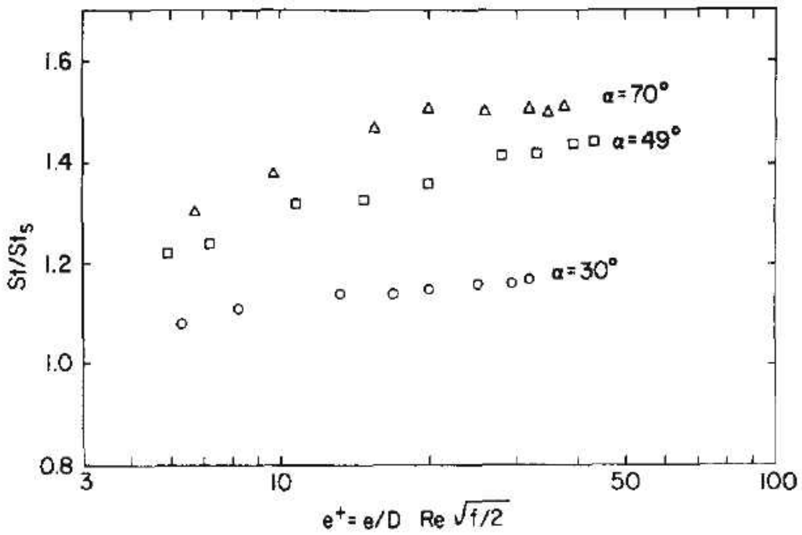

Figure 2.4.11: St/St$_s$ vs. e^+ by Gee et al. [15].

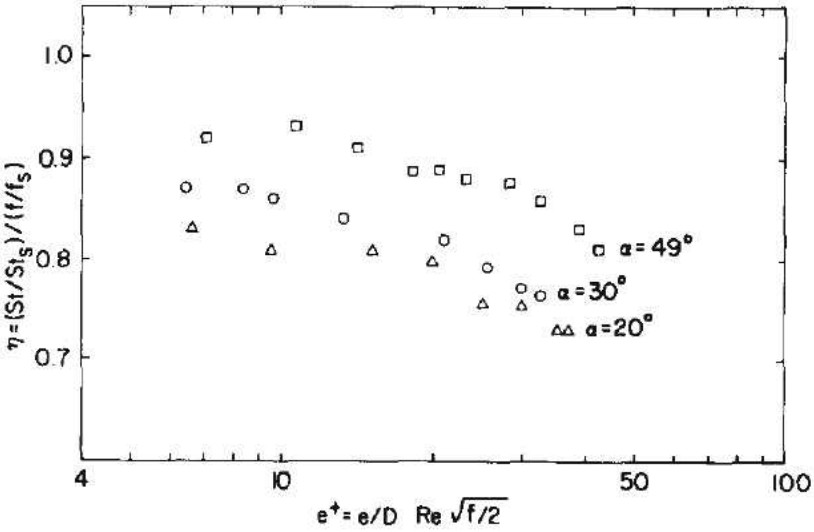

Figure 2.4.12: Efficiency index η vs. e^+ by Gee et al. [15].

is known, using the recommended design condition $e^+ = 20$, and the helix angle $\alpha = 49°$, leads to the value of e/D that should be used.

Considering the efficiency index η, Sethumadhavan & Rao (1982) found that, for their test fluid in helical-wire-coil inserted tubes, the optimum helix angle α was 55° for water (Pr=5.2) and 60° for 50% glycerol (Pr=32). They concluded that the optimum helix angle increased slightly with an increase in Prandtl number.

More recently, Vicente et al. (2004) [16] used the criterion R3 outlined by Bergles et al. (1974) [127] to quantify the benefits of corrugated tubes. The criterion is defined by $R3 = \mathrm{Nu}_g/\mathrm{Nu}_{g,s0}$, where $\mathrm{Nu}_{g,s0}$ is the Nusselt number obtained in an smooth tube for equal pumping power and heat exchange surface area. To satisfy the constraint of equal pumping power, $\mathrm{Nu}_{g,s0}$ is evaluated at the equivalent smooth tube Reynolds number Re_{s0} which matches $f_g\mathrm{Re}^3 = f_{g,s0}\mathrm{Re}_{s0}$. In addition, to characterize the tube roughness, they used the severity index defined by $\phi = e^2/pD$ as the unique geometrical parameter.

Fig. 2.4.13 plots the performance parameter $R3$ *vs* ϕ for corrugated tubes at Prandtl numbers 6 and 60. It is first observed that the performance improves with increasing Prandtl number as expected. Comparison between different values of the severity index ϕ shows that, the highest ϕ gives the best performance at low Reynolds numbers (Re<5000), while intermediate roughness is more suitable at high Reynolds numbers.

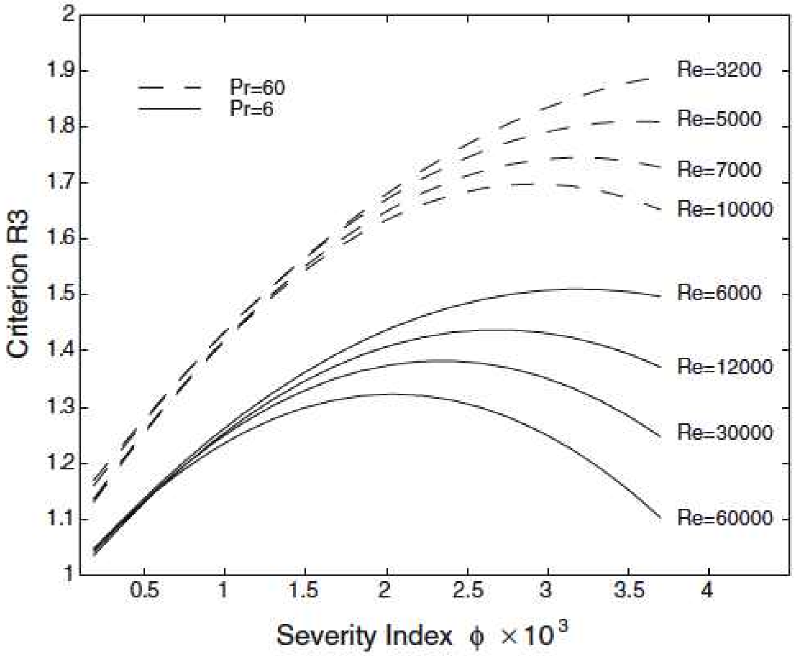

Figure 2.4.13: Performance evaluation criterion $R3$ vs. severity index ϕ for Prandtl 6 and 60 [16].

2.4.4 Conclusions

In summary, if the same general trends have been found by many authors, many quantitative correlations exist with give different results and can not be used directly. The general trends are:

- e/D increase leads to increase both friction and heat transfer,
- p/D increase leads to decrease both friction and heat transfer.

Other impact: rib shape

Less attention has been paid to the impact of rib shape. In 1996, Ravigururajan & Bergles [122] developed general correlations for friction factor and heat transfer in rough tubes considering the then-known results, and introduced an empirical shape factor Sh in the friction factor correlation:

$$Sh = 1 + 2.94(\sin\beta)/n \qquad (2.4.28)$$

where ribs are classified with the number n of sharp corners facing the flow (two for triangular and rectangular ribs, and infinity for smoother profiles), and the contact angle β (the real measured angle for triangular, and 90° for rectangular, semi-circular and circular profiles) as shown in Fig. 2.4.14. This suggestes that when the number of shape corners increases, friction decreases, and that friction is proportional to the sinus value of the contact angle. On contrary, no marked influence of the profile shape on heat transfer was found.

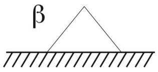

Figure 2.4.14: Sketch of the contact angle β of rib.

Chandra et al. (1998) [128] published results on the effect of rib shapes on turbulent channel flow friction and heat transfer. Fig. 2.4.15 shows the experimental setup, with the same rib height and pitch for different rib shapes. Similar results as Ravigururajan & Bergles (1996) [122] were found for friction: first, with the same Reynolds number, square ribs produce the largest friction, as this type of ribs has the smallest number of sharp corners and highest sinus value of contact angle (equal to 1); second, the triangular shape gives a greater friction than the slant-edged ribs (case E in Fig. 2.4.15c) because $\sin 60°/2 > \sin 90°/3$; finally, the circular and semi-circular ribs have the smallest friction with the largest number of sharp corners (infinity). Moreover, results also showed that square ribs produced the highest heat transfer increase at a given friction factor.

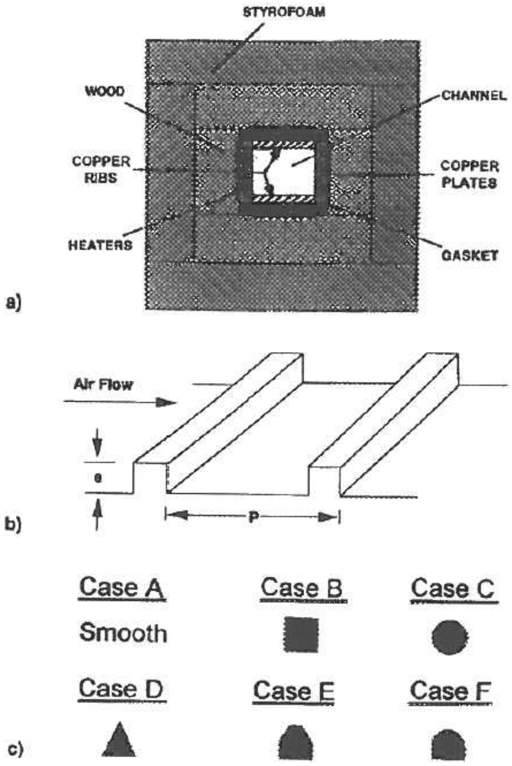

Figure 2.4.15: Test cases of Chandra et al. [128]: a) cross section of test channel, b) ribbed wall geometry, c) cases with various rib profiles

2.5 Turbulent flow in ribbed tubes: reviews of numerical simulations

As mentioned in previous section, most experimental investigations of ribbed tubes are directed to measure the global friction factor and Nusselt number and to develop predictive correlations for these quantities, but most correlations tend to have large uncertainties because of insufficient accounting of appropriate physics involved in the flow and limited experimental data. On the other hand, experimental measurement of local quantities is too expensive [129]. For this reason, the numerical simulation has become an important research tool.

2.5.1 General review of numerical simulations of flow over ribbed wall

Many numerical investigations were conducted for ribbed plate/channels. Leonardi et al. (2004) [113], Ashrafian et al. (2004) [130], Nagano et al. (2004) [114], Lee & Sung (2007) [117] and Lee et al. (2009) [111] have conducted DNS for ribbed channel and shown similar results comparing with experiments, as mentioned in section 2.3. LES investigations can be found in [21, 112, 131–140], and RANS have been conducted in [101, 141–148]. Agreement with the experimental results are reported and effects of various parameters are tested.

Less numerical simulations were conducted for ribbed tube. In particular, no DNS investigations could be found.

The regularly ribbed tube (i.e., tubes with transversal ribs) was studied using LES by Jordan (2003) [149], Vijiapurapu & Cui (2007,2010) [150, 151], and using RANS by Shub (1993) [152] and Vijiapurapu & Cui (2010) [151]. Details are given in Section 2.5.3.

For the helically ribbed tube, only RANS results are reported in the literature. The multi-started helically ribbed tubes (i.e., finned tubes) were investigated by Liu & Jensen (2001) [153], Kim et al. (2004) [129, 154] and Ağra et al. (2011) [155]. Only Hossainpour & Hassanzadeh (2011) [156] reported RANS results on a single-started helically ribbed tube, i.e., the geometry studied in the present work. and it is detailed in the next section.

2.5.2 Turbulent flow in helically ribbed tubes: RANS investigations

Hossainpour & Hassanzadeh (2011) [156] used a finite volume based CFD code using SIMPLE algorithm [157]. The length of the tubes is 500 mm and inside diameter is 24 mm, with e/D ranging from 0.02 to 0.06 and p/D from 0.6 to 1.2. The Reynolds number range is 25 000 to 80 000. The temperature, total relative pressure, velocity magnitude fields, and streamwise velocity contours are reported, showing reattachment at x/e=3-4. The global friction factor and Nusselt number for cases with various geometrical parameters at tested range of Reynolds number, showed that decreasing p/D or increasing e/D, which leads to decreasing p/e, increases the friction factor and Nusselt number. The global Nusselt number results for e/D = 0.02, p/D = 0.8 (thus p/e = 40) and e/D = 0.04, p/D = 1.2 (thus

$p/e = 30$) are validated with experimental data from Ravigururajan & Bergles (1996) [122]. For the case $e/D = 0.06$, $p/D = 0.8$ (thus $p/e \sim 13$), which is closest to the case studied in this work, the friction factors are found to be around 3 times higher than the friction factor in smooth tube, and the Nusselt numbers are about 2 times higher.

2.5.3 Turbulent flow in regularly ribbed tubes: LES investigations

To give more insight to the study of ribbed tube, the LES results of regularly ribbed tube from Vijiapurapu & Cui (2007) [150] is also discussed in this section.

Numerical settings

The LES model in the commercial CFD software Fluent is used, with the dynamic subgrid-scale model, which employs the Boussinesq hypothesis [158] as in RANS models. Tubes with $p/e = 2, 5$ and 10 are simulated, with $e/D \sim 0.05$, and the length of computational domain is $0.6R, 1.5R$ and $2R$ respectively, using periodic boundary conditions combined with an imposed force along the flow direction to ensure a fully developed flow. The first grid points above the wall falls into $y^+ =$ 1-2 and the wall condition is no-slip.

Mean streamwise velocity

Streamlines of the mean flow show that in the near-wall region, the velocity profiles are affected by the presence of ribs, while little impact is found towards the center region of the tubes. Again, the length of reattachment is found to be around $3e$-$4e$ for the case $p/e = 10$. Mean streamwise velocity profiles for three cases $p/e = 2, 5$ and 10 at the location where the recirculation zone ends, is compared with experimental results by Nourmohammadi et al. [93], and good agreement is found. In addition, regions affected by the ribs are larger with increasing p/e.

Pressure variation and local friction

Local friction factors show similar distribution (but not the same values) as the experimental results of turbulent flow in ribbed channel by Lee et al. (2008) [97] (section 2.3.5). Unlike in the smooth tube, where the mean pressure profile stays unchanged along the tube (in a periodic configuration), the local pressure varies a lot due to the presence of ribs, and the local pressure coefficient is introduced:

$$C_p = \frac{P - P_{ref}}{1/2 \rho_b U_b^2} \tag{2.5.1}$$

where the pressure at the downstream corner of the rib has been chosen as the reference P_{ref}, so that C_p is equal to zero there by the definition. Fig. 2.5.1 shows the local pressure coefficient distribution along the wall for the case $p/e = 10$, which is close to the geometry studied in our work. Note that the front side and back of ribs are aligned in this figure. Two valleys of minimum values of C_p are observed from front-side-top conjunction to top center, and it increases towards zero till the rib top ($x/e = 0$). Slight perturbations are observed

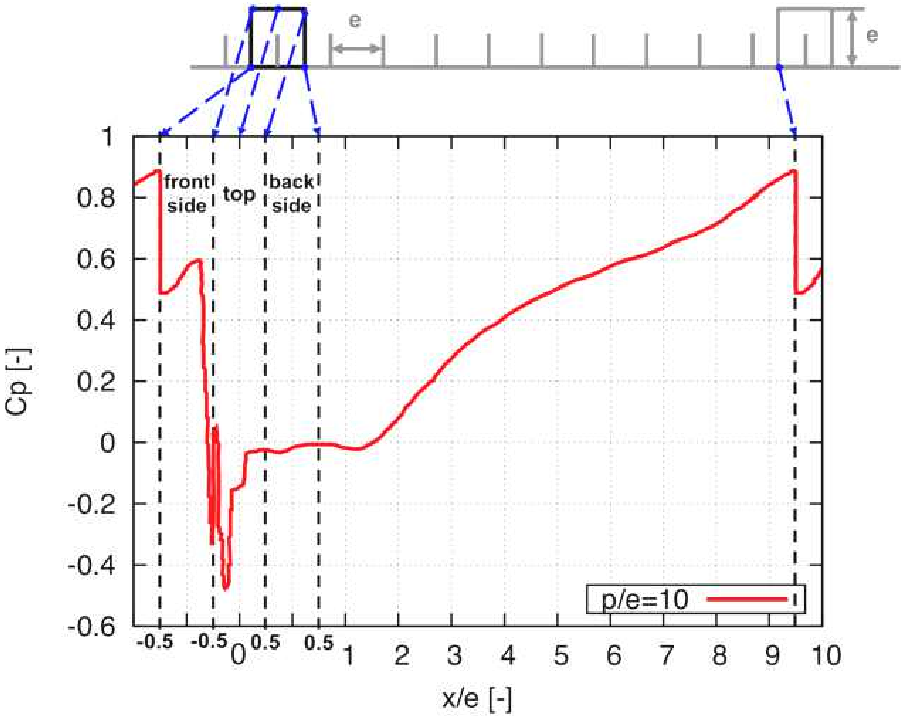

Figure 2.5.1: Distribution of local pressure coefficient over ribbed wall ($p/e = 10$) [150].

on the back side of the ribs, then after a slightly decrease behind the back side of rib-wall conjunction, C_p increases again till the front side of next rib. Finally, on the front side of the ribs, C_p mainly decreases, with a secondary peak appearing. The maximum value of pressure coefficient is about 70 times higher than that of friction coefficient.

The pressure drag D_p (computed from the pressure difference between the front the back faces of the ribs) and friction drag D_f (including that from the groove and the rib top) both contribute to the total drag force. In periodic smooth tubes, pressure drag is zero but only the friction drag $D_{f,s}$ compensates the motion source force. According to the results by Vijiapurapu & Cui (2007) [150], for the the ribbed tube where $p/e = 10$, the pressure drag $D_p \sim 282 D_{f,s}$ and the friction drag $D_f \sim 7 D_{f,s}$ at Reynolds number equal to 50 000. The total drag agrees well with the motion source force in their study.

According to previous data, the global friction factor f_g, which is defined in Eq. 2.1.49, should be around $282+7 = 289$ times higher than in smooth tube at the same Reynolds number of 50 000, or 420 times higher for Re=100 000. However, Vijiapurapu & Cui (2007) [150] reported a friction factor f_g in ribbed tube ($p/e = 10$) equal to 0.0812 (without mentioning the Reynolds number), which is only 15 (if Re=50 000) to 20 (if Re=100 000) times higher than the friction factor in smooth tube. This is in disagreement with the results on the drags, which remains to be validated.

2.6 CFD of thermal cracking chemistry

RANS has been widely used to carry out coupled simulations of the flow, combustion, radiative heat transfer and thermal cracking reaction processes in the cracking furnace, where the tubes and the burners in the furnace are modeled as a global system, in order to provide informations for the optimization of the geometrical structure and operational parameters of the cracking furnace (examples are in [159–165]). The feedstock can range from light distillate fractions such as ethane or propane [165] to heavy fractions like naphtha [159–161, 164] or gas oil. The simulations were conducted with detailed radical kinetics with around 100 reactions [165] or using reduced schemes containing only 20 reactions [164]. The product (especially the ethylene) yields, coke deposition, the distribution of the skin temperature of tubes and the pressure distribution were evaluated.

However, such CFD simulations for smooth or finned cracking pipes coupling with the chemistry are rarely carried out. RANS of reacting flow in smooth and finned tubes using Fluent can be found in Schietekat (2014) [166], in which detailed free-radical chemistry of propane cracking of 26 species and 203 elementary reactions was used. The results are dedicated to the temperature and pressure distribution and product yields, together with the optimization of fin parameters, e.g., fin height, number of fins, and helix angle (to maximize heat transfer). According to their observation, optimal fin parameters can reduce the tube metal skin temperature by up to 50 K compared to conventional tubular reactor, and coking rates are reduced up to 50%. However, the pressure drop increases by a factor from 1.22 to 1.66 causing shifts in light olefin selectivity, e.g., ethylene selectivity drops while propene and 1,3-butadiene selectivity increase.

No discussion on the physical phenomena occurring in the reacting turbulent flow in smooth/ribbed tubes used in thermal cracking furnaces can be found in the existing literature for lack of LES or DNS of this kind of flows. Because of the increasing interest to reveal the impact of finned/ribbed tubes on the thermal cracking process, LES appears as a favorable tool for this kind of study.

2.7 LES and the LES code AVBP

2.7.1 Definition of Wall-Resolved LES and Wall-Modeled LES approach

Both Wall-Modeled LES (WMLES) and Wall-Resolved LES (WRLES) approaches can be used for LES. WRLES fully resolves the wall-layer structures and requires an increased computational cost compared to WMLES where a wall model is used to evaluate the shear stress and does not require such a refined grid. Chapman (1979) [167] proposed the first complete analysis of grid-resolution requirement for LES of turbulent boundary layers. Examining the resolution requirements for inner and outer layers separately, he found that the number of grid points required for WMLES is proportional to $N_{WM} \sim \mathrm{Re}^{2/5}$, while it is proportional to $N_{WR} \sim \mathrm{Re}^{9/5}$ for WRLES. Recently, Choi & Moin (2012) [53] confirmed this estimation to $N_{WR} \sim \mathrm{Re}^{13/7}$.

WRLES is more accurate than WMLES when the wall flow has dominant effects on the whole field and when the classical wall models are inaccurate. The objective of the present work being to study reacting wall flows in turbulent pipes, the WRLES approach is used.

The mesh resolution of the boundary layer plays a key role as the first cell size on the wall directly impacts the velocity gradient at the wall when WRLES is used. The typical first node distance from the wall for a turbulent boundary layer flow using WRLES is $\Delta y^+ = 1$ [168, 169]. The stretching ratio of the mesh has little impact on the skin friction, mean and fluctuating axial velocity, but a non-negligible impact on transverse velocity fluctuations, which are important in swirling flows [170]. As a result, LES of turbulent flow in helically ribbed tubes where rotational motion occurs requires higher mesh quality in terms of stretching ratio than LES in smooth tubes.

2.7.2 Numerical tools in this study: the LES code AVBP

All simulations in this work were conducted with the in-house high-fidelity LES code AVBP [171–173] developed by CERFACS and IFP-EN. AVBP solves the three-dimensional compressible Navier-Stokes equations for turbulent reacting flows, using both the DNS and LES approaches on unstructured and hybrid meshes.

Sub-grid scale model

The filtered compressible N-S equations exhibit SGS tensors and vectors describing the interactions between the non-resolved and the resolved motions. The influence of SGS on the resolved motion is taken into account in AVBP by a SGS model based on a turbulent kinematic viscosity ν_t. Such an approach assumes that the effect of the SGS field on the resolved field is purely dissipative. Various SGS models are available in AVBP, only differing in the estimation of ν_t. The Smagorinsky model and its dynamic version [174] are more appropriate when performing WMLES. The WALE (Wall Adapting Linear Eddy) model proposed by Nicoud and Ducros (1999) [175] gives the correct scaling of turbulent viscosity when approaching walls and determining transition from laminar to turbulent flow, and is therefore recommended for WRLES.

Numerical schemes

The discretization of the governing equations is based on the finite volume (FV) method, and the cell-vertex approach is used for implementing FV methods in AVBP. To discretize the convective fluxes, i.e., the hyperbolic part of the Navier-Stokes (N-S) equations, different numerical schemes are available in AVBP. Both the third-order in space, fourth-order in time numerical scheme TTGC [176] and the second-order in space, third-order in time numerical scheme Lax-Wendroff (LW) [177] are used in this work. Two diffusion operators called 4Δ and 2Δ [178] are available in AVBP, and the latter is recommended. A brief theoretical demonstration shows the advantage of the 2Δ operator when capturing wall flows in Appendix A.

Artificial viscosity

As small-scale oscillations may be generated due to the centered schemes used in AVBP, artificial viscosity (AV) may be locally added into the discrete equations to avoid wiggles and to smooth very strong gradients. A sensor detects whether the solution is well resolved on the grid or if strong local variations appear, requiring the use of AV. A certain amount of 2nd or

4th order AV is then applied, depending on the sensor value and on user-defined parameters. The Colin sensor [179] is more suitable for most unsteady turbulent computations, and is used in this work. Note that the 2nd order operator which smoothes strong gradients and introduces artificial dissipation is applied only when required. On the contrary, the 4th order operator is applied everywhere once being set.

Boundary conditions

Two types of wall boundary conditions are implemented in AVBP, using the classical law of the wall or a no-slip condition. For the first one, the velocity profile is obtained by imposing Eq. 2.1.36 with $\kappa = 0.41$ and $C^+ = 5.4$, and the temperature profile is obtained by the Kader law in Eq. 2.1.38 [37] with $\kappa_\Theta = 0.47$ and $\beta_\Theta = (3.85\mathrm{Pr}^{1/3} - 1.3)^2 + 2.12 \log(\mathrm{Pr})$. In a non-isothermal case, when significant density/temperature variations appear close to the wall, an improved velocity/temperature coupled wall-model is used, where the velocity profile is based on the Van Driest transformation [180] and the expression for temperature profile is coupled with velocity. More details can be found in the PhD thesis of O. Cabrit (2009) [92]. For the no-slip condition, which is used in the present work, the velocity is simply forced to zero at the wall.

Turbulence-chemistry model

The Damköhler number measures the interaction between chemistry and turbulence and is defined as:

$$\mathrm{Da} \equiv \frac{\tau_t}{\tau_{chem}}, \tag{2.7.1}$$

where τ_t is a turbulent timescale and τ_{chem} a chemical timescale.

If $\mathrm{Da} \ll 1$, turbulence is much faster than chemistry, leading to a rapid mixing of products and reactants. On the contrary if $\mathrm{Da} \gg 1$, chemistry is much faster than turbulence and the reaction front is generally smaller than the standard mesh size used for LES. To solve the reaction front on a LES mesh, the Dynamic Thickened Flame (DTF) model that thickens the flame front has been developed in AVBP [173].

In the present work, τ_{chem} (order of magnitude $[10^{-8}, 10^{-6}]$s) is smaller than τ_t (order of magnitude $[10^{-5}, 10^{-4}]$s), leading to $\mathrm{Da} > 1$ in a comparable order, so no turbulence-chemistry model is imposed to solve the reacting flow.

Chapter 3

LES of non-reacting isothermal flow in ribbed and smooth tubes

Contents

In this chapter, the academic case of a non-reacting, isothermal flow is introduced. Simulations are conducted in both smooth and ribbed tubes, having the same diameter to facilitate the comparison. The aim of this chapter is to investigate the dynamic properties of the turbulent flow including the friction drag and pressure drag in ribbed tube compared with the smooth one, and to find out the impact of mesh resolution and of numerical scheme. In particular, simulations are conducted with both a wall-resolved and wall-modeled approach. In the first case, the boundary-layer is solved in a DNS-like mode to capture all its dynamic features, and two LES codes, AVBP and CharLes^X[1], are used and compared to validate the results. In the second case, a coarse mesh is evaluated by comparison with the WRLES results. The objective is to understand the ribs' impact on pressure loss and give first trends for the design of an optimum rib geometry.

---

[1] Simulations with CharLes^X were performed by Dr. Julien Bodart from ISAE/DAEP, ENSICA, Toulouse, France during CTR summer program 2014.

3.1 Configuration

3.1.1 Geometry

Fig. 3.1.1 displays the ribbed pipe geometry named R51 used in this work. It is a cylindrical tube of diameter $D = 51$ mm in which helicoidal ribs with semi-circular shape have been inserted, as illustrated in Fig. 3.1.1. As mentioned in chapter 2, ribbed pipes can be characterized by the rib height e and the pitch p (axial distance between two ribs). The semi-circle rib height is $e = 1.875$ mm thus the width is $2e = 3.75$ mm. The two main geometrical parameters are $p/D = 0.42$ and $e/D = 0.036$ respectively. These quantities are relevant to the targeted petrochemical applications. The rib height being very small compared to the pipe diameter, there is no blocking effect. In addition, as $p/e = 11.6 > 4$, this roughness is kind of "K-type" according to the classification introduced in section 1.2.2. According to [19, 20], the flow outside the boundary layer stays undisturbed for $p/e < 4$. When p/e exceeds 4, eddies of the size of the roughness height are shed from the roughness elements and penetrate into the bulk flow toward the pipe center. The studied configuration clearly falls in the second category, which is consistent with the objective of increasing turbulent mixing close to the wall.

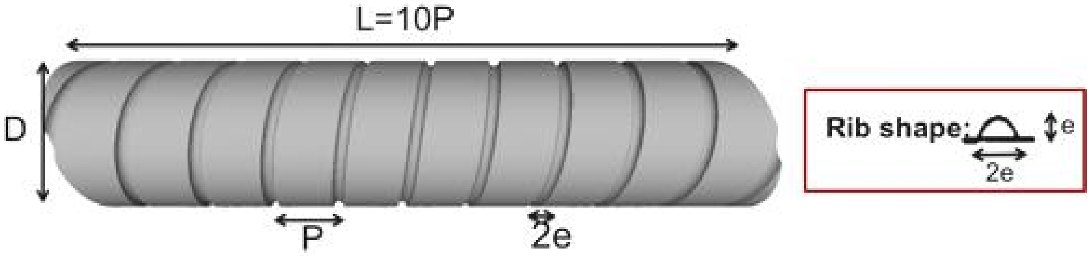

Figure 3.1.1: Configuration of helically ribbed tube with 10 periodic patterns.

For comparison purposes, the same pipe without ribs (smooth pipe) named S51 is also computed. The results of the smooth tube can also be compared with theoretical and experimental data from the literature to validate the numerical method used in this study.

3.2 Mesh

3.2.1 Unstructured meshes

AVBP uses only unstructured meshes, with hexahedra, tetrahedra or a combination of both. Meshes are generated with the commercial software Centaur. Two resolutions of the mesh are used in this study for both R51 and S51. Mesh Y1, is refined in the close wall region, to solve the boundary-layer in a DNS-like mode, requiring a distance to the wall of the closest node in wall units of $y^+ = 1$ [181]. As the friction velocity is not known *a priori* and changes along the ribbed wall, preliminary simulations were conducted to gradually adapt the mesh and reach the $y^+ = 1$ constraint everywhere in the tube. Note that a hybrid mesh is used, with tetrahedra everywhere except in a thin layer along the wall meshed with prisms (Fig. 3.2.1b for the ribbed tube R51 and Fig. 3.2.1a for the smooth tube S51). This allows a better control of y^+ and improved behavior of the numerical scheme in the wall region. In addition, this reduces the cell number of the mesh. About 10 prism layers are used for the wall in both ribbed and smooth tubes, while a reduced number of layers (only about 5 layers) are meshed around the ribs to adapt the geometry. The mesh is significantly coarsened toward the pipe center, where it corresponds to a typical LES resolution.

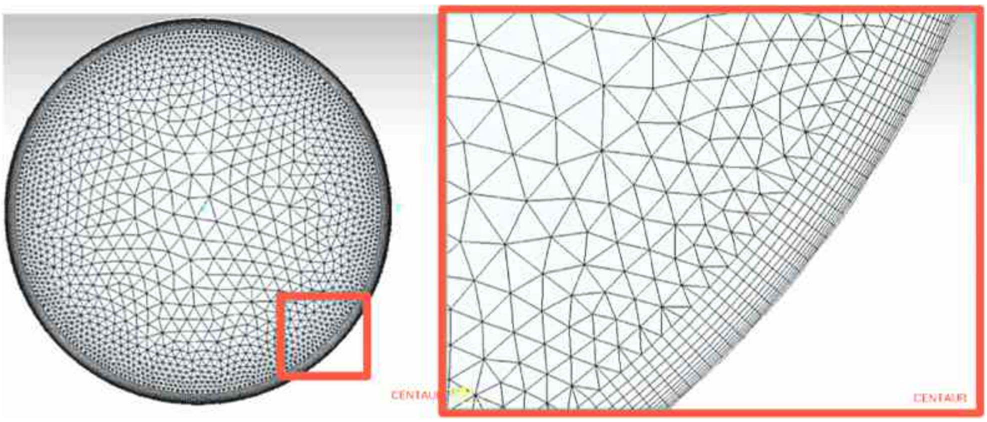

(a) Smooth tube S51 on mesh Y1: $y^+ = 1$ with prism layers near the wall and tetrahedra elsewhere.

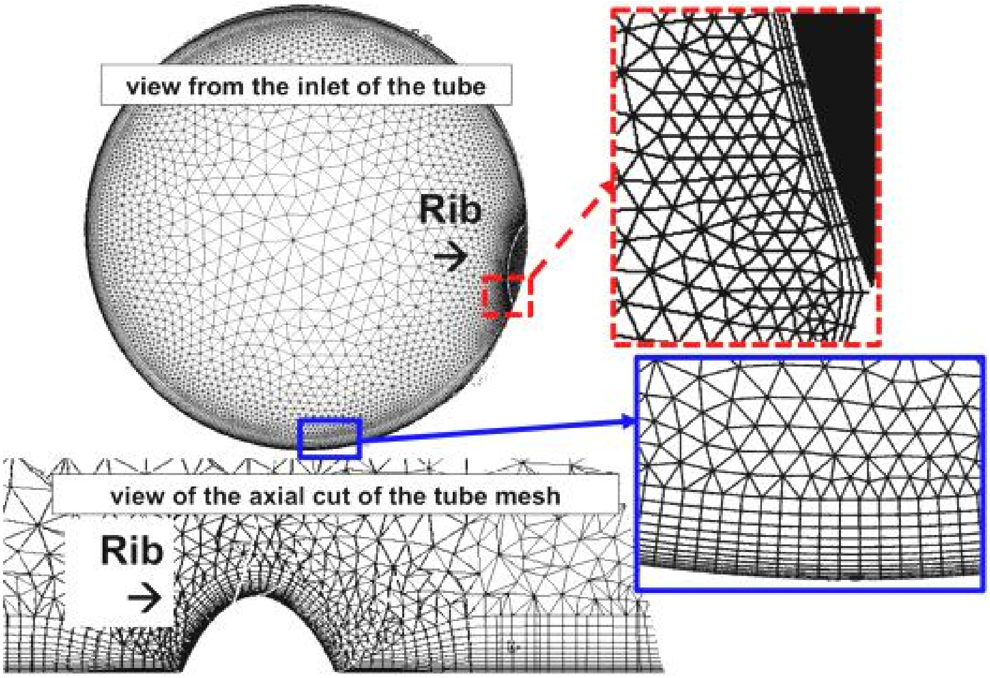

(b) Ribbed tube R51 on mesh Y1: $y^+ = 1$ with prism layers near the wall and tetrahedra elsewhere.

Figure 3.2.1: Meshes Y1 for smooth (S51) and ribbed (R51) tubes.

To decrease the CPU cost for the target industrial application, two coarser meshes with full tetrahedra (mesh Y10t) or prism layers close to the wall combined with tetrahedra toward the center (mesh Y10pt) are also tested. Fig. 3.2.2 illustrates both meshes Y10t and Y10pt for the ribbed tube R51. For the smooth tube S51 only Y10t was tested.

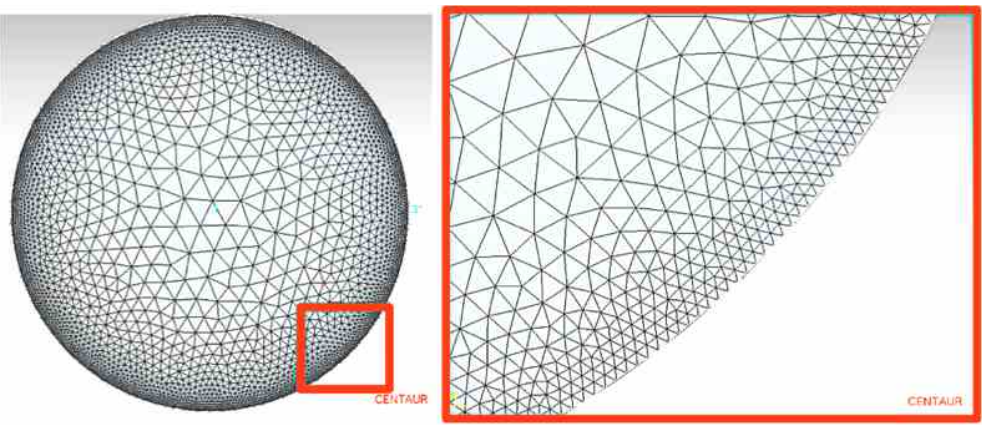

(a) Smooth tube S51 on mesh Y10t: $y^+ = 10$ with tetrahedra.

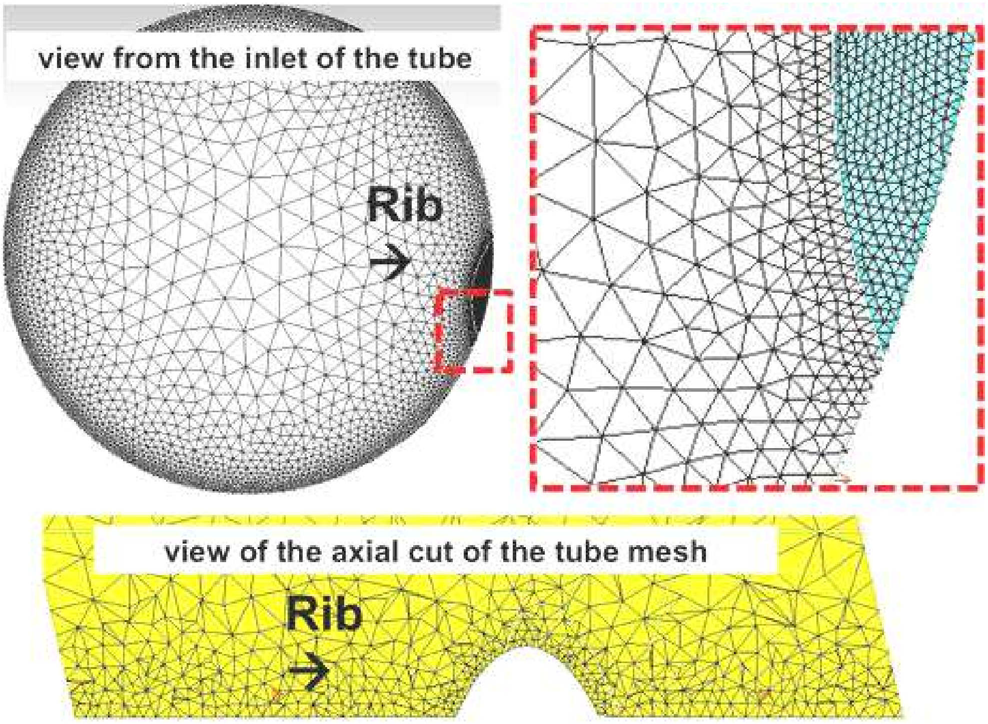

(b) Ribbed tube R51 on mesh Y10t: $y^+ = 10$ with tetrahedra.

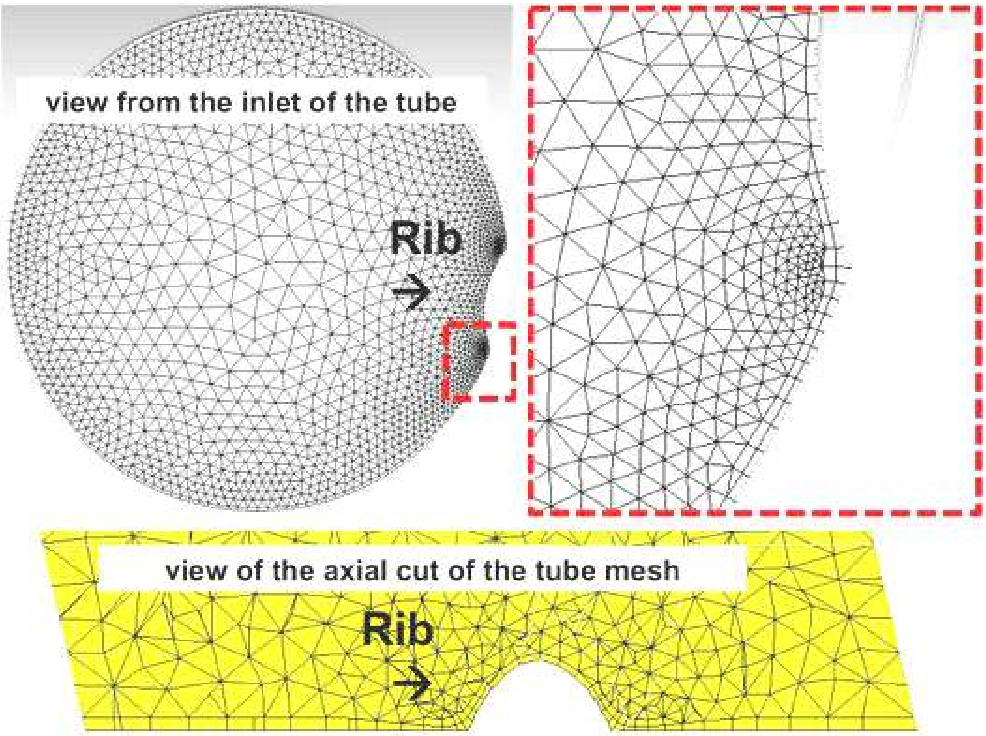

(c) Ribbed tube R51 on mesh Y10pt: $y^+ = 10$ prism layers near the wall and tetrahedra elsewhere.

Figure 3.2.2: Meshes S51Y10t (a), R51Y10t (b) and R51Y10pt (c)

For a tube length of one pitch, the mesh information, as the cell number, node number, and the smallest cell volume, are given in Table. 3.2.1.

Mesh	Cell number	Node number	Smallest tetrahedra volume [m^3]	Smallest prism volume [m^3]	Tetra stretching ratio	Prism stretching ratio
S51Y1	1.16 million	491 660	2.98×10^{-12}	1.32×10^{-12}	1.05-1.2	1.2
R51Y1	2.22 million	800 706	2.21×10^{-14}	1.13×10^{-13}		
S51Y10t	0.82 million	160 661	2.0×10^{-12}	-		-
R51Y10t	0.94 million	191 946	1.97×10^{-13}	-	1.05-1.5	-
R51Y10pt	0.34 million	78 488	8.12×10^{-14}	4.80×10^{-12}	1.02-1.5	-

Table 3.2.1: Mesh information for all the unstructured meshes for both S51 and R51.

3.3 Numerical Methodology

The fluid used in all the non-reacting academic cases is gaseous air, at a bulk temperature of 973 K and a pressure of 1 atm, leading to a bulk density of 0.036 kg/m^3. The methodology to maintain turbulent flows in periodic tube is described below.

3.3.1 Steady flow in a periodic tube

As periodic boundary conditions are applied in the axial direction of the tubes, the flow has to be maintained with an imposed mean pressure gradient, added in the form of an additional source term S_{qdm} in the axial momentum equation, together with its work counterpart uS_{qdm} added to the total energy equation, as shown in Eqs. 3.3.3:

$$\frac{\partial \rho}{\partial t} + \frac{\partial (\rho u_i)}{\partial x_i} = 0, \tag{3.3.1}$$

$$\frac{\partial (\rho u_i)}{\partial t} + \frac{\partial (\rho u_i u_j)}{\partial x_j} = -\frac{\partial p}{\partial x_i} + \frac{\partial \tau_{ij}}{\partial x_j} + S_{qdm,i}, \tag{3.3.2}$$

$$\rho \frac{DE}{Dt} = -\frac{\partial q_i}{\partial x_i} + \frac{\partial}{\partial x_j}(\tau_{ij} u_i) - \frac{\partial}{\partial x_i}(p u_i) + \dot{w}_T + u_i S_{qdm,i}. \tag{3.3.3}$$

This imposed source term S_{qdmx} is constant, and directly linked to the global pressure loss. It can be related to the global fanning friction coefficient f_g in a pipe as :

$$S_{qdm} = \frac{2 f_g \rho_b U_b^2}{D}, \tag{3.3.4}$$

where U_b is the streamwise bulk velocity. As the exact total pressure loss in the simulation is not known *a priori*, the source term is adjusted manually from preliminary simulations to ensure that the simulated flow reaches the target bulk velocity.

3.3.2 Numerical set-up

To evaluate the impact of the numerical scheme, both LW (second order) and TTGC (third order) schemes are used. The wall is simply no-slip and the wall temperature is set at value $T_w = T_b = 973\,\mathrm{K}$. The sub-grid scale model is WALE. All the cases presented in this chapter are listed in Table. 3.3.1.

Case	Tube	Mesh	Numerical scheme
S51_Y1_TT	Smooth	Y1	TTGC
S51_Y10t_TT		Y10t	
S51_Y1_LW		Y1	LW
S51_Y10t_LW		Y10t	
R51_Y1_TT	Ribbed	Y1	TTGC
R51_Y10t_TT		Y10t	
R51_Y10pt_TT		Y10pt	
R51_Y1_LW		Y1	LW
R51_Y10t_LW		Y10t	

Table 3.3.1: Non-reacting isothermal flow in smooth (S51) and ribbed (R51) tubes: list of test cases.

3.4 Preliminary tests on the tube length

Primary tests have been done to verify the independence of the results on the number of periodic patterns. The motivation is to find the minimum numbers of patterns to save CPU time. As fully developed turbulent flow is considered, the only causes of possible variation along the tube would be accumulation effects, or phenomena having spatial scale larger than one pattern. It is therefore important to verify that none of these mechanisms exist here.

LES have been conducted on helically ribbed tubes having 1, 3 or 5 periodic patterns, as shown in Fig. 3.4.1. The meshes used here are different from the ones presented in the previous section and are based on tetrahedra only, with $y^+ \sim 1$ at the wall. The benefit of prisms at the wall was found later and was not applied here. However the mesh has little, even probably no impact on the conclusions about the effect of the number of patterns, as the $y^+ \sim 1$ constraint is respected. The mesh for the 1 rib case 1RIB contains about 20 millions tetrahedra elements and the 3 and 5 ribs cases (3RIBs and 5RIBs) are meshed with exactly 3 and 5 times more elements by repeating the same periodic pattern 3 and 5 times respectively.

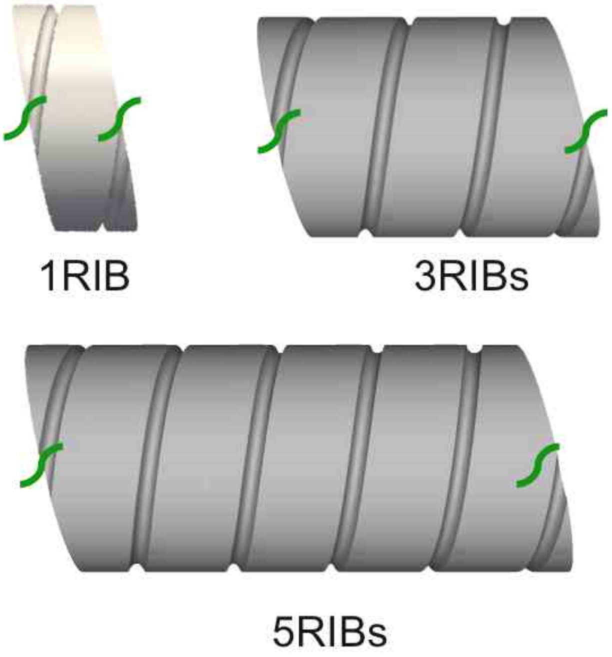

Figure 3.4.1: Configurations of helicoidally ribbed tubes with 1, 3 or 5 periodic patterns.

The numerical scheme TTGC was used only for the 1RIB case to validate the results obtained with the LW scheme, otherwise applied to all the three cases. The same pressure gradient S_{qdm} was imposed in the axial direction in all the cases. The Reynolds number Re and the global friction factor f_g have been calculated after around 300 flow through times (based on the length of one pattern), and averaged over about 20 flow through times. For the three cases, it was proven that the inner turbulent flow varies very little, having a Reynolds number Re around 23 000 and a friction factor $f_g \sim 0.032$, as shown in Fig. 3.4.2. This confirms that the number of periodic patterns has little impact on the results and that only one periodic pattern is sufficient. This will be then systematically applied from now on, to

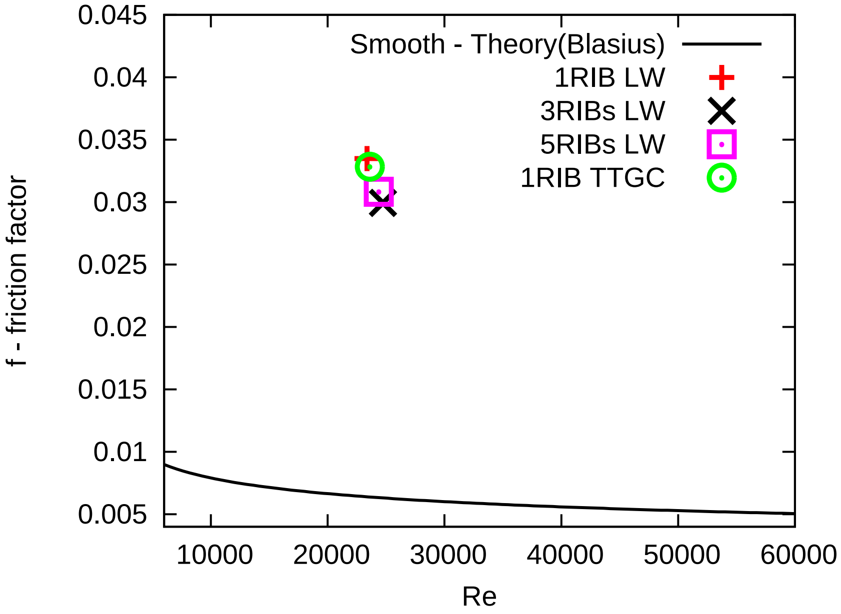

Figure 3.4.2: Friction factor vs Reynolds number of helically ribbed tube R51 with 1, 3 or 5 periodic patterns.

economize computational cost.

3.5 WRLES of turbulent flow in smooth tube S51: the reference case with mesh Y1

Since the mesh Y1 is the most refined close to the wall and TTGC is the most accurate scheme, WRLES is firstly conducted with mesh Y1 and TTGC to obtain the reference case. The numerical scheme LW is also applied on mesh Y1 for validation purposes. The convergence time τ_c, being the number of the flow through times after which the data are averaged, and the average time τ_a, being the number of flow through times over which the time-averaged solutions are obtained, together with the CPUs cost per iteration (in seconds), and the CPUh cost for the simulations (in hours), are summarized in Table. 3.5.1 for cases S51_Y1.

Case	τ_c	τ_a	Time step [s]	CPUs [s]	CPUh [h]
S51_Y1_TT	551	1100	6.1×10^{-8}	0.038	23 766
S51_Y1_LW	499	887	6.1×10^{-8}	0.079	11 515

Table 3.5.1: Simulation information of case S51_Y1_TT.

The simulations in current study were carried out on Neptune of CERFACS, a Bullx B510, by using 128 compute processes.

As a constant S_{qdm} is applied to approach as close as possible the target operating point, the solutions are not exactly at this operating point, and the effective obtained operating points are given in Table. 3.5.2.

Case	S_{qdm} [Pa/m]	U_b [m/s]	Re [-]
S51_Y1_TT	290	59.89	26 938
S51_Y1_LW	360	60.25	27 103
Theory	312	59.9	27 000

Table 3.5.2: Effective operating points of cases S51_Y1_TT and S51_Y1_LW.

To obtain a Reynolds number around 27 000, leading to a bulk velocity $U_b = 59.9$ m/s, the value of S_{qdm} has been found to be 290 Pa/m in case S51_Y1_TT and 360 Pa/m in case S51_Y1_LW. Note that case S51_Y1_TT is closer to the theoretical value 312 Pa/m obtained with Eq. 3.3.4 and the Blasius correlation [81] Eq. 2.2.4 at Re=27 000.

3.5.1 Velocity profiles

The mean axial velocity profiles of turbulent pipe flow S51_Y1_TT and S51_Y1_LW are plotted in Fig. 3.5.1. The normalized centerline velocity U_c/U_b for both numerical simulations is around 1.23, and the results agrees well with the power law of Eq. 2.1.40 (section 2.1.7), with $n = 7$ and $U_c/U_b = 1.23$.

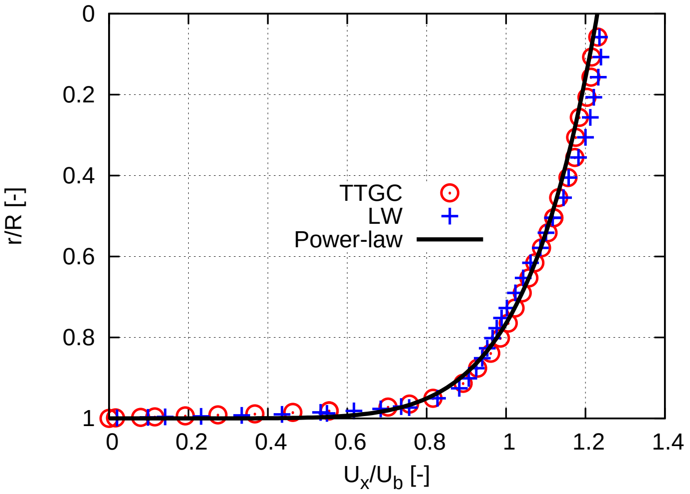

Figure 3.5.1: Mean axial velocity profile in smooth tube S51: cases S51_Y1_TT (circles) and S51_Y1_LW (crosses), compared to the power law of turbulent pipe flow velocity (solid line).

The RMS of the velocity fluctuations $u'^{+}_{x,rms}$, $u'^{+}_{\theta,rms}$ and $u'^{+}_{r,rms}$, normalized with the friction velocity u_τ (3.22 m/s) obtained from the simulation by averaging at the first nodes above the wall against y^+, are shown in Fig. 3.5.2, compared with available turbulent pipe flow data from Laufer (1954) (experiments, at Re=50 000) [34], Eggels (1994) (DNS, Re=5300) [39], Toonder & Nieuwstadt (1997) (experiments, Re=24 580, only providing data on $u'^{+}_{x,rms}$) [182] and Wu & Moin (2008) (DNS, Re=44 000) [183]. The same scale (from 0 to 3.5) is used for the three components as usually done, to show the relative intensity in each direction. Similar behaviors between the current WRLES results and the existing data are observed in the vicinity of the wall, while deviations are found in the outer region: both S51_Y1_TT and S51_Y1_LW overpredict $u'^{+}_{x,rms}$, while S51_Y1_TT gives better results, and underpredict $u'^{+}_{\theta,rms}$ and $u'^{+}_{r,rms}$.

More detailed comparisons in boundary layer are given in the following section 3.5.3.

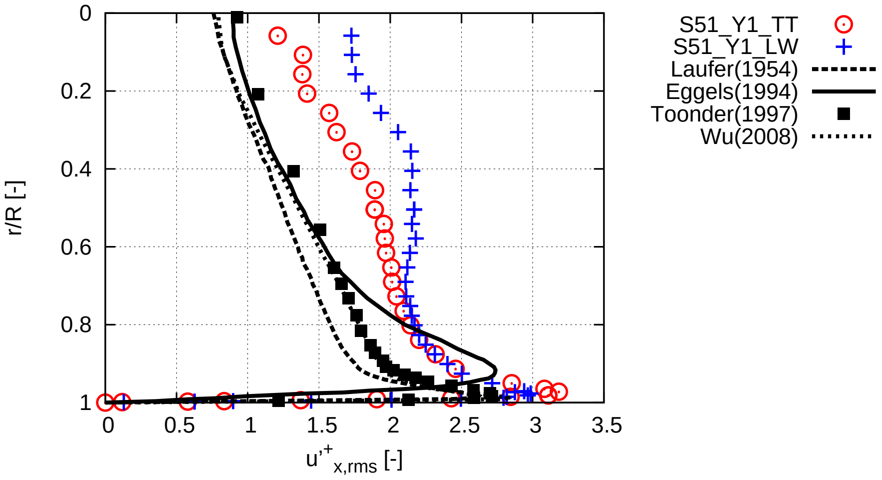

(a) RMS of $u'^{+}_{x,rms}$.

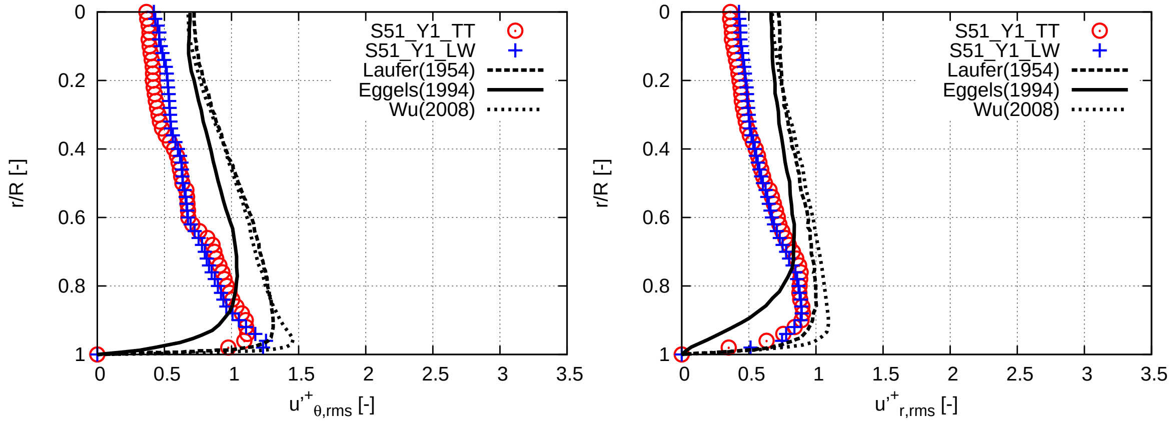

(b) RMS of $u'^{+}_{\theta,rms}$.

(c) RMS of $u'^{+}_{r,rms}$.

Figure 3.5.2: RMS of velocity fluctuations $u'^{+}_{x,rms}$, $u'^{+}_{\theta,rms}$ and $u'^{+}_{r,rms}$ in smooth tube S51 on mesh Y1, compared with existing experiments/DNS data.

3.5.2 Energy spectrum and turbulent viscosity

At two points respectively at the tube center and 1/4 radius as indicated in Fig. 3.5.3, the kinetic energy spectra in both cases S51_Y1_TT and S51_Y1_LW are plotted in Fig. 3.5.4. Similar results are observed.

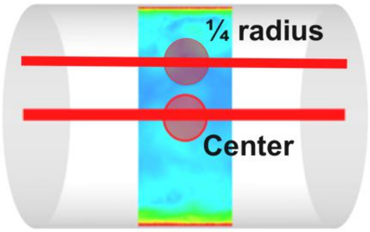

Figure 3.5.3: Tube center and 1/4 radius points.

The turbulent viscosity ν_t fields are shown on the transverse plane (one pattern) of the tube S51 in Fig. 3.5.5. Case S51_Y1_TT shows stronger turbulent viscosity, correspondent to the lower RMS of $u'^{+}_{x,rms}$ in Fig. 3.5.2a.

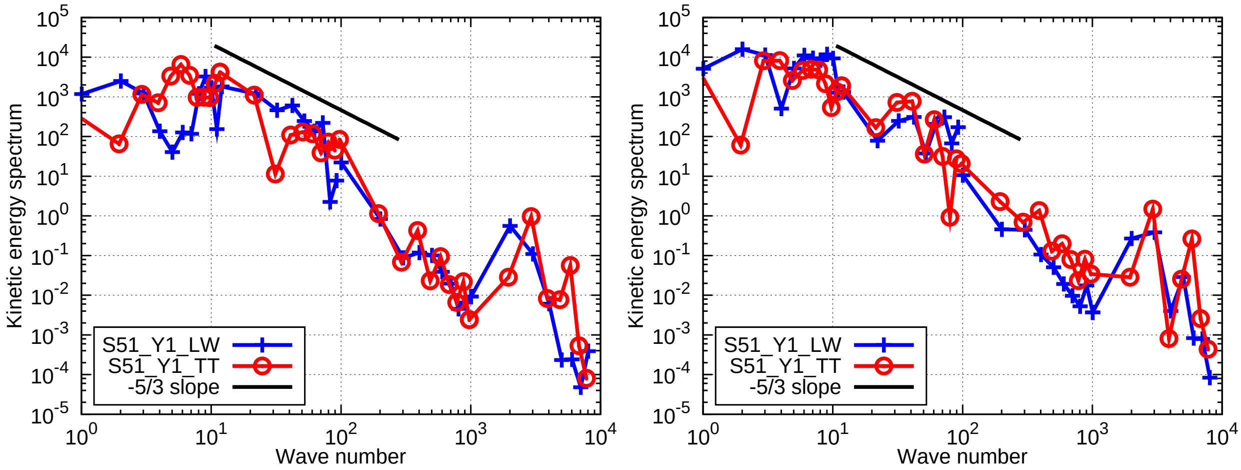

(a) Center. (b) 1/4 radius.

Figure 3.5.4: Kinetic energy spectrum in both cases S51_Y1_TT and S51_Y1_LW at two locations.

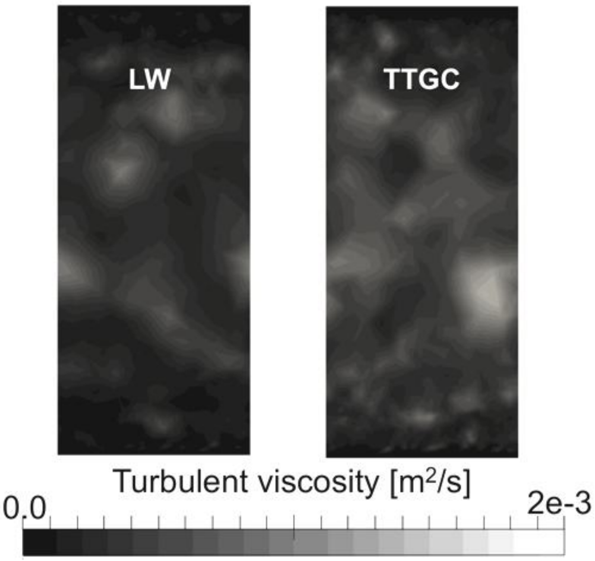

Figure 3.5.5: Turbulent viscosity on the transverse plane in both cases S51_Y1_TT and S51_Y1_LW.

3.5.3 Boundary layer behavior

The boundary layer thickness δ_{th} is here taken as the distance from the wall where the mean axial velocity $U_x = 99\% U_b$. The thickness normalized with the radius of tube δ_{th}/R for S51_Y1_TT is 0.206 ($y^+ \sim 145$) while for S51_Y1_LW is 0.25 ($y^+ \sim 206$), as expected, the boundary layer is thicker when the turbulent flow is solved with the lower order LW scheme. It is also observed in Fig. 3.5.6, plotting u^+ (Eq. 2.1.32, normalized with the friction velocity u_τ (3.22 m/s), compared with the classical wall laws for turbulent channel flows, and the DNS results of Eggels (1994) (pipe flow) [39]. Case S51_Y1_TT agrees well with the DNS data, following the linear law in the viscous sublayer and deviating a little from the classical log law after $y^+ \sim 20$, while S51_Y1_LW underpredicts u^+ in the log law region.

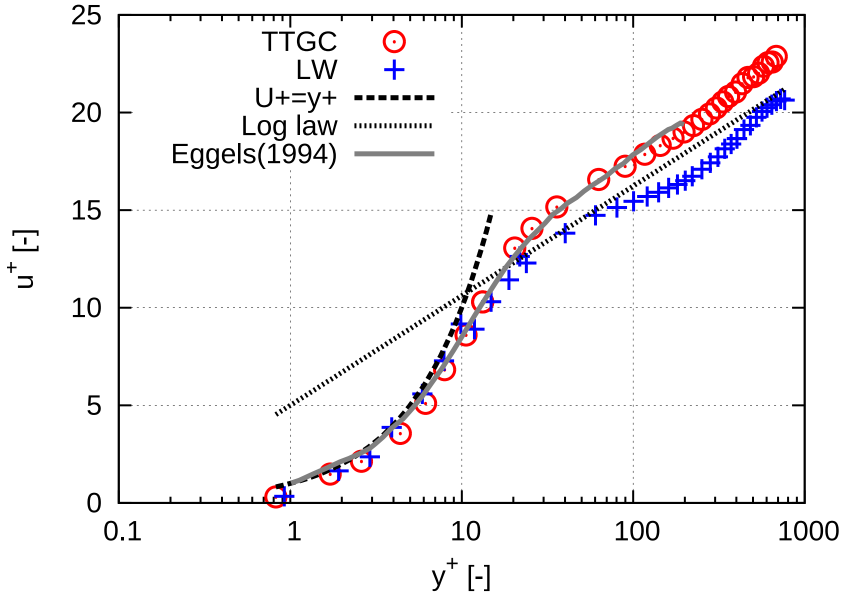

Figure 3.5.6: Wall flow in the smooth tube S51 on mesh Y1: WRLES results compared with the law of the wall and the DNS results from Eggels (1994) [39].

Turbulence intensity

The RMS of velocity fluctuations normalized by u_τ, $u'^+_{x,rms}$, $u'^+_{\theta,rms}$ and $u'^+_{r,rms}$, are plotted against y^+ in the boundary layer, compared with the DNS results from Wu & Moin (2008) (DNS, Re=44 000) [183] (data is provided only till $y^+ < 100$), as shown in Fig. 3.5.7. The peak value and position for $u'^+_{x,rms}$ are close to the DNS results, and similar results are also observed for the two other components. Note that the Reynolds number is different and may be responsible for the discrepancy observed.

Friction factor

The simulated global friction factor for the S51 tube is found to be 0.0057 (S51_Y1_TT) and 0.007 (S51_Y1_LW), from Eq. 2.1.49, where the source term S_{qdmx} was used to evaluate the pressure loss. The values are very close to the value 0.0062 obtained from the empirical correlation of Blasius [81] (Eq. 2.2.4) at Re=27 000.

3.5.4 Conclusions

The flow in the smooth tube S51 simulated by WRLES with a full resolution of the wall flow is found similar to existing theoretical/empirical/DNS results, especially in the boundary layer, although some discrepancy is observed in the outer region. TTGC gives overall better results and the numerical methodology (hybrid mesh Y1 with TTGC scheme) is validated as a reference.

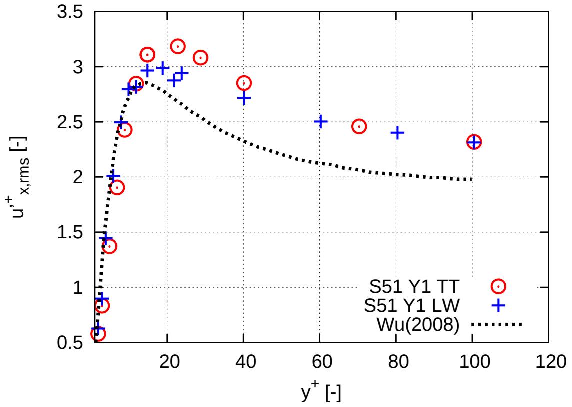

(a) $u'^{+}_{x,rms}$.

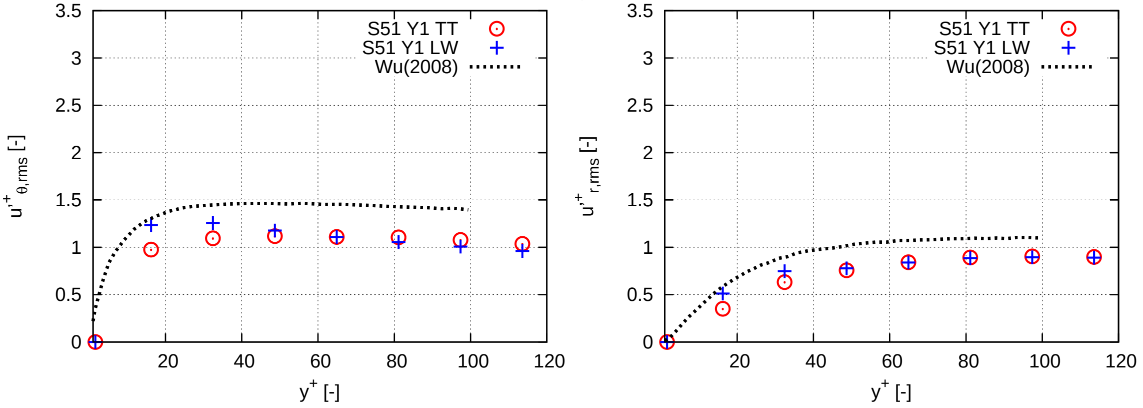

(b) $u'^{+}_{\theta,rms}$.

(c) $u'^{+}_{r,rms}$.

Figure 3.5.7: RMS of velocity fluctuations normalized by u_τ, $u'^{+}_{x,rms}$, $u'^{+}_{\theta,rms}$ and $u'^{+}_{r,rms}$, in the boundary layer of smooth tube S51 on mesh Y1, compared with DNS data from Wu & Moin (2008) (DNS, Re=44 000) [183].

3.6 Impact of the mesh: turbulent flow in smooth tube S51 on tetrahedra coarse meshes Y10t

As the objective of this project is to finally resolve the industrial problem, it is important to find the best trade-off between accuracy and computational cost. In fact, later in the discussion on the results of the ribbed tube, it will be found that it is reasonable to use the coarse mesh having $y^{+} \sim 10$. For the reason of comparison, the mesh Y10 ($y^{+} \sim 10$) is also tested and compared to the results of the reference case for the smooth tube S51_Y1_TT.

The convergence times information of the cases on mesh Y10t is listed in Table. 3.6.1.

Case	τ_c	τ_a	Time step [s]	CPUs [s]	CPUh [h]
S51_Y10t_TT	1660	1660	1.20×10^{-7}	0.039	12 484
S51_Y10t_LW	830	1466	1.33×10^{-7}	0.019	4207

Table 3.6.1: Convergence and CPU times of cases S51_Y10t_TT and S51_Y10t_LW.

Half less CPU cost is found with the coarse mesh Y10t than on refined mesh Y1.

The imposed source term S_{qdm}, the final bulk velocity and the Reynolds number are given in Table. 3.6.2, compared to the reference case S51_Y1_TT.

Case	$S_{qdm}[Pa/m]$	U_b [m/s]	Re [-]
S51_Y1_TT (ref)	290	59.89	26 938
S51_Y10t_TT	223	60.09	27 031
S51_Y10t_LW	185	60.12	27 042

Table 3.6.2: Operating conditions of the turbulent heated flow in smooth tube S51, using mesh Y10t and the two numerical schemes TTGC and LW, compared to the reference case S51_Y1_TT.

3.6.1 Velocity profiles

The mean axial velocity profiles of turbulent flow in smooth tube S51, on mesh Y1 and Y10t, are plotted in Fig. 3.6.1. Very similar profiles are found in cases S51_Y10t_TT ($U_c/U_b = 1.22$) and S51_Y10t_LW ($U_c/U_b = 1.21$) compared to the reference case S51_Y1_TT ($U_c/U_b = 1.23$). The scheme TTGC better reproduces the profile than the scheme LW.

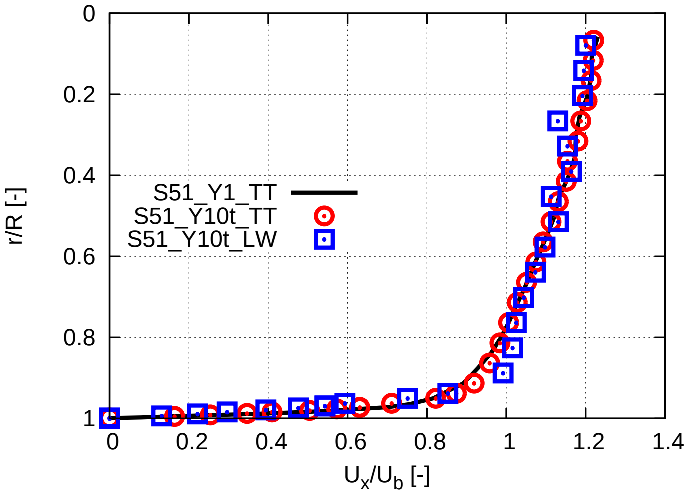

Figure 3.6.1: Mean axial velocity profiles in smooth tube S51: the reference case S51_Y1_TT, S51_Y10t_TT and S51_Y10t_LW.

3.6.2 Energy spectrum and turbulent viscosity

The kinetic energy spectra at center and 1/4 radius in both cases S51_Y10t_TT and S51_Y10t_LW are plotted in Fig. 3.6.2, compared with the reference case S51_Y1_TT. Similar results are observed.

The turbulent viscosity ν_t fields are shown on the transverse plane (one pattern) of the tube S51 in Fig. 3.6.3. Similar results are found in both TTGC cases, stronger ν_t than the LW case is observed.

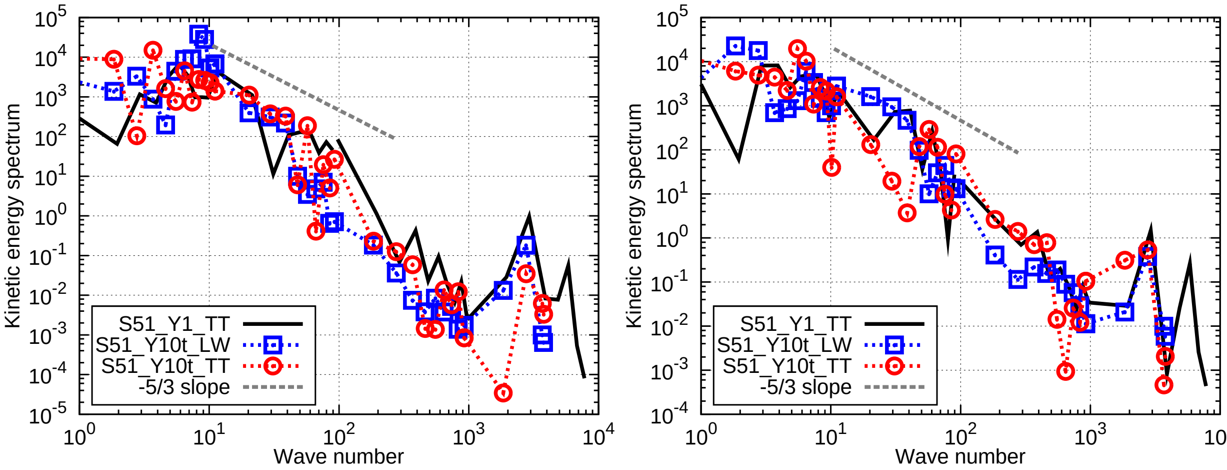

(a) Center. (b) 1/4 radius.

Figure 3.6.2: Kinetic energy spectrum in both cases S51_Y10t_TT and S51_Y10t_LW at two locations, compared to the reference case S51_Y1_TT.

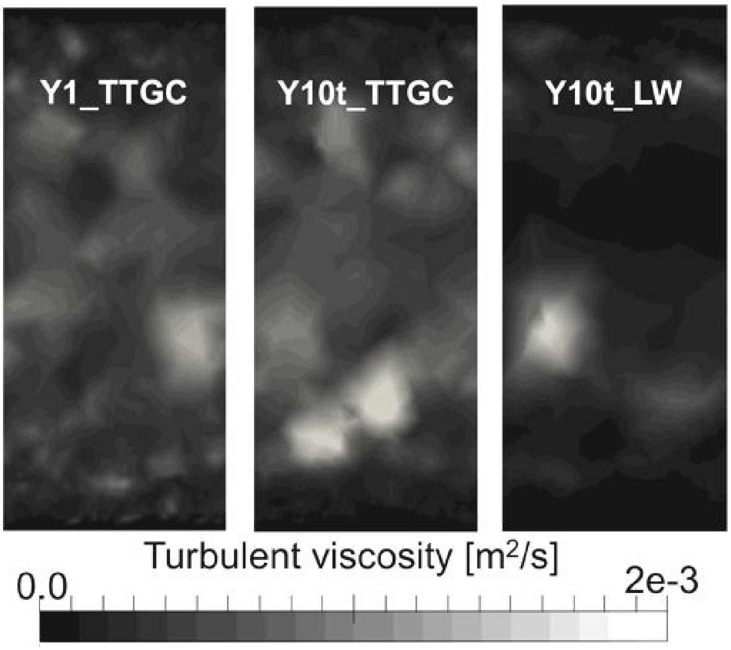

Figure 3.6.3: Turbulent viscosity on the transverse plane in cases S51_Y1_TT, S51_Y10t_TT and S51_Y10t_LW.

3.6.3 Boundary layer behavior

The thickness of the boundary layer (defined using $U = 99\% U_b$) normalized with the radius of tube δ_{th}/R is 0.2 and 0.11 for S51_Y10t_TT and S51_Y10t_LW respectively, compared to 0.206 for the reference case S51_Y1_TT. It is observed in Fig. 3.6.1 that the axial velocity profile of case S51_Y10t_LW shows a sharp increase at around $U/U_b = 1$, which explains the thinner boundary layer. To better understand the near-wall flow, the dimensionless velocity u^+ is plotted against y^+ in Fig. 3.6.4. As expected, the coarser mesh can not well reproduce the log law behavior, and the scheme LW has more deviation than the scheme TTGC on mesh Y10t, compared to the reference case. On the contrary, both TTGC and LW on mesh

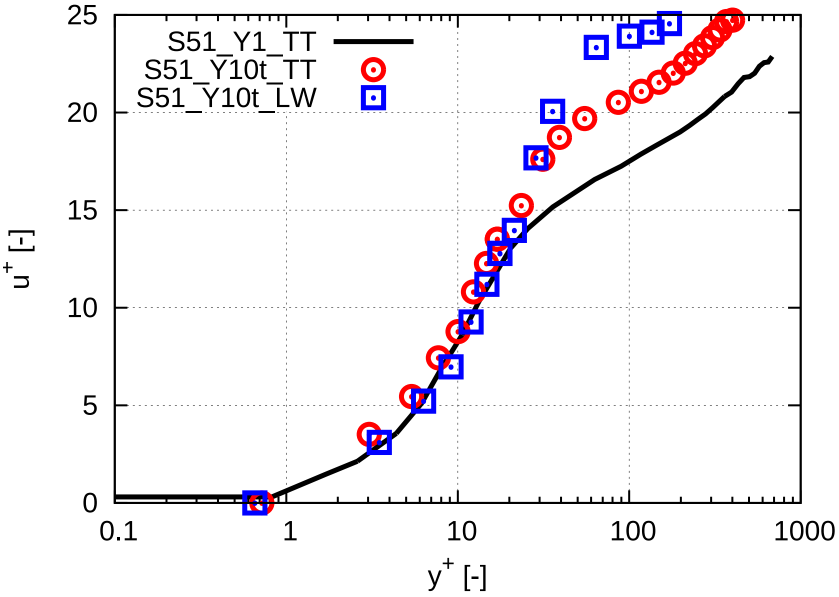

Figure 3.6.4: Non-dimensional velocity profile for cases S51_Y10t_TT and S51_Y10t_LW, compared to S51_Y1_TT.

Y10t well predict the linear region of the wall flow.

Turbulence intensity

The RMS of velocity fluctuations normalized by u_τ, $u'^{+}_{x,rms}$, $u'^{+}_{\theta,rms}$ and $u'^{+}_{r,rms}$, are plotted against y^+ in the boundary layer, as shown in Fig. 3.6.5, comparing the results on coarse mesh Y10t and refined mesh Y1. Both TTCG and LW on mesh Y10t over-predict $u'^{+}_{x,rms}$, by errors up to 17% and 40% respectively, while they under-predict $u'^{+}_{\theta,rms}$ and $u'^{+}_{r,rms}$, with deviation up to 14% and 30% respectively. In addition, the positions of the peaks move toward the center of tube on the mesh Y10t.

Friction factor

Finally, the global friction factor of the turbulent pipe flow is obtained equal to 0.0044 and 0.0036 for S51_Y10t_TT and S51_Y10t_LW on coarse mesh, i.e., is under-predicted by 23% and 37% compared to value 0.0057 obtained in the reference case S51_Y1_TT.

3.6.4 Conclusions

Tests for the simulation of the turbulent flow in the smooth tube S51 on the coarser mesh Y10t are conducted in this section. Neither the numerical scheme TTGC nor LW can well predict the flow, as expected. However, case S51_Y10t_TT shows better results than S51_Y10t_LW, with an error up to 23% compared to the reference case S51_Y1_TT, in terms of mean axial velocity, RMS of velocity fluctuations and global friction. Considering the best trade-off between accuracy and computational cost, the mesh Y10t is acceptable for further industrial applications to conduct the simulation of turbulent flow in the smooth tube S51, in order to compare with the results obtained in the ribbed tube R51.

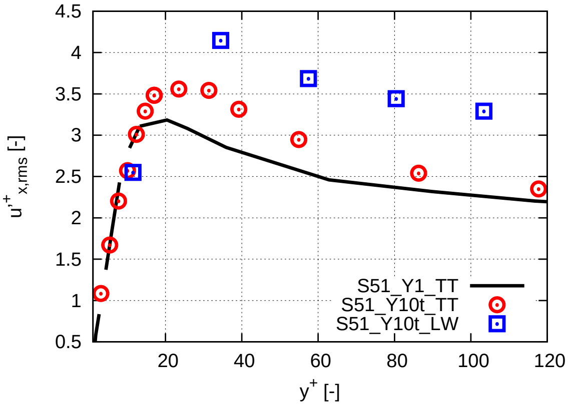

(a) $u'^{+}_{x,rms}$.

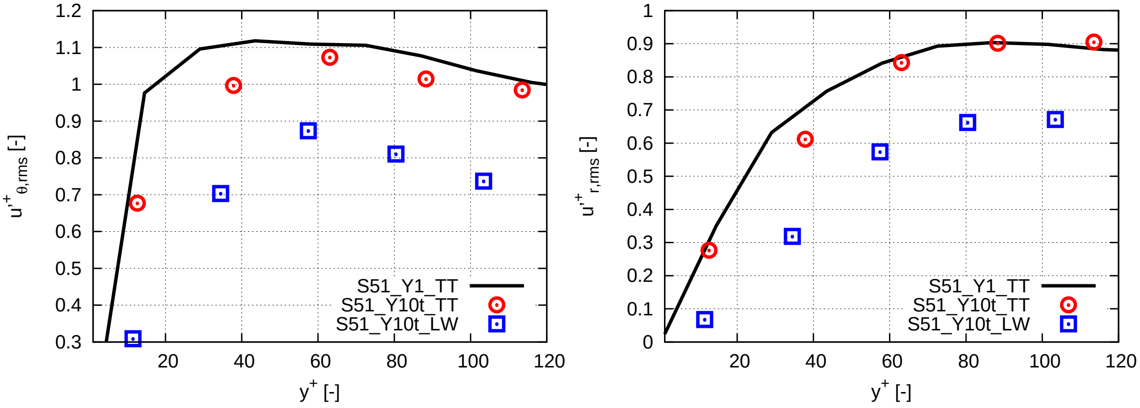

(b) $u'^{+}_{\theta,rms}$.

(c) $u'^{+}_{r,rms}$.

Figure 3.6.5: RMS of velocity fluctuations normalized by u_τ, $u'^{+}_{x,rms}$, $u'^{+}_{\theta,rms}$ and $u'^{+}_{r,rms}$, in the boundary layer of smooth tube S51 on mesh Y10t, compared to S51_Y1_TT.

3.7 WRLES of turbulent flow in ribbed tube R51: the reference case with mesh Y1 and TTGC scheme

The same numerical methodology as in the section 3.5 is now used to study the dynamics and wall flow in the ribbed tube R51. This section gives a first view of the results, and details are given in the next sections, in particular the comparison with the results in the smooth tube S51_Y1_TT. The convergence/averaging times and CPU cost of the ribbed tube case R51_Y1_TT are listed in Table. 3.7.1.

Case	τ_c	τ_a	Time step [s]	CPUs [s]	CPUh [h]
R51_Y1_TT	381	386	2.27×10^{-8}	0.193	83 838

Table 3.7.1: Convergence/averaging times and CPU cost of case R51_Y1_TT.

The effective operating point is given in Table. 3.7.2. As for the smooth case S51, the value of the source term S_{qdm} is adjusted manually to obtain a Reynolds number around 27 000, and is found to be 1830 Pa/m.

Case	S_{qdm} [Pa/m]	U_b [m/s]	Re [-]
R51_Y1_TT	1830	59.97	26 974.2

Table 3.7.2: Operating point for the ribbed tube case R51_Y1_TT.

3.7.1 Q-criterion

Figure 3.7.1 shows a snapshot of a Q-criterion iso-surface in one periodic pattern, colored by the axial velocity component[2]. As expected, the flow appears highly turbulent with elongated vortical structures in the wall region. Recirculating flow is visible downstream the ribs and the turbulence intensity seems slightly higher behind the ribs.

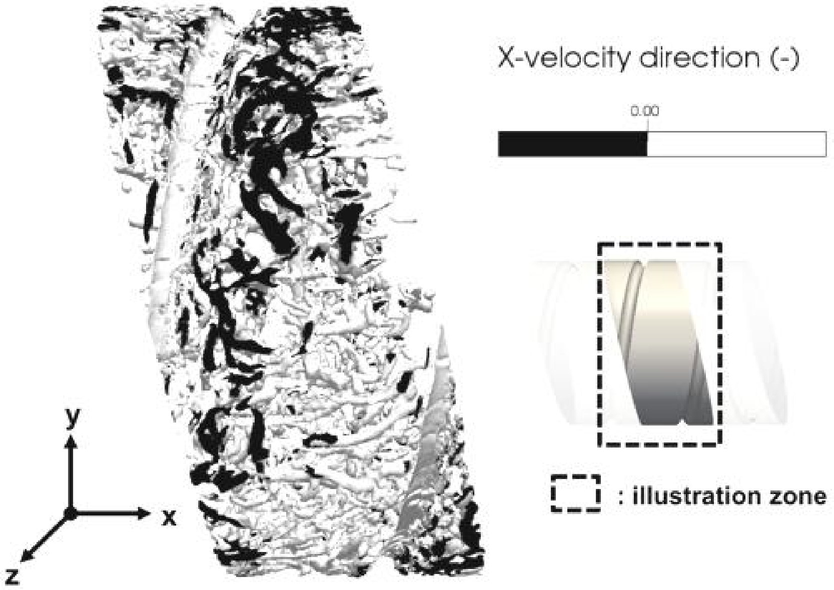

Figure 3.7.1: Turbulent flow in the ribbed tube R51_Y1_TT: instantaneous Q-criterion iso-surface, colored by axial velocity. Black corresponds to recirculating flow.

3.7.2 Mean velocity

Both transverse and axial cut planes are used to illustrate the fields of various mean quantities, as indicated in Fig. 3.7.2. For the axial cut plane, only half of the computational domain is illustrated due to symmetry.

The mean fields are helically axisymmetric, so they are independent of the axial position by rotating in the same way as the helical ribs, as illustrated on Fig. 3.7.3, showing the mean axial velocity fields normalized by the bulk velocity U_b in transverse planes at three positions A, B and C along the tube. Only the transverse cut plane at position A will be used in following.

The mean axial velocity field normalized by bulk velocity U_b is presented on Fig. 3.7.4, in both transverse and axial cut planes. A persistent recirculation zone is observed close to the wall, starting just behind the rib. With the the zero axial velocity contours marked with a

---

[2] Flow in the tube is from left to right, and the same for all figures.

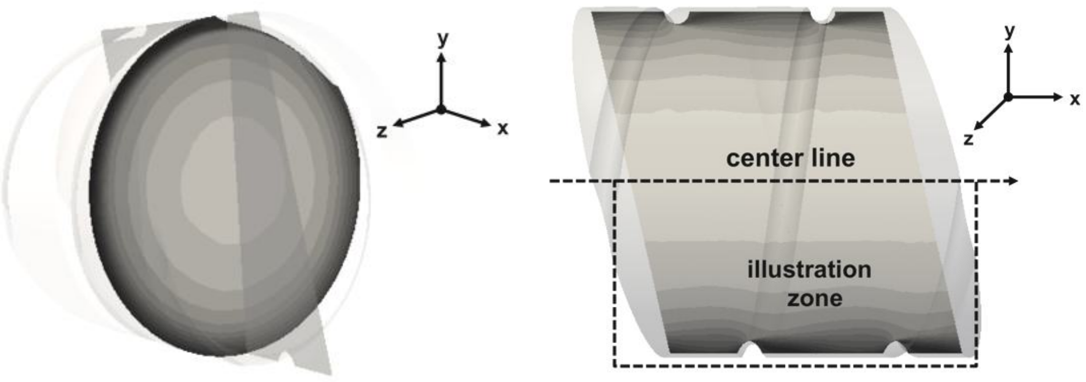

(a) Transverse cut plane. (b) Axial cut plane with two patterns.

Figure 3.7.2: Transverse and axial cut planes in ribbed tube R51.

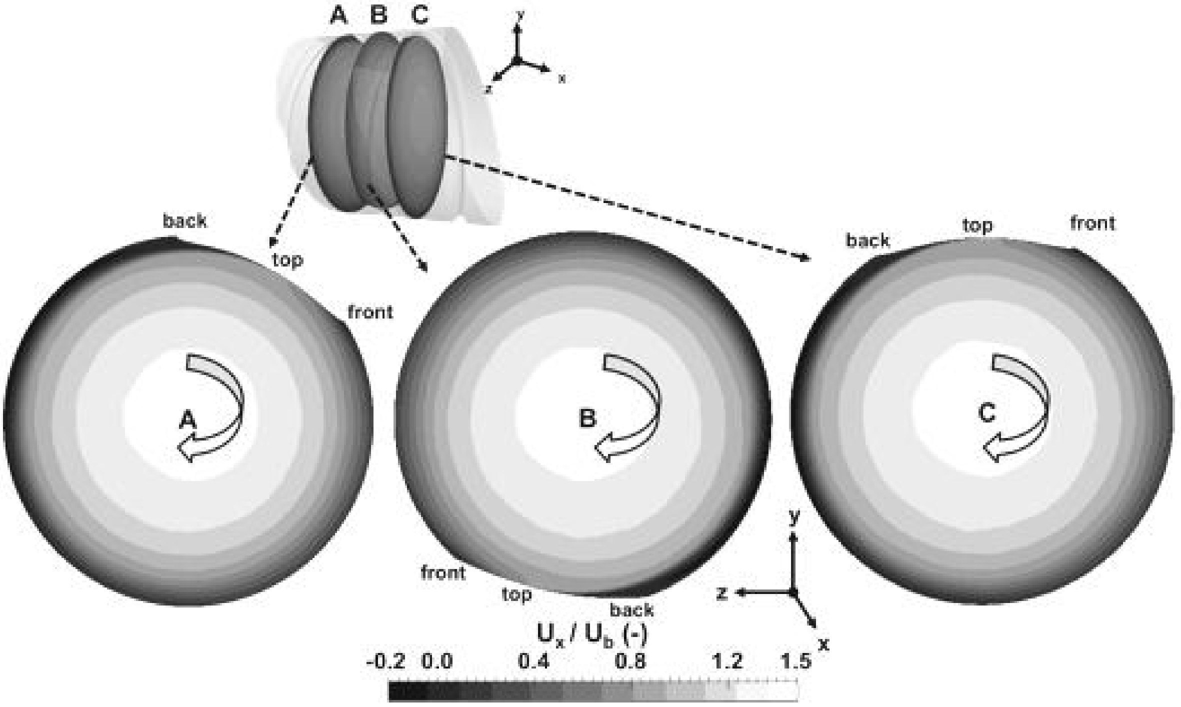

Figure 3.7.3: Mean axial velocity fields normalized by U_b in transverse planes at three positions in ribbed tube R51.

white line, a small upstream recirculation zone and a longer recirculation zone downstream the rib are shown. The latter starts at the top of the rib and extends downstream over a distance of 4-5e, in good agreement with the existing results from literature [108] (section 2.3.1) on ribbed walls having $10 < p/e < 20$. This confirms the strongly separated character of the wall flow, with a direct impact on the wall friction, and leading to a thicker boundary layer between ribs. In addition, the flow accelerates on the top of the rib, resulting in a locally thinner boundary layer in this zone.

Another remarkable feature of this flow is the rotating motion, illustrated by the azimuthal velocity $U_\theta = (U_y\ z - U_z\ y)/R$ (where y and z are the cartesian coordinates on the axial cut plane), normalized by U_b, in Fig. 3.7.5. The rib geometry creates a non-zero

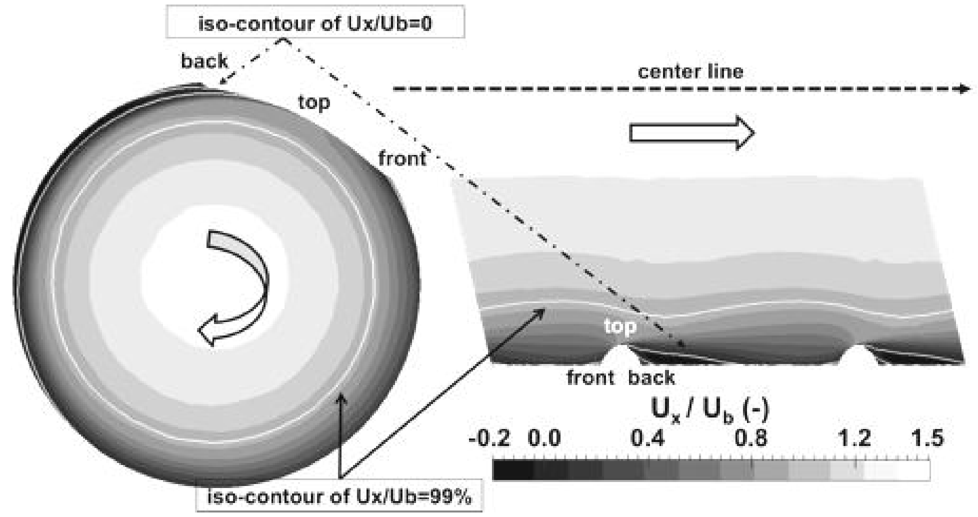

Figure 3.7.4: Mean axial velocity field normalized by U_b in the ribbed tube case R51_Y1_TT. The white lines mark zero axial velocity and the 99% of bulk velocity. Left: transverse cut; Right: half of axial cut, repeated on two periodic patterns.

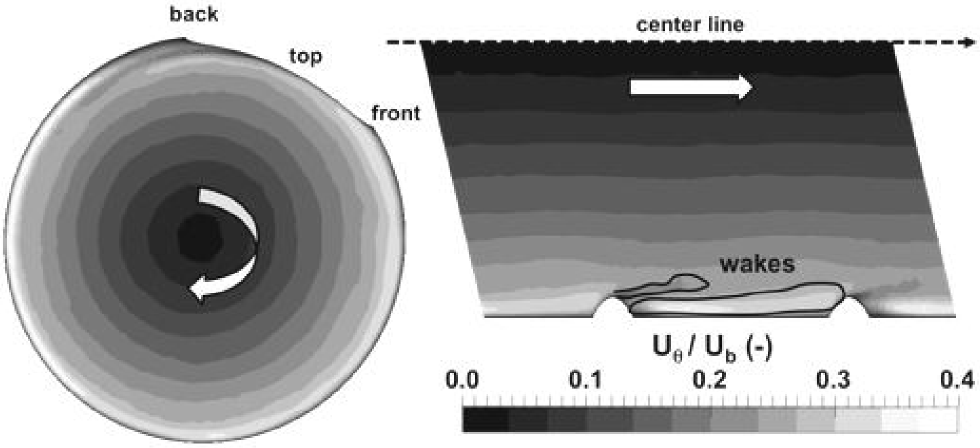

Figure 3.7.5: Mean azimuthal velocity field normalized by U_b in the ribbed tube case R51_Y1_TT. Left: transverse cut. Right: half of axial cut.

azimuthal velocity developing mostly between the ribs, and this rotating motion helps the flow to keep helical axisymmetry and contributes to the pressure loss as it extracts energy from the imposed pressure gradient. Moreover, two wakes appear downstream the rib: one is attached to the top of the rib,; the other appears behind the rib, due to the enhancement of the recirculation zone by the rotation motion, and where a maximum value of the azimuthal velocity is observed. The azimuthal velocity naturally decreases gradually from the wall region to the center of the tube.

A more quantitative insight on the effect of the ribs on the wall flow is given in Fig. 3.7.6, where the mean axial and azimuthal profiles (normalized by U_b) are plotted at a series of locations along the ribbed tube. The radial distance from the centerline r is normalized with the radius of tubes R, and the the axial distance from the rib top is normalized by the

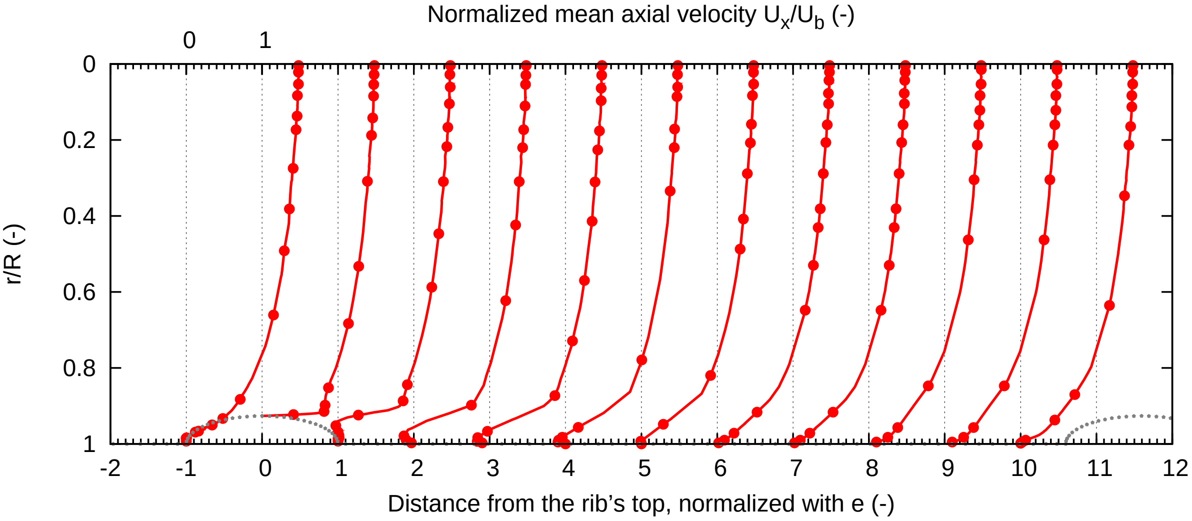

(a) Normalized mean axial velocity U_x/U_b.

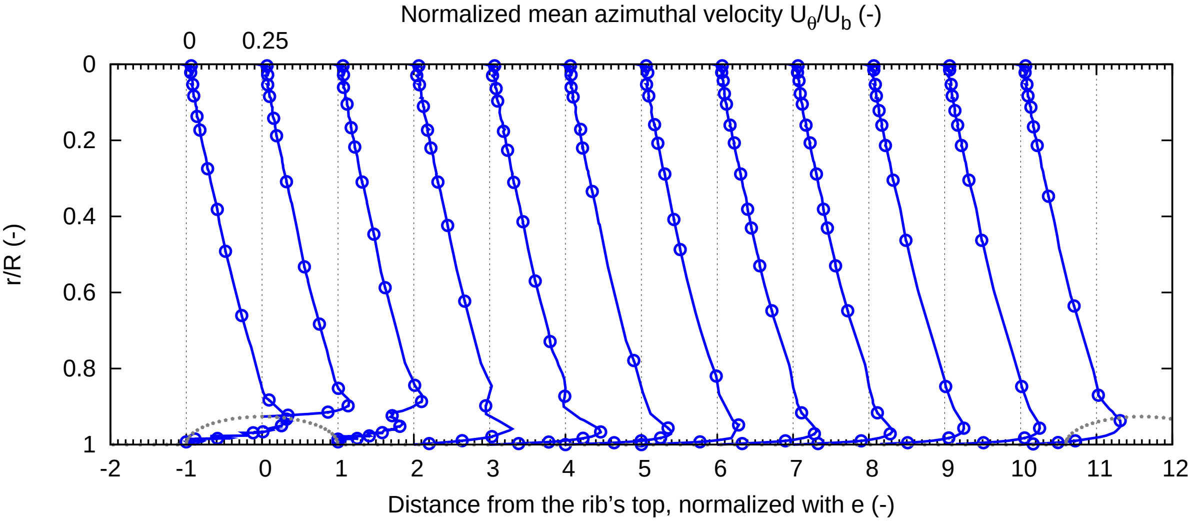

(b) Normalized mean azimuthal velocity U_θ/U_b.

Figure 3.7.6: Mean axial and azimuthal velocity profiles normalized by U_b, at various locations along the ribbed tube case R51_Y1_TT.

rib height e, as introduced in section 2.3.3 (Fig. 2.3.3). 12 locations are investigated from -1e to 10e. The scale of the velocity is indicated on top of the figures for location -1e, and is the same for all locations. Due to the presence of ribs, the velocity profiles vary a lot at the different locations, nevertheless, as explained in Fig. 3.7.3, the velocity profiles stay helically axisymmetric. The shape of the profiles differ mainly in the near-wall region, while both axial and azimuthal velocity components stay unchanged on the central axis, being respectively $U_{x,c}/U_b \sim 1.45$ and $U_{\theta,c}/U_b = 0$. This confirms the limited blocking effect of the small-size ribs, whose impact stays mostly confined to the wall region. The axial velocity shows important deviations from a smooth tube wall flow due to both the acceleration on the rib top and the recirculation zones. The length of the downstream recirculation zone is observed clearly between 4-5e. The peak values of the azimuthal velocity (normalized by U_b) vary from 0.25 to 0.45, and stays almost at the same distance from wall. A second peak is observed at location 1e to 4e, corresponding to the downstream recirculation zone.

3.7.3 RMS of velocity fluctuations

Finally the impact of the ribs on turbulence may be viewed from Fig. 3.7.7 showing the RMS of the axial fluctuating velocity u'_{rms} normalized by U_b. There is a clear trace of the rib, with turbulence production in the separation induced shear layer. The inter-rib distance is too large in this case to observe interaction between the turbulent wakes of two successive ribs and there seems to be no cumulative effect in the axial direction. This is consistent with the observation that the simulation seems insensitive to the number of rib patterns involved. The zone of maximum turbulence intensity is maintained at a fixed wall distance corresponding to the rib top, which is therefore an important geometrical feature to maximize mixing and enhance heating in the final application.

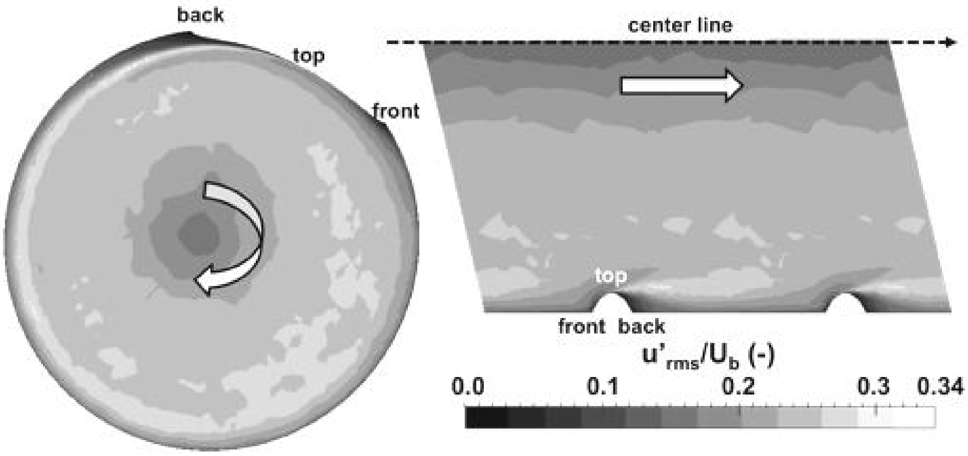

Figure 3.7.7: RMS of the axial fluctuating velocity field u'_{rms} normalized by U_b in the ribbed tube case R51_Y1_TT. Left: transverse cut. Right: half of axial cut.

3.7.4 Pressure variation

As mentioned in section 2.5.3, unlike in the periodic smooth tube, pressure in the ribbed tube varies a lot along the tube. The coefficient C_p (defined in Eq. 2.5.1) can be used as a normalized pressure to illustrate the pressure variation. The pressure in the downstream corner of the rib is taken as the reference P_{ref} in Eq. 2.5.1, so that by definition C_p is always equal to zero at this location. The mean field of C_p is shown on Fig. 3.7.8 in the transverse and axial cut planes. Although the pressure increases in front of the rib and decreases behind in the viscous region, it stays undisturbed in the outer flow. These pressure variations are clearly correlated to the upstream and downstream recirculation zones and play a key role in the global pressure loss.

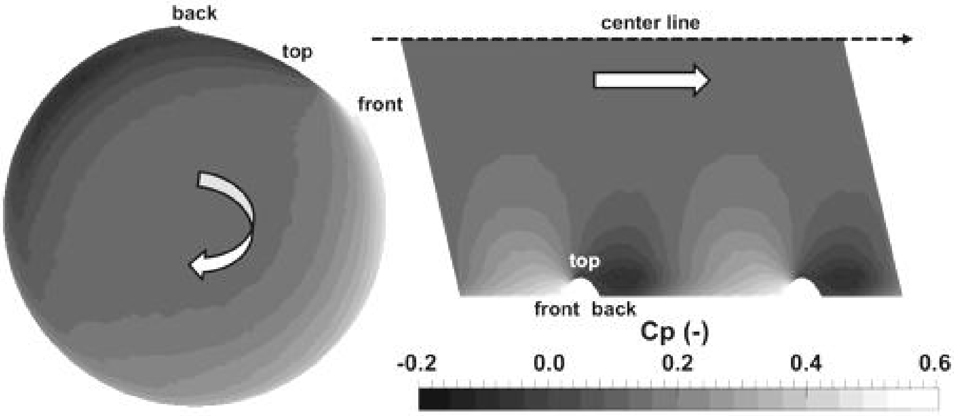

Figure 3.7.8: Mean pressure coefficient fields in the ribbed tube case R51_Y1_TT. Left: transverse cut. Right: axial cut.

3.8 Impact of ribs: comparison between the ribbed tube R51 and smooth tube S51

3.8.1 Boundary layer thickness

Two cases both with mesh Y1 and TTGC scheme are compared to analyze the difference between the ribbed tube R51 and smooth tube S51, i.e., R51_Y1_TT and S51_Y1_TT. Five locations are taken from the ribbed tube R51 for further comparisons with S51, which are respectively on the upstream corner (-1*e*), the top (0*e*), the downstream corner (1*e*) of ribs, in the downstream recirculation zone (3*e*), and out of the recalculation zone (7*e*) (index referred to Fig. 3.7.6). The boundary layer thickness δ_{th} (where $U_x = 99\% U_b$) at these locations normalized by the pipe radius R are given in Table. 3.8.1, and compared to S51.

	Locations in R51					S51
	-1*e*	0*e*	1*e*	3*e*	7*e*	
δ_{th}/R	0.232	0.137	0.201	0.202	0.235	0.206

Table 3.8.1: Boundary layer thickness at different locations in ribbed tube R51, compared to the smooth tube S51.

Note that at the location 0*e*, the distance is measured from the top of the rib. It agrees well with what was shown by the iso-contour of $U_x = 99\% U_b$ in Fig. 3.7.4, the boundary layer thickness in the downstream recirculation in R51 being very close to the value in S51. Then it increases and becomes thicker than that in S51, and finally decreases when the flow accelerates on the top of the ribs, leading there to a thinner boundary layer than in S51.

The global $\tau_{w,g}$ (see Appendix B) in tubes obtained using Eq. 2.1.48 (using the value of the imposed source term as the pressure loss) is preferred to define the global friction velocity $u_{\tau,g}$. With this notion, the dimensionless boundary layer thickness $\delta_{th}^{+} = (u_\tau \delta_{th})/\nu$ at the five locations in the ribbed tube case R51_Y1_TT are rewritten in Table. 3.8.2.

	Locations in R51					S51
	-1e	0e	1e	3e	7e	
δ_{th}^+	420	248	363	365	426	145

Table 3.8.2: Dimensionless boundary thickness at different locations in ribbed tube R51, compared to the smooth tube S51.

Note that δ_{th}^+ at the location 0e is larger than in the smooth tube S51, due to the high global friction velocity in the ribbed tube R51.

3.8.2 Velocity profiles

Using the global wall shear stress $\tau_{w,g}$ (obtained from $\tau_{w,g} = S_{qdm} D/4$ using Eq. 2.1.48, refer to Appendix B), the dimensionless velocity $u^+ = u/u_{\tau,g}$ (where $u_{\tau,g} = 8.04\,\mathrm{m/s}$, compared to $3.22\,\mathrm{m/s}$ in the smooth tube case S51_Y1_TT) is plotted against $y^+ = (u_{\tau,g} y)/\nu$ in Fig. 3.8.1. A similar behavior of u^+ is found at the five locations for $y^+ > 400$, i.e., in the outer region, with the same shift $\Delta u^+ \sim 13$ compared to the smooth tube S51. This observation agrees well with the observations in [95, 112] (as mentioned in section 2.3.3). On the contrary, in the log law region of the boundary layer $50 < y^+ < 400$, only the locations -1e and 7e are similar, keeping the shift $\Delta u^+ \sim 13$ with S51, while the profiles vary a lot at other locations, due to the impact of the rib, e.g., the downstream recirculation zone leading to the negative value at location 3e.

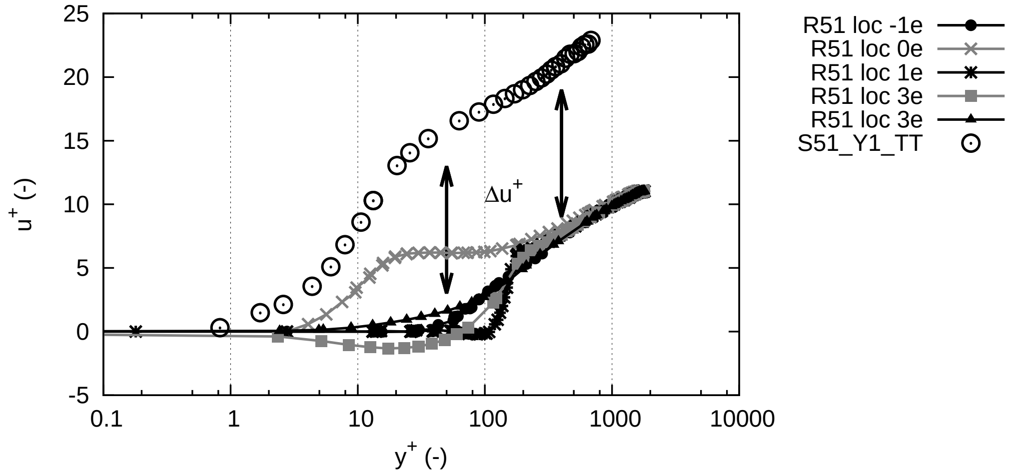

Figure 3.8.1: u^+ (normalized by global $u_{\tau,g}$) *vs* y^+ at five locations in the ribbed tube R51, compared to results in the smooth tube S51.

3.8.3 Turbulence intensity

The value of u_τ averaged over the surface, equal to $1.62\,\mathrm{m/s}$, is now used to non-dimensionalize velocity fluctuations in the boundary layer, plotted in Fig. 3.8.2 for case R51_Y1_TT and compared to the results in the smooth tube case S51_Y1_TT.

First, in a general view, the velocity fluctuations are all stronger in R51 than in S51 (re-

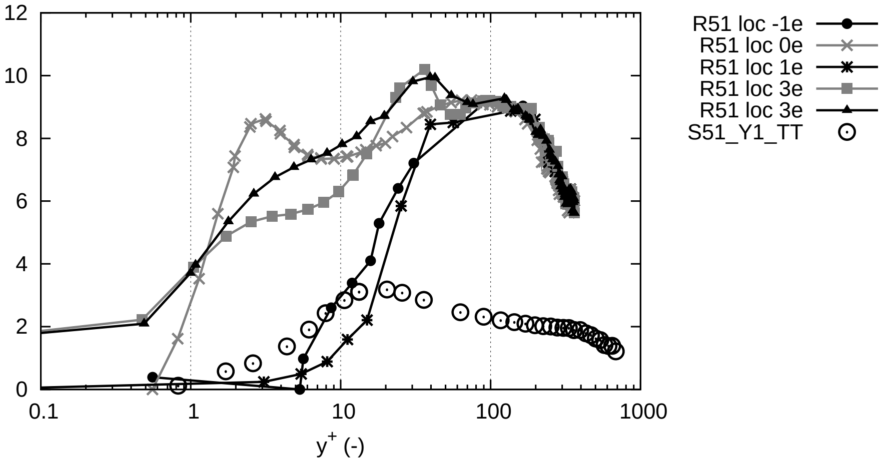

(a) $u'^{+}_{x,rms}$.

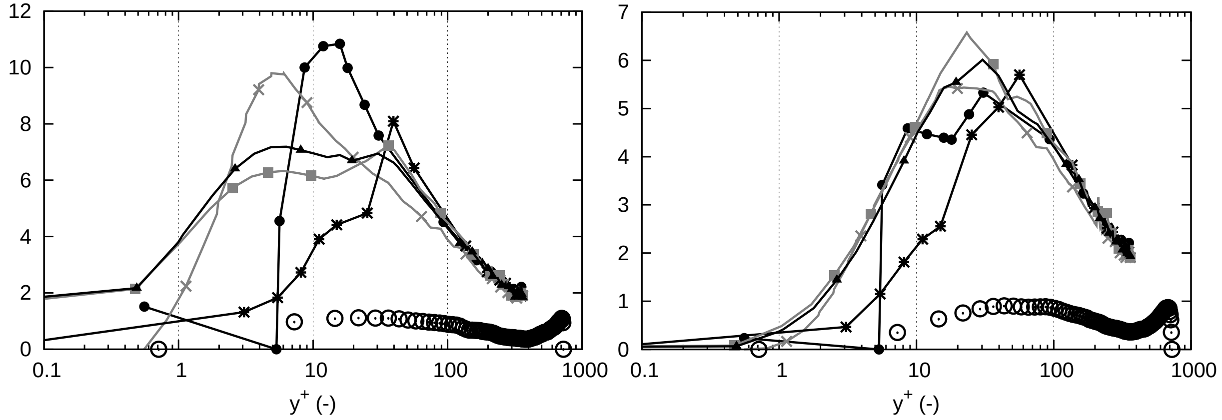

(b) $u'^{+}_{\theta,rms}$.

(c) $u'^{+}_{r,rms}$.

Figure 3.8.2: RMS of velocity fluctuations normalized by surface averaged u_τ: $u'^{+}_{x,rms}$, $u'^{+}_{\theta,rms}$ and $u'^{+}_{r,rms}$, in the ribbed tube R51 at 5 locations, compared to data in smooth tube S51.

spectively 3, 6 and 6 times higher for $u'^{+}_{x,rms}$, $u'^{+}_{\theta,rms}$ and $u'^{+}_{r,rms}$), and differ at the five different locations, especially for $u'^{+}_{x,rms}$ and $u'^{+}_{\theta,rms}$, as the axial and azimuthal motions are dominant. Second, unlike in the smooth tube, where only the axial motion is dominant, the intensities of both $u'^{+}_{x,rms}$ and $u'^{+}_{\theta,rms}$ in helically ribbed tube R51 are at the same level (peak values at around 10), twice higher than $u'^{+}_{r,rms}$;
Third, for $u'^{+}_{x,rms}$, peak locations shift toward the tube center in R51 compared to S51, due to the thicker boundary layer, and two peaks are observed at location 0e (on top of the rib) and 3e (in the downstream recirculation zone). Moreover, almost the same profile is found at location -1e and 1e (the two corners of the rib) in R51, while the profile shape at location 7e is very similar (but with higher value) to the one in S51, and the profile at location 3e is intermediate between the profiles at locations 0e and 7e;
Finally, for $u'^{+}_{\theta,rms}$, the largest peak value is observed at location -1e in R51, where the rotation motion starts to develop, while the second largest peak value is at location 0e (rib top). Similar behaviors are observed at location 3e and 7e.

The RMS of velocity fluctuations normalized with the bulk velocity are also plotted against r/R in Fig. 3.8.3 for cases R51_Y1_TT and S51_Y1_TT.

To summarize, the turbulence intensity is significantly increased in the helically ribbed

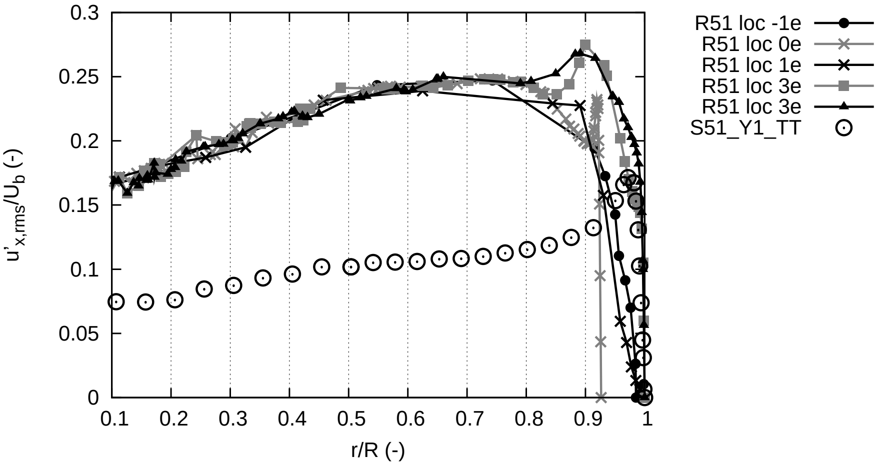

(a) $u'_{x,rms}/U_b$.

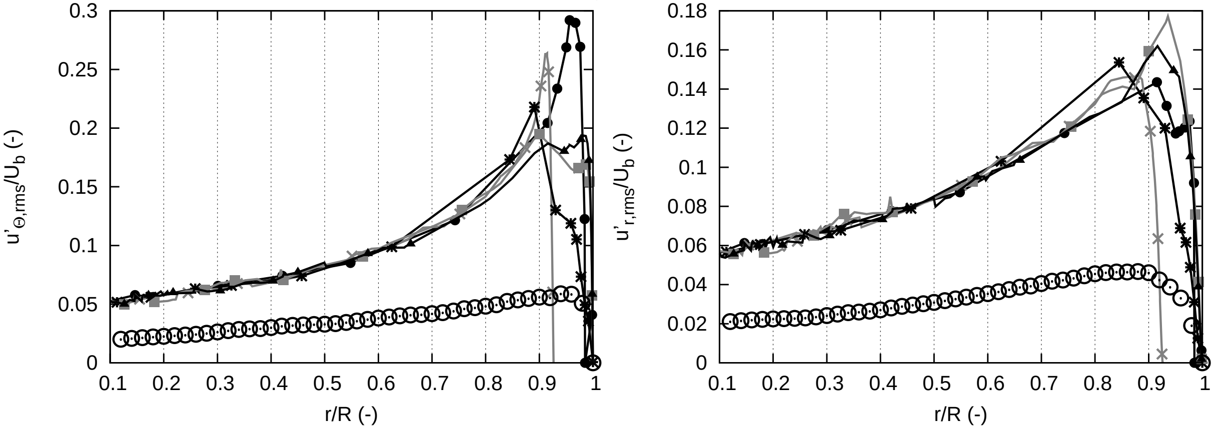

(b) $u'_{\theta,rms}/U_b$.

(c) $u'_{r,rms}/U_b$.

Figure 3.8.3: RMS of velocity fluctuations normalized by U_b in the ribbed tube R51 at 5 locations, compared to smooth tube S51.

tube R51, compared to the smooth tube S51, and the rotation motion becomes also as dominant as the streamwise flow in R51.

3.8.4 Energy spectrum and turbulent viscosity

The kinetic energy spectra at center and 1/4 radius in both tubes S51 and R51 are plotted in Fig. 3.8.4. At 1/4 radius, the spectra in case R51_Y1_TT are plotted at 3 locations and similar results are found. The -5/3 slope is always observed, but more energy is found in the highest frequency range in R51.

The turbulent viscosity ν_t fields are shown on the transverse plane (one pattern) of the tubes S51 and R51 in Fig. 3.8.5. Consistently with the higher fluctuation levels and smaller turbulence scales in the ribbed tube R51, globally stronger value is observed in the smooth tube while the turbulent viscosity close to the wall is zero in both tubes.

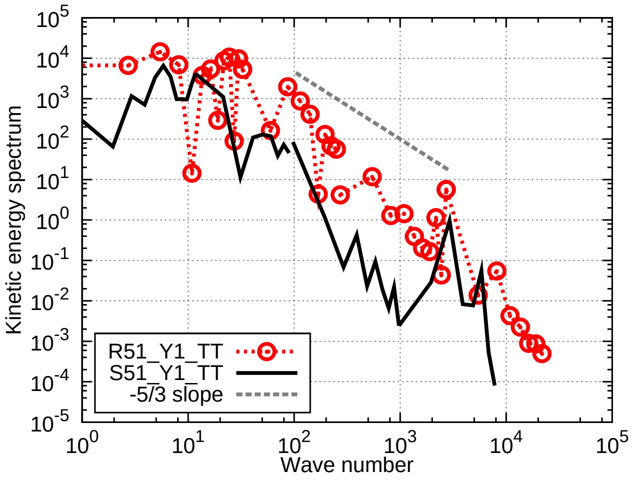

(a) Center.

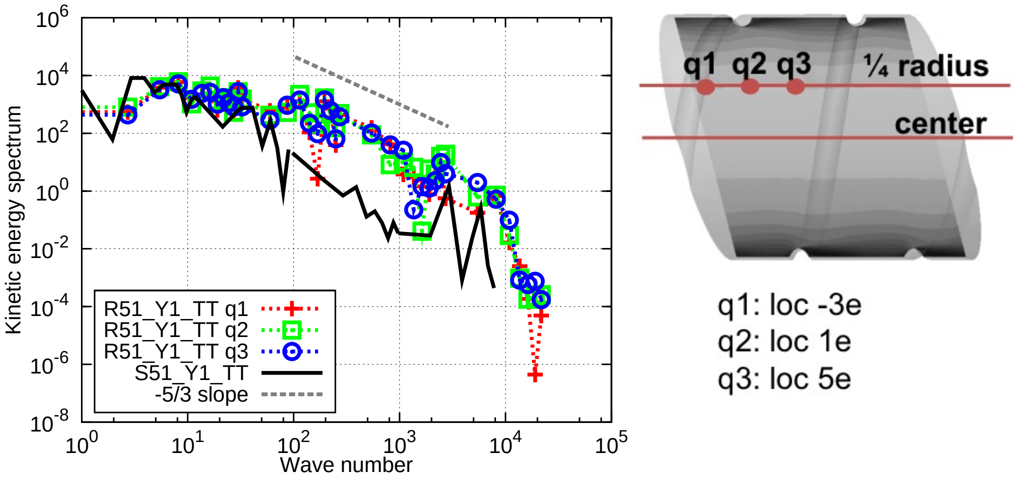

(b) 1/4 radius.

(c) Illustration.

Figure 3.8.4: Kinetic energy spectrum in both tubes S51 and R51: cases S51_Y1_TT and R51_Y1_TT.

3.8.5 Pressure drag and friction drag

The global friction factor (Eq. 2.1.49) in the ribbed tube R51 is equal to 0.0356, i.e., much higher than all measured values for a Reynolds number of 27 000 in Fig. 2.4.7, replotted here in Fig. 3.8.6. Compared to 0.0057 in the smooth tube, it shows an increased global friction factor of 524%.

To better understand the global friction factor, the momentum equation of steady flow in a tube with periodic configuration is considered:

$$\rho \frac{d\vec{u}}{dt} = -\vec{\nabla} P + \nabla \cdot \overline{\overline{\tau}} + \vec{F}_{vol}, \tag{3.8.1}$$

where the volume force is related to the imposed source term S_{qdm} in Eq. 3.3.3. From this

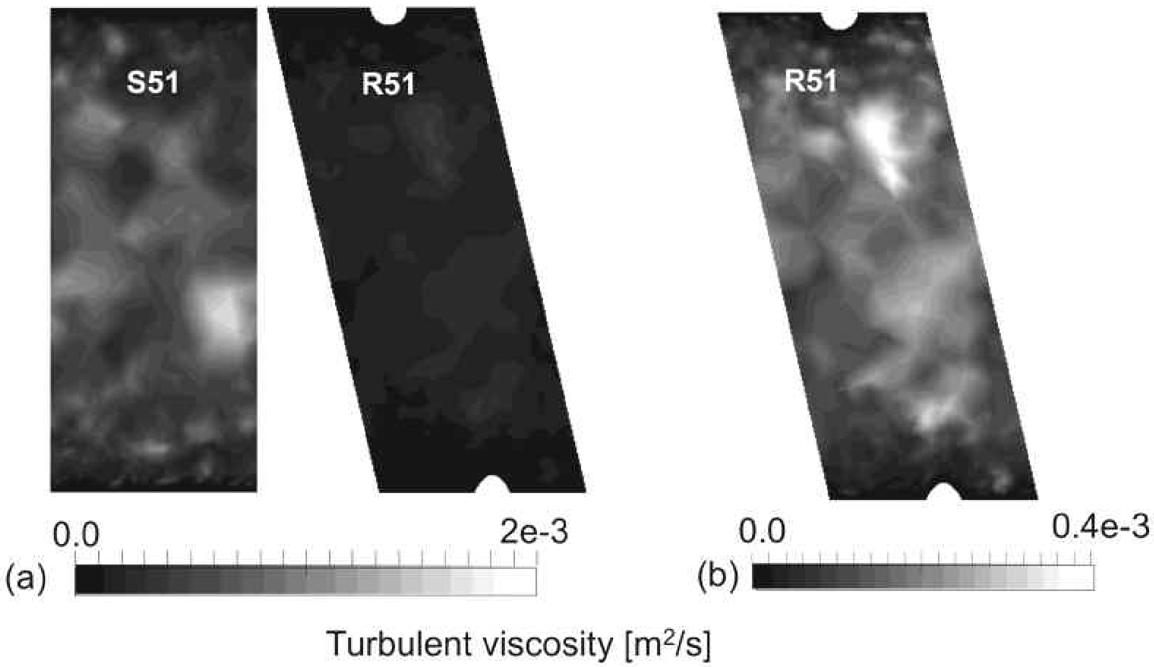

Figure 3.8.5: Turbulent viscosity on the transverse plane in cases S51_Y1_TT and R51_Y1_TT.

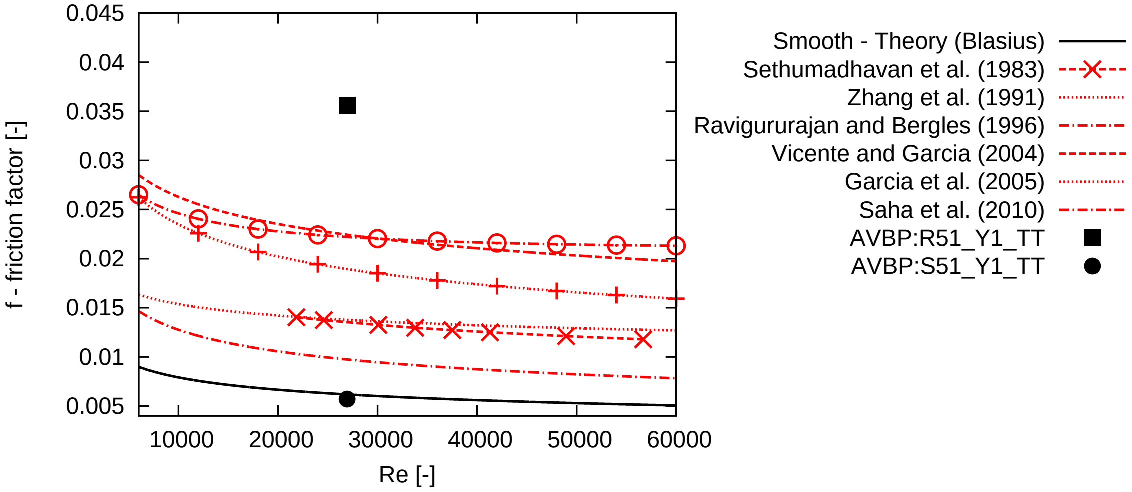

Figure 3.8.6: Friction factors versus Reynolds number in ribbed tube R51 and smooth tube S51, compared to published experimental works.

equation, a balance equation is written for the axial momentum:

$$0 = \underbrace{-\oint Pn_x \mathrm{d}S}_{pressure\ \ drag} + \underbrace{\oint \vec{\tau}(x)\mathrm{d}S}_{friction\ \ drag} + \underbrace{\int S_{qdm,x}\mathrm{d}V}_{total\ \ imposed\ \ force} \quad , \tag{3.8.2}$$

where n_x is the axial component of the wall-normal vector and $\vec{\tau}(x)$ is the axial component of the stress vector (see Appendix B).

In a smooth periodic tube pressure drag is zero because the pressure keeps spatially constant. The imposed force generated by the source term S_{qdm} is totally balanced by the friction drag. On contrary, as mentioned in section 3.7.4, pressure variation is observed in the ribbed tube R51. With the definition of the local pressure coefficient C_p (Eq. 2.5.1) over the wall and of the local skin-friction coefficient C_f (Eq. 2.3.1), Eq. 3.8.2 can be rewritten as:

$$0 = \underbrace{-\frac{1}{2}\rho_b U_b^2 \oint (C_p n_x + C_f)\mathrm{d}S}_{total\ \ drag} + \underbrace{\int S_{qdm,x}\mathrm{d}V}_{total\ \ imposed\ \ force} \tag{3.8.3}$$

The evolution of C_p and C_f along the wall surface in both ribbed (R51_Y1_TT) and smooth (S51_Y1_TT) tubes are illustrated in Figs. 3.8.7 and 3.8.8.

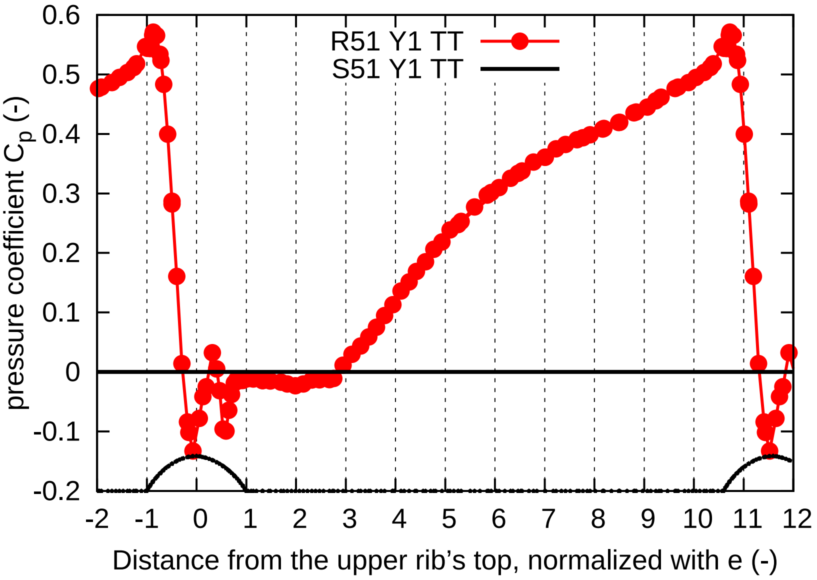

Figure 3.8.7: Evolution of the pressure coefficient C_p along the wall surface in both ribbed (R51_Y1_TT) and smooth (S51_Y1_TT) tubes.

As done in section 3.7.4, the pressure in the downstream corner of the rib is taken as the reference P_{ref} in Eq. 2.5.1, so that C_p is zero at this location. Local data P and $\vec{\tau}(x)$ are taken at the first node above the wall of the time-averaged solution of ribbed tube R51_Y1_TT. As there is no pressure gradient in axial direction, C_p in the smooth tube S51 is zero. On the contrary, the local pressure coefficient C_p in the ribbed tube R51 gradually increases from the downstream location $2e$ until the location around $10.6e$ (the upstream corner of the next rib), where a recirculation zone is observed, reaching a maximum value of around 0.58, then decreases on windward of the rib till the top of the rib where is located the minimum value. After small perturbations on leeward of the rib, C_p remains almost constant in the downstream corner region from $1e$ to $2e$. This qualitatively agrees well with the distribution of local pressure coefficient over the surface in a ribbed tube observed by Vijiapurapu & Cui (2007) [150]. Note however that the contribution of pressure $C_p n_x$ in Eq. (3.8.3) is non-zero only on the rib surface, where $\vec{n}$ has a non-zero axial component.

The local wall shear stress (related to the local friction coefficient C_f) in the ribbed tube R51 exhibits a strong peak just before the rib top, with a maximum of $C_f = 0.0375$ ($\vec{\tau}_x \cdot \vec{n} = 27$ Pa), about 8 times higher than in the smooth tube S51 (Fig. 3.8.8). C_f is around zero between $1e$ to $2e$ (the downstream corner region of the rib of a length e), where

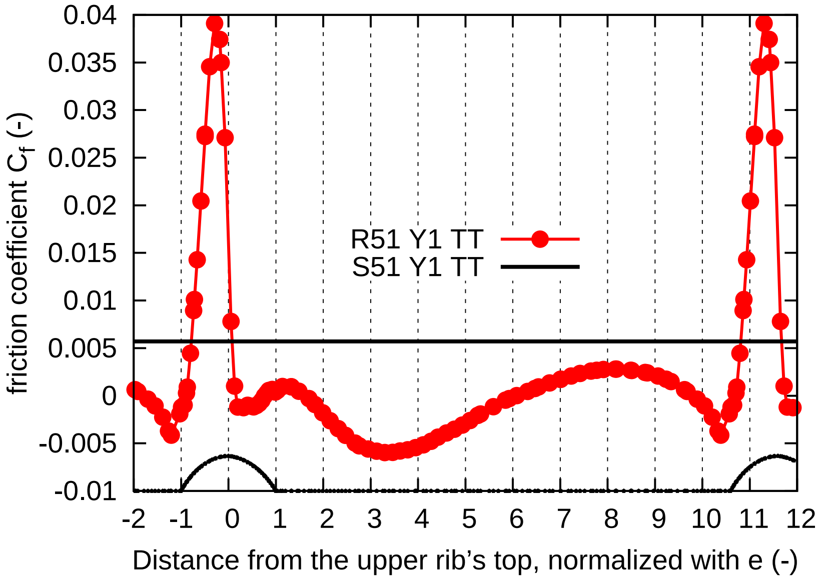

Figure 3.8.8: Evolution of the skin friction coefficient C_f along the wall surface in both ribbed (R51_Y1_TT) and smooth (S51_Y1_TT) tubes.

flow separation occurs, then becomes negative in the recirculation zones between $1e$ to $4e$ (downstream of the rib) and $10e$ to $11e$ (upstream of the next rib). Between the ribs the wall shear stress is always below the smooth tube value, due to the effect of the separation and reattachment. This also is in good qualitative agreement with the distribution of local friction factor over ribbed wall observed by Lee et al. (2008) [97]. Note that the maximum value of C_p is about 20 times higher than the maximum value of C_f.

Table 3.8.3 gives the results of the axial momentum balance in both ribbed (R51_Y1_TT) and smooth (S51_Y1_TT) tubes. In this table, the total drag is the sum of pressure and friction drag in Eq. 3.8.2. The calculated drag components and imposed force are all normalized by $\rho U_b^2 L^2$, where $L = p$ is the tube length. Results are also expressed in terms of percentage of the total imposed force in the smooth tube S51_Y1_TT, taken as a reference.

	Pressure drag	Friction drag	Total drag	Total imposed force
R51	1.28×10^{-1} (609.5%)	5.37×10^{-3} (25.5%)	1.33×10^{-1} (635%)	1.30×10^{-1} (619%)
S51	0 (0%)	2.1×10^{-2} (100%)	2.1×10^{-2} (100%)	2.1×10^{-2} (100%)

Table 3.8.3: Axial momentum equation balance in both ribbed (R51_Y1_TT) and smooth (S51_Y1_TT) tubes.

The increased total drag and the imposed force in R51 agree with the increase of global friction factor compared to S51. Not surprisingly the total axial drag in the ribbed tube is mainly due to the pressure drag created by the ribs: the flow separation induced by the ribs results in a contribution as high as 96% of the total drag through its pressure contribution. Consistently the friction force is reduced in comparison to the smooth case S51, as significant portions of the flow are detached.

Flow separation and its effects regarding the total drag provide some guidance to setup simulations of the same configuration at a reduced cost: (i) The flow separation is a critical feature that requires significant resolution to be accurately represented. Strongly under-resolved mesh in the vicinity of the wall would poorly capture this feature and lead to inaccurate results regarding the total drag estimation. (ii) This test case is a good candidate for roughness-type modeling of wall flows in which an empirical sink term is added to the momentum equation, accounting for the local pressure loss created by the rib. This kind of modeling can potentially generate significant savings, especially regarding mesh generation as the computation would be carried out in a smooth tube, the pressure jump produced by the rib being fully modeled. The model should help recovering the correct swirl properties of the flow field by providing the correct torque. However, questions arise regarding the turbulence intensity generated by the rib wake. Such modeling approach should be tested in further studies, but was not investigated in the present work.

3.9 Comparison of WRLES of turbulent flow in ribbed tube R51 between the LES codes AVBP and CharLes^X

In this section, the objective is to compare the results in the tube R51 obtained in AVBP with another high-fidelity LES code, CharLes^X, as there is no experimental data available yet. The simulations and post-processing using CharLes^X were conducted by Dr. Julien Bodart[1] and his student Emmanuel Tabeko[1].

3.9.1 Description of the CharLes^X solver, grid and operating points

Description of the CharLes^X solver

CharLes^X is a high-fidelity unstructured compressible flow solver for LES, developed by CTR (Center for Turbulence Research) at Stanford University and ISAE/DAEP, ENSICA. It solves the spatially-filtered compressible N-S equations, using a finite volume formulation, control-volume based discretization on unstructured hexahedral meshes [184,185]. The background scheme is only non-dissipative for perfectly regular grids, but adds a small amount of numerical dissipation on irregular grids to aid the robustness [186]. Two sub-grid scale modeling options are available in the code: the dynamic Smagorinsky model [187–189] and a dynamic version of the Vreman model [190,191]. A mole detailed description of CharLes^X can be found in Khalighi et al. (2011) [184].

Structured mesh for code CharLes^X

The LES code CharLes^X requires a full hexahedra structured mesh, which turned to be quite difficult to generate. To generate the mesh with hexahedra in the ribbed tube R51, the rib geometry had to be slightly modified (Fig. 3.9.1) due to different CAD treatment, as well as the inlet and outlet of the periodic domain (Fig. 3.9.2). While the rib have the same shape, their orientation is different. This may impact the wall flow structure close to the rib and should be kept in mind for further comparison of the two codes.

Fig. 3.9.2 displays the grid used in CharLes^X. The mesh resolution also holds $y^+ = 1$

---

[1] ISAE/DAEP, ENSICA, Toulouse France

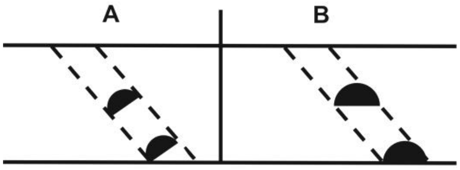

Figure 3.9.1: Difference in rib geometry in the configuration R51 for AVBP (A) and CharLes^X (B).

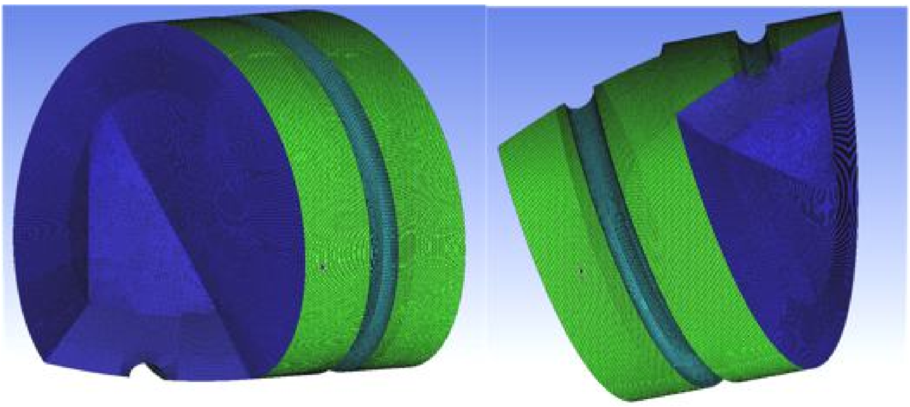

Figure 3.9.2: Mesh of ribbed tube for LES code CharLes^X: $y^+ = 1$ with hexahedra (by Dr. Julien Bodart).

near the wall to compare with the mesh Y1 used in AVBP. The mesh contains 14 million cells.

Operating points

The objective is to compare the case R51_Y1_TT of AVBP with CharLes^X. The effective operating point simulated with CharLes^X slightly differ from the one calculated with AVBP. Table. 3.9.1 compares them.

Case	Code	U_b [m/s]	Re	μ [kg/(ms)]	ρ_b [kg/m]	T_b [K]	P_b [Pa]
R51_Y1_TT	AVBP	59.97	26 974.2	4.10×10^{-5}	0.36	973	101 356.5
R51_Y1h	CharLes^X	54.09	28 200	6.34×10^{-5}	1.3	290	110 500

Table 3.9.1: Operating points for ribbed tubes cases: R51_Y1_TT using AVBP and R51_Y1h using CharLes^X.

The Reynolds number of the turbulent flow is close to 27 000 in both simulations. The differences in laminar viscosity μ and mass density ρ are mainly due to the different flow temperatures: case R51_Y1_TT with AVBP is run at 973 K as it is the typical temperature of the cracking process, while case R51_Y1h using CharLes^X uses an ambient temperature 290 K. This difference in bulk temperature (and bulk pressure) has however no impact on the results, as all comparisons are conducted for the same non-dimensionless parameters, related to the tube geometry and the Reynolds number.

The convergence time for CharLes^X (noted R51_Y1h) are summarized in Table. 3.9.2:

Case	Code	τ_c	τ_a	Time step [s]	CPUs [s]	CPUh [h]
R51_Y1h	CharLes^X	3-4	8	1.15×10^{-7}	1368	10 000

Table 3.9.2: Convergence and CPU times of case R51_Y1h using CharLes^X.

3.9.2 Velocity

All the fields are compared in the half axial cut plane of the ribbed tube R51. In this section, the illustration domain and the color scales of the AVBP results are adapted to the ones used for the CharLes^X results. Fig. 3.9.3 shows the time-averaged fields of axial velocity normalized by U_b. The white arrow indicates the flow direction. The fields obtained with the two codes are very similar, both of them showing the acceleration on rib top and the recirculation zones upstream and downstream the rib, visualized with the zero-velocity contours (white line). The length of the downstream recirculation zone simulated with CharLes^X is slightly shorter than in the AVBP case, equal to around $4e$ and $4.5e$ respectively.

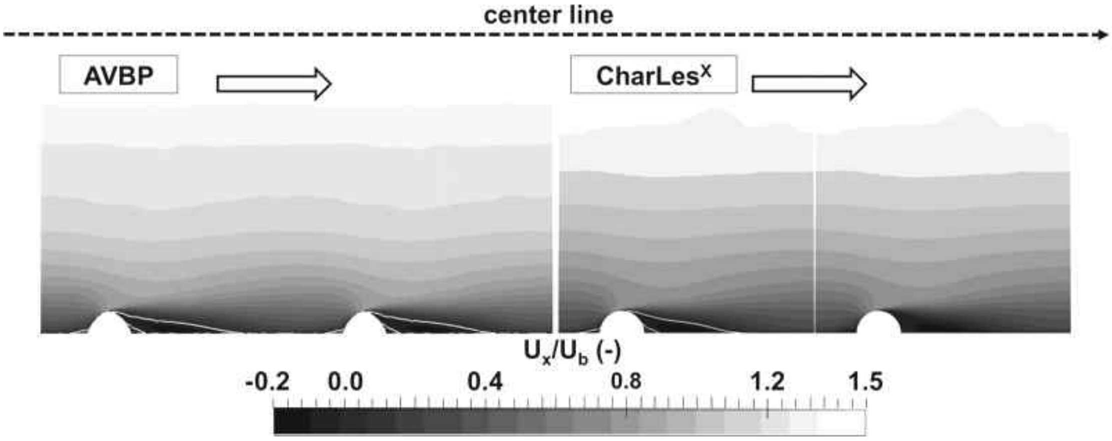

Figure 3.9.3: Mean axial velocity fields normalized by U_b in ribbed tube R51. Left: R51_Y1_TT using AVBP; Right: R51_Y1h using CharLes^X.

The rotational motion induced by the helical ribs in the tube is analyzed looking at the mean azimuthal velocity fields normalized by the bulk velocity U_b, shown in Fig. 3.9.4. The same flow topology is recovered by AVBP and CharLes^X. The difference between AVBP and CharLes^X results lays in the strength of the rotational motion, which is about twice larger in the AVBP simulation and has therefore a more important impact on the outer region. This may explain the longer length of the downstream recirculation zone in the AVBP results. This difference may be due to the different geometries and the difference between two codes, and further analysis is needed.

For quantitative comparison, time-averaged profiles of axial (Fig. 3.9.5) and azimuthal velocity (Fig. 3.9.6) (normalized by U_b) are plotted along the tube at different locations of the ribbed tube R51. Note that the data of CharLes^X are provided only at 7 locations (from -1e to 5e). A zoom near the wall ($0.8 < r/R < 1$) is given in the bottom of the figures. Very similar axial velocity profiles are found between AVBP and CharLes^X, even in the near wall region, where good agreement is observed. However, the azimuthal velocity shows larger differences, as already observed in Fig. 3.9.4. A stronger rotational motion is observed in

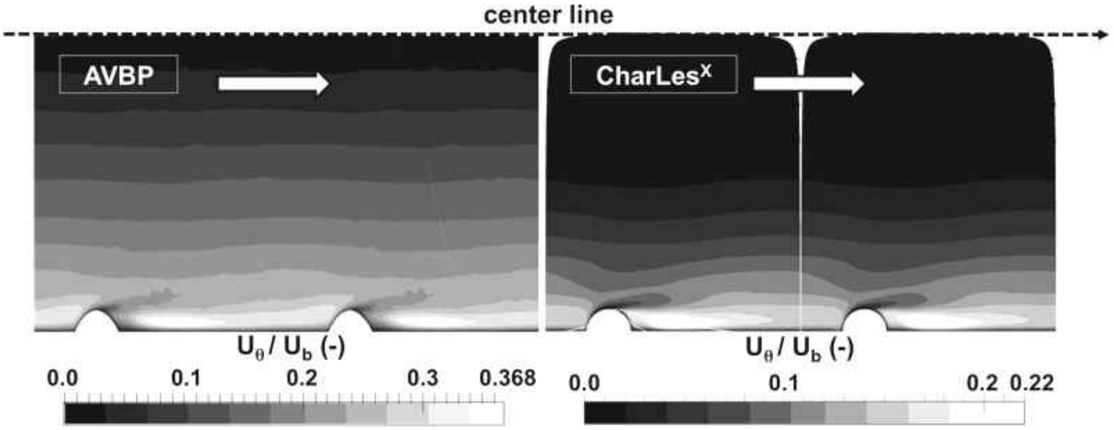

Figure 3.9.4: Mean azimuthal velocity field normalized by U_b in ribbed tube R51. Left: R51_Y1_TT using AVBP; Right: R51_Y1h using CharLes^X.

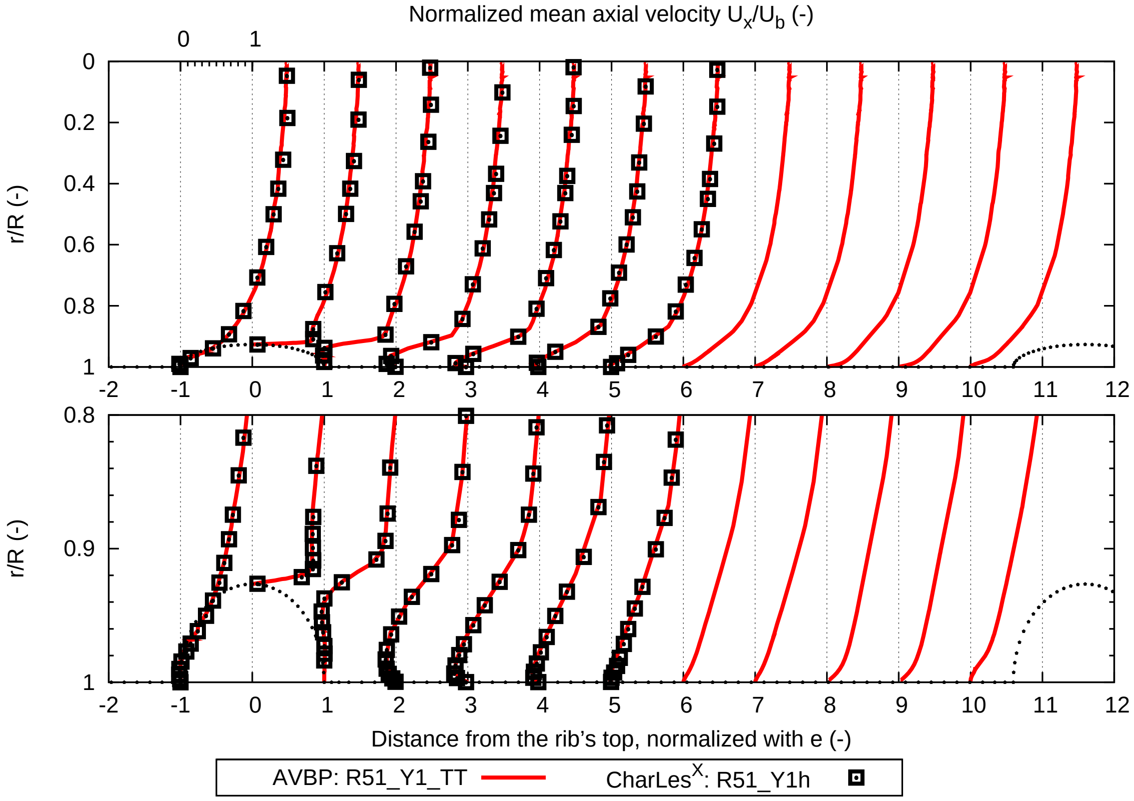

Figure 3.9.5: Time-averaged axial velocity profiles (normalized by U_b) in ribbed tube R51 with AVBP and CharLes$X$. A zoom on the boundary layer is shown in the bottom part of the figure.

the AVBP simulation, which is almost twice larger than in the CharLes^X simulation, and the two peaks at location $1e$ appearing with AVBP are not present for CharLes^X (as shown in the profile at the bottom of Fig. 3.9.6).

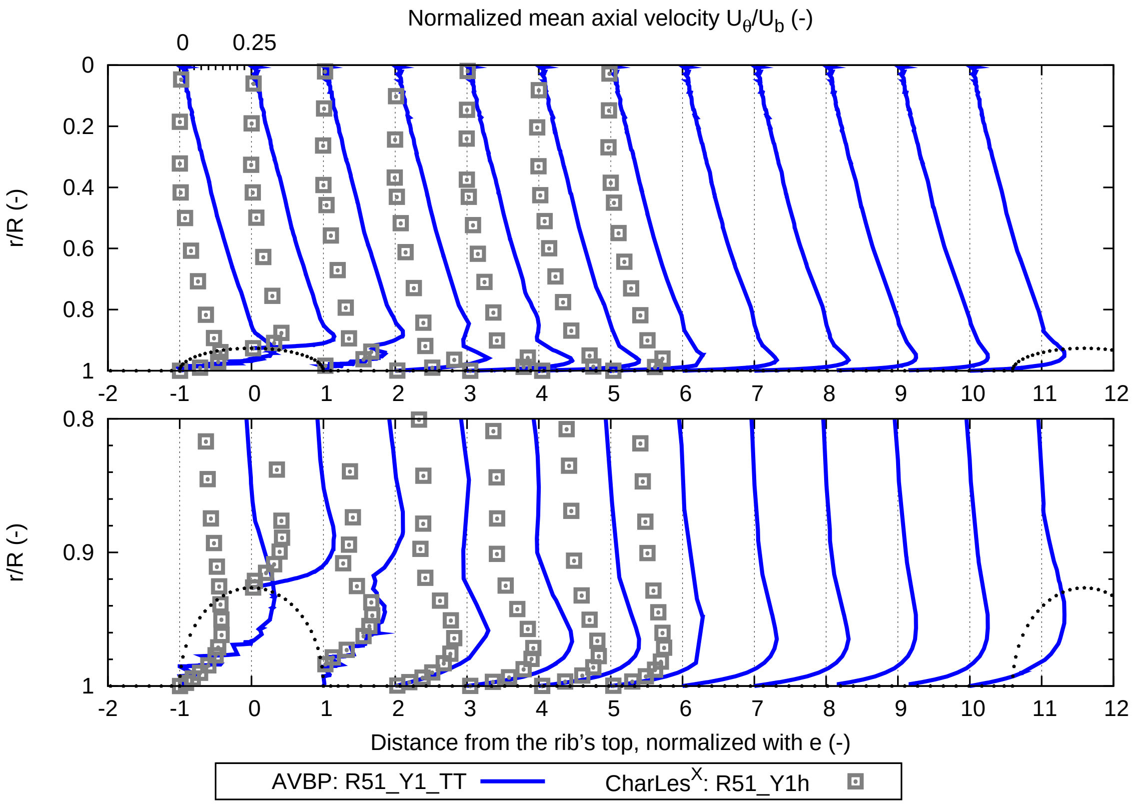

Figure 3.9.6: Time-averaged azimuthal velocity profiles normalized by U_b in ribbed tube R51 with AVBP and CharLes$X$. A zoom on the boundary layer is shown in the bottom part of the figure.

3.9.3 Axial fluctuating velocity

The impact of ribs on turbulence is illustrated by the RMS of axial fluctuating velocity $u'_{x,rms}$ normalized by U_b in Fig. 3.9.7. A clear trace of the rib is observed in both simulations: turbulence is generated in the wake of the rib top, then develops downstream and finally

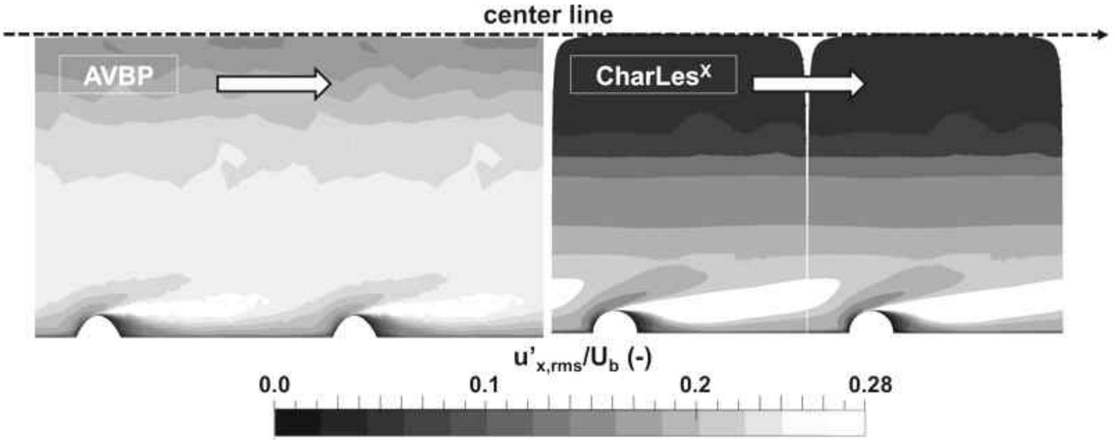

Figure 3.9.7: RMS of axial fluctuating velocity fields normalized by U_b in ribbed tube R51. Left: R51_Y1_TT using AVBP; Right: R51_Y1h using CharLes^X.

dissipates before the next rib in a very similar process. However stronger turbulence is observed in the AVBP solution, especially in the outer region. The difference may be due to more dissipative characteristics of code CharLes^X.

3.9.4 Pressure variation and shear stress

Fig. 3.9.8 gives the comparison between AVBP and CharLes^X in terms of pressure coefficient C_p. Both results show very similar distributions: the pressure increases in front of the rib and decreases behind the rib, which is correlated to the upstream and downstream recirculation zones, and a minimum value on the top of rib is observed. The pressure is undisturbed in the outer flow, and the disturbed region has similar thickness in both simulations.

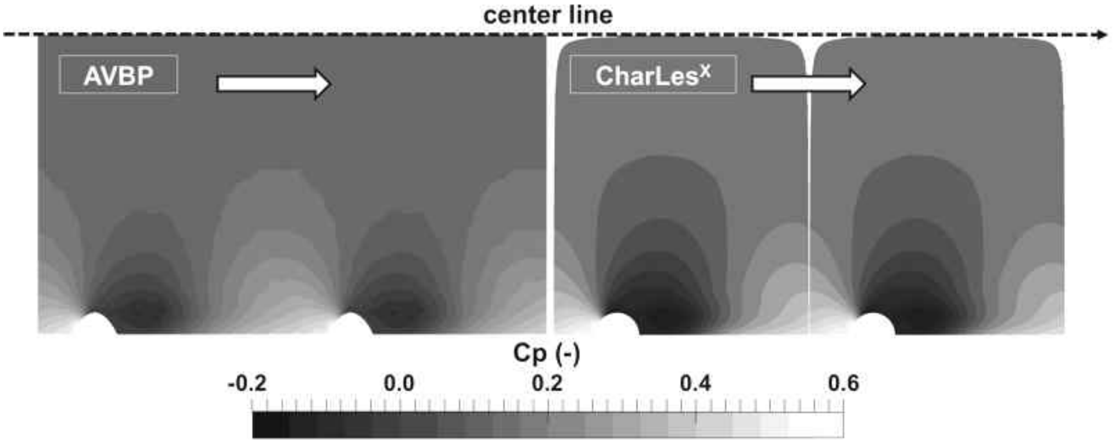

Figure 3.9.8: C_p fields in ribbed tube R51. Left: R51_Y1_TT using AVBP; Right: R51_Y1h using CharLes^X.

The global friction factor in ribbed tube R51 computed using CharLes^X is 0.034, very close to the value 0.0356 obtained with AVBP. Note that the Reynolds number of case R51_Y1h using CharLes^X is slightly higher than the case R51_Y1_TT with AVBP (see Table. 3.9.1). It is therefore reasonable to have a weaker friction factor, according to the Blasius correlation for turbulent pipe flow and the existing results on the flow in ribbed tubes, as shown in Fig. 3.8.6. As in previous section, the pressure coefficient C_p (Eq. 2.5.1) and the local skin-friction coefficient C_f (Eq. 2.3.1) are plotted along the inner surface of the tube R51, in Figs. 3.9.9 and 3.9.10. Comparison between AVBP and CharLes^X shows very similar results on both quantities. Small differences on C_p are observed in the zone $0e$ to $1e$, where the results of CharLes^X are smoother, and in the region from $2e$ to $7e$, where CharLes^X predicts a slightly higher C_p. The peak value of C_f obtained with CharLes^X is smaller than that obtained with AVBP, which may be due to the first node distance to the wall y^+ that is locally higher than 1 on the top of the rib in the mesh used with CharLes^X, as shown in Fig. 3.9.11.

Considering the axial momentum balance in Eqs. 3.8.2 and 3.8.3, Table 3.9.3 gives the different terms (normalized by $\rho U_b^2 L^2$) obtained with AVBP and CharLes^X. Results are also expressed in percentage of the imposed source term in the smooth tube as in Table 3.8.3.

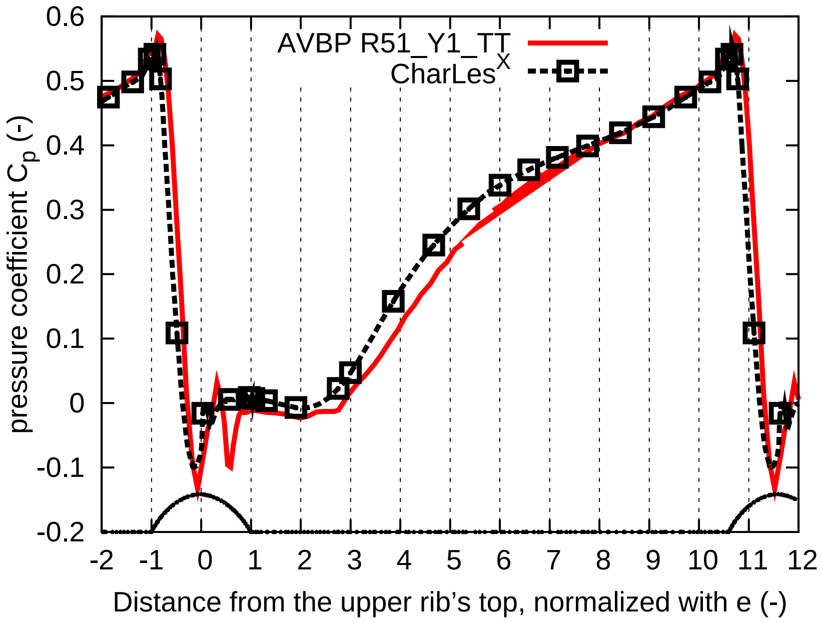

Figure 3.9.9: Evolution of the pressure coefficient C_p along the wall surface for AVBP and CharLes$X$ simulations.

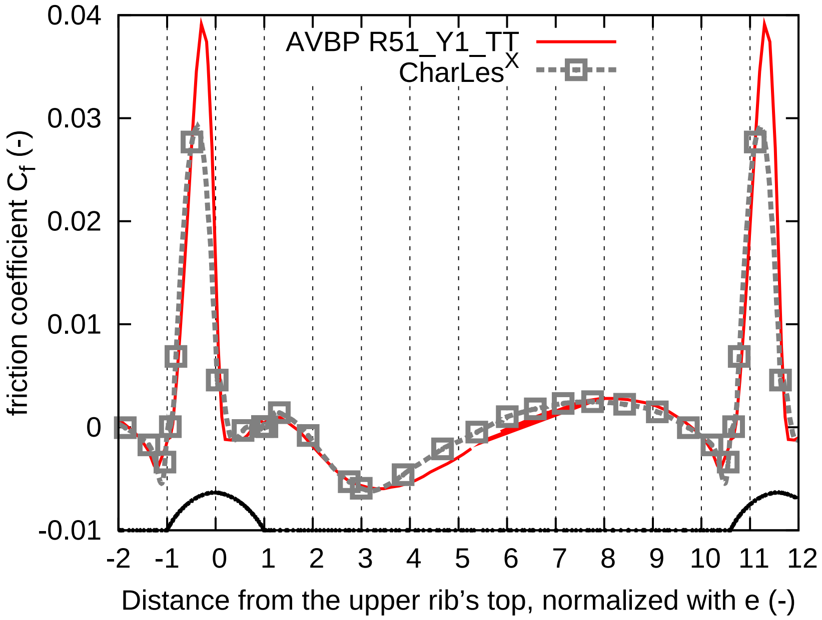

Figure 3.9.10: Evolution of the skin friction coefficient C_f along the wall surface for AVBP and CharLes$X$ simulations.

	Pressure drag	Friction drag	Total drag	Total imposed force
AVBP	1.28×10^{-1} (609.5%)	5.37×10^{-3} (25.5%)	1.33×10^{-1} (635%)	1.30×10^{-1} (619%)
CharLes^X	1.18×10^{-1} (561.9%)	4.73×10^{-3} (22.5%)	1.227×10^{-1} (584.4%)	1.24×10^{-1} (590.5%)

Table 3.9.3: Axial momentum balance in ribbed tube R51 computed using AVBP and CharLes^X.

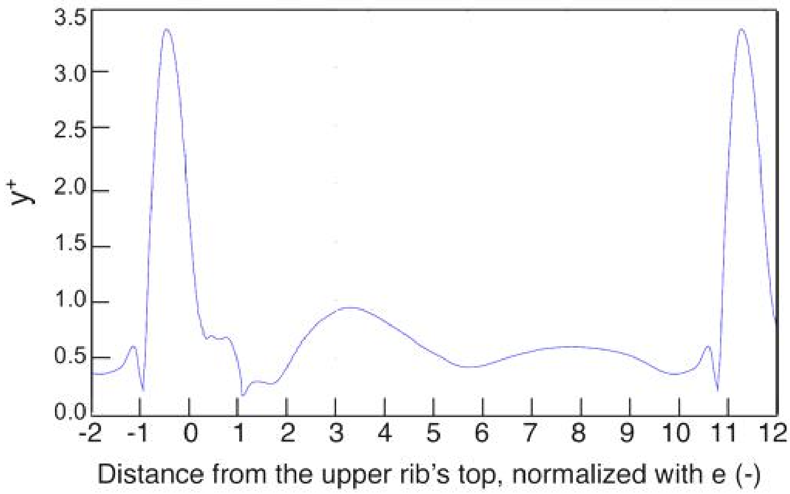

Figure 3.9.11: Dimensionless distance y^+ of the closest node to the wall of the mesh used in the CharLes^X simulation.

Similar results are found in terms of pressure drag, friction drag and total imposed force. Note that the smaller values in CharLes^X simulations are related to the higher Reynolds number. The difference is however small and the results are comparable.

3.9.5 Conclusions

The numerical simulations are validated by comparing two LES codes. Similar fields and profiles of mean axial velocity, RMS of axial velocity fluctuation, pressure variation and evolution of the pressure/friction coefficient are found. The main difference is observed for the mean azimuthal velocity which is almost twice higher with AVBP. Further investigation as the two-points correlation can be conducted to understand the differences.

3.10 Impact of the mesh

It is important to find the best trade-off between accuracy and computational cost for the industrial applications. Considering the results of the previous sections, meshes with $y^+ = 10$ are interesting to evaluated: indeed most pressure loss and turbulence enhancement are associated to phenomena of size $\sim e$, i.e., $y^+ \sim 50$. Two meshes with $y^+ = 10$ have therefore been used, Y10t with only tetrahedra (Fig. 3.2.2b) and Y10pt with prisms layers at the wall (Fig. 3.2.2c). The numerical scheme TTGC is used and convergence time of case R51_Y10t_TT and R51_Y10pt_TT are listed in Table. 3.10.1.

Case	τ_c	τ_a	Time step [s]	CPUs [s]	CPUh [h]
R51_Y10t_TT	1659	481	6.22×10^{-8}	0.045	19 923
R51_Y10pt_TT	559	605	4.95×10^{-8}	0.052	15 982

Table 3.10.1: Convergence and CPU times of cases R51_Y10t_TT and R51_Y10pt_TT.

A significant reduction of the CPU cost by 3/4 of the reference case R51_Y1_TT is found.

The effective operating point obtained in the different cases are given in Table. 3.10.2.

Case	S_{qdm} [Pa/m]	U_b [m/s]	Re [-]
R51_Y1_TT	1830	59.97	26 974.2
R51_Y10t_TT	1813	60.10	27 032.08
R51_Y10pt_TT	1900	58.89	26 486.52

Table 3.10.2: Effective operating points of the ribbed tube simulations on different meshes.

All three cases are conducted under the same conditions, the imposed source term S_{qdm} being adjusted manually to obtain the Reynolds number around 27 000. The final deviation of about 2% on Re is acceptable.

3.10.1 Velocity

Fig. 3.10.1 shows the time-averaged field of axial velocity normalized by U_b for the three meshes. The fields are very similar, especially between the reference case R51_Y1_TT and R51_Y10pt_TT, which are both using prism layers. First, similar boundary layers are indicated by the white iso-contour of $U_x = 99\% U_b$, while R51_Y10t_TT gives a thinner boundary layer between $1e$ to $2e$, due to a stronger impact of the flow acceleration on top of the rib. Second, the recirculation zones are still observed upstream and downstream of the rib, but they are shorten in coarse meshes Y10t and Y10pt, because the near wall region is not as well resolved as in the reference case R51_Y1_TT ($y^+ = 1$). It is also observed that the

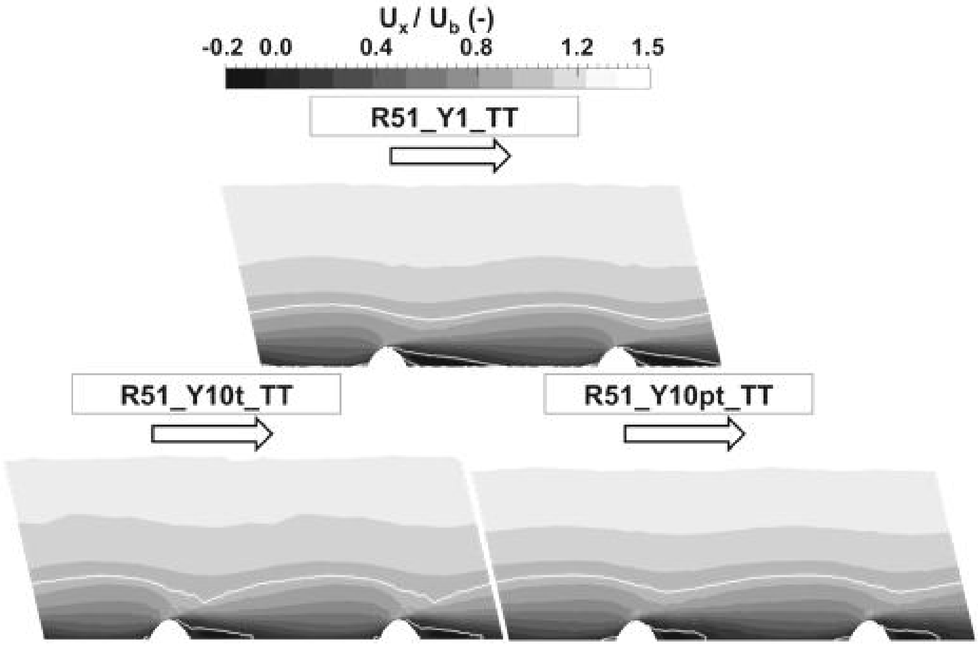

Figure 3.10.1: Time-averaged axial velocity fields normalized by U_b in ribbed tube R51. Upper: R51_Y1_TT; Bottom left: R51_Y10t_TT; Bottom right: R51_Y10tp_TT.

upstream recirculation zone is better predicted by R51_Y10pt_TT, while the downstream recirculation zone of R51_Y10t_TT looks more similar to R51_Y1_TT.

The time-averaged fields of azimuthal velocity U_θ normalized by U_b shows the rotational motion induced by the helical ribs. The same flow topology is observed for the three meshes in Fig. 3.10.2. The wakes appearing in the rib region are well captured by all meshes. The rotational motion is weaker in R51_Y10pt_TT, because the size of the prism elements of the mesh Y10pt at the wall in the azimuthal direction is larger, around $x_\theta^+ \sim 30$, compared to $x_\theta^+ \sim 10$ in meshes Y1 and Y10t, so that the smallest eddies in this direction may be not solved correctly. On the contrary, results of R51_Y10pt_TT are in good agreement qualitatively and quantitatively with the reference case R51_Y1_TT, with only little difference on the wakes generated by the ribs.

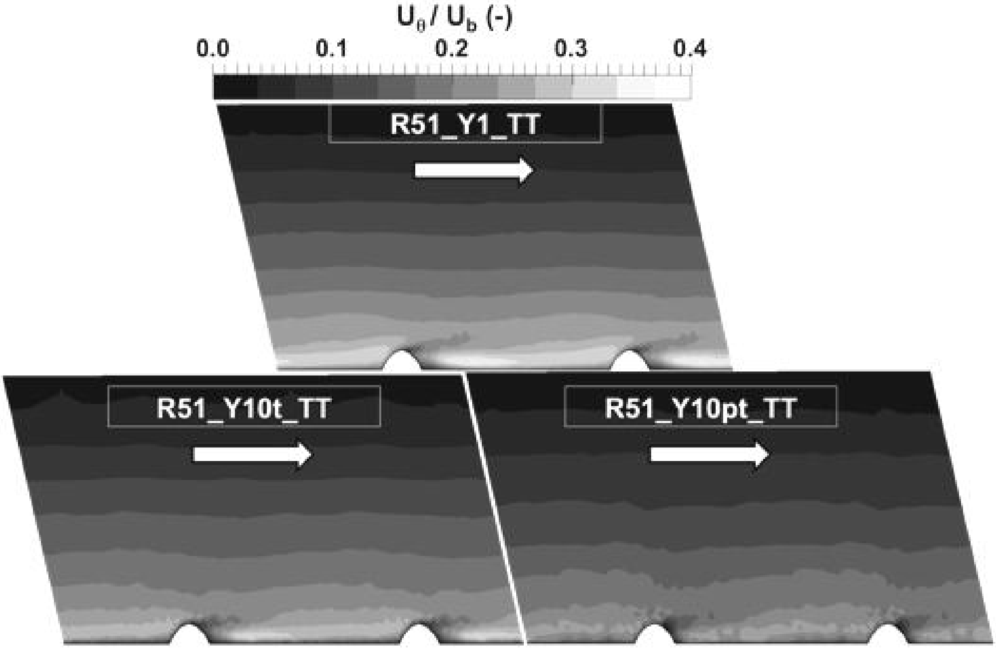

Figure 3.10.2: Time-averaged azimuthal velocity fields normalized by U_b in ribbed tube R51. Upper: R51_Y1_TT; Bottom left: R51_Y10t_TT; Bottom right: R51_Y10pt_TT.

Time-averaged profiles of axial and azimuthal velocity normalized by U_b are now given for quantitative comparison in Figs. 3.10.3 and 3.10.4,

in the same way as Fig. 3.9.5. All profiles are very similar among the three meshes. In Fig. 3.10.3, the recirculation zone behind the rib disappears at a distance of around $4e$ on all the three meshes, with a slightly shorten zone in the coarse meshes. However, in Fig. 3.10.4, it is clear that R51_Y10t_TT reproduces better the profiles of U_θ/U_b obtained with the reference case R51_Y1_TT, in particular, the two peaks observed at location $1e$ are well reproduced, while the case R51_Y10tp_TT always underpredict the azimuthal velocity.

3.10.2 Impact of ribs on turbulence

The RMS of axial fluctuating velocity u'_{rms} normalized by U_b in Fig. 3.10.5 illustrates the impact of ribs on turbulence for the three meshes. The similarity among the fields on the

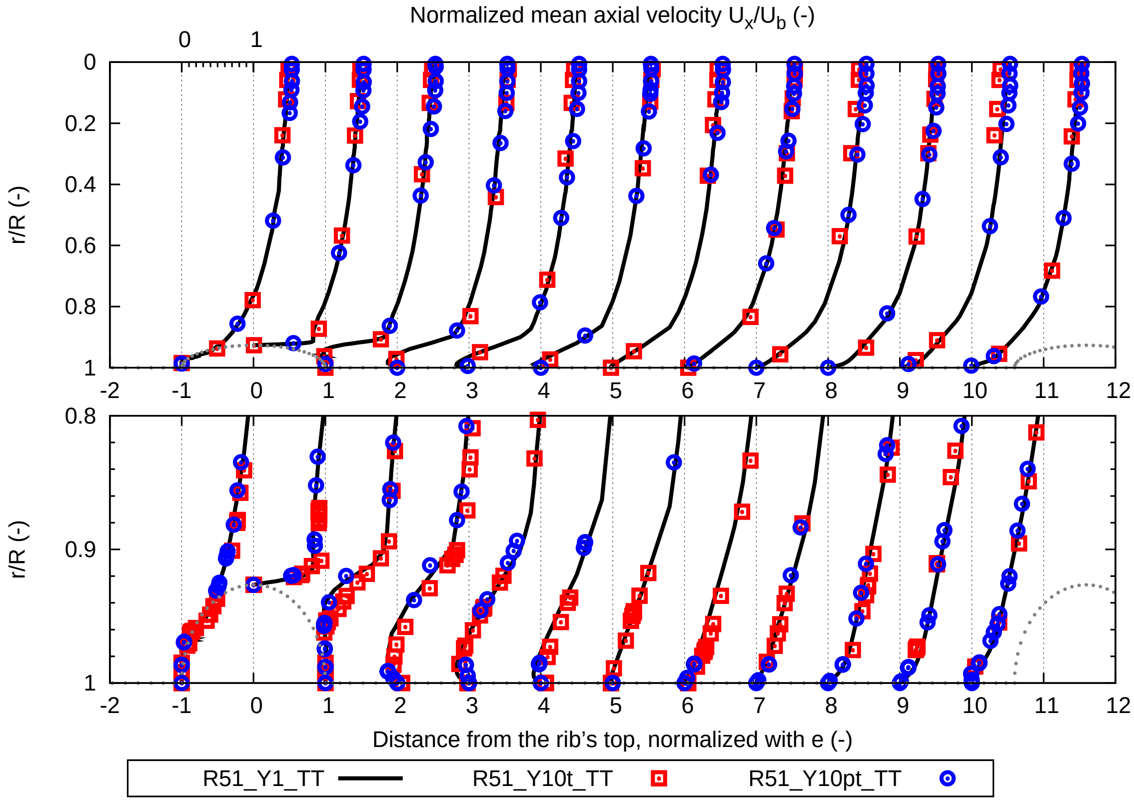

Figure 3.10.3: Time-averaged axial velocity profiles normalized by U_b in ribbed tube R51 on the three meshes Y1, Y10t and Y10pt. A zoom on the boundary layer is shown in the bottom part of the figure.

three meshes is again observed. Results of case R51_Y10t_TT show stronger turbulence in the outer layer region than that of Y1, with a difference however less than 10%. On the other hand, stronger turbulence is found on the top of ribs in case R51_Y10tp_TT.

3.10.3 Pressure variation and shear stress

The time-averaged fields of the pressure coefficient C_p (defined in Eq. 2.5.1) in Fig. 3.10.6 show qualitatively similar pressure variations on the meshes Y1, Y10t and Y10pt. In particular, good agreement in the viscous layers among the three solutions is observed. However, some wiggles are found near the ribs in the case R51_Y10tp_TT, especially on the region of transition from prism elements to tetrahedra.

The evolutions of C_p (Eq. 2.5.1) and C_f (Eq. 2.3.1) on the inner surface of the tube are plotted in Fig. 3.10.7 and 3.10.8 for the three meshes. Similar evolution of the pressure coefficient C_p is obtained, while discrepancies appear only around the rib top where R51_Y10t_TT has a stronger peak. However, since it is only the integral of the pressure variation on the wall (i.e., the total pressure drag) that contributes to the pressure loss, deviations at a few locations will not affect the global performance, as will be seen later with the momentum balance.

The friction coefficients are more different, which is expected, as the wall shear stress is well resolved only when $y^+ \leq 1$. Lower peak values on the top of ribs and less negative

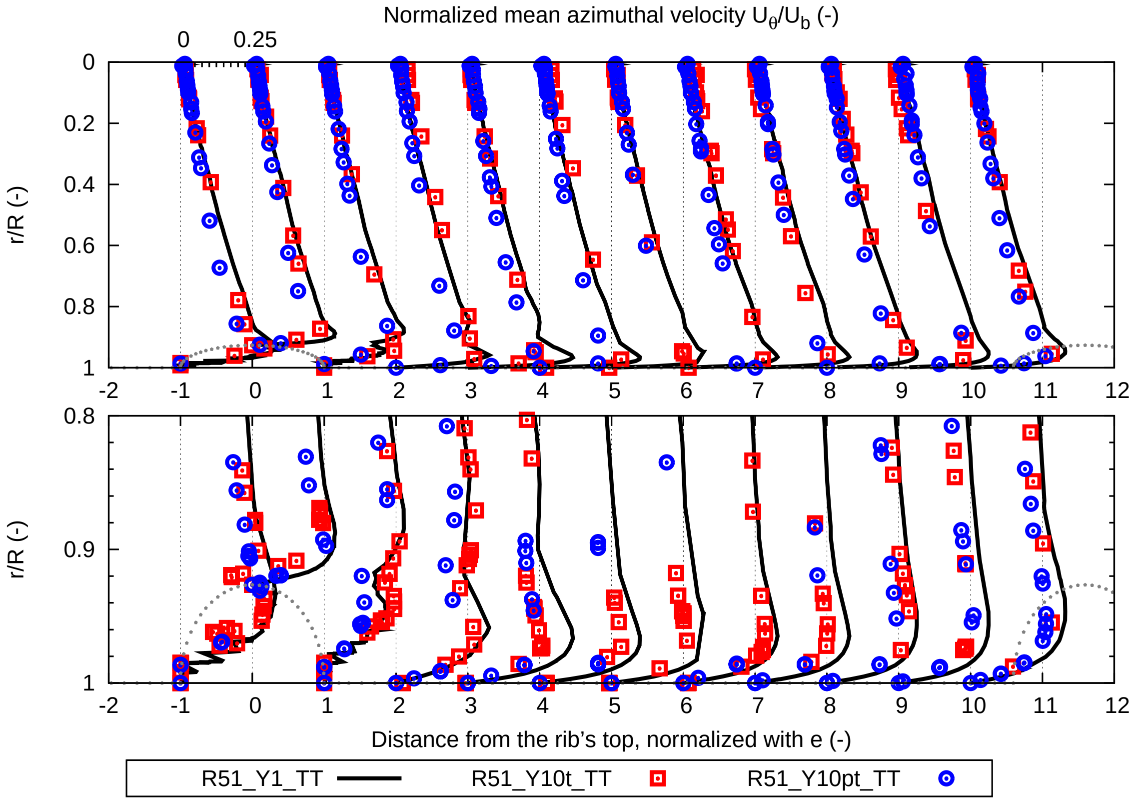

Figure 3.10.4: Time-averaged azimuthal velocity profiles normalized by U_b in ribbed tube R51 on the three meshes Y1, Y10t and Y10pt. A zoom on the boundary layer is shown in the bottom part of the figure.

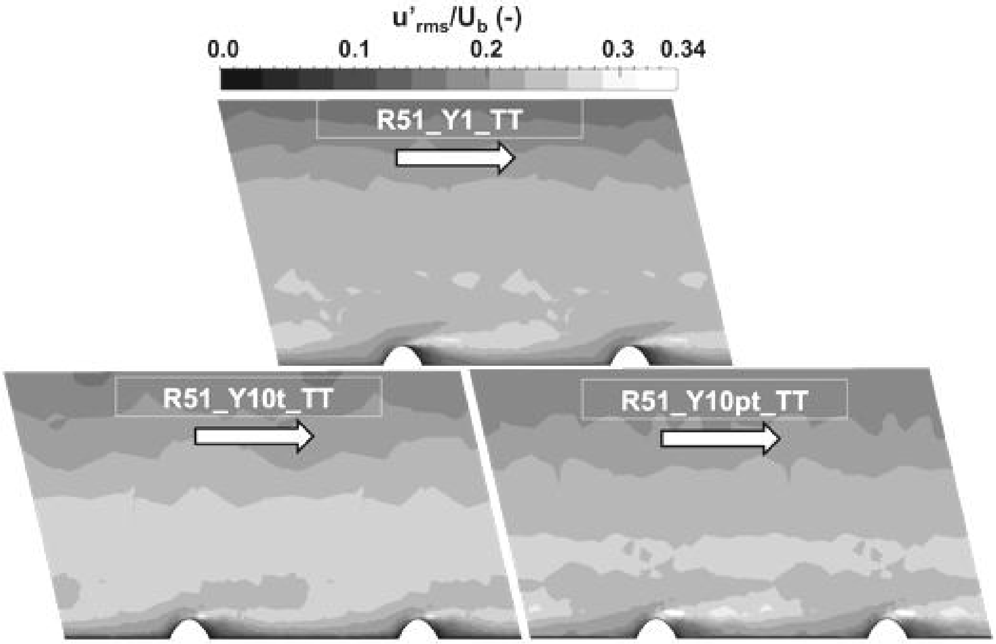

Figure 3.10.5: RMS of axial fluctuating velocity fields normalized by U_b in ribbed tube R51. Upper: R51_Y1_TT; Bottom left: R51_Y10t_TT; Bottom right: R51_Y10tp_TT.

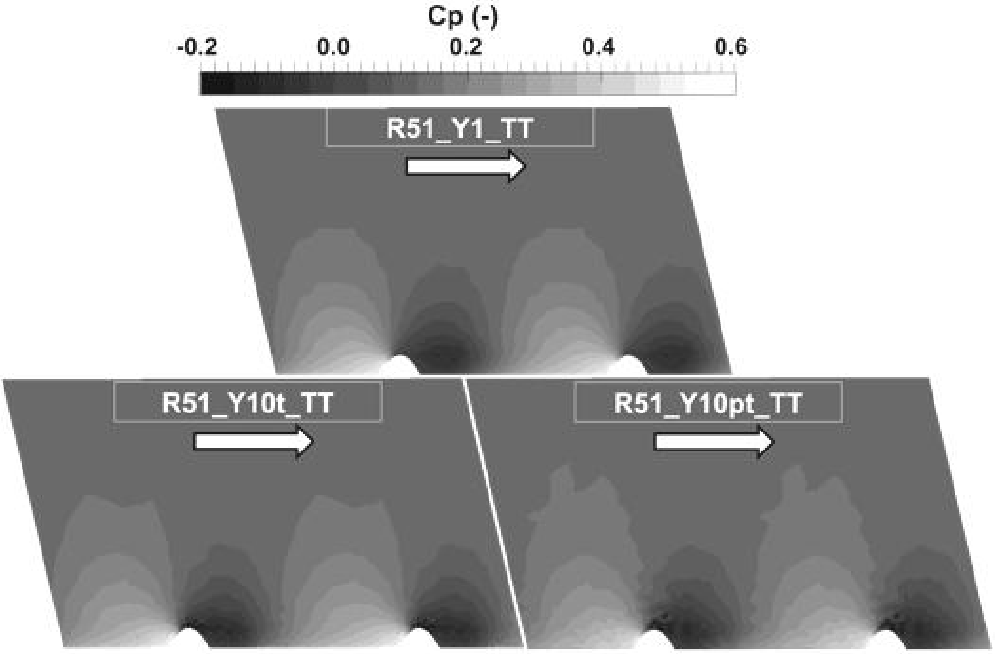

Figure 3.10.6: Time-averaged pressure coefficient fields in ribbed tube R51. Upper: R51_Y1_TT; Bottom left: R51_Y10t_TT; Bottom right: R51_Y10tp_TT.

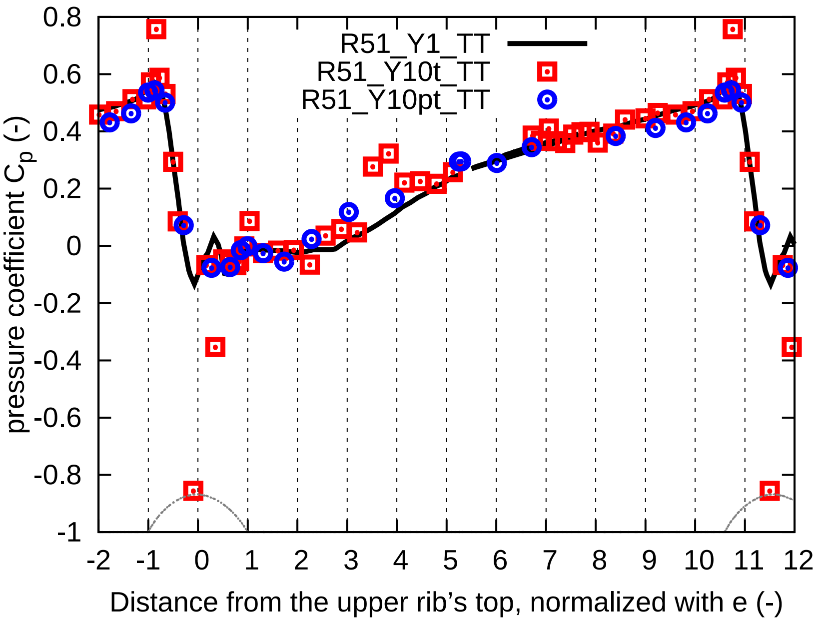

Figure 3.10.7: Evolution of the pressure coefficient C_p along the wall surface on the three meshes Y1, Y10t and Y10pt.

values from $2e$ to $8e$ are observed for coarse mesh cases R51_Y10t_TT and R51_Y10pt_TT, and the latter is in agreement with the shorter length of the recirculation zone. However it was demonstrated that, in ribbed tubes, the wall friction is not the dominant contribution to the total pressure loss, so that inaccuracy on this term has little impact on the final estimation of the pressure loss in ribbed tubes.

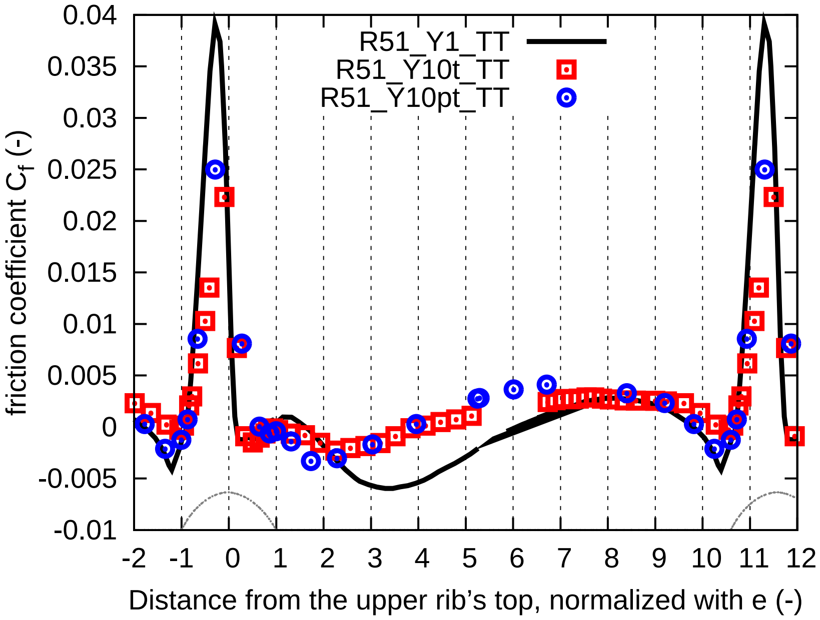

Figure 3.10.8: Evolution of the skin friction coefficient C_f along the wall surface on the three meshes Y1, Y10t and Y10pt.

Considering finally the balance of axial momentum (Eqs. 3.8.2 and 3.8.3), Table 3.10.3 gives the different drag terms and the imposed force (all normalized by $\rho U_b^2 L^2$) for the three meshes.

Mesh	Pressure drag	Friction drag	Total drag	Total imposed force
Y1	1.28×10^{-1} (609.5%)	5.37×10^{-3} (25.5%)	1.33×10^{-1} (635%)	1.30×10^{-1} (619%)
Y10t	1.41×10^{-1} (671.4%)	7.32×10^{-3} (34.9%)	1.48×10^{-1} (706.3%)	1.29×10^{-1} (614.3%)
Y10pt	1.91×10^{-1} (909.5%)	1.03×10^{-2} (49.0%)	2.02×10^{-1} (958.5%)	1.37×10^{-1} (652.4%)

Table 3.10.3: Axial momentum balance in ribbed tube R51 on the three meshes Y1, Y10t and Y10pt, with numerical scheme TTGC.

Results are also expressed in percentage of the imposed source term in the smooth tube S51_Y1_TT as in Table 3.8.3, for a direct comparison between the ribbed and smooth tubes. More discrepancy between the total drag and the total imposed force is observed in both cases R51_Y10t_TT and R51_Y10pt_TT. The difference on the pressure drag between R51_Y10t_TT and the reference case R51_Y1_TT is only 10%, and on the total imposed force is only 0.8%. However, larger difference appears in the results of R51_Y10pt_TT, with 50% error on the pressure drag (this may due to the wiggles behavior on the pressure observed in Fig. 3.10.6) and 5.4% error on the total imposed force.

3.10.4 Conclusions

The impact of mesh resolution on results of the ribbed tube R51 simulations is discussed by comparing three meshes Y1, Y10t and Y10pt. Results show that the mesh Y10t reproduces well the reference case R51_Y1_TT and gives better results than mesh Y10pt in terms of the rotational motion and the momentum balance. As a consequence, the mesh Y10t can be used for the study of ribbed tubes with a good accuracy and lower computational cost.

3.11 Impact of the numerical scheme

In this section, the results of the turbulent flow in the ribbed tube R51 solved with two numerical schemes TTGC (TT) and LW are compared, with the two meshes Y1 and Y10t. The convergence times of the two cases introduced here, R51_Y1_LW and R51_Y10t_LW, are listed in Table. 3.11.1.

Case	τ_c	τ_a	Time step [s]	CPUs [s]	CPUh [h]
R51_Y1t_LW	97	773	2.27×10^{-8}	0.0696	34 317
R51_Y10t_LW	305	1246	6.21×10^{-8}	0.022	7081

Table 3.11.1: Convergence and CPU times of cases R51_Y1_LW and R51_Y10t_LW.

Only about half of the CPUh is cost compared to correspondent case with TTGC as expected.

The effective operating points of these two cases using LW scheme are given in Table. 3.11.2.

Case	S_{qdm} [Pa/m]	U_b [m/s]	Re [-]
R51_Y1_LW	2025	60.04	27 003.43
R51_Y10t_LW	1900	60.20	27 077.4

Table 3.11.2: Effective operating points of the turbulent flow in ribbed tube R51 with LW scheme on meshes Y1 and Y10t.

As usual, the source term S_{qdm} is adjusted to maintain a Reynolds number around 27 000. First insight in this table shows that S_{qdm} of case R51_Y10t_LW is closer to previous ones using the scheme TTGC (R51_Y1/Y10t/Y10pt_TT).

3.11.1 Velocity

Figs. 3.11.1 and 3.11.2 show the time-averaged field of the axial velocity U_x and the azimuthal velocity U_θ, normalized by U_b. As in previous discussions, the white curves indicate the zero-velocity contours and the $99\% U_b$ contours to show the recirculation zones and the boundary layer. The comparison among R51_Y1_TT, R51_Y10t_TT, R51_Y1_LW and R51_Y10t_LW shows very similar results, except the upstream recirculation zone no longer visible in the R51_Y10t_LW case. Comparing the two schemes TTGC and LW, on the mesh Y1, i.e., R51_Y1_TT and R51_Y1_LW, thicker boundary layer is observed with LW, and perturbations occur in the near wall region, while the recirculation zones appear similar. On the other hand, for R51_Y10t_TT and R51_Y10t_LW on the coarse mesh, the same boundary layer thickness is obtained, and slightly modified boundary layer on the top of ribs is observed with LW, showing stronger effect of the flow acceleration there.

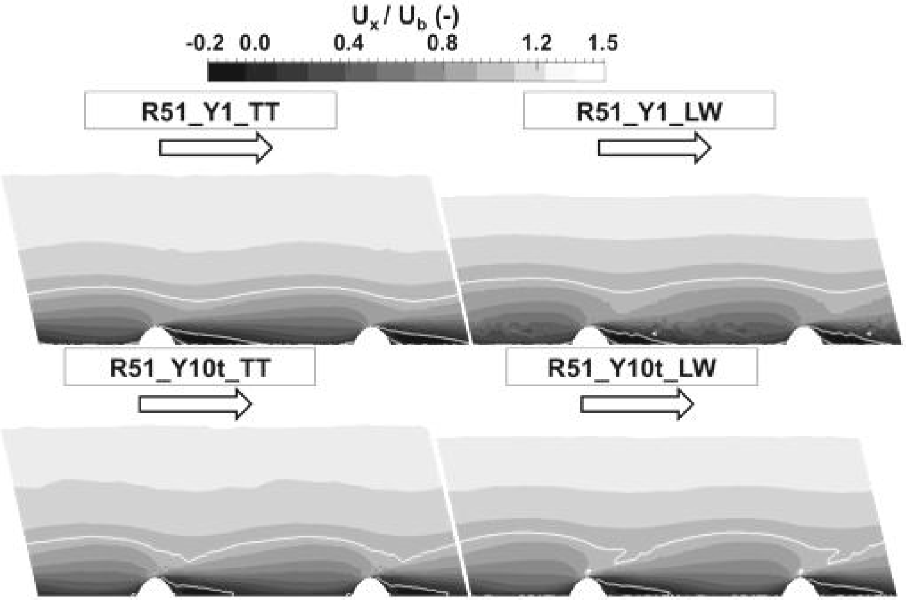

Figure 3.11.1: Mean axial velocity fields normalized by U_b in ribbed tube R51. Top left: R51_Y1_TT; Top right: R51_Y10t_TT; Bottom left: R51_Y1_LW; Bottom right: R51_Y10t_LW.

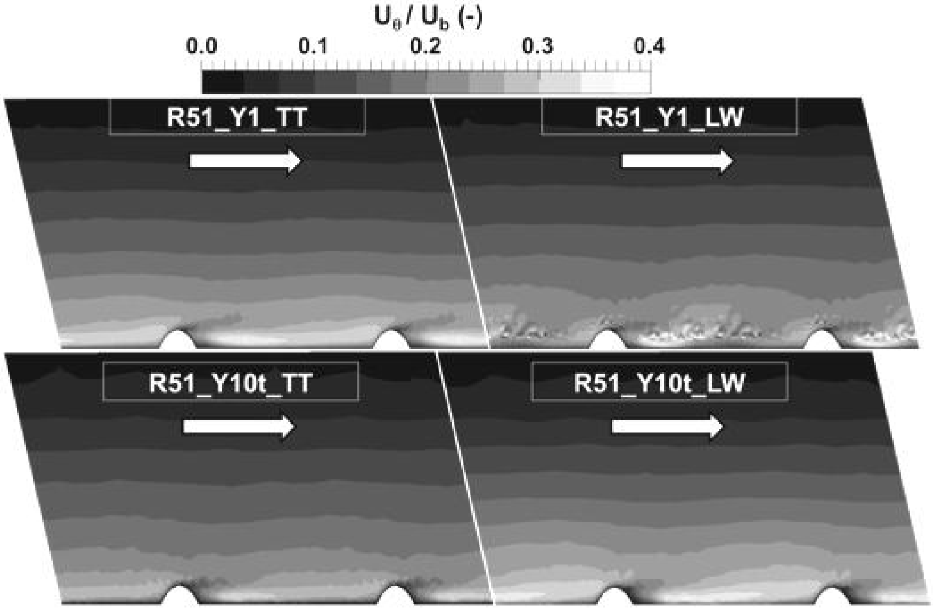

Figure 3.11.2: Mean azimuthal velocity fields normalized by U_b in ribbed tube R51. Top left: R51_Y1_TT; Top right: R51_Y10t_TT; Bottom left: R51_Y1_LW; Bottom right: R51_Y10t_LW.

In Fig. 3.11.2, the same flow topology is observed on the time-averaged fields of azimuthal velocity, showing the rotational motion. Note that perturbations appear in the near wall region of the case R51_Y1_LW, i.e., the numerical scheme LW performs better on the mesh Y10t than on the hybrid mesh Y1. In addition, the field of R51_Y10t_LW looks more similar to the reference case R51_Y1_TT, even more than R51_Y10t_TT.

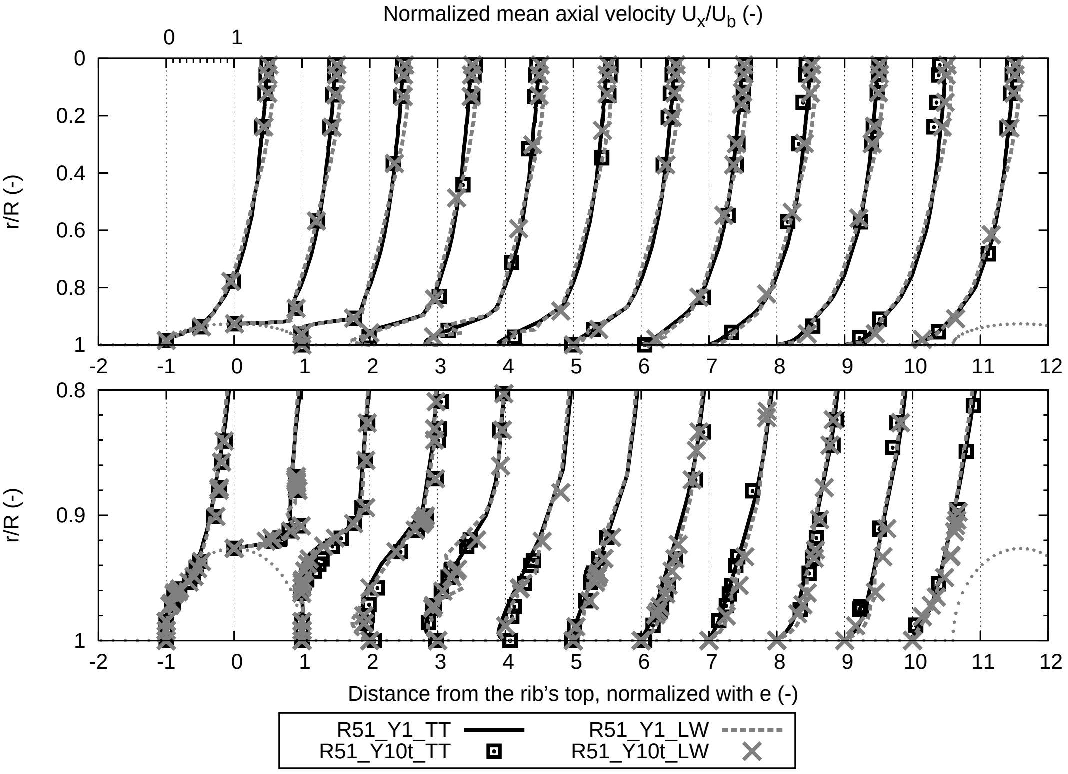

Figure 3.11.3: Mean axial velocity profiles normalized by U_b in ribbed tube R51, using two meshes and two numerical schemes. A zoom on the boundary layer is shown in the bottom part of the figure.

The time-averaged profiles and the zoom in the near wall region of the axial (Fig. 3.11.3) and azimuthal velocity (Fig. 3.11.4) are plotted for quantitative comparison, in the same way as Figs. 3.9.5 and 3.9.6. Compared to the reference case R51_Y1_TT, the case R51_Y1_LW shows higher axial velocity U_x/Ub near the centerline $0.4 < r/R < 0$, while R51_Y10t_LW agrees better with the reference results, also in the near wall region. Similar to the results on U_x/Ub, U_θ/U_b is also better predicted by R51_Y10t_LW than R51_Y1_LW, and the zoom on the near wall region shows that LW obtains better profiles, even better than TTGC on the coarse tetrahedra mesh Y10t.

3.11.2 Impact of ribs on turbulence

In Fig. 3.11.5, both the numerical schemes TTGC and LW on mesh Y10t capture the similar phenomena to the reference case R51_Y1_TT in terms of RMS of axial fluctuating velocity u'_{rms} (normalized by U_b), and again perturbations are observed in case R51_Y1_LW.

3.11.3 Pressure variation and shear stress

Fig. 3.11.6 shows the time-averaged fields of the pressure coefficient C_p (Eq. 2.5.1). The case R51_Y10t_LW is in better agreement with the reference case R51_Y1_TT, while R51_Y1_LW generates perturbations in the near wall region.

The evolution of the pressure coefficient C_p and the skin-friction coefficient C_f (Eq. 2.3.1)

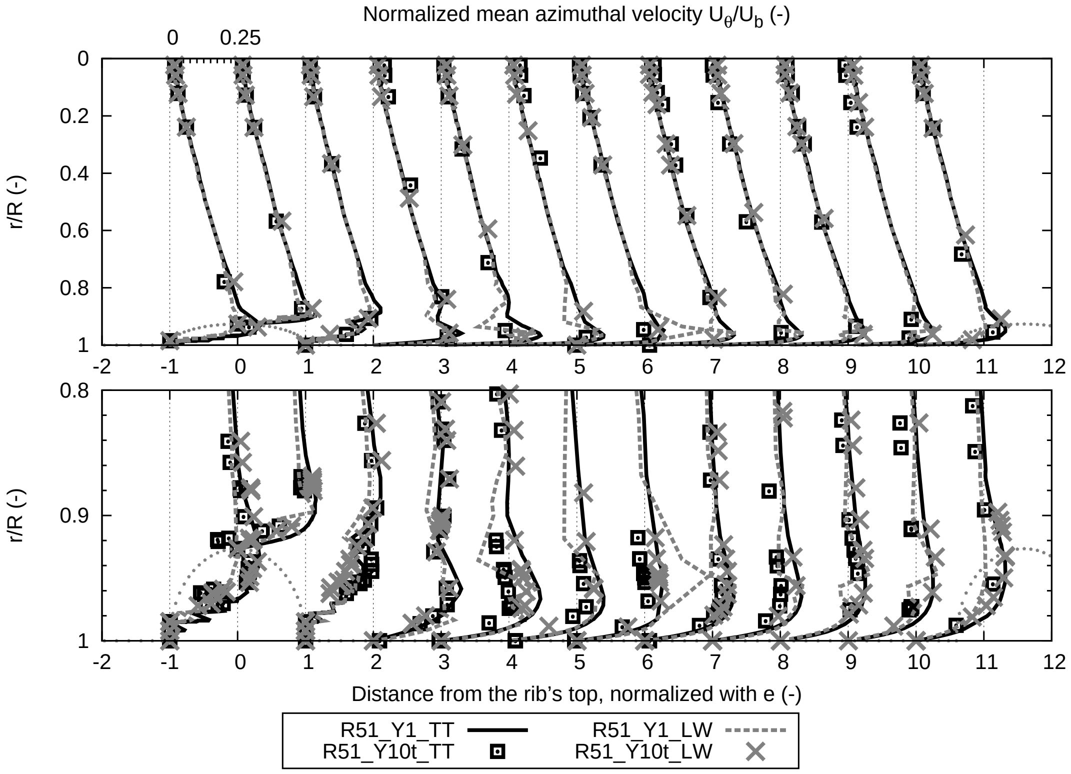

Figure 3.11.4: Mean azimuthal velocity profiles normalized by U_b in ribbed tube R51, using two meshes and two numerical schemes. A zoom on the boundary layer is shown in the bottom part of the figure.

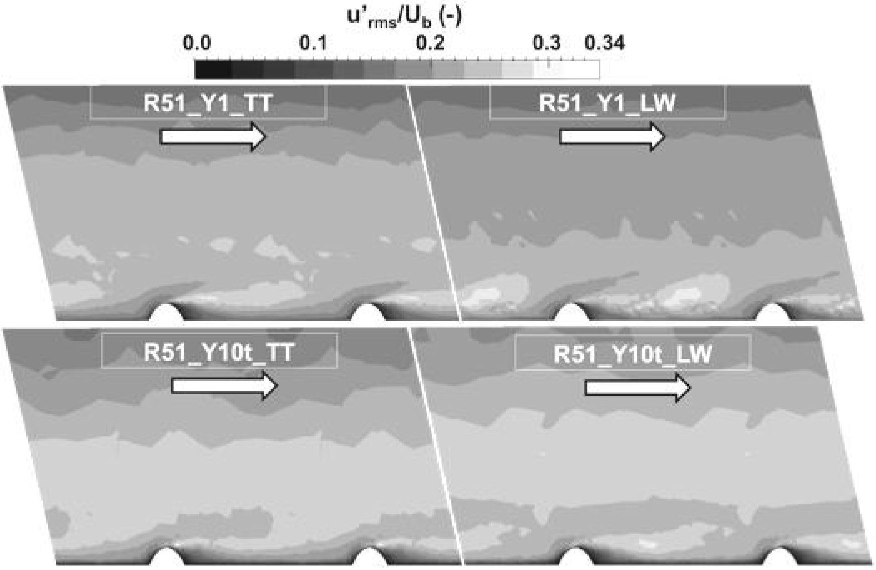

Figure 3.11.5: RMS of axial fluctuating velocity fields normalized by U_b in ribbed tube R51, using two meshes and two numerical schemes.

on the inner surface are plotted in Fig. 3.10.7 and 3.11.8. R51_Y10t_LW shows a stronger amplitude of C_p on the rib top, which however does not affect much the total drag as the normal has a 0 component in the axial direction at this location, as explained in section 3.10.3.

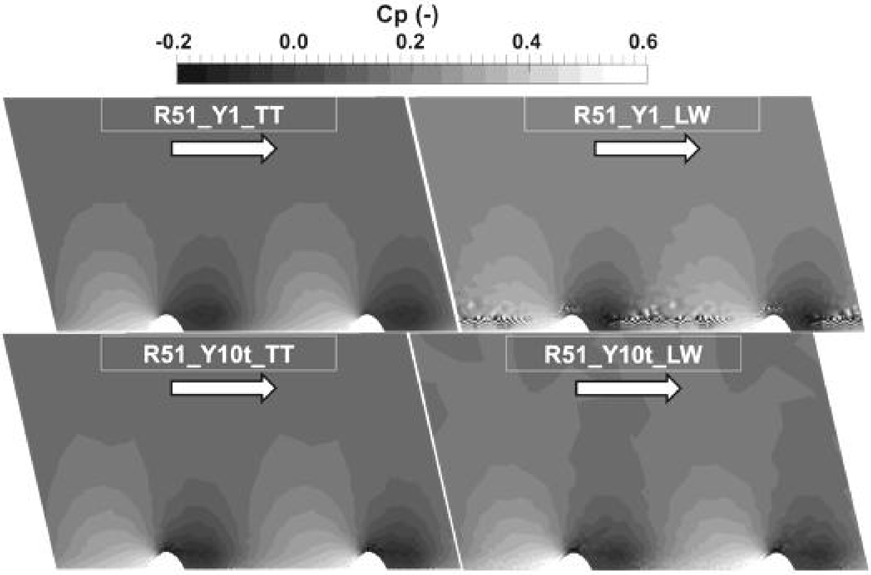

Figure 3.11.6: Time-averaged pressure variation fields in ribbed tube R51. Top left: R51_Y1_TT; Top right: R51_Y10t_TT; Bottom left: R51_Y1_LW; Bottom right: R51_Y10t_LW.

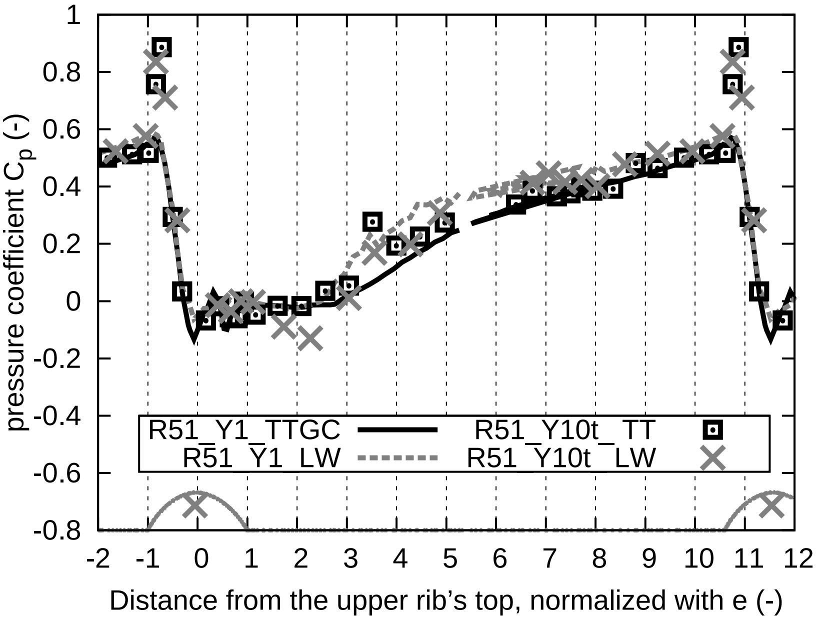

Figure 3.11.7: Evolution of the pressure coefficient C_p along the wall surface of ribbed tube R51, using two meshes and two numerical schemes.

The friction coefficient C_f (Fig. 3.11.8) depends significantly on y^+ at the wall, as already seen in section 3.10.3. However, C_f is less controlled by y^+ in the downstream recirculation zone (from $1e$ to $5e$), where R51_Y1_LW shows also differences with R51_Y1_TT, maybe due to the perturbations on hybrid mesh Y1.

Finally the balance of axial momentum (Eqs. 3.8.2 and 3.8.3) is given in Table 3.11.3 in the same manner as Table 3.8.3.

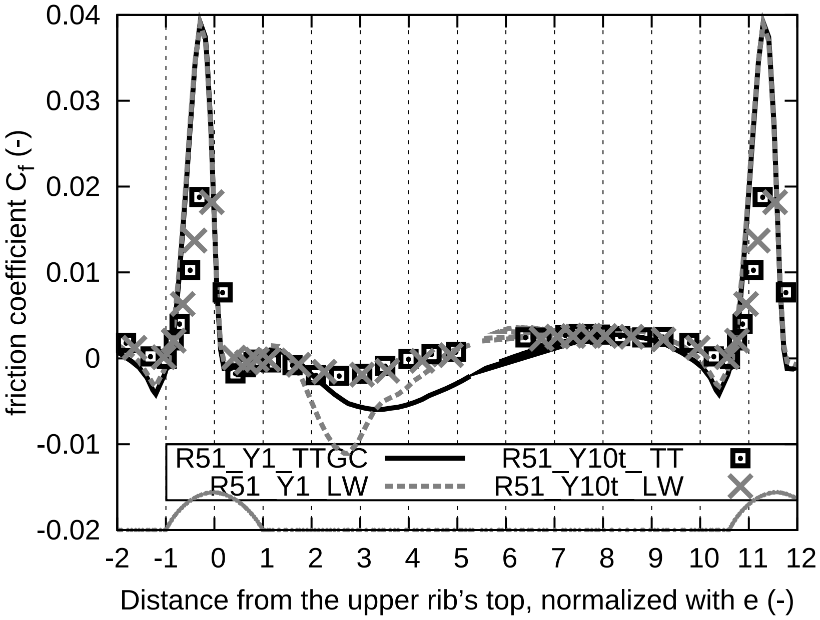

Figure 3.11.8: Evolution of the skin friction coefficient C_f along the wall surface of ribbed tube R51, using two meshes and two numerical schemes.

R51	Pressure drag	Friction drag	Total drag	Total imposed force
Y1_TT	1.28×10^{-1} (609.5%)	5.37×10^{-3} (25.5%)	1.33×10^{-1} (635%)	1.30×10^{-1} (619%)
Y1_LW	1.37×10^{-1} (652.4%)	8.6×10^{-3} (41.0%)	1.46×10^{-1} (693.4%)	1.44×10^{-1} (685.7%)
Y10t_TT	1.41×10^{-1} (671.4%)	7.32×10^{-3} (34.9%)	1.48×10^{-1} (706.3%)	1.29×10^{-1} (614.3%)
Y10t_LW	1.46×10^{-1} (695.2%)	6.32×10^{-3} (30.1%)	1.52×10^{-1} (725.3%)	1.34×10^{-1} (638.1%)

Table 3.11.3: Axial momentum balance in ribbed tube R51, using two meshes and two numerical schemes.

All cases demonstrate again that the pressure drag is the dominant contribution to the total drag (so to the pressure loss), compensated with the imposed source term. The total imposed source term in case R51_Y10t_LW shows 3% discrepancy and the pressure drag is over-estimated by 14% compared to the reference case R51_Y1_TT. Note that, while R51_Y1_LW has less error on the pressure drag, it is less accurate on friction probably due to the combination of the numerical scheme LW with the hybrid mesh.

3.11.4 Conclusions

In comparison to the reference case R51_Y1_TT, though better results on mean velocity profiles are observed in R51_Y10t_LW rather than R51_Y10t_TT, the pressure drag is over-estimated and leads to more total imposed force, but the error stays acceptable. On the refined mesh, perturbations are observed in the near wall region with LW, leading to worse results. As a consequence, it is concluded that the scheme LW should be used only on full tetrahedra meshes even with larger $y^+ \sim 10$ at the wall, rather than on hybrid meshes with a refined mesh at the wall $y^+ \sim 1$.

3.12 Conclusions

In this chapter, the non-reacting isothermal turbulent flow in both smooth (S51) and ribbed (R51) tubes has been investigated with the LES code AVBP. The impact of the mesh and the numerical scheme has been evaluated. The reference case of smooth tube S51_Y1_TT has been validated against theoretical/empirical results, while the results of S51_Y1_LW shows that the numerical scheme LW works not as well as TTGC. The methodology of using periodic configuration with a computational domain $L = p < D$ (where p corresponds to the ribs pitch of ribbed tube R51, thus the length of one pattern), combined with a source term S_{qdm} in the flow equations solved on a hybrid mesh having $y^+ = 1$ at the wall with the numerical scheme TTGC, is found to give accurate results and is used to compute reference solution.

For this reason, the Y1 mesh with TTGC scheme applied to ribbed tube R51 is also taken as a reference case. Comparison of the results with different meshes and numerical schemes on R51 show that mesh Y10t with scheme TTGC or LW can both well capture the dynamics of the turbulent flow, allowing to reduce significantly the computational cost. Results show that, contrary to the smooth tube where the pressure loss is mainly due to the friction drag, in ribbed tubes the pressure drag is dominant, and can be well predicted on a coarse mesh with $y^+ = 10$ at the wall. As it is an effect of the pressure, the classical wall law does not work and the WRLES will be used.

To validate further the simulations, the LES code CharLes^X has been also applied to the R51 geometry. The same flow topology in terms of mean axial velocity, axial velocity fluctuation, pressure variation, etc, are observed, and similar results are obtained for the momentum balance. Discrepancy is however observed for the rotational motion, which requires further investigation and analysis.

Chapter 4

LES of non-reacting heated flow in ribbed and smooth tubes

Contents

As the tubes in the cracking furnace are heated from the outside through the wall, the heat transfer efficiency is a key factor for the chemical process and the occurrence of coking phenomena. In this chapter, the non-reacting heated flow in both smooth and ribbed tubes is discussed. Similarly to the isothermal flow studied in the previous chapter, academic configurations of periodic tubes are used. After discussing the numerical set-up, impact of mesh resolution, and numerical scheme, results are analyzed and compared to show the effect of ribs on heat transfer.

4.1 Numerical methodology

The fluid used in the heated case is the same as presented in Section 3.3.2, in terms of composition (gaseous air), bulk temperature (973 K), pressure (1 atm) and bulk density (0.036 kg/m^3).

The geometries S51 and R51 for both smooth and ribbed tubes and meshes (S51_Y1, S51_Y10t, R51_Y1 and R51_Y10t, presented in Section 3.2) are exactly the same as in Chapter 3. The simulations are performed with AVBP. The methodology to heat the tube is described below.

4.1.1 Steady heated flow in a periodic tube

To establish a stationary regime of the flow heated from the wall in the periodic tube, where the temperature at the wall T_w is higher than the bulk temperature T_b, an additional source term S_e (of negative value) expressed in [W/m^3] is added to the energy equation to maintain the bulk temperature at a steady mean value. This source term S_e is used to evacuate the heat coming from the hot wall at a higher temperature: without this source term, the temperature in the tube would keep increasing until reaching the wall temperature.

This source term comes in addition to S_{qdm} presented earlier in the previous chapter, so that the flow equations which are now solved are:

$$\frac{\partial \rho}{\partial t} + \frac{\partial (\rho u_i)}{\partial x_i} = 0, \tag{4.1.1}$$

$$\frac{\partial (\rho u_i)}{\partial t} + \frac{\partial (\rho u_i u_j)}{\partial x_j} = -\frac{\partial p}{\partial x_i} + \frac{\partial \tau_{ij}}{\partial x_j} + S_{qdm,i}, \tag{4.1.2}$$

$$\rho \frac{DE}{Dt} = -\frac{\partial q_i}{\partial x_i} + \frac{\partial}{\partial x_j}(\tau_{ij} u_i) - \frac{\partial}{\partial x_i}(p u_i) + \dot{w}_T - S_e + u_i S_{qdm,i} \tag{4.1.3}$$

Unlike the source term S_{qdm} which keeps a fixed value during the simulation, S_e is adjusted during the simulation, following the variation of bulk properties. At each time step, a new value is computed as in Eq. 4.1.4 so that the bulk temperature T_b tends to the target value T_b^{target}:

$$S_e = S_e^{constant} + \rho_b^{target} C_{v,b}^{target} \frac{T_b^{target} - \dfrac{\int_V \rho u T \mathrm{d}V}{\int_V \rho u \mathrm{d}V}}{\tau_{S_e}} \tag{4.1.4}$$

where $\int_V \rho u T \mathrm{d}V / \int_V \rho u \mathrm{d}V$ is the instantaneous bulk temperature in the computational domain, and τ_{S_e} is a relaxation time, typically set as $(V/S)/(3\sqrt{\tau_w/\rho_b})$. The quantities ρ_b^{target} and $C_{v,b}^{target}$ are the target bulk density, and bulk heat capacity at constant volume, and $S_e^{constant}$ is an initial estimation of S_e. When a balance between the source term S_e and the wall heat flux is established, S_e reaches a constant value:

$$S_e = -\frac{q_w S}{V}, \tag{4.1.5}$$

expressing that heat $q_w S$ transferred from the wall to the fluid is subtracted from the volume of fluid as $S_e V$, and leading to a final bulk flow temperature T_b close to the T_b^{target}.

4.1.2 Numerical set-up

To evaluate the impact of the numerical scheme, both LW (second order) and TTGC (third order) schemes are tested. The sub-grid scale model is WALE, as in the isothermal flow simulations. The wall temperature is set at $T_w = 1200$, i.e., the wall is hot compared to the fluid, and a constant heat flux q_w establishes between the wall and the fluid. All the cases presented in this chapter are listed in Table. 4.1.1, the first letter "H" referring to "Heated".

Case	Tube	Mesh	Numerical scheme
HS51_Y1_TT	Smooth	Y1	TTGC
HS51_Y10t_TT		Y10t	
HS51_Y10t_LW			LW
HR51_Y1_TT	Ribbed	Y1	TTGC
HR51_Y10t_TT		Y10t	
HR51_Y10t_LW			LW

Table 4.1.1: Non-reacting heated flow in smooth (S51) and ribbed (R51) tubes.

4.2 WRLES of heated flow in the smooth tube S51 on the hybrid refined mesh Y1

According to the results of the previous chapter, the case HS51_Y1_TT using TTGC on mesh Y1 with fully resolved boundary layer is considered as a reference and presented here.

The convergence times of case HS51_Y1_TT is listed are Table. 4.2.1.

Case	τ_c	τ_a	Time step [s]	CPUs [s]	CPUh [h]
HS51_Y1_TT	865	474	5.55×10^{-8}	0.078	24 054

Table 4.2.1: Convergence and CPU times of case HS51_Y1_TT.

The imposed source term S_{qdm}, the Reynolds number, the bulk velocity, the bulk temperature and the final value of S_e are given in Table. 4.2.2.

Case	$S_{qdm}[Pa/m]$	U_b [m/s]	Re [-]	S_e [W/m^3]	q_w [W/m^2]	T_b [K]	T_w [K]
S51_Y1_TT	290	59.89	26 938	-	-	973.0	973.0
HS51_Y1_TT	290	60.67	27 251	1 439 737.2	18 574.8	975.02	1200.0

Table 4.2.2: Operating conditions of the turbulent heated flow in the smooth tube HS51_Y1_TT, compared with the reference case of the isothermal flow S51_Y1_TT.

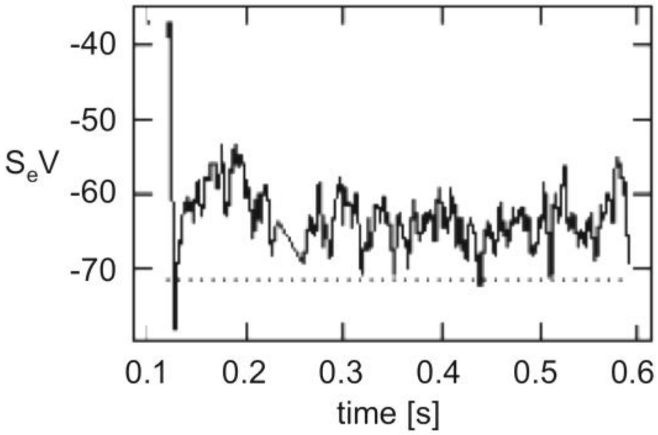

Figure 4.2.1: Temporal evolution of S_eV in heated smooth tube HS51_Y1_TT (solid line), and the initial estimation $S_e^{constant}V$ (dashed line).

Fig. 4.2.1 gives the temporal evolution of S_eV (which subtract the heat q_wS from the wall, as explained in Eq. 4.1.5 and demonstrated with values in Table. 4.2.2) to show the convergence history of the simulation of HS51_Y1_TT.

Note that in Table. 4.2.2, though the target bulk temperature in Eq. 4.1.4 is set to be 973 K for HS51_Y1_TT, the obtained bulk temperature differs slightly, and this can be explained by the difference between the final value of S_e and the initial estimation $S_e^{constant}$ as illustrated in Fig. 4.2.1. This however will have little impact as the results are analyzed with dimensionless quantities. Not also that the same S_{qdm} in both cases leads to different Re and U_b, due to the impact of the non-isothermal flow on the skin friction. This is discussed in the following section.

4.2.1 Flow dynamics

Velocity

Fig. 4.2.2 shows the profile of the mean axial velocity U_x normalized by the bulk velocity U_b in the smooth tube HS51_Y1_TT, compared to the isothermal flow S51_Y1_TT. The same profile is observed for both heated and isothermal case, thus a similar boundary layer thickness δ_{th}/R (0.191 for HS51_Y1_TT compared to 0.206 for S51_Y1_TT) is found (with the definition $U = 99\% Ub$). The difference of temperature close to the wall is not sufficient to change the flow dynamics.

Boundary layer

Fig. 4.2.3 plots the dimensionless velocity u^+ in function of y^+ for both cases. Again, very

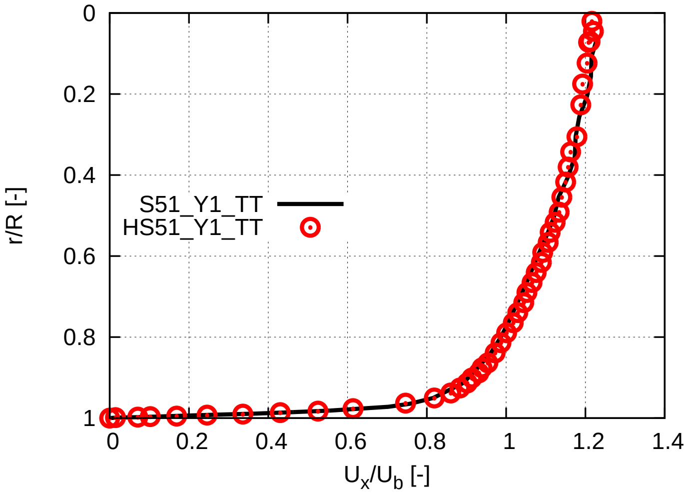

Figure 4.2.2: Profile of the mean axial velocity U_x normalized by the bulk velocity U_b of the heated flow in the smooth tube HS51_Y1_TT, compared to the isothermal flow S51_Y1_TT.

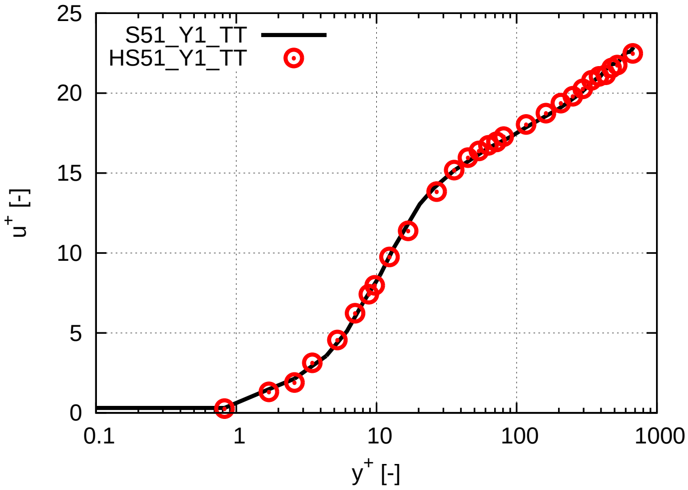

Figure 4.2.3: Law of the wall of the heated flow in the smooth tube HS51_Y1_TT, compared to the isothermal flow S51_Y1_TT.

good agreement is found between the two cases.

RMS of the velocity fluctuations $u'^{+}_{x,rms}$, $u'^{+}_{\theta,rms}$ and $u'^{+}_{r,rms}$ in the boundary layer are plotted against y^+ in Fig. 4.2.4. The scale of the three figures is the same to allow a direct comparison. Same results are observed between HS51_Y1_TT and S51_Y1_TT, demonstrating again that the heated flow behaves the same as the isothermal flow in the boundary layer.

Friction factor

The friction factor of the heated flow in the smooth tube (HS51_Y1_TT) is found to be 0.00556 from the source term S_{qdm} as the value of the pressure loss, compared to 0.0057 of isothermal flow (S51_Y1_TT). This difference on f_g is due to the slight difference on T_b (thus ρ_b) and U_b. The flow heated from the wall has variable properties as the temperature gradient leads to a variation of the mass density etc in the flow. As mentioned in Section 2.2.3, the correlation on the friction factor for this kind of flow can be made by multiplying $(T_w/T_b)^{0.1}$, as proposed by Kays [75], which is the most widely used, and leads to a value of 0.0057,

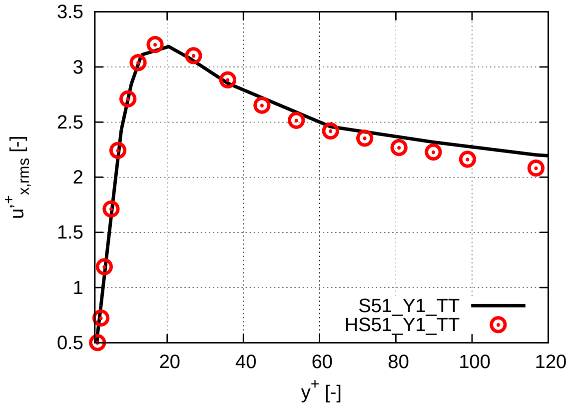

(a) $u'^{+}_{x,rms}$.

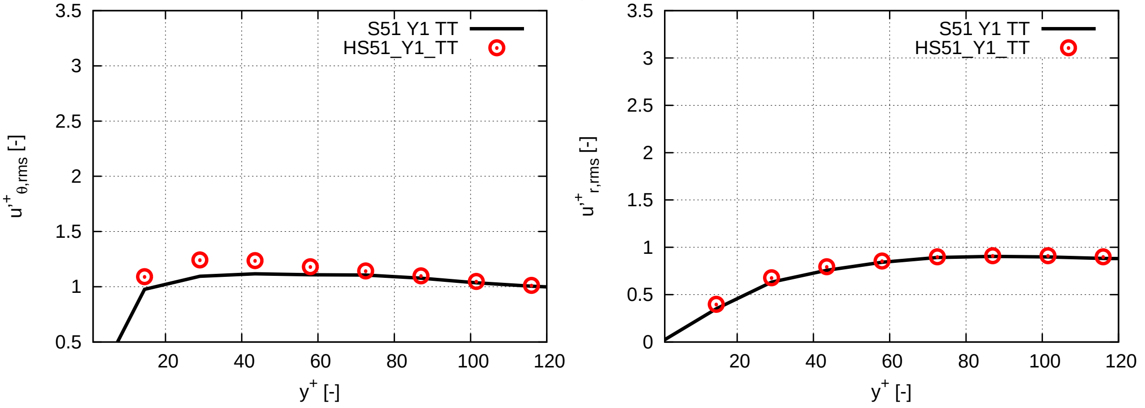

(b) $u'^{+}_{\theta,rms}$.

(c) $u'^{+}_{r,rms}$.

Figure 4.2.4: RMS of velocity fluctuations normalized by u_τ, thus $u'^{+}_{x,rms}$, $u'^{+}_{\theta,rms}$ and $u'^{+}_{r,rms}$, in the boundary layer of the heated flow (HS51_Y1_TT), together with the isothermal flow (S51_Y1_TT), in smooth tube S51 on mesh Y1.

the same as for the isothermal flow S51_Y1_TT. In fact, in the current case, the difference between the wall temperature and the bulk temperature is not too large (about 20%), thus the temperature gradient is not too sharp, the impact of the variable properties is relatively small.

4.2.2 Thermal behavior

Temperature profile

The time-averaged profile of the non-dimensional temperature Θ defined in Eq. 2.1.26 is plotted in Fig. 4.2.5, together with the dimensionless velocity U_x/U_b profile. The value at the center line is around 1.2 and a profile similar to the velocity profile is observed.

Thermal boundary layer

The thermal boundary layer thickness δ_T is here defined as the distance from the wall where the temperature T verifies $T_w - T = 99\%(T_w - T_b)$. It is found to be $0.281R$ for the reference case HS51_Y1_TT, i.e., thicker than the velocity boundary layer thickness $0.191R$. The temperature in the thermal boundary layer can be also investigated by plotting Θ^+ against

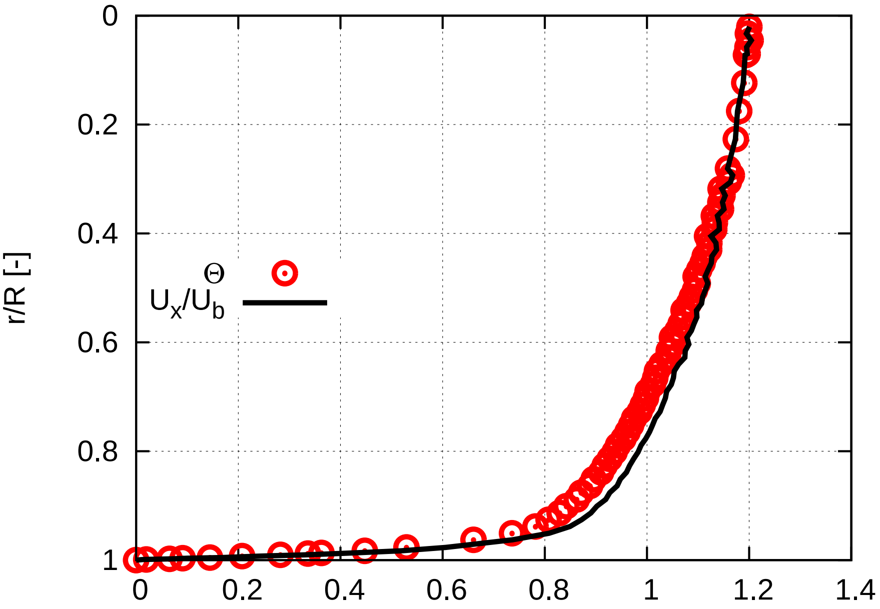

Figure 4.2.5: Time-averaged non-dimensional temperature Θ profile (circles), compared to the dimensionless velocity U_x/U_b profile (solid line): case HS51_Y1_TT.

y^+, as shown in Fig. 4.2.6. Theoretical/empirical laws of the wall for temperature in the linear region (Eq. 2.1.37) and in the log law region are also reported. In the log law region, the proposition by Redjem-Saad et al. (2007) [43] and Kays [75] are used (using $\kappa_\Theta = 0.34$ in Eq. 2.1.38 as the the Prandtl number in current work is equal to 0.71). Both linear and logarithmic behaviors are well reproduced, and a closer agreement is found with the law of Redjem-Saad et al. (2007).

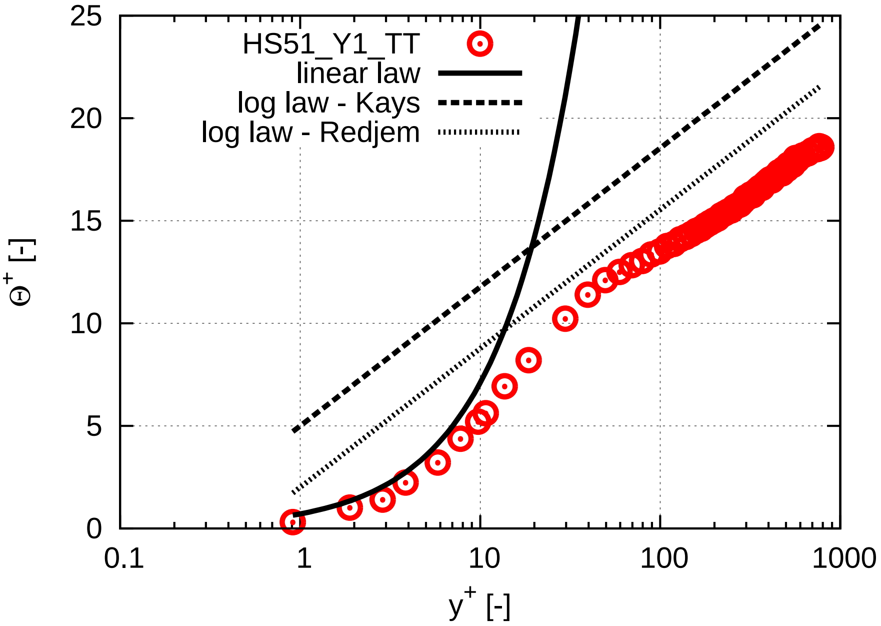

Figure 4.2.6: Non-dimensional temperature profile Θ^+ *vs* y^+ for case HS51_Y1_TT.

Temperature fluctuation

The dimensionless RMS of temperature fluctuation Θ'^{+}_{rms} is plotted against y^+ in Fig. 4.2.7, The peak is located around $y^+ = 30$ and is equal to 2.5, compared to the DNS results of turbulent pipe flow with fixed wall temperature reported by Redjem et al. (2007) with $y^+(peak) = 20$ and $\Theta'^{+}_{rms}(peak) = 1.5$ in Fig. 2.1.9. Note that the Reynolds number in their case is only 5500, much lower than 27 000 in the present work.

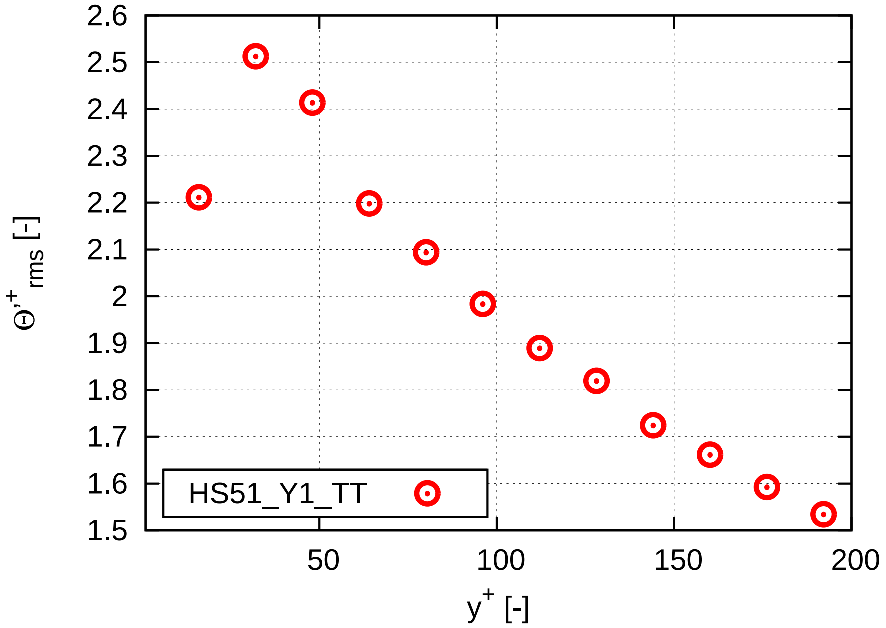

Figure 4.2.7: Dimensionless RMS of temperature fluctuation Θ'^{+}_{rms} of the heated flow in case HS51_Y1_TT.

Nusselt number

In smooth tubes, the Nusselt number is uniform along the wall and equal to the mean value. It is calculated here to be Nu = 72.4 from Eq. 2.1.55. Using the correlation for variable properties of Eq. 2.2.16, the correlated Nusselt number Nu_{corr} is equal to 76.2. Using the empirical formula of Dittus-Boelter (Eq. 2.2.11 for heating) leads to 74.3. The Dittus-Boelter approximation directly holds for small fluid/solid temperature differences, and can be compared directly to the non-corrected Nu = 72.4 showing a very good agreement (2.5% error).

The obtained results for both the velocity and temperature fields for case HS51_Y1_TT confirms that this case may be used as a reference.

4.3 Impact of the mesh

To reduce the CPU cost of the final applications, the use of coarser mesh is evaluated here as was done for the isothermal cases in Chapter 3. The mesh is Y10t presented in Section 3.2.1, and both numerical schemes LW and TTGC are compared with the reference case HS51_Y1_TT of the previous section.

The convergence times of the cases on mesh Y10t are listed in Table. 4.3.1.

Case	τ_c	τ_a	Time step [s]	CPUs [s]	CPUh [h]
HS51_Y10t_TT	818	993	1.21×10^{-7}	0.039	7528
HS51_Y10t_LW	666	1665	1.20×10^{-7}	0.019	4664

Table 4.3.1: Convergence and CPU times of cases HS51_Y10t_TT and HS51_Y10t_LW.

The imposed source term S_{qdm}, the Reynolds number, the bulk velocity, the steady bulk temperature and the final value of S_e are given in Table. 4.3.2, compared to the reference case HS51_Y1_TT.

Case	$S_{qdm} [Pa/m]$	U_b [m/s]	Re [-]	S_e [W/m^3]	q_w [W/m^2]	T_b [K]	T_w [K]
HS51_Y1_TT (ref)	290	60.67	27 251	1 439 737.2	18 574.8	975.02	1200
HS51_Y10t_TT	205	59.65	26 861	1 061 676.7	13 819.7	973.92	
HS51_Y10t_LW	185	60.32	27 118	888 003.1	11 038.7	973.80	

Table 4.3.2: Operating conditions of the turbulent heated flow in smooth tube S51, using mesh Y10t and the two numerical schemes TTGC and LW, compared to the reference case HS51_Y10t_TT.

As the dynamics of heated flow is very similar to the isothermal flow, this section focuses on the comparison of thermal behavior of the three cases.

4.3.1 Temperature profiles

Time-averaged non-dimensional temperature profiles for cases HS51_Y1_TT, HS51_Y10t_TT and HS51_Y10t_LW are plotted in Fig. 4.3.1. Very similar profiles are observed for the three cases.

4.3.2 Thermal boundary layer

The normalized thermal boundary layer thickness δ_T/R for HS51_Y10t_TT and HS51_Y10t_LW is respectively 0.307 and 0.297, i.e., 9% and 5% discrepancy compared to $\delta_T/R = 0.281$ for HS51_Y1_TT. The dimensionless temperature Θ^+ is plotted against y^+ in Fig. 4.3.2. It is expected that WRLES on the coarse mesh ($y^+ \sim 10$) does not predict the flow behavior on the wall as well as the reference case. Both HS51_Y10t_TT and HS51_Y10t_LW over predict Θ^+ in the region $y^+ > 20$, i.e., in the buffer layer and the log law region. This results agrees with the fact that HS51_Y1_TT better predicts the temperature gradient at the wall, leading to a higher higher wall normal heat flux (i.e., friction temperature) than on the coarse mesh Y10t. This is also demonstrated by the higher S_e in Table. 4.3.2.

4.3.3 Temperature fluctuation

The normalized RMS of the temperature fluctuation Θ'^+_{rms} is shown in Fig. 4.3.3. Both cases HS51_Y10t_TT and HS51_Y10t_LW overpredict Θ'^+_{rms} by up to 30%, which is also explained by the higher temperature near the wall.

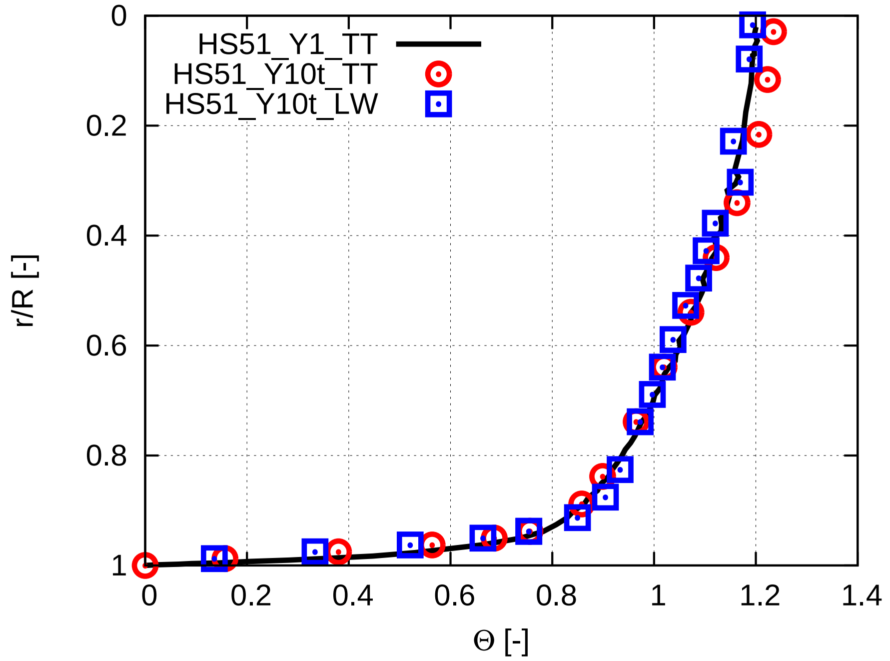

Figure 4.3.1: Time-averaged non-dimensional temperature Θ for cases HS51_Y10t_TT and HS51_Y10t_LW on coarse mesh, compared to the reference case HS51_Y1_TT.

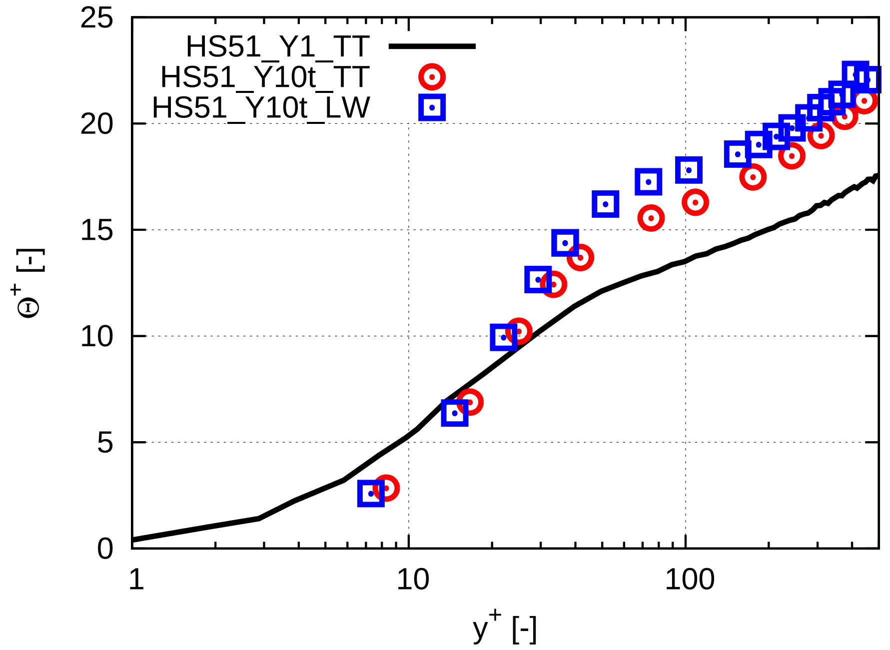

Figure 4.3.2: Dimensionless temperature Θ^+ for cases HS51_Y10t_TT and HS51_Y10t_LW on coarse mesh, compared to the reference case HS51_Y1_TT.

4.3.4 Nusselt number

Both HS51_Y10t_TT and HS51_Y10t_LW on the coarse mesh Y10t underpredict the Nusselt number compared to the empirical formula of Nu proposed by Dittus-Boelter in Eq. 2.2.11, by 22% and 34% respectively. This result agrees with the previous observation that the wall normal heat flux solved by the coarse mesh Y10t is smaller than in the reference case.

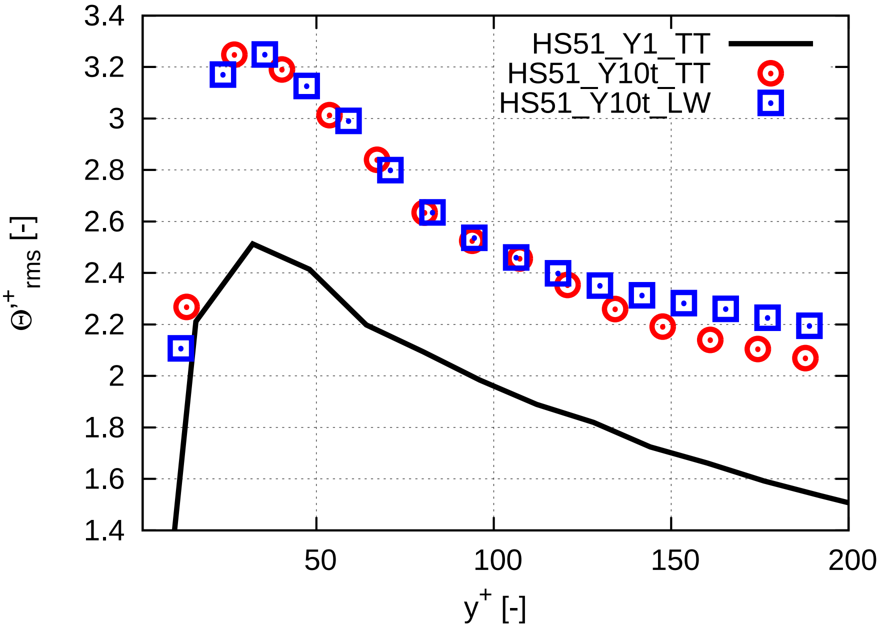

Figure 4.3.3: Normalized RMS of the temperature fluctuation Θ'^{+}_{rms} for cases HS51_Y10t_TT and HS51_Y10t_LW on coarse mesh, compared to the reference case HS51_Y1_TT.

4.4 WRLES of heated flow in the ribbed tube R51 on hybrid refined mesh Y1 using TTGC

In this section, a reference case is computed for the heated flow in the ribbed tube R51 which is presented in Chapter 3. WRLES is conducted on the hybrid refined mesh Y1 using the TTGC scheme. The convergence times of this case HR51_Y1_TT are listed in Table. 4.4.1.

Case	τ_c	τ_a	Time step [s]	CPUs [s]	CPUh [h]
HR51_Y1_TT	284	284	2.08×10^{-8}	0.193	65 817

Table 4.4.1: Convergence and CPU times of case HR51_Y1_TT.

Table. 4.4.2 gives the operating conditions of the case HR51_Y1_TT.

Case	$S_{qdm}[Pa/m]$	U_b [m/s]	Re [-]	S_e [W/m^3]	q_w [W/m^2]	T_b [K]	T_w [K]
HR51_Y1_TT	1830	61.7	27 557	3 367 643.0	43 329.3	984.48	1200
HS51_Y1_TT	290	60.67	27 251	1 439 737.2	18 574.8	975.02	

Table 4.4.2: Operating condition of the case HR51_Y1_TT.

In the following sections, the comparison of HR51_Y1_TT with the isothermal flow in ribbed tube R51_Y1_TT is first conducted to show the impact of the heat transfer on the flow dynamics. Then the results are compared to the heated flow in the smooth tube HS51_Y1_TT to show the impact of ribs on the heat transfer.

4.4.1 Flow dynamics: comparison between heated and isothermal flows in ribbed tube R51

Mean velocity

The mean axial and azimuthal velocity fields normalized by the bulk velocity are shown in Figs. 4.4.1 and 4.4.2 respectively. Similarly to the smooth tube S51, nearly the same flow is observed in both heated and isothermal ribbed tube R51. Quantitive comparisons between the two cases of the normalized axial and azimuthal velocity profiles at 12 different axial locations are given in Figs. 4.4.3 and 4.4.4, in the same way as done in the previous chapter, and a zoom on the near wall region is provided in the bottom part. Very similar velocity profiles for both cases R51_Y1_TT and HR51_Y1_TT are observed, with only a very small discrepancy on the azimuthal velocity profiles. This shows that the flow heating is too small to have an impact on the mean velocity.

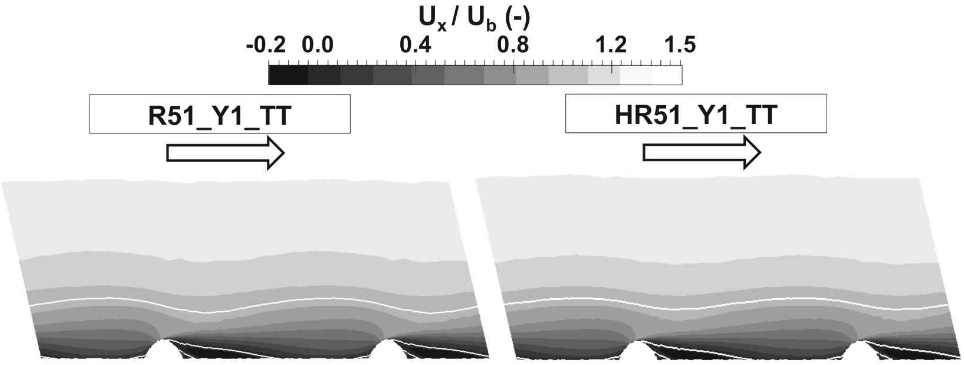

Figure 4.4.1: Normalized axial velocity fields in a axial cut plane. Left: R51_Y1_TT; Right: HR51_Y1_TT.

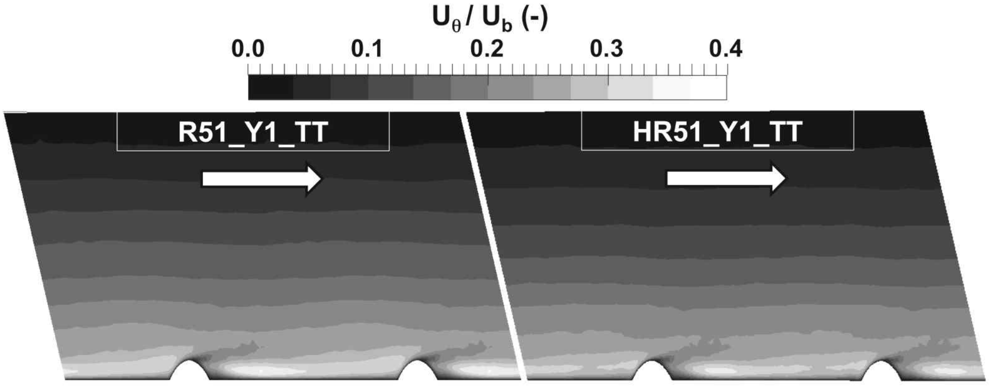

Figure 4.4.2: Normalized azimuthal velocity fields in a axial cut plane. Left: R51_Y1_TT; Right: HR51_Y1_TT.

RMS of velocity fluctuation

The fields of the RMS of the axial velocity fluctuation normalized by U_b is illustrated on Fig. 4.4.5. Again, similar fields are observed, especially in the near wall region. It is then

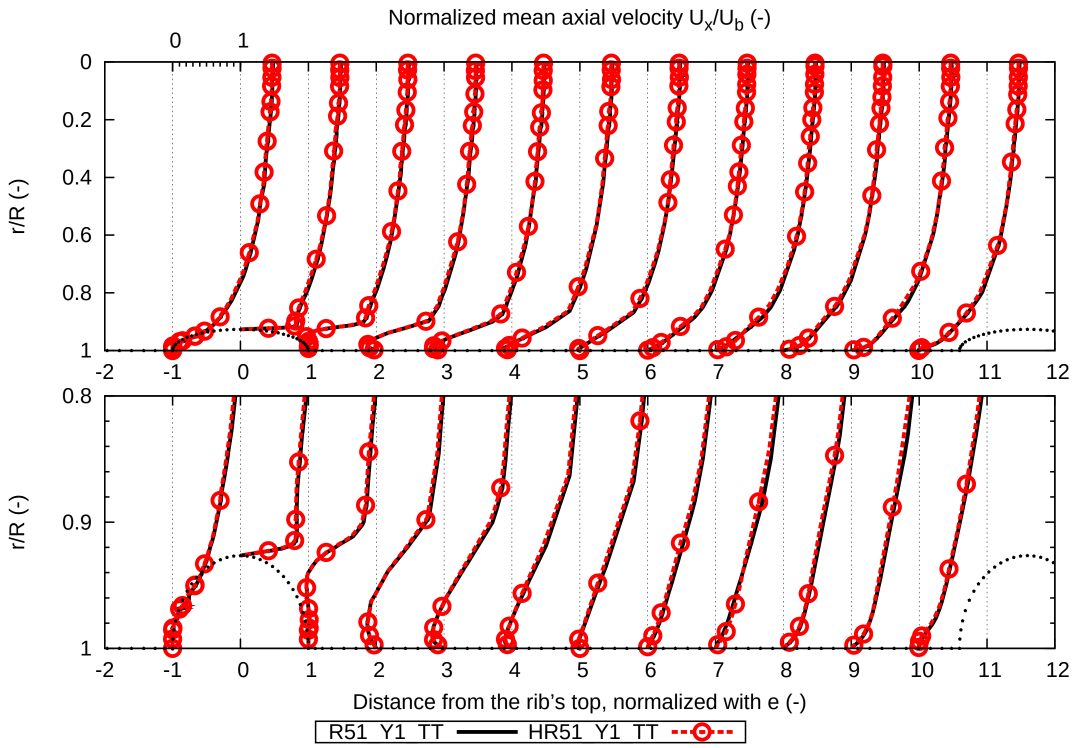

Figure 4.4.3: Normalized axial velocity profiles of cases R51_Y1_TT and HR51_Y1_TT. Top: profiles from the pipe center ($r/R = 0$) to the wall ($r/R = 1$); Bottom: zoom in the near wall region.

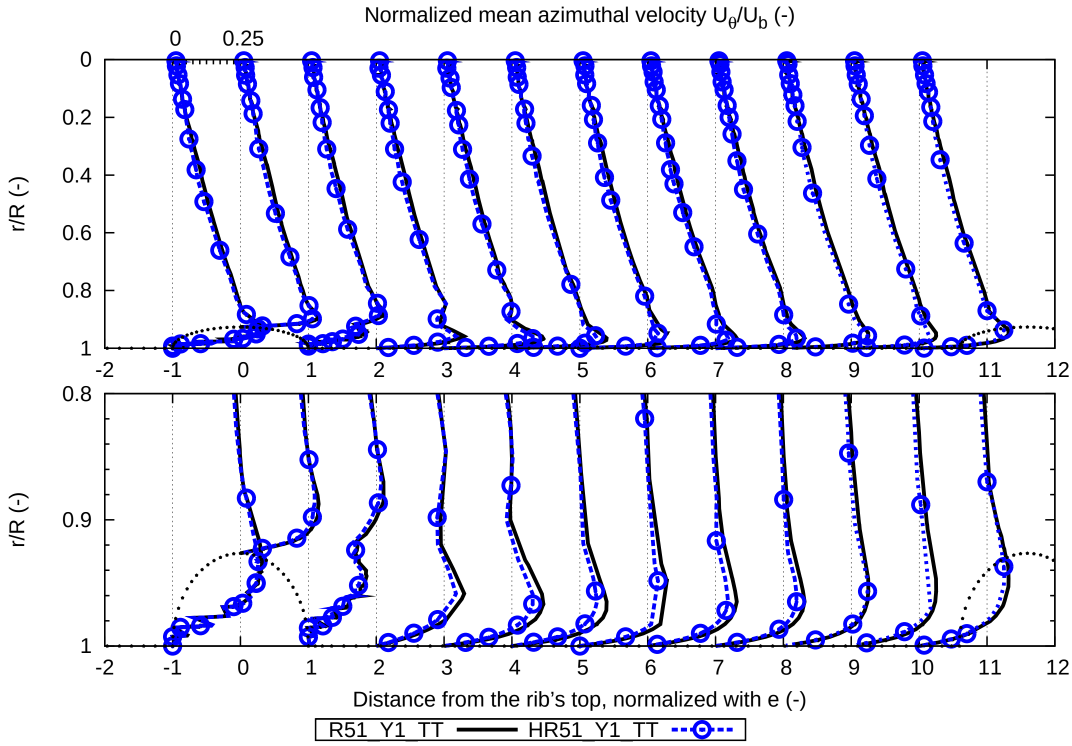

Figure 4.4.4: Normalized azimuthal velocity profiles of cases R51_Y1_TT and HR51_Y1_TT. Top: profiles from the pipe center ($r/R = 0$) to the wall ($r/R = 1$); Bottom: zoom in the near wall region.

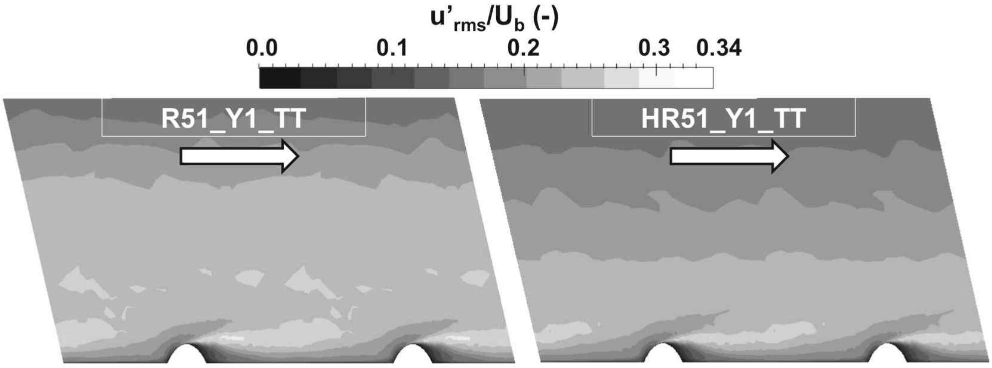

Figure 4.4.5: Normalized RMS of the axial velocity fluctuation fields in a axial cut plane. Left: R51_Y1_TT; Right: HR51_Y1_TT.

concluded that the heating does not have any effect on the turbulence.

Pressure variation and shear stress

The pressure variation in the ribbed tube R51 of both isothermal and heated cases is presented by the pressure coefficient C_p (Eq. 2.5.1), as shown in Fig. 4.4.6. Similar pressure

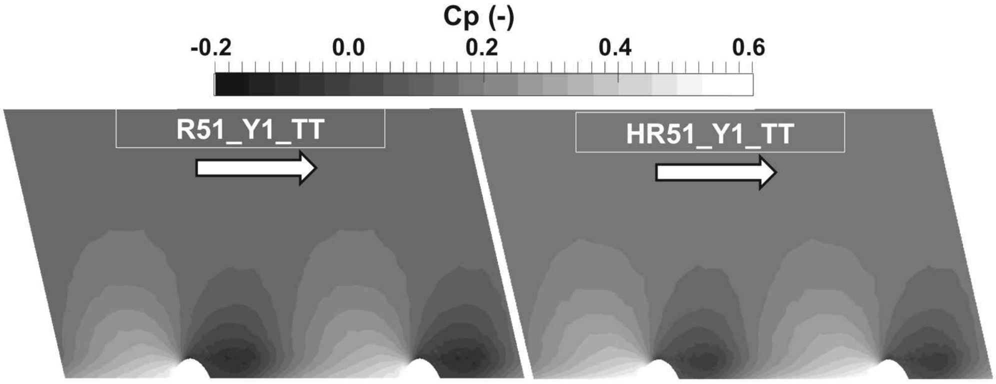

Figure 4.4.6: Pressure coefficient fields in a axial cut plane. Left: R51_Y1_TT; Right: HR51_Y1_TT.

variation is found for R51_Y1_TT and HR51_Y1_TT. In addition, the evolutions of C_p and C_f (Eq. 2.3.1) along the wall surface in both cases are illustrated on Figs. 4.4.7 and 4.4.8. No significant impact of the heating condition to C_p and C_f along the wall of the ribbed tube R51 is observed. The main difference is the peak value slightly higher in the heated case. This is consistent with the fact that the same imposed source term $S_{qdm} = 1830\,\mathrm{Pa/m}$ was used to maintain Re $\sim 27\,000$ for both cases (Table. 3.7.2 and 4.4.2).

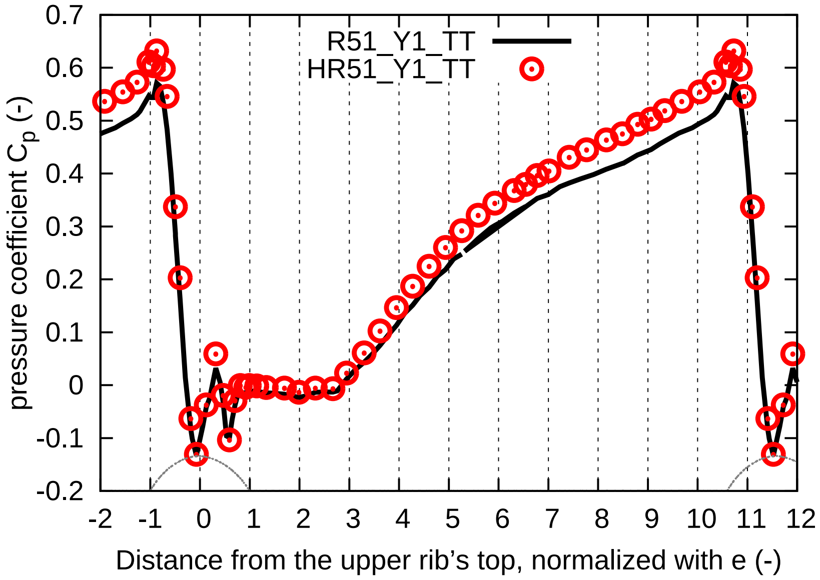

Figure 4.4.7: Evolution of the pressure coefficient C_p along the wall surface of both cases R51_Y1_TT and HR51_Y1_TT.

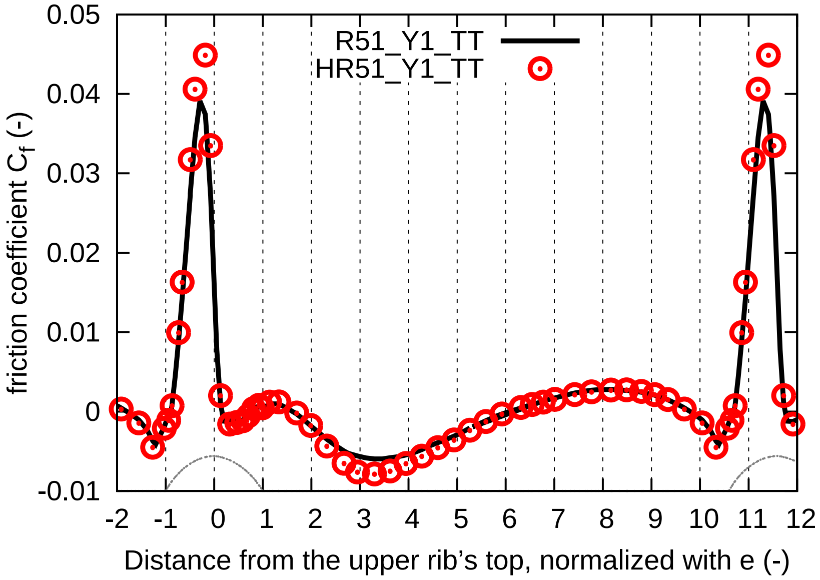

Figure 4.4.8: Evolution of the skin friction coefficient C_f along the wall surface of both cases R51_Y1_TT and HR51_Y1_TT.

4.4.2 Thermal behavior: comparison with the heated flow in smooth tube S51

Mean temperature

The time-averaged normalized temperature Θ fields (Eq. 2.1.26) for the heated flow in both smooth (HS51_Y1_TT) and ribbed (HR51_Y1_TT) tubes are illustrated on Fig. 4.4.9, with the iso-contour of $\Theta = 0.99$ (thus $T_w - T = 99\%(T_w - T_b)$) in black and $\Theta = 0.75$ in white respectively. The iso-contour of $\Theta = 0.99$ indicates that the boundary layer is thicker in the

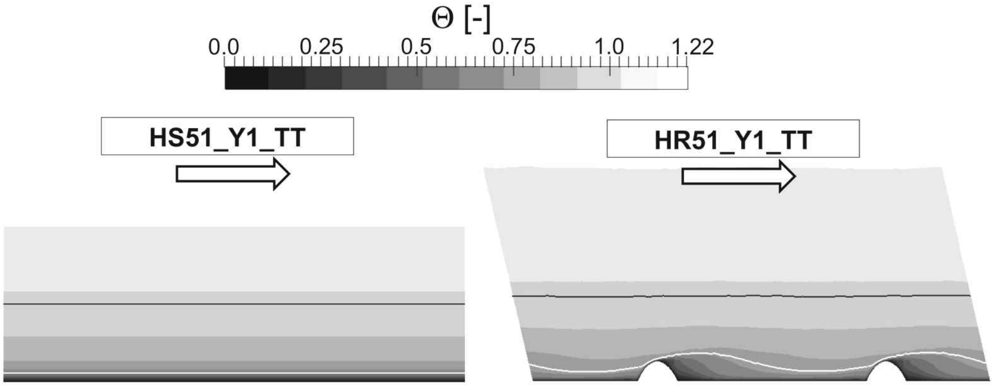

Figure 4.4.9: Normalized mean temperature fields in a axial cut plane. Left: HS51_Y1_TT; Right: HR51_Y1_TT.

ribbed tube R51, due to the more intensive heat transfer induced by the helical ribs. The other iso-contour $\Theta = 0.75$, indicating a sublayer close to wall, shows how the temperature distribution is affected by the ribs in case HR51_Y1_TT: this sublayer is very thin on top of the ribs and becomes thicker in the downstream recirculation zone, then reduces again towards the next rib.

Details are shown in Fig. 4.4.10, plotting the mean normalized temperature profiles in

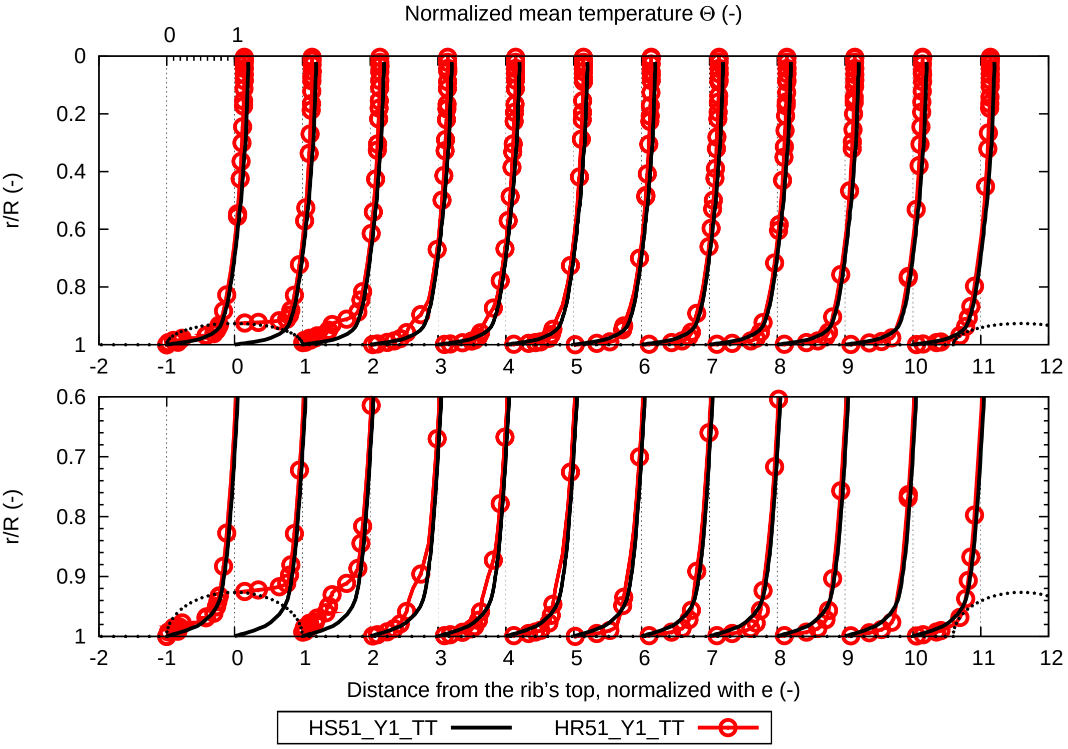

Figure 4.4.10: Mean normalized temperature profiles of the heated flow at various locations in both smooth (HS51_Y1_TT) and ribbed (HR51_Y1_TT) tubes.

both heated smooth (HS51_Y1_TT) and ribbed (HR51_Y1_TT) tubes, with a zoom on the boundary layer for $0.6 < r/R < 0$. The profiles vary along the wall of the ribbed tube R51, while it keeps the same shape in the smooth tube S51. The profiles mostly different at the back corner of the rib attaching to the wall (locations $1e$), where the temperature close to the wall is higher and thus the temperature gradient at the wall is smaller in the ribbed tube. This is due to the recirculation zone behind the rib, which accumulates the heat from the rib surface at T_w in this zone, thus decreasing heat transfer and leading to a thicker thermal boundary layer.

On the contrary, at locations from 3e to 10e (a zoom on location 5e is given in Fig. 4.4.11 as an example for a better illustration), the profiles are similar. At these locations, two effects can be observed by separating the thermal boundary layer into two parts depending on the normal distance from the wall: the sublayer goes from the wall to the rib height e, and the outer layer starts at the rib height. On one hand, lower temperature (higher value of Θ) is found in the sublayer of the ribbed tube R51, thus a greater temperature gradient is observed, leading to greater heat transfer. On the other hand, in the outer layer, the gradient of the temperature in R51 is smaller than in the smooth tube HS51_Y1_TT, due to the better turbulent mixing, leading to a thicker thermal boundary layer and a higher temperature (smaller value of Θ) in this region. Moreover, more heat is brought from the sublayer into this region, thus enhancing the first effect.

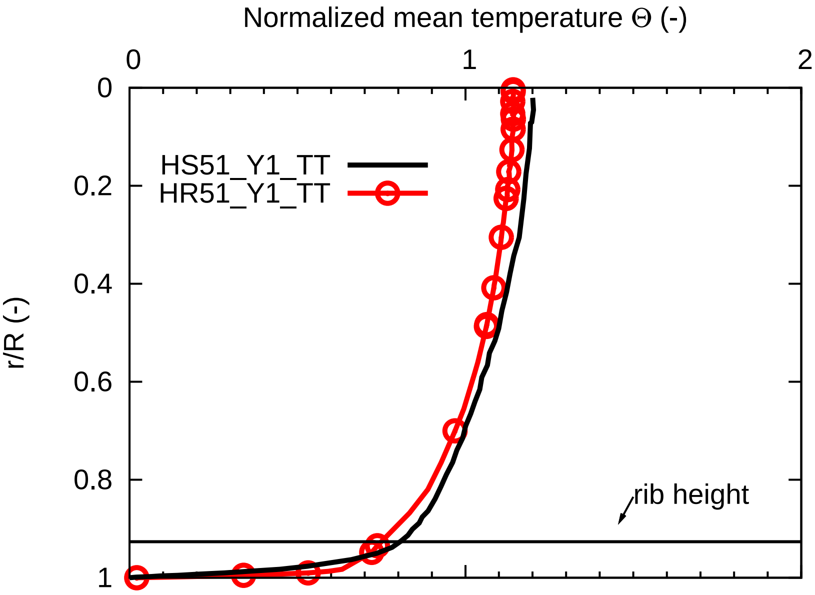

Figure 4.4.11: Mean normalized temperature profiles of the heated flow at location 5e in both smooth (HS51_Y1_TT) and ribbed (HR51_Y1_TT) tubes.

Thermal boundary layer

Like in the analysis of the isothermal flow in previous chapters, the five locations, respectively at the upstream corner (-1e), the top (0e), the downstream corner (1e) of ribs, in the downstream recirculation zone (3e), and out of the recalculation zone (7e) (index referred to Fig. 4.4.3) are used to conduct the comparison with the heated flow in the smooth tube S51. The dimensionless temperature Θ^+ *vs* y^+ is plotted in Fig. 4.4.12, using the global friction velocity $u_{\tau,g}$ (as explained in Section 3.8.1), and the global friction temperature $T_{\tau,g}$ (Eq. 2.1.33, using $u_{\tau,g}$ and q_w calculated from S_e by Eq. 4.1.5). In the two corners of the rib attached to the wall, i.e., locations -1e and 1e, similar behavior is observed: due to the recirculation zone, the temperature profile is very different from the smooth tube. At the

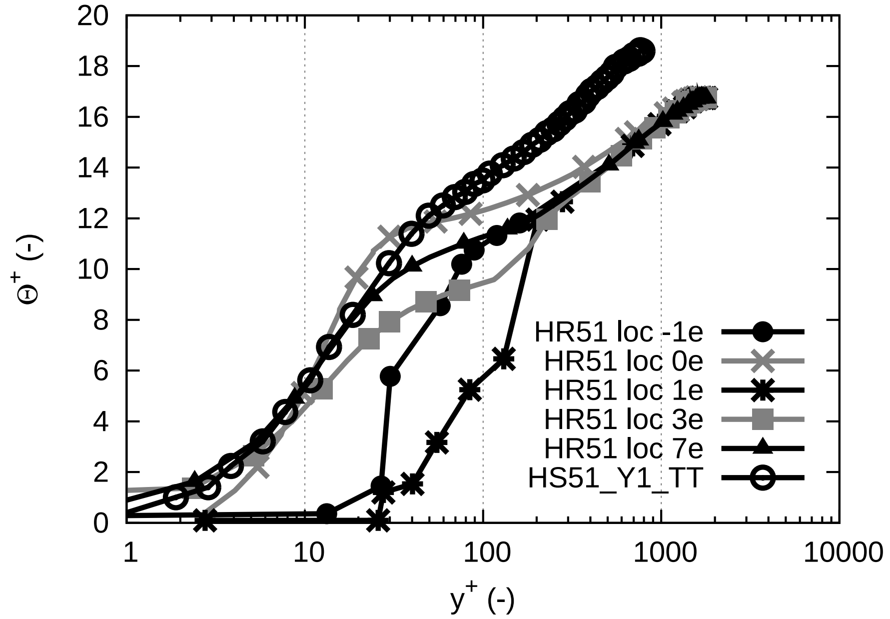

Figure 4.4.12: Dimensionless temperature Θ^+ *vs* y^+ of the heated flow at 5 various locations in the ribbed tube HR51_Y1_TT, compared to the heated smooth tube HS51_Y1_TT.

other locations, the linear law as in the smooth tube HS51_Y1_TT is reproduced, while a shift in the log law region is observed, due to the enhanced turbulent mixing as always seen.

Temperature fluctuation

The profiles of dimensionless RMS of temperature fluctuations Θ'^+_{rms} at the five locations along the wall of ribbed tube HR51_Y1_TT are plotted against y^+, and compared to the heated flow in the smooth tube HS51_Y1_TT in Fig. 4.4.13. In the near wall region ($y^+ < 200$), the peak is the same order of the smooth tube solution but appears close to the wall, consistently with the observation on the mean temperature. In the outer layer ($y^+ > 200$), stronger temperature fluctuation in the ribbed tube is observed at the five locations, again in agreement with the temperature.

Nusselt number

The evolution of the Nusselt number along the wall of the ribbed tube (HR51_Y1_TT) is plotted in Fig. 4.4.14, where the value in the smooth tube HS51_Y1_TT is also reported. The Nusselt number is always higher in the ribbed tube, except in the back corner of the rib (location 1e), in agreement with the previous observation on the profiles of the non-dimensional temperature Θ. The Nusselt number peaks on the upstream side of the rib, then decreases to a minimum value just behind the rib, and increases again to reach a plateau between the ribs.

The global Nusselt number of the ribbed tube HR51_Y1_TT is found to be 175.4, which is 2.4 times higher than that of smooth tube HS51_Y1_TT. This means a significant enhancement of the heat transfer, to be compared to the pressure loss increase, of 6 times higher than in the smooth tube.

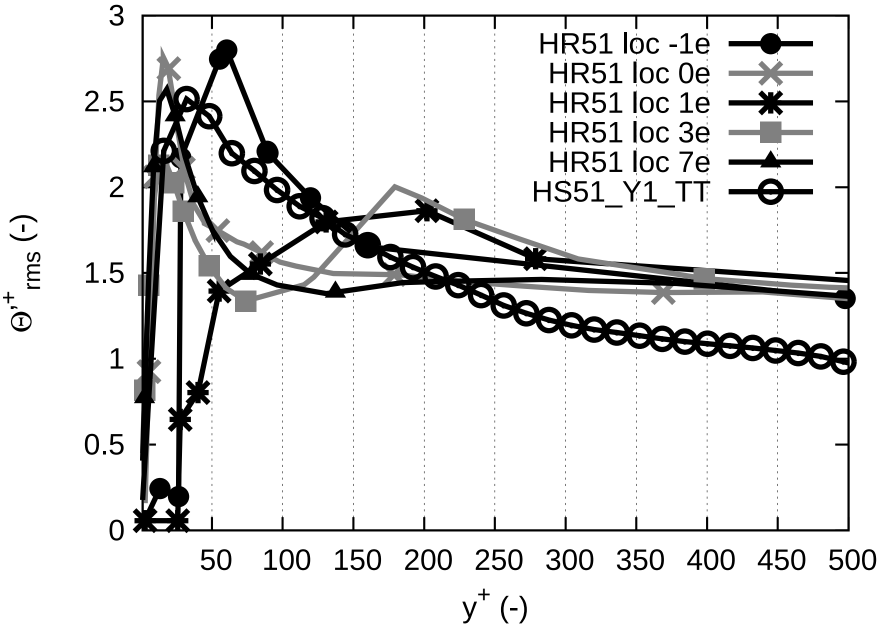

Figure 4.4.13: Dimensionless RMS of temperature fluctuations Θ'^{+}_{rms} of the heated flow at 5 various locations in the ribbed tube HR51_Y1_TT, compared to the heated smooth tube HS51_Y1_TT.

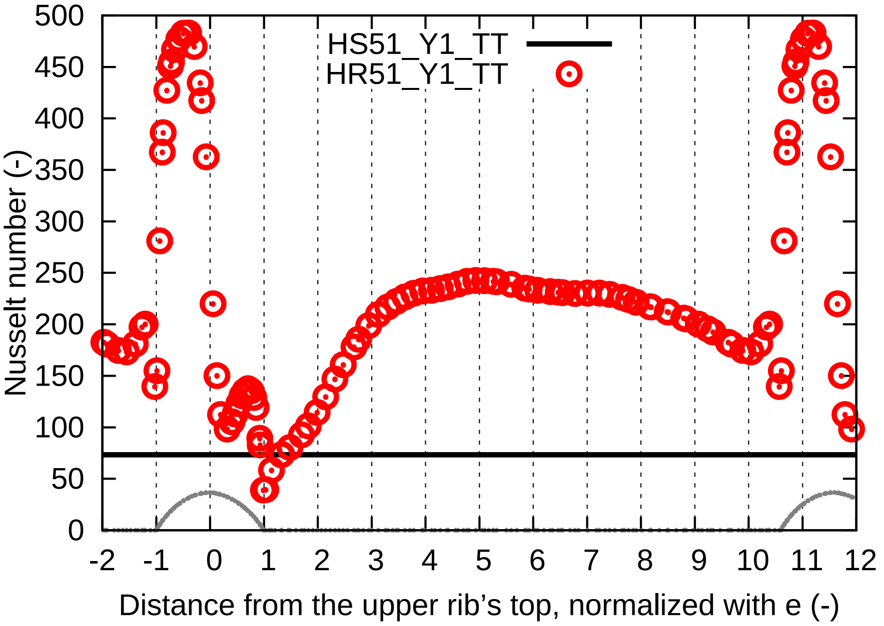

Figure 4.4.14: Evolution of the Nusselt number Nu along the wall surface of case HR51_Y1_TT, compared to case HS51_Y1_TT.

4.5 Impact of the mesh and the numerical scheme on WRLES of heated flow in the ribbed tube

In this section, the results of heated ribbed tubes on the coarser mesh Y10t using the two numerical schemes LW (HR51_Y10t_LW) and TTGC (HR51_Y10t_TT) are compared to the reference case HR51_Y1_TT on mesh Y1 using TTGC. No results using the scheme LW on the hybrid mesh Y1 is shown, it has been demonstrated in previous chapters that the use of LW with Y1 having prism layers generates errors in the near wall region. The convergence times of these cases are listed in Table. 4.5.1.

Case	τ_c	τ_a	Time step [s]	CPUs [s]	CPUh [h]
HR51_Y10t_TT	392	280	5.70×10^{-8}	0.045	6711
HR51_Y10t_LW	425	227	5.69×10^{-8}	0.022	3174

Table 4.5.1: Convergence and CPU times of cases on the mesh Y10t using the two numerical schemes LW and TTGC.

Table. 4.5.2 shows the operating conditions of cases HR51_Y10t_LW and HR51_Y10t_TT, compared to the reference case HR51_Y1_TT.

Case	$S_{qdm}[Pa/m]$	U_b [m/s]	Re [-]	S_e [W/m^3]	T_b [K]	T_w [K]
HR51_Y1_TT (ref)	1 830	61.7	27 557	4 140 944.4	984.48	1200
HR51_Y10t_TT	1 800	60.8	27 159	3 837 078.5	984.54	
HR51_Y10t_LW	1 900	61.6	27 555	3 385 463.8	982.15	

Table 4.5.2: Operating conditions of the turbulent heated flow in ribbed tubes R51 solved on the mesh Y10t using the two numerical schemes LW and TTGC, compared to the reference case.

As the impact of heating on the flow dynamics is minor, and different mesh and numerical schemes have been already evaluated for the isothermal flow in Chapter 3, no more comparison on flow dynamics will be conducted in this section and the following discussion focuses on the thermal behavior.

4.5.1 Temperature fields and profiles

Fig. 4.5.1 shows time-averaged temperature fields of the heated ribbed tube for the cases HR51_Y1_TT (the reference case), HR51_Y10t_TT and HR51_Y10t_LW, with the iso-contour of $\Theta = 99\%$ in black and $\Theta = 75\%$ in white. Similar topologies are observed, with almost exactly the same solution with the numerical scheme TTGC, and only slight differences appearing between TTGC and LW schemes. In particular the thermal boundary layer (defined with $\Theta = 99\%$) is thicker and the iso-contour of $\Theta = 75\%$ shows more sharpen variations and becomes thinner in the upstream of the ribs in case HR51_Y10t_LW.

Profiles of Θ at various locations along the wall of R51 are plotted in Fig. 4.5.2 for comparison among the three cases. Again similar profiles are observed, including around the ribs where the profiles deviate from the classical boundary layer behavior.

Fig. 4.5.3 shows the RMS of temperature fluctuation normalized by T_b in the heated ribbed tubes of all these cases. HR51_Y10t_TT is in good agreement with the reference case HR51_Y1_TT, but HR51_Y10t_LW underpredicts the intensity of the temperature fluctuation in the tube, while capturing the behavior near the wall.

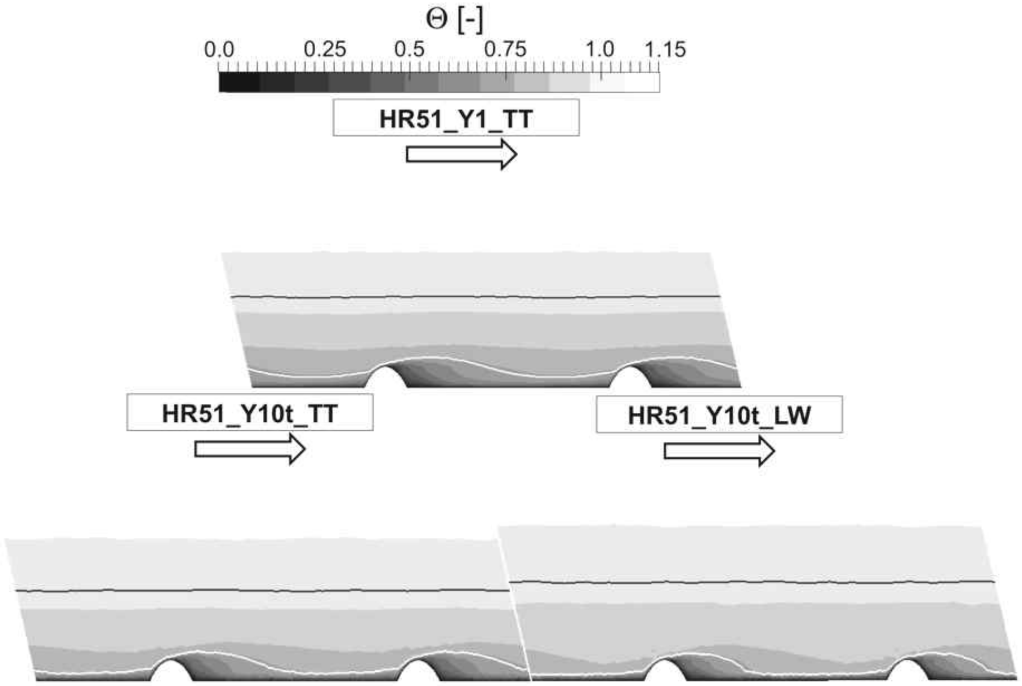

Figure 4.5.1: Time-averaged fields of the normalized temperature Θ in the heated ribbed tube R51. Top: HR51_Y1_TT; Bottom left: HR51_Y10t_TT; Bottom right: HR51_Y10t_LW.

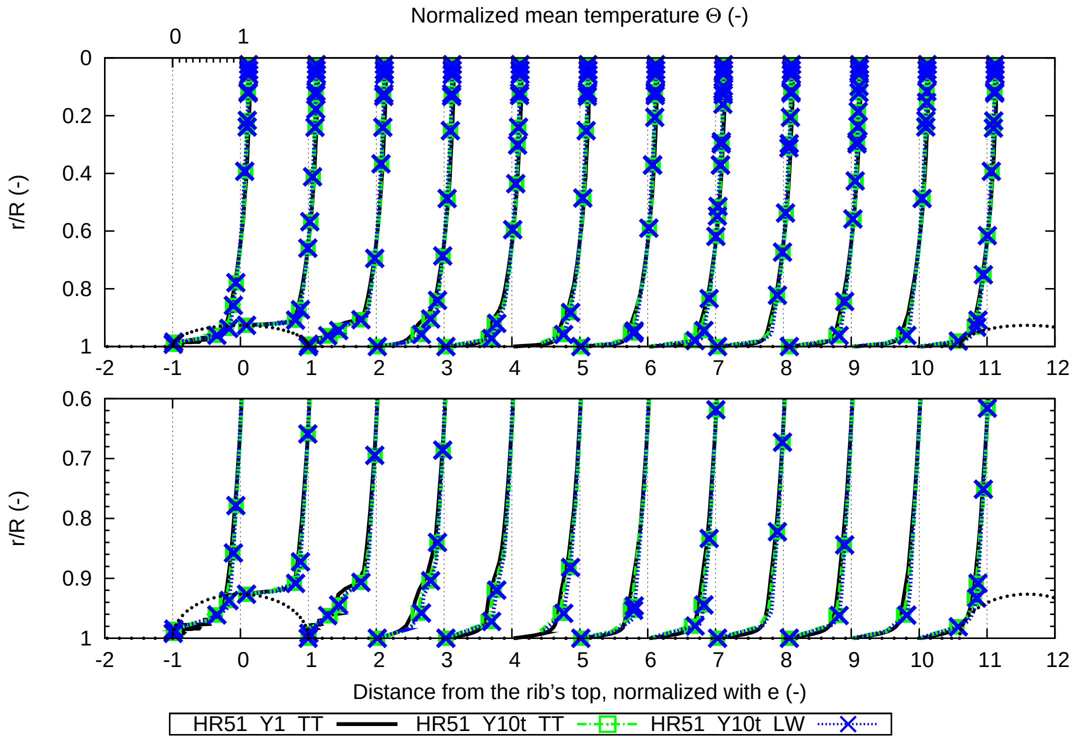

Figure 4.5.2: Time-averaged profiles of the normalized temperature Θ of the heated flow in the ribbed tube R51. Top: HR51_Y1_TT; Bottom left: HR51_Y10t_TT; Bottom right: HR51_Y10t_LW.

4.5.2 Nusselt number

The evolution of the local Nusselt number along the wall of the ribbed tube is plotted in Fig. 4.5.4 for the cases HR51_Y1_TT (the reference case), HR51_Y10t_TT and HR51_Y10t_LW.

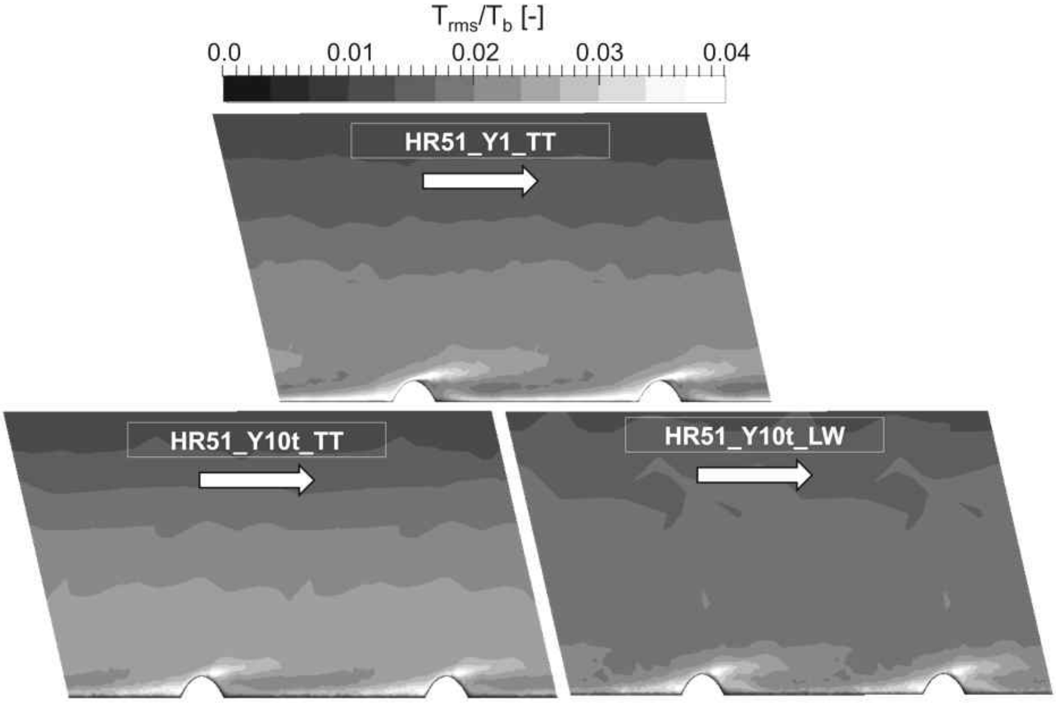

Figure 4.5.3: Time-averaged fields of the RMS of the fluctuating temperature T_{rms} (normalized by the bulk temperature T_b) of the heated flow in the ribbed tube R51. Top: HR51_Y1_TT; Bottom left: HR51_Y10t_TT; Bottom right: HR51_Y10t_LW.

Very similar evolutions are observed. HR51_Y10t_LW is very close to the reference case HR51_Y1_TT except at some singles points. HR51_Y10t_TT overpredicts clearly the values on the top of the ribs, which has however no significant impact on the global Nusselt number.

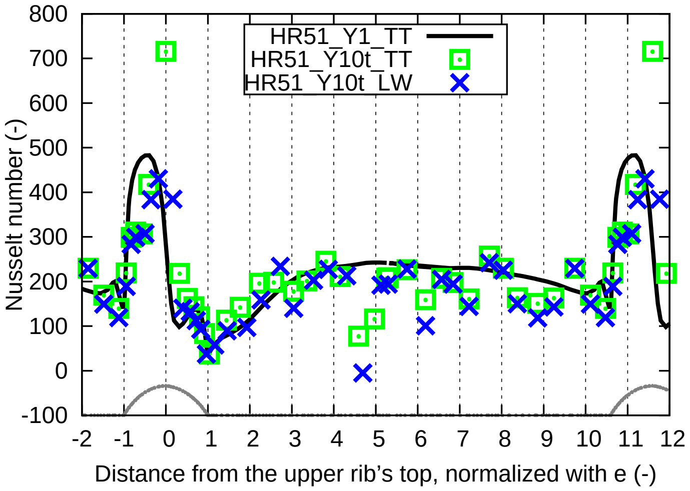

Figure 4.5.4: Evolution of the Nusselt number along the wall surface in the heated ribbed tube R51, on meshes Y1/Y10t, with TTGC/LW.

The global Nusselt numbers are 162.55 and 142.05 in cases HR51_Y10t_TT and HR51_Y10t_LW, i.e., respectively underpredict by 7% and 20% the reference value 175.4 of case HR51_Y1_TT. Fig. 4.5.5 plots the results compared to the formula from the literature presented in Chapter 2, and similar results with Vicent et al. (2004) [16] are found.

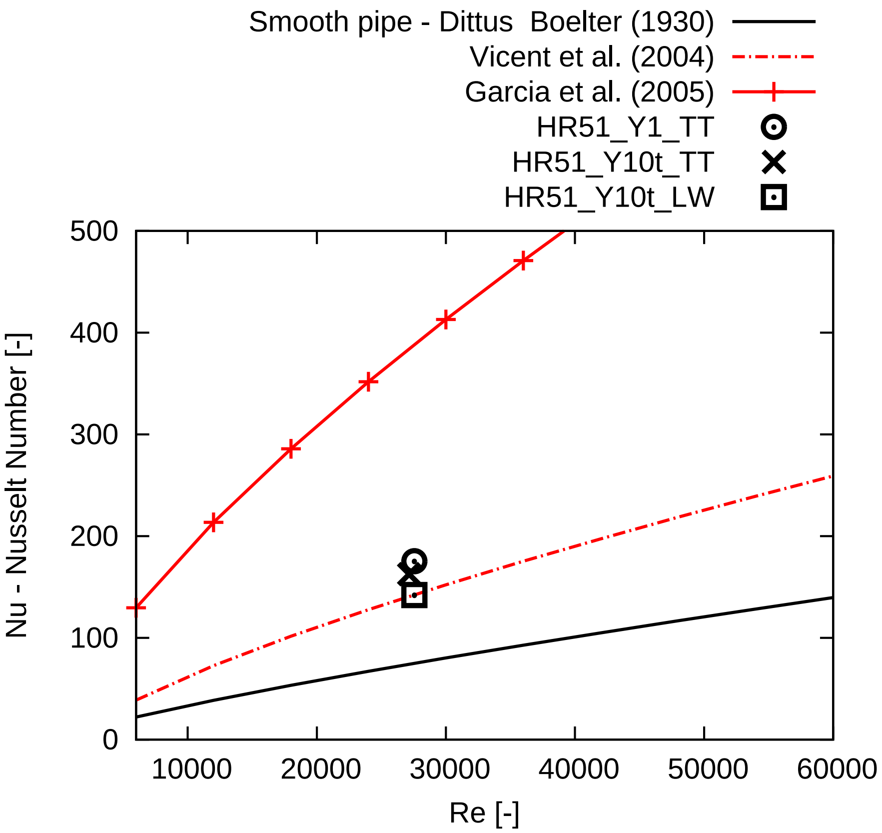

Figure 4.5.5: Global Nusselt number correlations versus Reynolds number of the ribbed tube R51 simulated by AVBP, compared to the correlation proposed by Vicent et al. (2004) [16] and Garcia et al. (2005) [123], and the Dittus-Boelter correlation for the smooth tube.

4.6 Conclusions

In this chapter, the non-reacting non-isothermal turbulent flow in both smooth (S51) and ribbed (R51) tubes has been investigated with the LES code AVBP. The comparisons with the isothermal flow in smooth and ribbed tubes respectively show that the heating condition has little impact on the flow dynamics. The impact of the mesh and the numerical scheme has also been evaluated on the thermal behavior. The reference case of smooth tube HS51_Y1_TT has been compared to theoretical/empirical results with some differences observed. The simulations of the heated smooth tube on coarser mesh ($y^+ \sim 10$) are in good agreement with the reference case HS51_Y1_TT in terms of the temperature profiles, despite the underprediction of the wall normal flux and the wall friction, that shows the possibility to use the coarse mesh for industrial application.

The methodology of using periodic configuration with a computational domain $L = p < D$ as in the previous chapter, combined with a source term S_{qdm} and a new source term S_e in the flow equations, a hybrid mesh Y1 having $y^+ = 1$ and the numerical scheme TTGC, has been taken again to conduct the reference case for the heated ribbed tube.

Comparisons between heated smooth and ribbed tubes show the impact of ribs on the thermal behavior, being a thicker thermal boundary layer, and enhanced heat transfer by a factor of 3. The results with different meshes and numerical schemes on R51 show that mesh Y10t fully on tetrahedra with scheme TTGC or LW can both well capture the thermal behavior of the turbulent flow, allowing to reduce significantly the computational cost.

Chapter 5

LES of reacting heated flow in ribbed and smooth tubes with ethane chemistry

Contents

In this chapter, reacting heated flow simulations are conducted in the academic configurations of both smooth (S51) and ribbed (R51) tubes. The ethane cracking process is studied, which involves an endothermic reactive system. An ethane chemical scheme provided by

Prof. Kevin Van Geem[1] [192] is implemented and tested in AVBP. To provide the heat flux required to maintain the temperature, the tubes are heated at a constant temperature of 1200 K.

An introduction of ethane chemistry is firstly given, followed by the numerical setting to conduct the reacting heated flow simulation in both smooth and ribbed tubes. At the end of this chapter, the impact of ribs on the ethane cracking process is investigated by comparison with the smooth tube results.

5.1 Ethane cracking chemistry

During the ethane cracking process, ethane decomposes into hydrogen and ethylene, as described by the global reaction:

$$C_2H_6 \rightarrow C_2H_4 + H_2 \tag{5.1.1}$$

In reality, this reaction proceeds via a number of radical reactions that include the following initiation and propagation steps [1]:

$$C_2H_6 \rightarrow CH_3 + CH_3 \tag{5.1.2}$$
$$CH_3 + C_2H_6 \rightarrow CH_4 + C_2H_5 \tag{5.1.3}$$
$$C_2H_5 \rightarrow C_2H_4 + H \tag{5.1.4}$$
$$H + C_2H_6 \rightarrow H_2 + C_2H_5 \tag{5.1.5}$$

The process is terminated by recombination reactions which form undesired products [1], e.g.,

$$H + C_2H_5 \rightarrow C_2H_6 \tag{5.1.6}$$
$$CH_3 + C_2H_5 \rightarrow C_3H_8 \tag{5.1.7}$$
$$C_2H_5 + C_2H_5 \rightarrow C_4H_{10}C_2H_4 + H \rightarrow C_2H_5 \tag{5.1.8}$$

As mentioned in Chapter 1, high temperature and low pressure conditions favor the olefin production, and the undesired reactions are better to be limited by controlling the residence time.

The reduced chemical kinetic scheme of the ethane steam cracking process used in this work contains 19 species and 32 irreversible reactions (the species name, the thermal database, and the description of the reactions are given in Appendix C). The initial composition of the gas mixture for the ethane cracking are 74.1% ethane C_2H_4 and 25.9% water H_2O (steam) in terms of mass fraction, and the main products are ethylene C_2H_4, hydrogen H_2 and methane CH_4 [193].

---

[1] Ghent University, Laboratory for Chemical Technology, Technologiepark 918 B-9052 Ghent, Belgium.

5.2 Ethane cracking in Perfectly Stirred Reactor

The Perfect Stirred Reactor (PSR) configurations is used to evaluate the reduced ethane chemistry scheme in three solvers: Cantera [194], Senkin [195] and AVBP. The PSR configuration is sketched in Fig. 5.2.1: at inlet, the initial composition of the mixture, the initial temperature and the initial pressure are set; after a given resident time τ, the final composition of the gas mixture, the temperature and the pressure are measured at outlet. The evolution of the mixture can be either at constant volume or constant pressure, an with either adiabatic or isothermal boundary conditions. Note that in the PSR configuration, the mixture is assumed perfectly homogeneous (i.e., species mix instantaneously), and no flow is present.

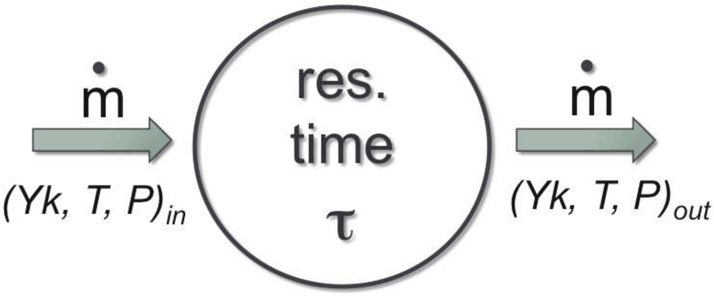

Figure 5.2.1: Illustration of a PSR configuration.

A series of test cases and their characteristics are given in Table. 5.2.1.

Solver		Constant volume	Constant pressure
SENKIN	Adiabatic	S-CV-A	S-CP-A
CANTERA	Adiabatic	C-CV-A	-
AVBP	Adiabatic	A-CV-A	-
	Isothermal	A-CV-I	-

Table 5.2.1: Summary of the PSR test cases of ethane chemistry in Senkin, Cantera and AVBP.

Only Senkin has the possibility to run constant pressure simulations, and only AVBP can impose isothermal boundary conditions. In the adiabatic cases, the temperature in PSR decreases due to the endothermic reactions, while the isothermal cases force the temperature to stay constant at 1200 K. The residence time is 0.5 s for all the PSR cases.

5.2.1 Impact of pressure variation on ethane chemistry

Two adiabatic PSR cases at constant volume (S-CV-A-T9P1) and constant pressure (S-CP-A-T9P1) were performed in the solver SENKIN, in order to investigate the impact of pressure variation, i.e., density variation, during the ethane cracking process. The operating points are listed in Table. 5.2.2:

Case	PSR	Inlet temperature [K]	Inlet pressure [atm]
S-CV-A-T9P1	Constant volume	973	1
S-CP-A-T9P1	Constant pressure		

Table 5.2.2: PSR tests of the ethane cracking of constant volume/pressure in Senkin.

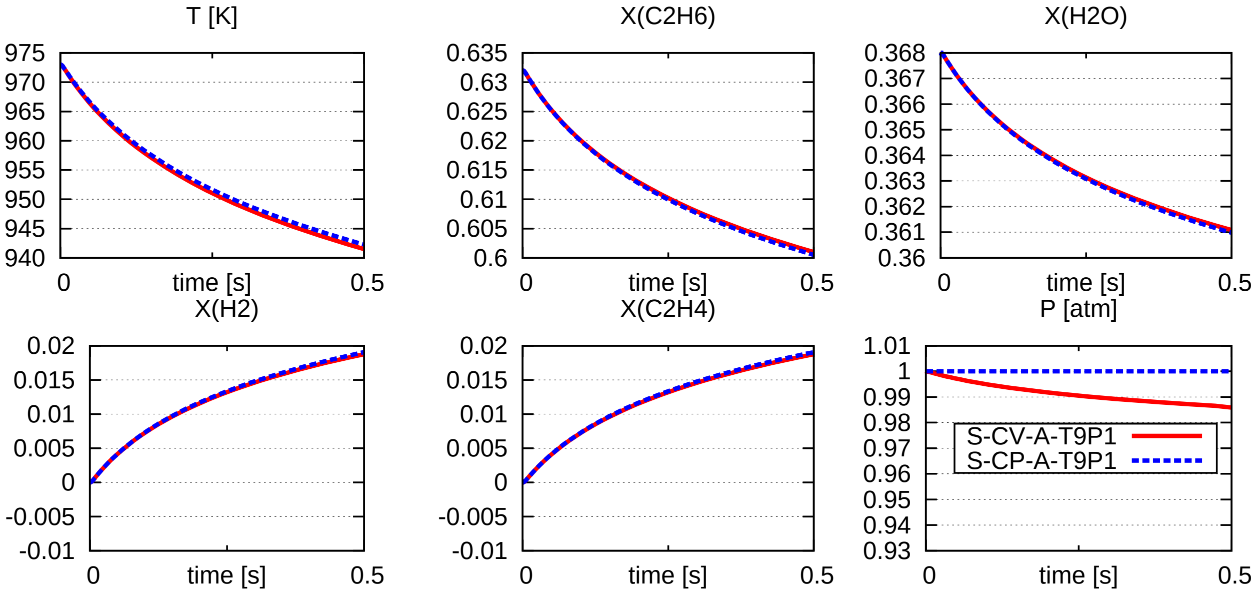

Figure 5.2.2: Temporal evolutions of the pressure, the temperature and the mole fractions of two reactants and two main products of the PSR cases for ethane cracking, with varying or constant pressure, obtained with Senkin.

The comparison between the two cases is shown in Fig. 5.2.2, plotting the temporal evolution of the temperature, the pressure, the mole fractions of the two reactants C_2H_6 and H_2O, and the mole fractions of two main products H_2 and C_2H_4. Very similar evolutions are found between these two cases with varying or constant pressure, showing that the influence of the pressure variation is negligible. In fact, the pressure dependence is not a key factor in the ethane steam cracking modeling, mentioned by Sabbe et al. (2011) [192]. For this reason, further simulations of the ethane steam cracking are all performed at constant volume.

5.2.2 Impact of initial pressure on ethane chemistry

Two adiabatic PSR cases at constant volume (C-CV-A-T9P1 and C-CV-A-T9P2), with an initial pressure fixed at 1 atm and 2 atm respectively, are realized in the solver Cantera, to investigate the impact of the initial pressure on the ethane cracking process. The residence time is 0.5 s, and the operating points are listed in Table. 5.2.3.

Case	PSR	Inlet temperature [K]	Inlet pressure [atm]
C-CV-A-T9P1	Constant volume	973	1
C-CV-A-T9P2			2

Table 5.2.3: PSR tests of the ethane cracking with different initial pressure in Cantera.

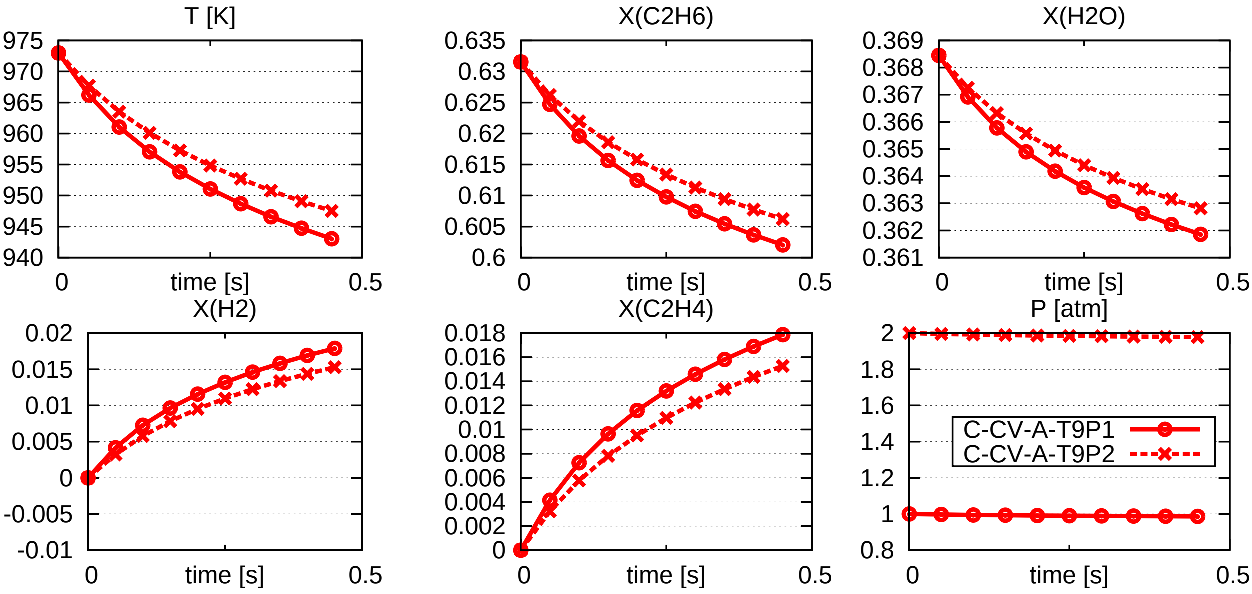

Figure 5.2.3: Temporal evolutions of the pressure, the temperature and the mole fractions of two reactants and two main products of the PSR cases for ethane cracking, with different initial pressure, obtained with Cantera.

Results are plotted in Fig. 5.2.3, showing that 1) As expected, the lower pressure favors reactions as faster consumption of C_2H_6 and production of C_2H_4 are observed; 2) the impact of the initial pressure is relatively small: when it increases by 100% from 1 atm to 2 atm, the conversion rate of ethane C_2H_6 decreases by 16%. In the real case, the initial pressure in ribbed tubes is about 15% higher (due to higher pressure loss), thus the impact on the conversion rate will be less than 1%. In the following cases, the initial pressure is always set at 1 atm.

5.2.3 Validation of the ethane chemistry in AVBP

Transport database

Schmidt number Sc for each species in the ethane cracking chemical scheme is obtained from Senkin and imposed in AVBP. To calculate the viscosity, the power law is used in AVBP:

$$\mu = \mu_0 \left(\frac{T}{T_0}\right)^b , \tag{5.2.1}$$

where the reference temperature has been chosen as 1200 K. The reference viscosity μ_0 is obtained in Cantera for the mixture of all species under $T_0 = 1200\,\mathrm{K}$, $P_0 = 1\,\mathrm{atm}$, which leads to a value of 3.29×10^{-5} kg/m/s. By calculating the viscosity of the initial gaseous mixture at various temperatures, the value of b in the power law is found to be 0.78. Note that the variation of composition during reactions are not taken into account in the calculation of μ.

PSR cases with AVBP

The adiabatic constant volume PSR cases conducted by Cantera, Senkin and AVBP in Table. 5.2.4 are now compared.

Case	Solver	Inlet temperature [K]	Inlet pressure [atm]
C-CV-A-T9P1	Cantera	973	1
S-CV-A-T9P1	Senkin		
A-CV-A-T9P1	AVBP		
C-CV-A-T12P1	Cantera	1200	
S-CV-A-T12P1	Senkin		
A-CV-A-T12P1	AVBP		
C-CV-A-T9P2	Cantera	973	2
A-CV-A-T9P2	AVBP		

Table 5.2.4: PSR test cases in Senkin.

For the cases with the inlet pressure at 1 atm, results are compared among the three solvers, for cases C/S/A-CV-A-T9P1, with the inlet temperature at 973 K (which is the bulk temperature of the flow in the tubes in the industrial application) in Fig. 5.2.4, and for cases C/S/A-CV-A-T12P1, with the inlet temperature at 1200 K, which is in the range of the wall temperature of the heating tubes in the real industrial application, in Fig. 5.2.5. Very similar evolutions are observed, with only a slight deviation observed on the evolution of the pressure in AVBP, which is negligible. Cases with the inlet pressure at 2 atm, namely C/A-CV-A-T9P2, are also compared in Fig. 5.2.6, where the cases C/A-CV-A-T9P1 are reported for comparison. The good agreement between AVBP and Cantera allows to conclude that the implementation of the ethane cracking reduced chemistry in AVBP is validated.

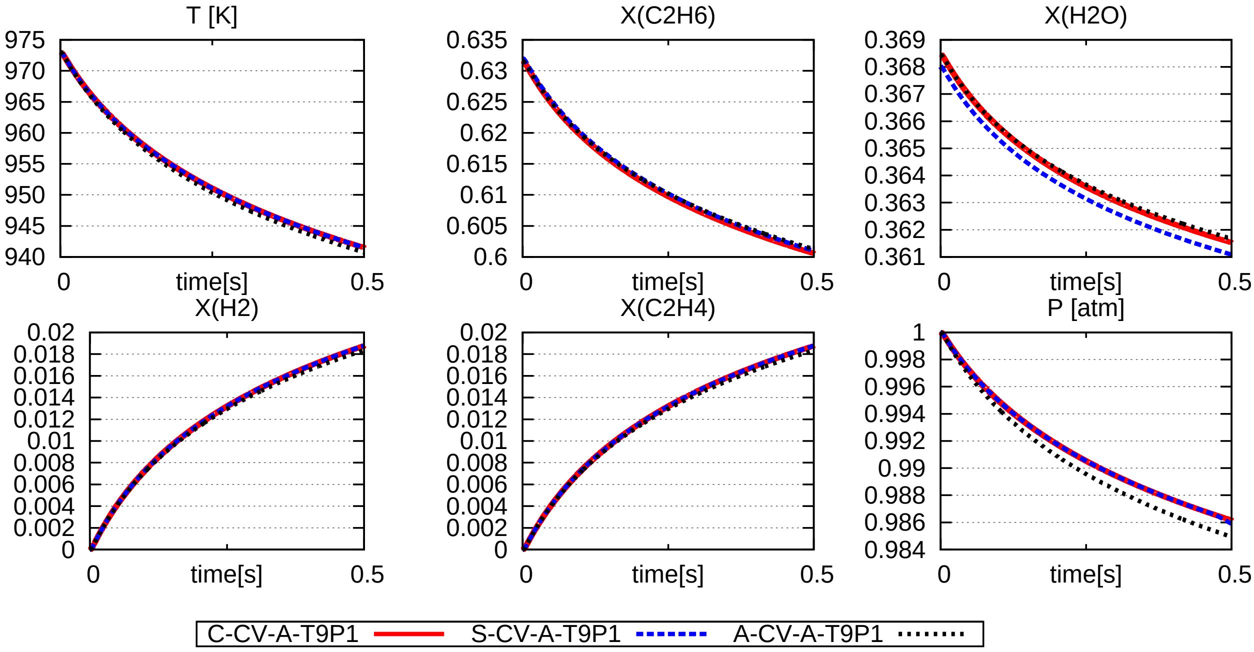

Figure 5.2.4: Cases C/S/A-CV-A-T9P1 by Cantera, Senkin and AVBP: inlet temperature at 973 K and inlet pressure at 1 atm.

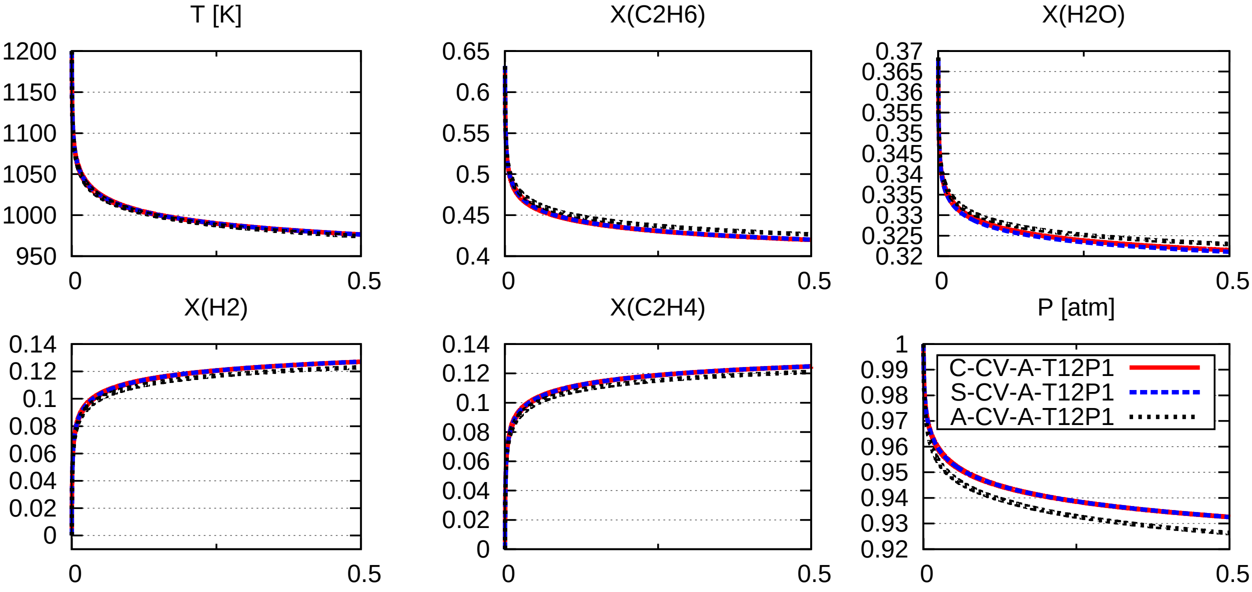

Figure 5.2.5: Cases C/S/A-CV-A-T12P1 by Cantera, Senkin and AVBP: inlet temperature at 1200 K and inlet pressure at 1 atm.

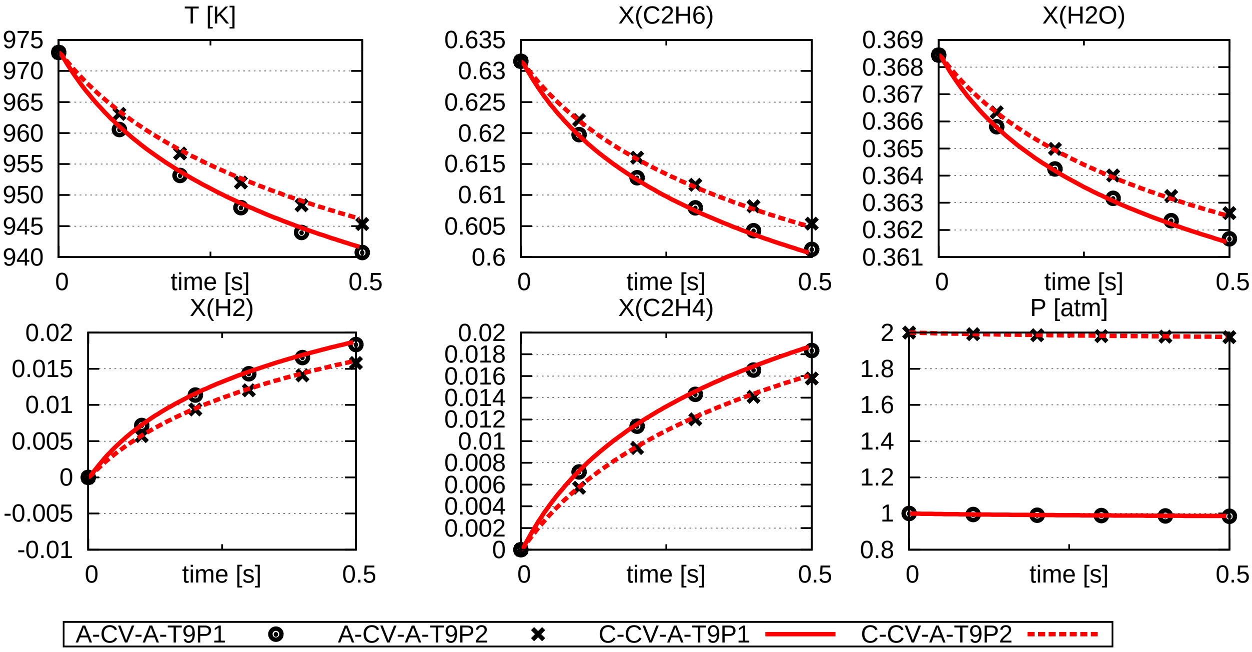

Figure 5.2.6: Cases C/A-CV-A-T9P2 by Cantera, Senkin and AVBP: inlet temperature at 973 K and inlet pressure at 1 atm/2 atm.

5.2.4 The zero mixing extreme cases

The zero mixing extreme cases (ZME) corresponds to an isothermal case at 1200 K (ZME-Isot), to mimic the limit case on the isothermal wall of the tubes (Fig. 5.2.7), and an adiabatic case with an initial temperature at 973 K (ZME-Ad), which represents the limit case at the center of the tubes where the heat flux is zero.

These two cases are calculated by AVBP for a residence time up to 1 s, and the operating

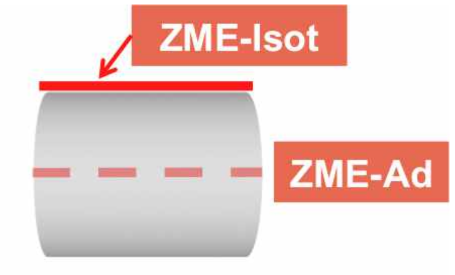

Figure 5.2.7: Illustration of the two zero mixing extreme conditions of ethane chemistry in tubes.

points are given in Table. 5.2.5:

Case	PSR	Inlet temperature [K]	Inlet pressure [atm]	Wall
ZME-Isot (A-CV-I-T12P1)	Constant	1200	1	Isothermal
ZME-Ad (A-CV-A-T9P1)	volume	973		Adiabatic

Table 5.2.5: Operating points of the two PSR zero mixing extreme cases.

The temporal evolutions of temperature, mole fractions of ethylene C_2H_4, and of the two reactants H_2O and C_2H_6 are shown in Fig. 5.2.8.

ZME-Isot consumes the reactant C_2H_6 very quickly at the beginning, while the mole fraction of product C_2H_4 reaches the maximum value (~ 0.255) at around 0.018 s, before decreasing due to undesirable reactions like Reaction 5.1.8. After 0.1s, the consumption of C_2H_6 slows down, and the mole fraction of C_2H_6 slowly tends to zero. Note that H_2O is not presented in the reactions in the ethane cracking scheme used here, so that any variation in mole fraction of H_2O is due to the change of number of moles, and consequently of mean molecular weight. For example, decreasing mole fraction of H_2O means an increase of number of moles, i.e., decreasing mean molecular weight when more lighter hydrocarbon are produced. For the case ZME-Isot, the mole fraction of H_2O first decreases rapidly, then increase slowly, correspondent to the variation of the total mole number when C_2H_4 is first produced then consumed according to Reaction 5.1.1.

On the other hand, in the case ZME-Ad, the reactant C_2H_6 is consumed very slowly due to the low temperature. The production of C_2H_4 keeps increasing and never reaches a maximum value during the computed residence time.

It is observed that these two limit cases are strongly different, and will help characterizing the cracking processes occurring in the heated tubes.

5.3 Numerical methodology of LES of the reacting heated flow in tubes S51 and R51

Fig. 5.3.1 illustrates the LES of the ethane cracking process in tubes. The gaseous mixture flow of reactants (C_2H_6 and H_2O) enters the tube, then is heated from the wall having a fixed temperature at 1200 K, to produce the desired hydrocarbons (C_2H_4 and other C_xH_y).

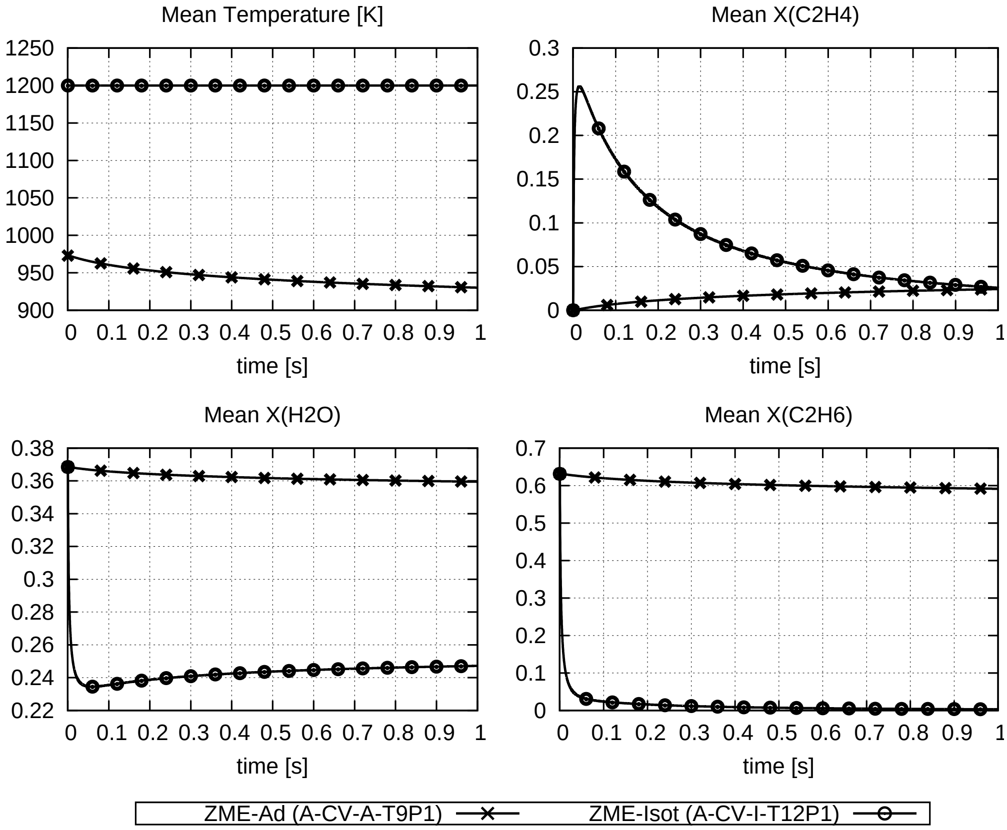

Figure 5.2.8: The temporal evolution of temperature, mole fraction of the main product ethylene C_2H_4, and of the two reactants H_2O and C_2H_6 of the two ZME lines.

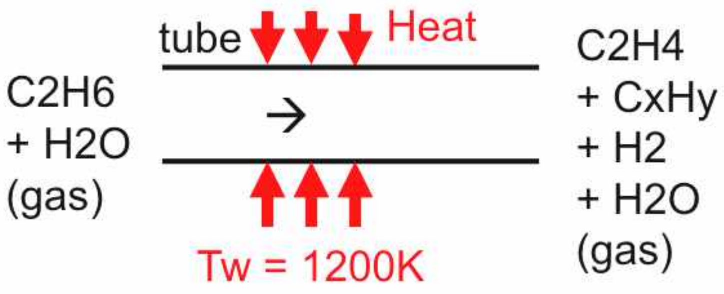

Figure 5.3.1: Sketch of the global process of reacting heated ethane flow in smooth/ribbed tubes.

5.3.1 Periodic configuration for unsteady regimes

By adding chemical reactions, the turbulent flow in the tube evolves from inlet to outlet. In the previous chapters where the isothermal and heated non-reacting flows were simulated in a steady regime, the periodic boundary conditions could be used thanks to volume source terms. In the present reacting case, the use of periodic configuration becomes not so straightforward and is explained below.

Imagine a simple steady flow in a tube of length 10 m where the temperature and the pressure increase from inlet to outlet. The evolution of the quantities are plotted along the distance *dist* in Fig. 5.3.2.

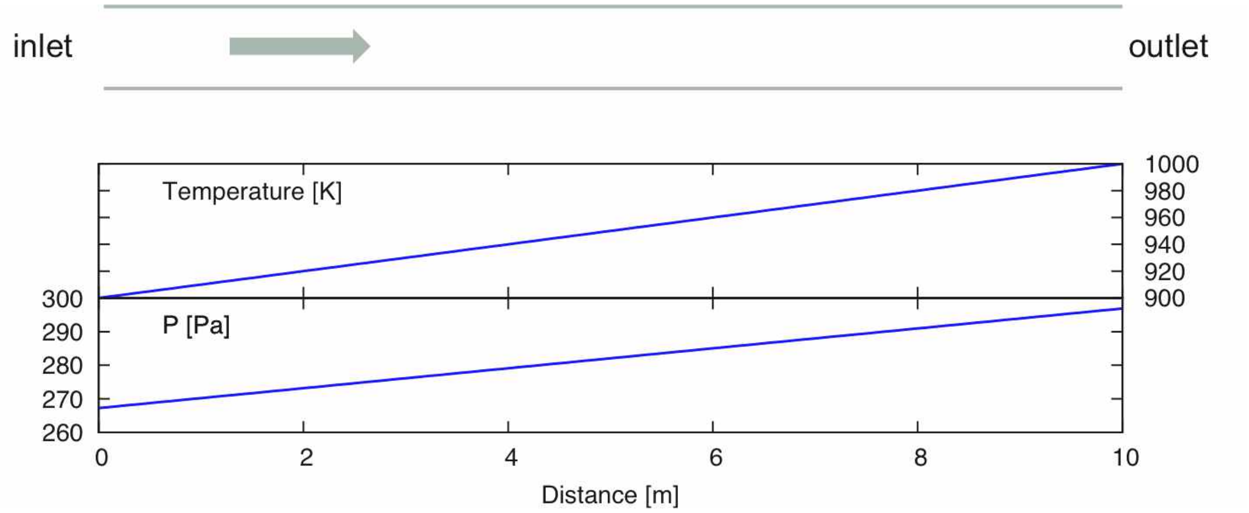

Figure 5.3.2: A simple tube flow with temperature and pressure variation along the axial distance.

This case can be converted into an unsteady flow in a periodic configuration as illustrated in Fig. 5.3.3. The periodic pattern is considered as running along the tube at the same velocity as the bulk velocity U_b of the flow, so that the spatial-averaged quantities (in this periodic configurations) vary with time. Time and distance are related as $dist = U_b t$ thus $T_{simulated}(t) = T_{real}(U_b t), P_{simulated}(t) = P_{real}(U_b t)$.

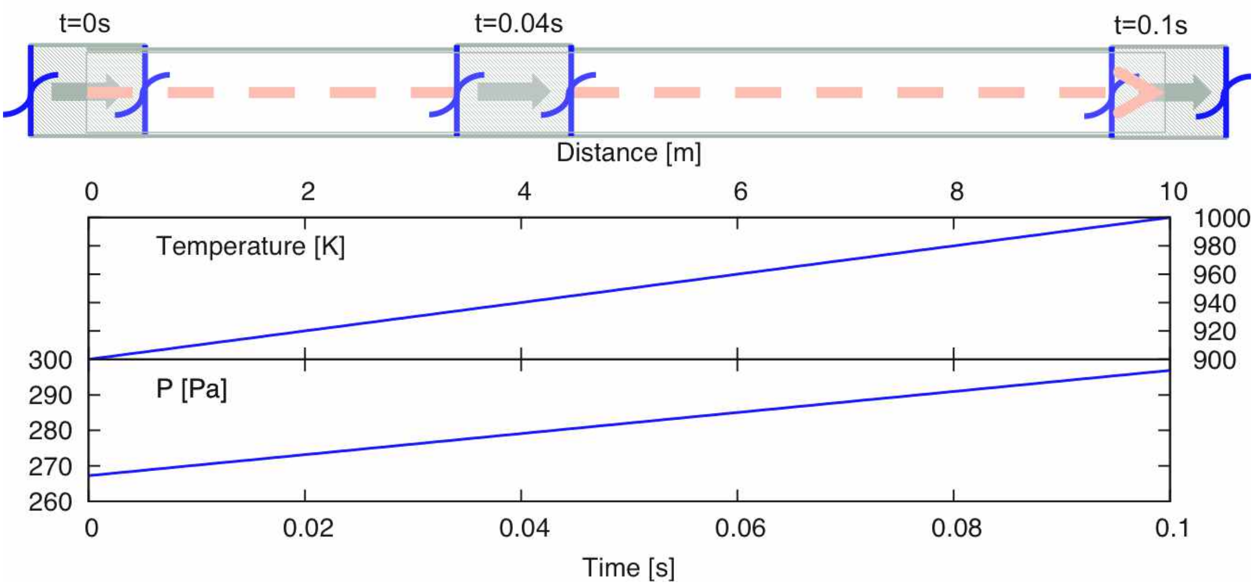

Figure 5.3.3: Unsteady flow in the periodic configuration: the temperature and pressure vary with time.

5.3.2 Numerical set-up and operating point

The configurations used for the reacting flow are the same as the ones of Chapter 3, the smooth tube S51 and the ribbed tube R51. The meshes are the Y10t ones, shown in

Fig. 3.2.2a for S51 and in Fig. 3.2.2b for R51. The numerical scheme TTGC is used.

The boundary condition at the wall is no-slip for the velocity and the wall temperature is set at 1200 K. Periodic conditions are applied at inlet and outlet, and a source term S_{qdm} is added in the N-S equations, to maintain the flow and reach the same Reynolds number 27 000 in both smooth and ribbed tubes. The initial flow is the same as in previous sections (74.1% C_2H_6 and 25.9% H_2O). The initial bulk temperature (i.e., the inlet temperature in the real tube) is 973 K and the initial bulk pressure (inlet pressure in the real tube) is equal to 1 atm. The initial fields of velocity and temperature are the steady solutions previously obtained with the non-reacting initial mixture (74.1% C_2H_6 and 25.9% H_2O).

The typical residence time for ethane cracking is 0.15 s (data from TOTAL). Here, the LES of S51 and R51 cases were running till 0.5 s and 0.23 s respectively, for that most phenomena are captured.

5.4 LES results of the reacting heated flow in tubes S51 and R51

5.4.1 Instantaneous and time-averaged axial velocity

Three instantaneous axial velocity fields, at 4 ms, 20 ms and 80 ms respectively, are chosen during the whole calculation time, as shown in Fig. 5.4.1. Stronger fluctuations are observed in the ribbed tube, helping flow mixing and heat transfer. The time-averaged fields are given in Fig. 5.4.2, where the recirculation zones in front of and behind the ribs and the acceleration on top of the ribs appear similarly to the non-reacting flows.

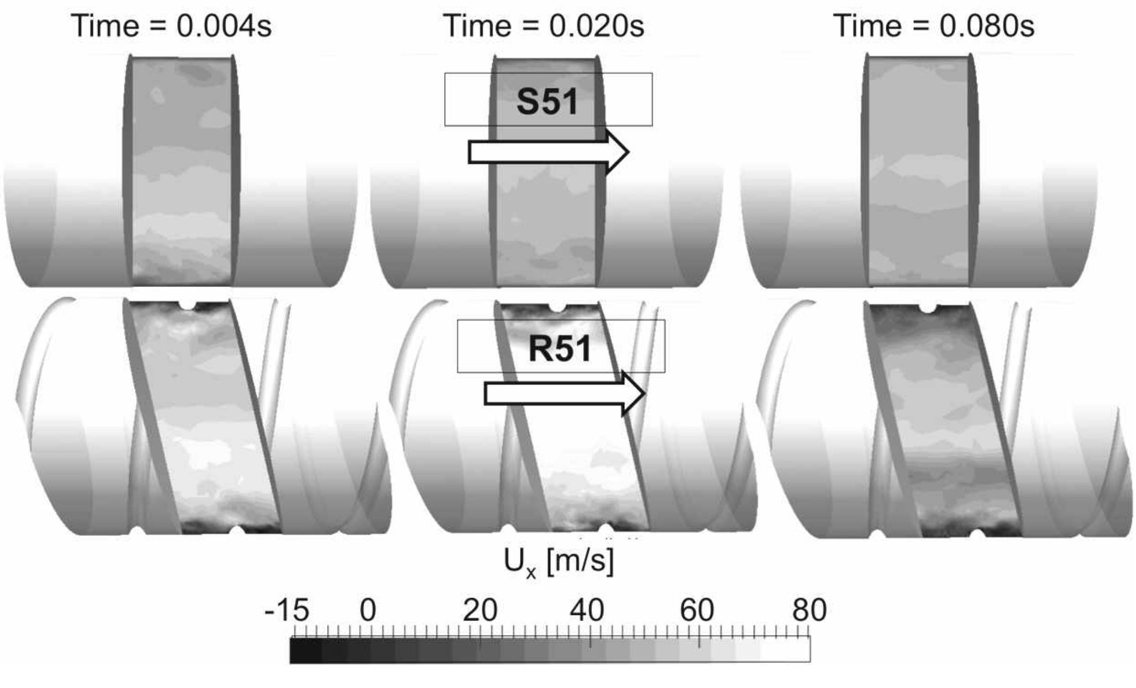

Figure 5.4.1: Three instantaneous axial velocity fields of the heated reacting flow in both smooth and ribbed tubes.

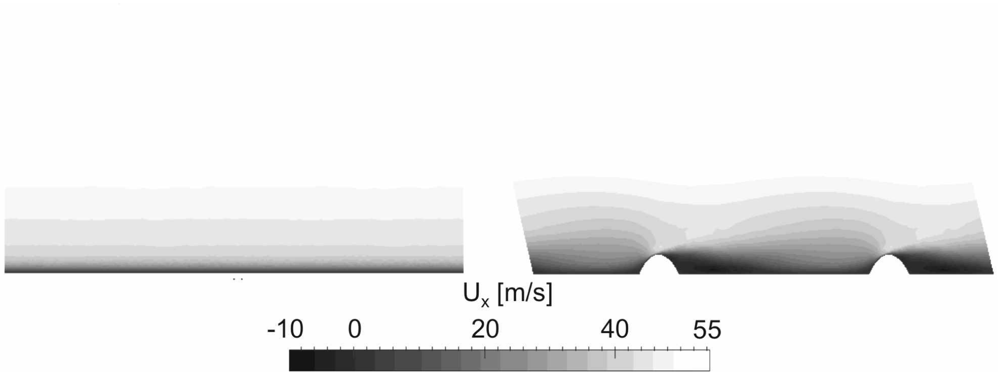

Figure 5.4.2: Time-averaged axial velocity field of the heated reacting flow in both smooth and ribbed tubes.

5.4.2 Instantaneous temperature

Three instantaneous temperature fields are shown in Fig. 5.4.3. As expected, the flow is heated faster in ribbed tube than in smooth tube. On the other hand, thicker thermal boundary layer and smoother temperature distribution in the radial direction are observed in the ribbed tube R51, thanks to the improved mixing due to the helical ribs. This agrees well with the results of heated non-reacting flow in Chapter 4. The more uniform radial profile of temperature will reduce the wall temperature and limit the coking.

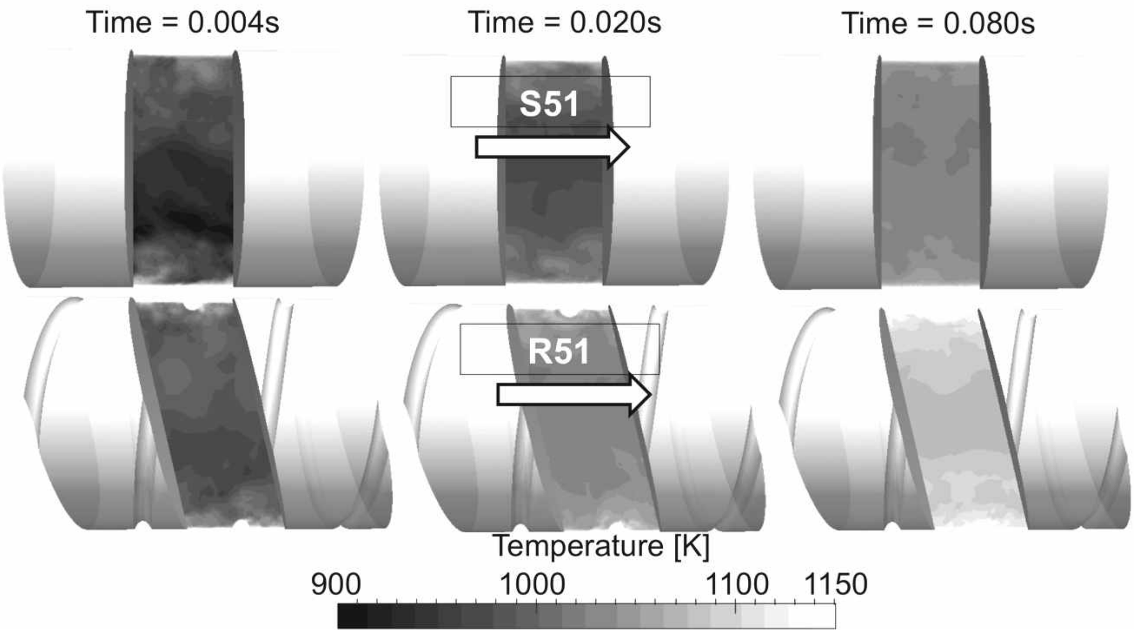

Figure 5.4.3: Three instantaneous temperature fields of the heated reacting flow in both smooth and ribbed tubes.

5.4.3 Instantaneous reaction rate

The reaction 1 described in Eq. 5.1.3 ($C_2H_6 \rightarrow CH_3 + CH_3$) is the main reaction of ethane cracking for producing the ethylene. Instantaneous fields of the reaction rate of this reaction are given in Fig. 5.4.4. Note that the scale of the reaction rate for the ribbed tube R51 is 10 times larger than for the smooth tube S51. The reaction rate and the temperature field have similar topology, as observed in Fig. 5.4.5, zooming in the near wall region of the solution at 80 ms, meaning that the reaction is mainly controlled by temperature. Highest reaction rate is found at the wall for both cases, and the global (i.e., volume integral) reaction rate

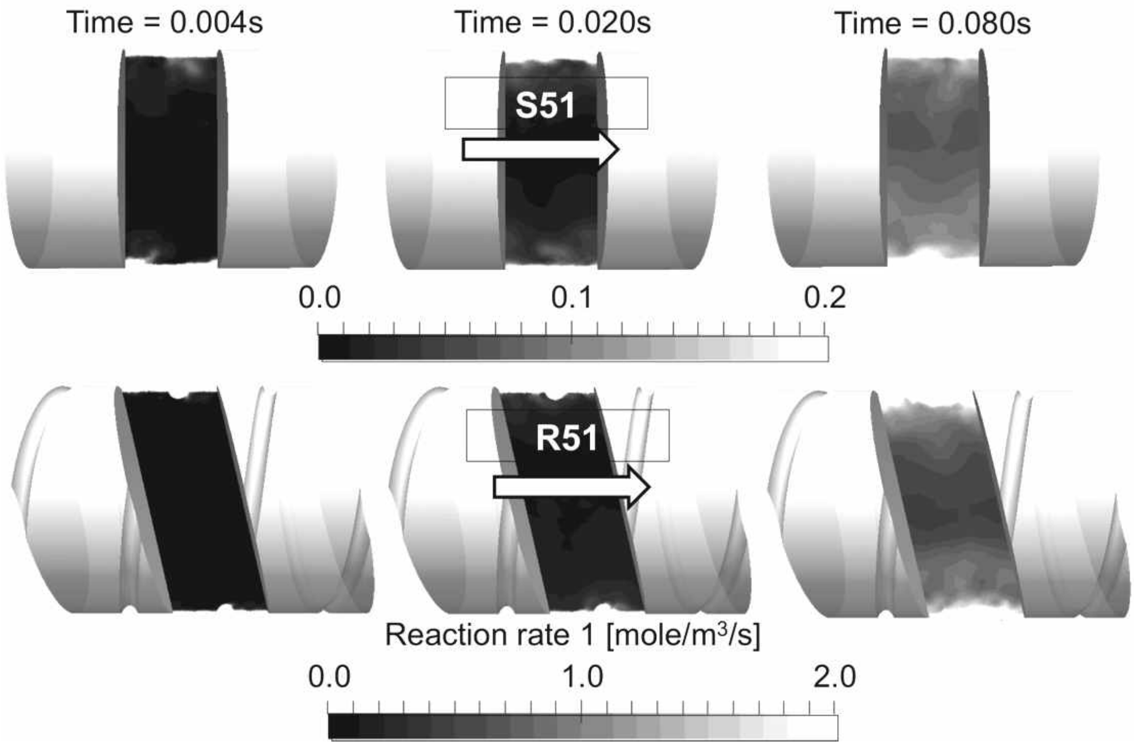

Figure 5.4.4: Three instantaneous reaction rate fields of the reaction $C_2H_6 \rightarrow CH_3 + CH_3$ of the heated reacting flow in both smooth and ribbed tubes.

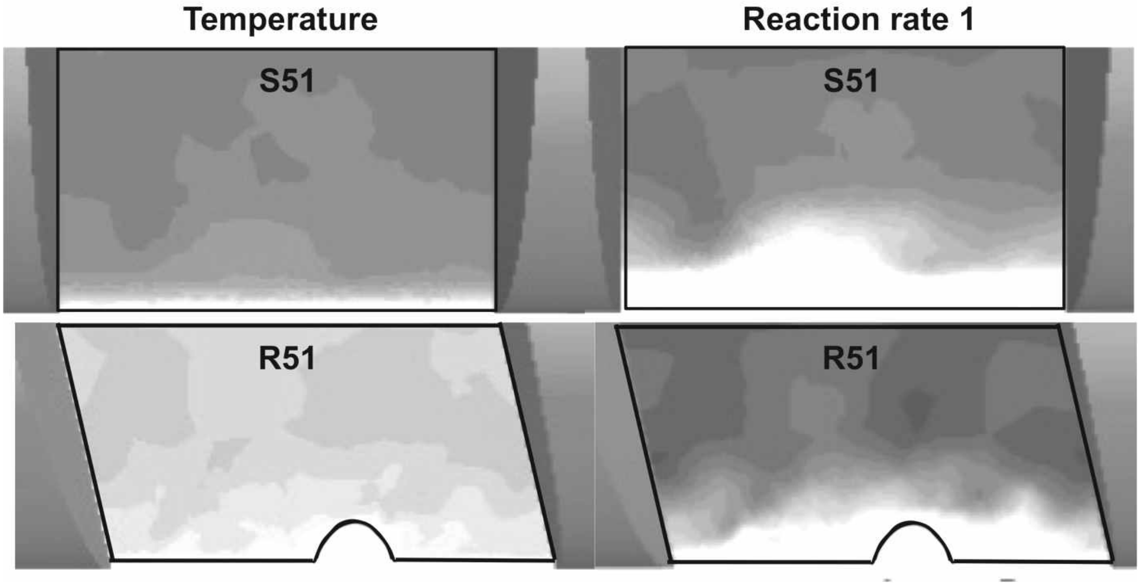

Figure 5.4.5: Temperature and reaction ($C_2H_6 \rightarrow CH_3 + CH_3$) rate fields in both smooth and ribbed tubes: zoom in the near wall region.

is greater in the ribbed tube R51.

5.4.4 Temporal evolution of spatially-averaged quantities

The temporal evolutions of spatially-averaged temperature, mole fraction of the product C_2H_4 and the two reactants H_2O and C_2H_6 are plotted in Fig. 5.4.6 for both smooth (S51) and ribbed (R51) tubes. In addition, the two ZME reference cases are also plotted for comparison.

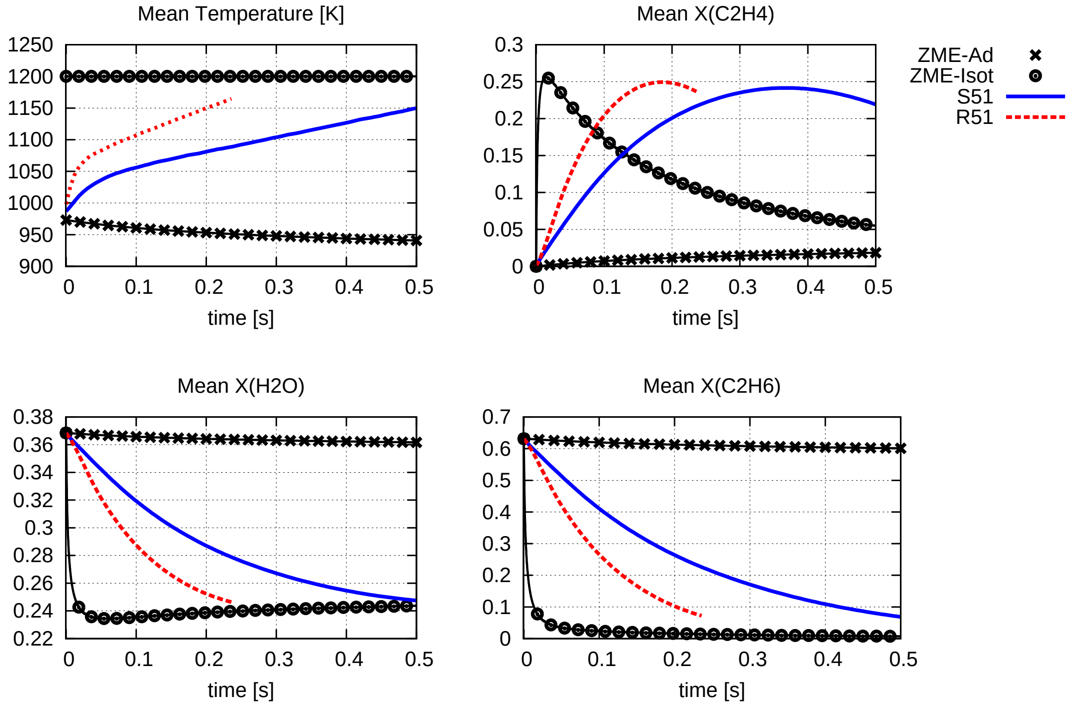

Figure 5.4.6: Temporal evolutions of spatially-averaged temperature, mole fraction of the product C_2H_4 and the two reactants H_2O and C_2H_6 for ethane cracking in both smooth and ribbed tubes.

The temperature in the ribbed tube increases more rapidly than in the smooth tube. Due to faster heating in the ribbed tube R51, higher reaction rate is observed during almost the whole resident time, as shown in Fig. 5.4.7. Thus ethane is consumed faster and the production of ethylene is faster. In both tubes, after a maximum value of ethylene has been reached, its consumption dominates due to undesirable reactions, and it slowly decreases. In the ribbed tube R51, the maximum value of the mole fraction of C_2H_4 is around 0.25 and occurs near 0.17 s, while in the smooth tube S51, the maximum value is slightly lower and occurs about 0.2 s later. The maximum value of C_2H_4 is close to the one of the ZME-Isot case, meaning that ZME-Isot corresponds to the limit maximum value of ethylene that the system can produce. From the global Reaction 5.1.1, and if 100% of ethane is converted into ethylene, the final mole fraction of ethylene would be 0.38: this ideal conversion rate is never reached.

After 0.15 s (the typical residence time in real case), a higher production of C_2H_4 is found in R51 than in S51, showing the advantages of the ribbed tube. The faster increase

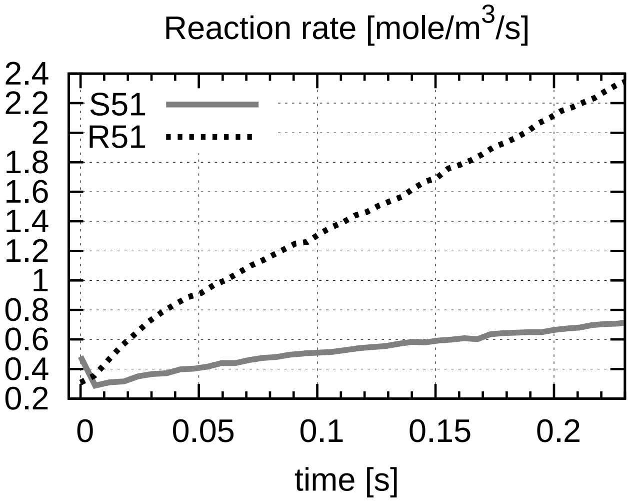

Figure 5.4.7: Spatially-averaged reaction rate for $C_2H_6 \rightarrow CH_3 + CH_3$ in both smooth (S51) and ribbed (R51) tubes.

of temperature in the ribbed tube is mainly due to stronger turbulence and better mixing, thus also resulting in stronger heat transfer. This mechanism is detailed in Section 5.4.6.

5.4.5 Impact of ribbed tube on ethane cracking

The dimensionless temperature Θ profiles are plotted in Fig. 5.4.8 from the instantaneous solution at 80 ms in both tubes S51 and R51. The bulk temperatures at 80 ms are 1042 K and 1091 K in the smooth and ribbed tube respectively. The radial distribution of temperature is

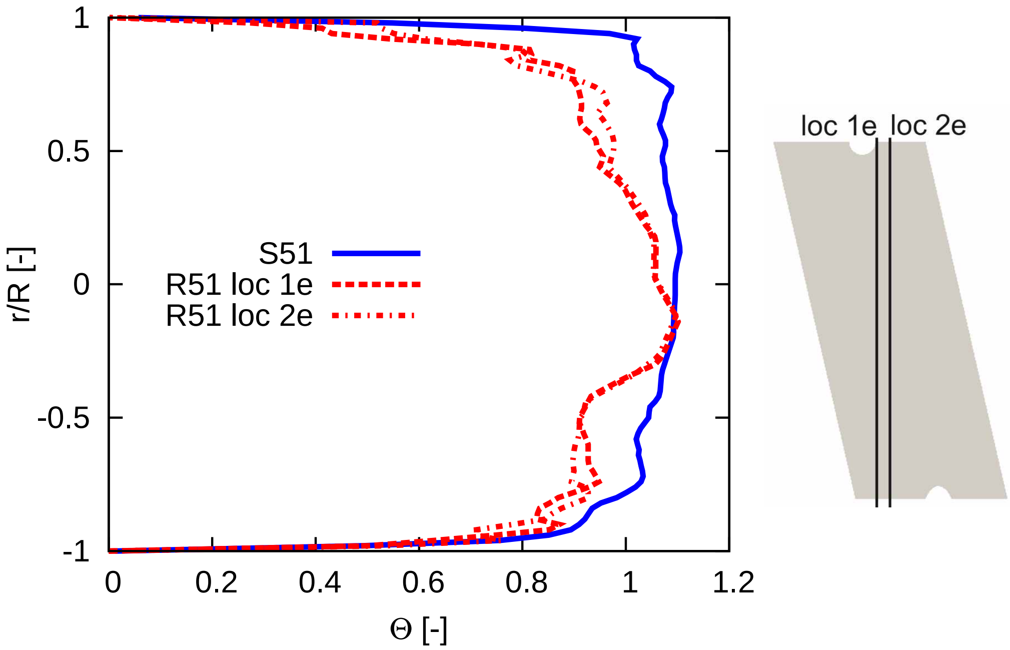

Figure 5.4.8: Dimensionless temperature profiles of the instantaneous solution at 80 ms in both smooth (S51) and ribbed (R51) tubes.

more homogeneous in the ribbed tube R51 thanks to the better mixing, leading to a thicker thermal boundary layer, thus favoring the desired reactions even towards the tube center.

Fig. 5.4.9 shows the relations between the averaged reaction rate of $C_2H_6 \rightarrow CH_3 + CH_3$, the temperature and the mass fraction of the reactant C_2H_6. These relations are very different in smooth tube S51 and ribbed tube R51. As shown in Fig. 5.4.9a, the reaction rate in ribbed tube R51 is higher than in smooth tube S51 for the same temperature, except in the range 1020 K to 1050 K. This phenomenon can be explained by the higher mass fraction of C_2H_6 in ribbed tube for the whole range of temperature, as observed in Fig. 5.4.9b, since higher concentration of a reactant leads to higher reaction rate. However, the temperature is the dominant factor in the range 1020 K to 1050 K and the reaction rate as function of temperature is the same. For the same value of mass fraction of C_2H_6, the reaction rate $C_2H_6 \rightarrow CH_3 + CH_3$ is always higher in the ribbed tube (Fig. 5.4.9c) due to higher temperature.

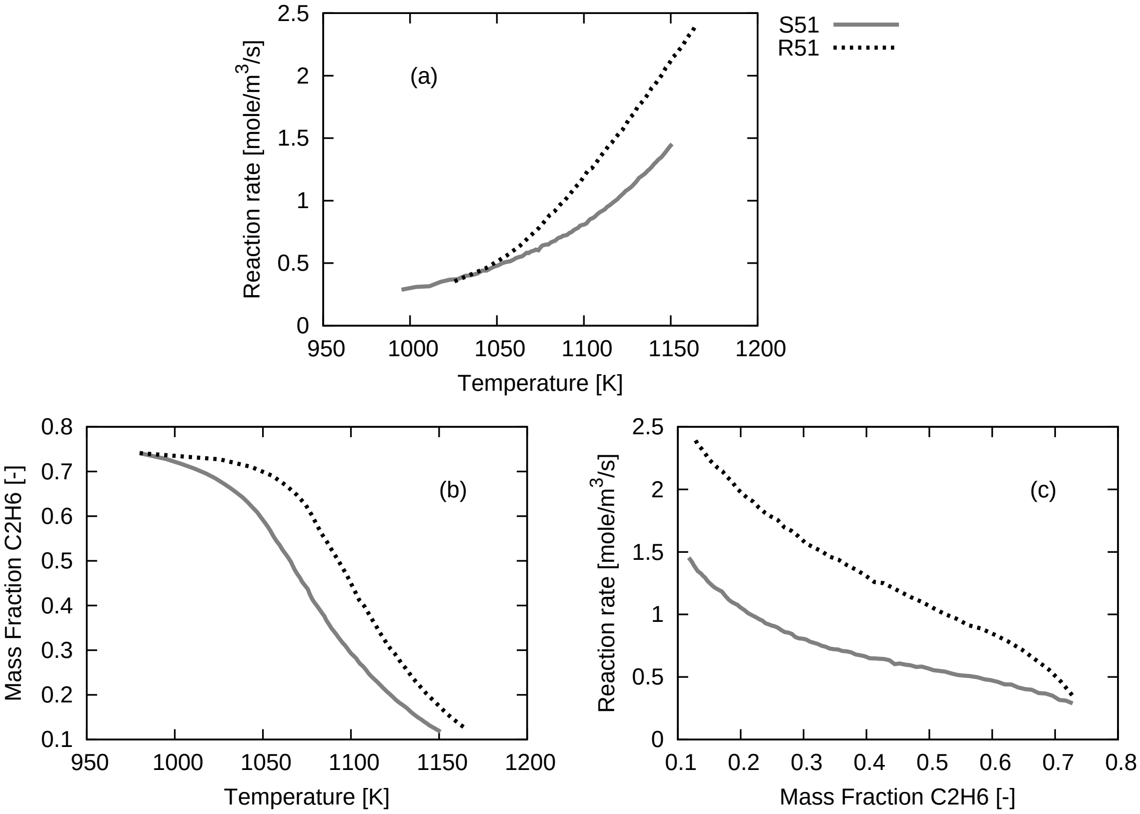

Figure 5.4.9: Relations between the reaction rate of $C_2H_6 \rightarrow CH_3 + CH_3$, the temperature and the mass fraction of the reactant C_2H_6 in both smooth (S51) and ribbed (R51) tubes.

These results demonstrate that the better performance of the ribbed tube is due to a contribution of different effects, and not simply owing to the stronger heat transfer.

5.4.6 Ethane - temperature correlation

Investigations on the distribution of the ethane versus temperature show the different behavior of the reacting flow in both smooth (S51) and ribbed (R51) tubes. The quantities at two points in the tubes are investigated: at the center of the tube and at a point at 1/4 radius ($r = 1/4R$).

Distribution of the ethane versus temperature at the center of the tubes

The quantities are investigated at a central point as illustrated in Fig. 5.4.10.

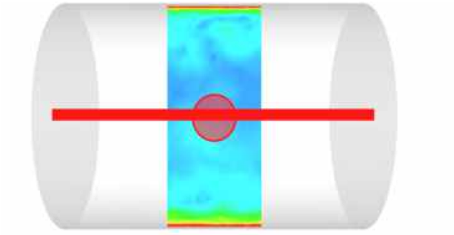

Figure 5.4.10: The tube center where the quantities are investigated.

The evolution of mass fraction of ethane with temperature in Fig. 5.4.11 shows a tendency very similar to the spatial-averaged values in Fig. 5.4.9b. Higher temperature and more dispersion are observed in the ribbed tube R51, due to better mixing. The temperature range is 1.5 times larger at $Y(C_2H_6) = 0.5$, and the ethane mass fraction is 2 times larger at $T = 1100\,\mathrm{K}$.

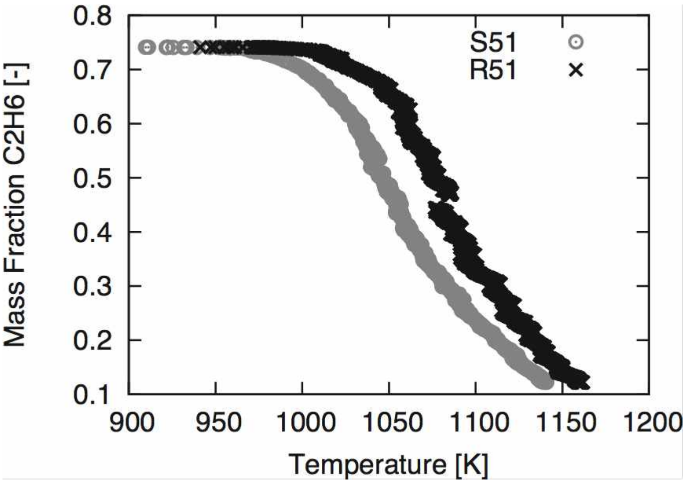

Figure 5.4.11: Evolution of mass fraction of ethane *vs* the temperature at the center of both smooth (S51) and ribbed (R51) tubes.

To understand this result, the temporal velocity evolutions are shown in Fig. 5.4.12 for the axial, radial and azimuthal directions respectively. The temporally-averaged radial and azimuthal velocities are both zero at this location in smooth and ribbed tubes, and the mean axial velocity is slightly higher in R51. The velocity fluctuations in R51 in the three directions are 3 times stronger than in S51, which explain the stronger dispersion behavior in Fig. 5.4.11.

Distribution of the ethane versus temperature at 1/4 radius

Another point in Fig. 5.4.13 at 1/4 radius is chosen to investigate the quantities.

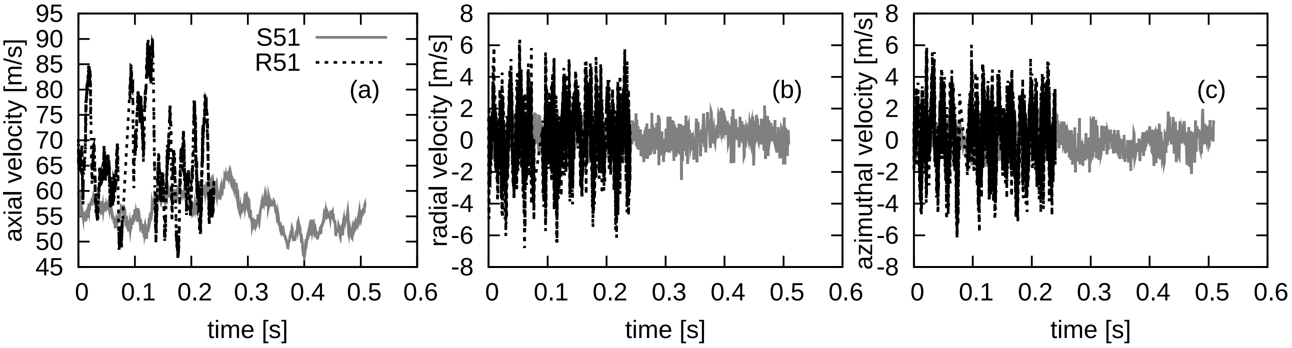

Figure 5.4.12: Temporal evolution of velocities at the center of both smooth (S51) and ribbed (R51) tubes: (a) axial velocity; (b) radial velocity; (c) azimuthal velocity.

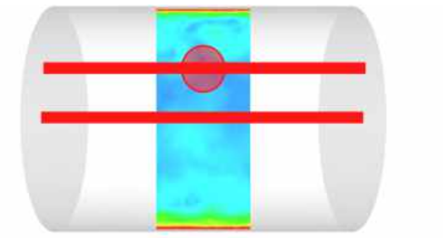

Figure 5.4.13: Location at 1/4 radius where the quantities are investigated.

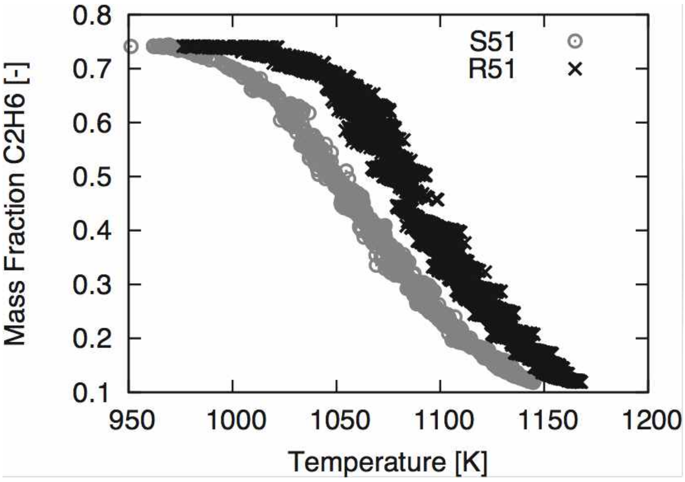

Figure 5.4.14: Evolution of mass fraction of ethane *vs* the temperature at 1/4 radius of both smooth (S51) and ribbed (R51) tubes.

Again, the evolution of mass fraction of ethane with temperature in Fig. 5.4.14 behaves very similarly to the spatial-averaged values in Fig. 5.4.9b. The range of temperature at a certain value of $Y(C_2H_6)$ at this 1/4 radius point is 2 times larger than at the central point in both S51 and R51 tubes, and so is $Y(C_2H_6)$, due to stronger fluctuations of the turbulent flow, as shown by comparing Fig. 5.4.15 to Fig. 5.4.12 (about 1.5 times stronger at the 1/4 radius point than at the central point). Stronger dispersion in the ribbed tube R51 is still observed. In addition, the azimuthal velocity is no longer equal to zero in the ribbed tube, which undoubtedly enforces the mixing effect.

To summarize, stronger dispersion and velocity fluctuations in the ribbed tube R51 than in the smooth tube S51 are always observed.

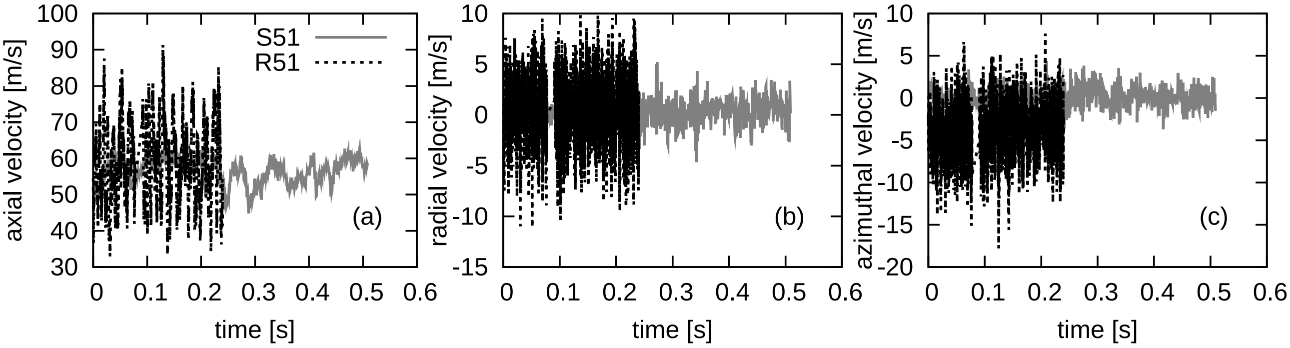

Figure 5.4.15: Temporal evolution of velocities at 1/4 radius of both smooth (S51) and ribbed (R51) tubes: (a) axial velocity; (b) radial velocity; (c) azimuthal velocity.

5.5 Conclusions

In this chapter, ethane cracking chemistry has been implemented in the code AVBP and validated against 0D PSR calculations, obtained with Cantera and Senkin. Simulations of ethane cracking within the configurations S51 and R51 showed better performance of the ribbed tube R51 on ethylene production, thanks to the stronger heat transfer, turbulent fluctuations and mixing.

Chapter 6

Industrial application: LES of reacting heated flow in ribbed and smooth tubes with butane chemistry

Contents

In this chapter, reacting heated flow simulations are conducted in the industrial configuration of ribbed tube R38, and is compared to the smooth tube S38 having the same diameter. For this application, butane thermal cracking process is considered, corresponding to an endothermic reactive system as for ethane cracking. A butane chemistry scheme provided by Prof. Kevin Van Geem[1] is implemented and tested in the code AVBP. The

---

[1] Ghent University, Laboratory for Chemical Technology, Technologiepark 918 B-9052 Ghent, Belgium.

boundary conditions and the source terms added in the flow equations are set according to the measurements in the real industrial case.

An introduction on butane cracking chemistry is first given, followed by the numerical set-up to conduct the reacting heated flow simulations in both smooth (S38) and ribbed (R38) tubes. At the end of this chapter, results in both tubes are investigated and compared.

6.1 Chemical kinetics scheme of butane steam cracking process

The reduced chemical scheme for butane steam-cracking process contains 20 species and 149 reversible reactions (the file which contains the species name, the thermal database, and the description of the reactions can be found in Appendix D). The 20 species are given in Table. 6.1.1 with their names and formula as used in Chemkin (i.e., in the original chemical scheme) and in AVBP (names were rewritten to be accepted by AVBP).

Species name	**hydrogen**	**methane**	**ethylene**	**ethane**	**propylene**
Chemkin	H_2	CH_4(11)	C_2H_4(10)	C_2H_6(8)	C_3H_6(15)
AVBP	H_2	CH_4	C_2H_4	C_2H_6	C_3H_6
Species name	**propane**	**1-butene**	**2-butene**	**1,3-butadiene**	**butane**
Chemkin	C_3H_8(12)	C_4H_8(28)	C_4H_8(29)	C_4H_6(173)	C_4H_{10}(1)
AVBP	C_3H_8	$a1C_4H_8$	$a2C_4H_8$	C_4H_6	C_4H_{10}
Species name	**hydro**	**methyl**	**ethyl**	**n-propyl**	**Isopropyl**
Chemkin	HJ(5)	CH_3J(2)	C_2H_5J(6)	C_3H_7J(3)	C_3H_7J(18)
AVBP	H	CH_3	C_2H_5	$a1C_3H_7$	$a2C_3H_7$
Species name	**sec-Butyl**	**n-butyl**	**t1-Methylallyl**	**t3-Butene-1-yl**	**water**
Chemkin	C_4H_9J(7)	C_4H_9J(4)	C_4H_7J(99)	C_4H_7J(136)	H_2O
AVBP	$a1C_4H_9$	$a2C_4H_9$	$a1C_4H_7$	$a2C_4H_7$	H_2O

Table 6.1.1: The 20 species in the reduced chemical scheme for butane steam cracking process.

The initial components of the gas mixture for butane cracking are butane C_4H_{10} and water H_2O (steam). The main products are ethylene C_2H_4, propylene C_3H_6, and methane CH_4.

6.1.1 Validation in Cantera and Senkin

The PSR (perfect stirred reactor) tests are conducted with this reduced chemistry scheme in Cantera and Senkin respectively. Note that they both use the same database as in Chemkin. The illustration of a PSR test was shown in Fig. 5.2.1 of the previous chapter.

The initial conditions for the PSR tests in Cantera and Senkin are given in Table. 6.1.2.

The PSR test in Cantera is a constant-volume adiabatic case, while constant-pressure adiabatic case is performed in Senkin.

Solver	PSR	Mixture		T [K]	Pressure
		Mole fraction	Mass fraction		
Cantera	Cst-Volume	40.8% C_4H_{10}	69.0% C_4H_{10}	1100	218 690 Pa (2.1583 atm)
Senkin	Cst-Pressure	59.2% H_2O	31.0% H_2O		

Table 6.1.2: Initial conditions for PSR cases tested in Cantera and Senkin

The residence time is chosen to be 0.15 s, which is close to the real residence time of the butane/steam gaseous mixture going through the tubes in the cracking furnace.

Fig. 6.1.1 and 6.1.2 show the temporal evolutions of the pressure, the temperature and the mole fractions of all the 20 species calculated by Cantera and by Senkin.

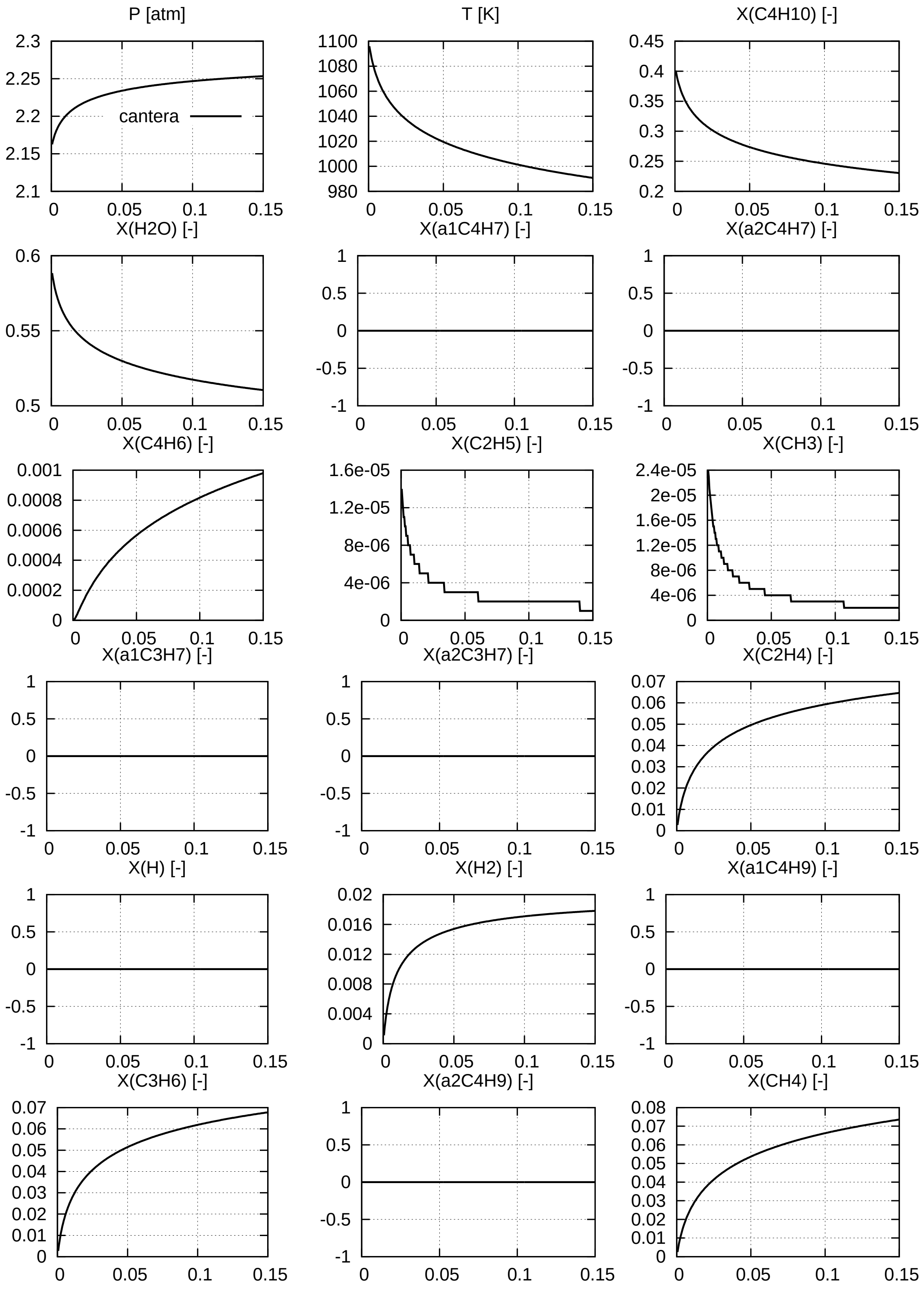
P [atm]
2.3
2.25
2.2
2.15
2.1
cantera
T [K]
1100
1080
1060
1040
1020
1000
980
X(C4H10) [-]
0.45
0.4
0.35
0.3
0.25
0.2
X(H2O) [-]
0.6
0.55
0.5
X(a1C4H7) [-]
X(a2C4H7) [-]
1
0.5
0
-0.5
-1
X(C4H6) [-]
0.001
0.0008
0.0006
0.0004
0.0002
0
X(C2H5) [-]
1.6e-05
1.2e-05
8e-06
4e-06
0
X(CH3) [-]
2.4e-05
2e-05
1.6e-05
1.2e-05
8e-06
4e-06
0
X(a1C3H7) [-]
X(a2C3H7) [-]
X(C2H4) [-]
0.07
0.06
0.05
0.04
0.03
0.02
0.01
0
X(H) [-]
X(H2) [-]
0.02
0.016
0.012
0.008
0.004
0
X(a1C4H9) [-]
X(C3H6) [-]
0.07
0.06
0.05
0.04
0.03
0.02
0.01
0
X(a2C4H9) [-]
X(CH4) [-]
0.08
0.07
0.06
0.05
0.04
0.03
0.02
0.01
0
0
0.05
0.1
0.15

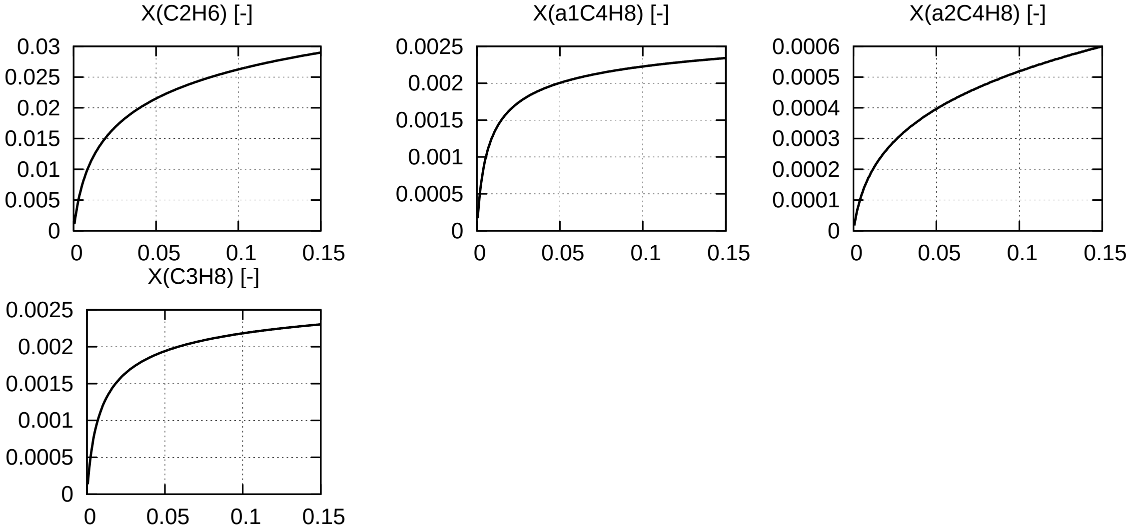

Figure 6.1.1: Temporal evolutions of the pressure, the temperature and the mole fractions of all the 20 species of the PSR case in Cantera (x-axis is time [s]).

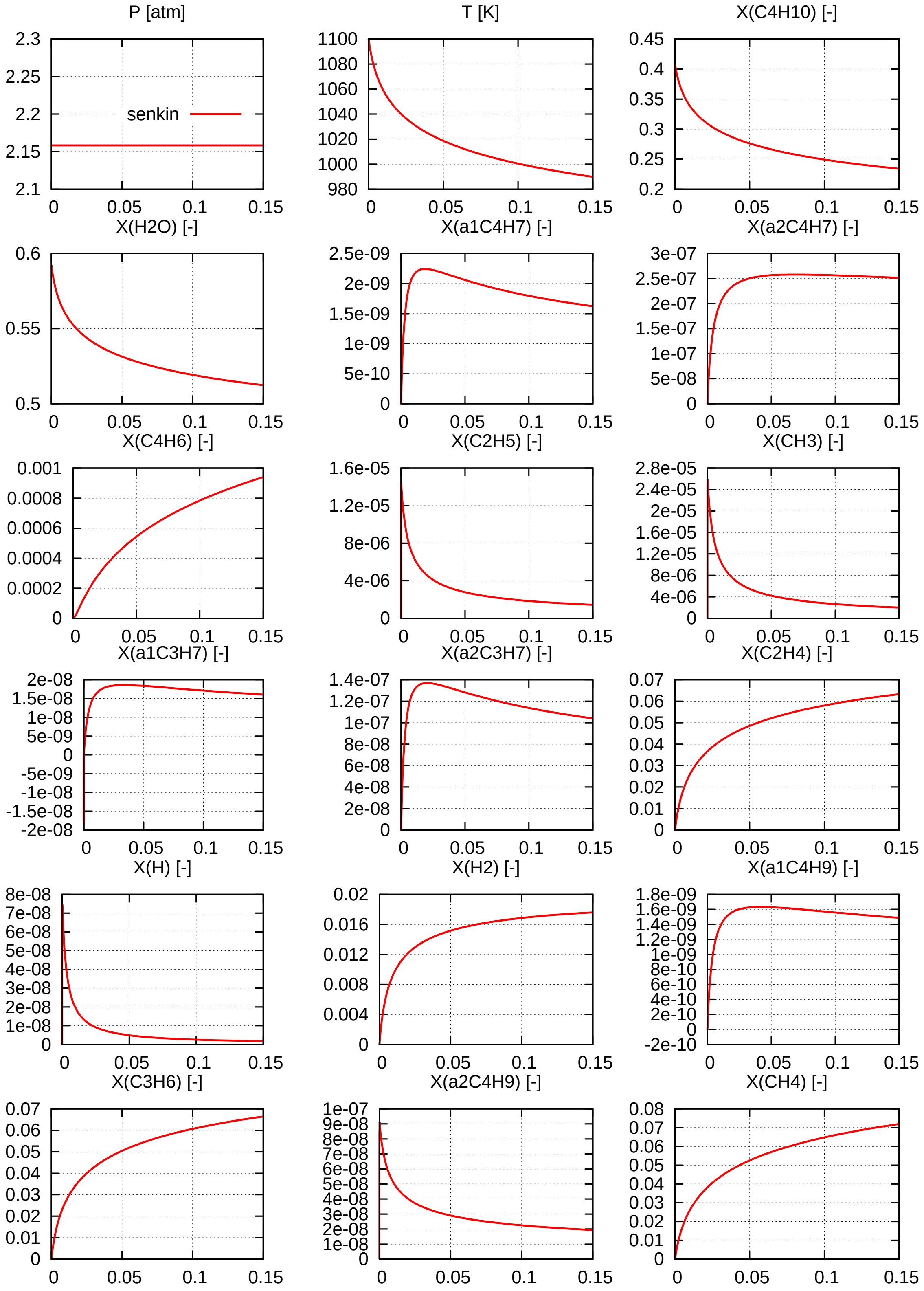
P [atm]
2.3
2.25
2.2
2.15
2.1
senkin
T [K]
1100
1080
1060
1040
1020
1000
980
X(C4H10) [-]
0.45
0.4
0.35
0.3
0.25
0.2
X(H2O) [-]
0.6
0.55
0.5
X(a1C4H7) [-]
2.5e-09
2e-09
1.5e-09
1e-09
5e-10
X(a2C4H7) [-]
3e-07
2.5e-07
2e-07
1.5e-07
1e-07
5e-08
X(C4H6) [-]
0.001
0.0008
0.0006
0.0004
0.0002
X(C2H5) [-]
1.6e-05
1.2e-05
8e-06
4e-06
X(CH3) [-]
2.8e-05
2.4e-05
2e-05
1.6e-05
1.2e-05
8e-06
4e-06
X(a1C3H7) [-]
2e-08
1.5e-08
1e-08
5e-09
-5e-09
-1e-08
-1.5e-08
-2e-08
X(a2C3H7) [-]
1.4e-07
1.2e-07
1e-07
8e-08
6e-08
4e-08
2e-08
X(C2H4) [-]
0.07
0.06
0.05
0.04
0.03
0.02
0.01
X(H) [-]
8e-08
7e-08
6e-08
5e-08
4e-08
3e-08
2e-08
1e-08
X(H2) [-]
0.02
0.016
0.012
0.008
0.004
X(a1C4H9) [-]
1.8e-09
1.6e-09
1.4e-09
1.2e-09
1e-09
8e-10
6e-10
4e-10
2e-10
-2e-10
X(C3H6) [-]
0.07
0.06
0.05
0.04
0.03
0.02
0.01
X(a2C4H9) [-]
1e-07
9e-08
8e-08
7e-08
6e-08
5e-08
4e-08
3e-08
2e-08
1e-08
X(CH4) [-]
0.08
0.07
0.06
0.05
0.04
0.03
0.02
0.01
0
0.05
0.1
0.15

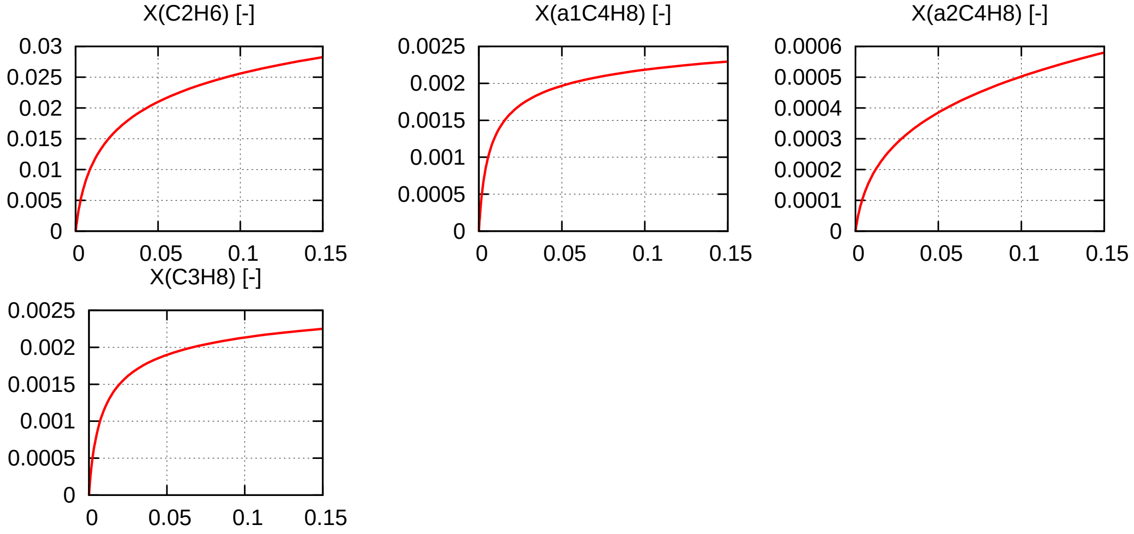

Figure 6.1.2: Temporal evolutions of the pressure, the temperature and the mole fractions of all the 20 species of the PSR case in Senkin (x-axis is time [s]).

It is observed that for both cases, the temperature decreases because the system of the 149 reversible reactions is globally endothermic. For the constant-volume case, the pressure increases. Considering the classical ideal gas law $P = \rho r T$, where $r = R/W$ is the specific gas constant defined as the ratio of the molar gas constant over the molar mass (W=total mass/total molar number) of the gas mixture, the combination of the increasing pressure and the decreasing temperature will lead to an increase of r, meaning that the total molar number of the gas mixture increases.

Comparing with the other species at the end of 0.15 s, the ethylene C_2H_4, propylene C_3H_6 and methane CH_4 are shown to be the main components of the production. To facilitate further comparisons, only the pressure, the temperature, the reactant butane C_4H_{10} and the three main products will be investigated.

6.1.2 Implementation of the butane chemistry in AVBP

Thermal and transport database

The settings of the thermodynamic database in AVBP is explained in Appendix E.

Same as in ethane cracking, Schmidt numbers Sc for the 20 species in the butane cracking chemical scheme are obtained from Senkin and imposed in AVBP. To calculate the viscosity, the reference temperature in the power law (Eq. 5.2.1) is chosen as 909.15 K, which is the initial temperature in the butane cracking process. The reference viscosity μ_0 is obtained from Cantera for the mixture of 20 species under $T_0 = 909.15\,\mathrm{K}$, $P_0 = 218.69\,\mathrm{kPa}$, which leads to a value of 2.38×10^{-5} kg/m/s. By calculating the viscosity of the initial gaseous mixture at temperatures 900 K, 905 K and 909.15 K, the value of b in the power law is found to be 0.88. Again, the variation of composition during reactions are not taken into account in the calculation of mu.

0D PSR cases with AVBP

As was done for ethane cracking in Chap. 5, butane cracking is also studied in PSR configurations in AVBP, to validate the implementation of the chemistry in the code by comparing to the results of Cantera.

By starting with a simulate time step at a very small value (1×10^{-10} s), the minimum value of the chemical time step τ_{chem} is found to be 2×10^{-7} s. This means that the simulate time step should never exceed 2×10^{-7} s. Tests have been done with different values $\Delta t = 1\times10^{-11}$ s, 1×10^{-9} s, 2×10^{-9} s, 3×10^{-9} s, 4×10^{-9} s, 5×10^{-9} s, 1×10^{-8} s, where the mole fraction of species C_2H_4 at the end of 2 ms is compared with the reference Cantera case: the relative values $X(C_2H_4)/X(C_2H_4)_{ref}$ are plotted against the Δt in Fig. 6.1.3. It shows that Δt should be less than 5×10^{-9} s to keep a relative error below 5%. Considering the trade-off between accuracy and computational cost for the further 3D cases, this time step $\Delta t = 5\times10^{-9}$ s is chosen. Fig. 6.1.4 gives the comparison of the temporal evolutions between the results of Cantera and AVBP with the time step $\Delta t = 5\times10^{-9}$ s, showing the very good agreement and demonstrating the correct implementation and calculate of butane cracking chemistry in AVBP.

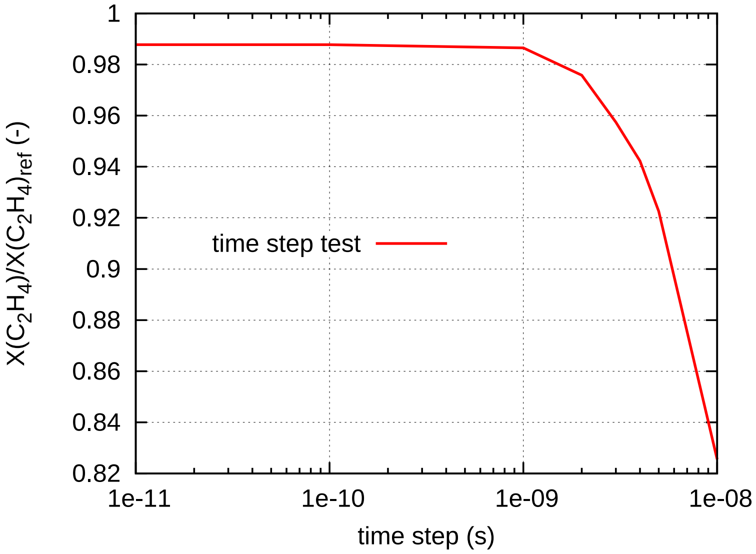

Figure 6.1.3: Influence of the simulate time step Δt in AVBP on the error on C_2H_4.

6.2 Numerical set-up for LES of reacting heated flow in tubes S38 and R38

6.2.1 Geometry

Fig. 6.2.1a and 6.2.1b display both the smooth and ribbed pipe geometries used in the industrial application. Similar to the ribbed tube R51 in previous chapters, the tube R38 is a cylindrical tube of diameter $D = 38.1$ mm in which helicoidal ribs are inserted, with a shape as illustrated in Fig. 6.2.1b.

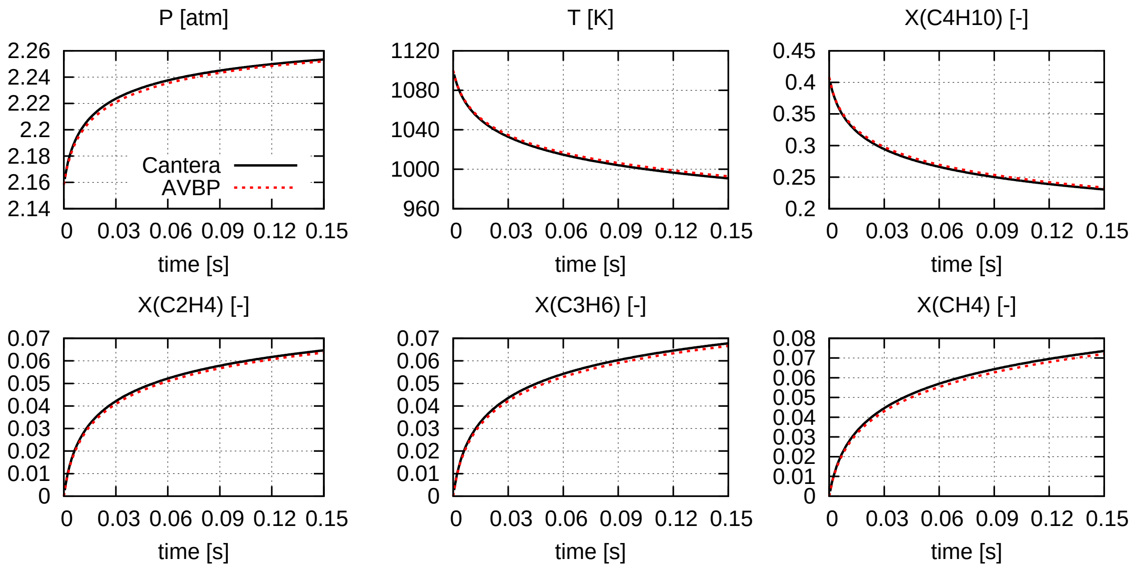

Figure 6.1.4: Comparison of the temporal evolutions of selected quantities obtained with Cantera (solid line) and AVBP (dashed line) ($\Delta t = 5\times10^{-9}$ s).

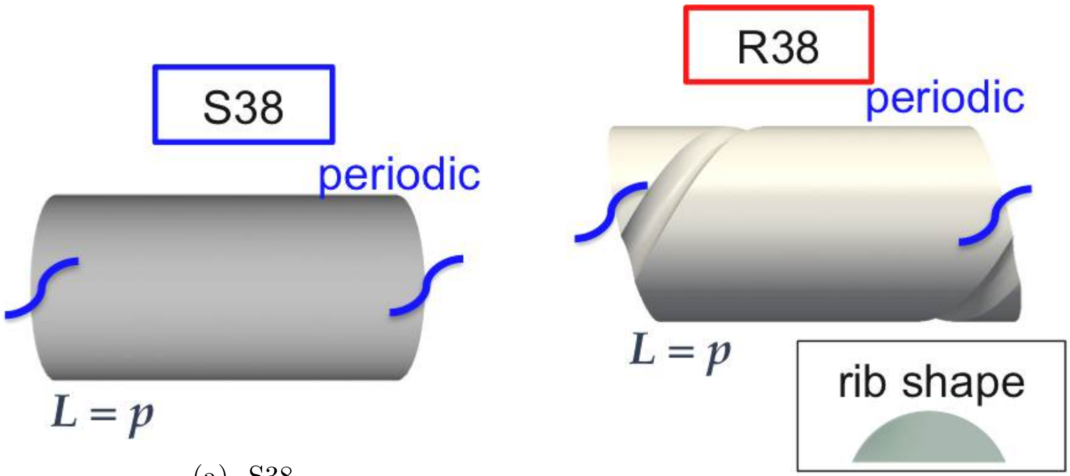

(a) S38.

(b) R38 with 1 periodic pattern.

Figure 6.2.1: Configuration of both smooth (S38) and ribbed tube (R38) used for the industrial application.

The ribbed tube R38 is characterized by the rib height $e = 2.13\,\text{mm}$ and the pitch $p = 69.11\,\text{mm}$, and the rib width $wth = 7\,\text{mm}$. The two dominant geometrical parameters are $p/D = 1.81$ and $e/D = 0.056$ respectively. In addition, as $p/e = 32.45 > 4$, this roughness is of kind “K-type” according to the classification introduced in section 1.2.2, as was the ribbed tube R51. The smooth tube S38 also has a diameter $D = 38.1\,\text{mm}$ and length p for comparison purposes.

6.2.2 Mesh

Following the methodology developed in the previous chapters, coarse meshes with y^+ of the order of 10 and no-slip wall boundary conditions are used. Unstructured meshes with tetrahedra holding a $y^+ \sim 20$ (at the Reynolds number equal to 72 110) at the wall were build for both tubes S38 and R38 and are shown in Fig. 6.2.2a and 6.2.2b.

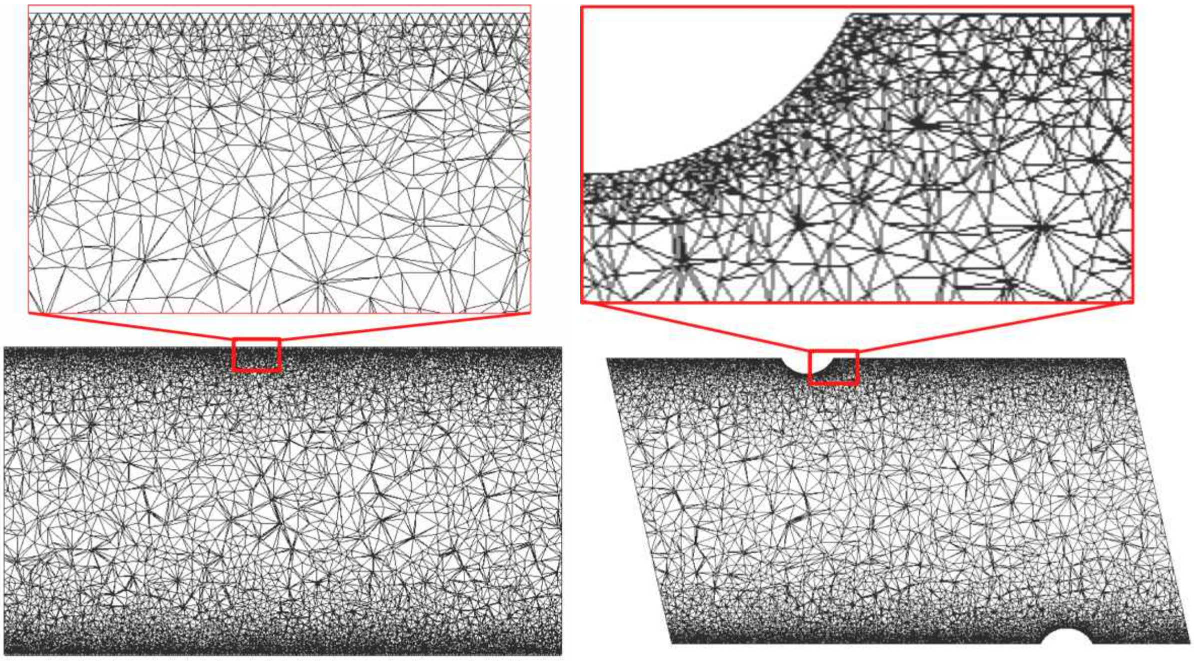

(a) S38.

(b) R38.

Figure 6.2.2: Axial cuts of meshes of both smooth (S38) and ribbed tube (R38).

The mesh information, cell number, node number, and the smallest cell volume, are given in Table. 6.2.1.

Mesh	Cell number	Node number	Smallest cell volume [m^3]
S38	3.14 million	602 442	1.95×10^{-13}
R38	3.68 million	713 958	7.03×10^{-14}

Table 6.2.1: Mesh information for the unstructured meshes for both S38 and R38.

6.2.3 Numerical Methodology

The simulations are performed using the numerical scheme LW for CPU cost consideration. Periodic conditions are applied at inlet and outlet, and a source term S_{qdm} is added in the flow equations, as for S51 and R51 cases in the previous chapters, to maintain a Reynolds number of 72 110. The initial flow is a mixture composed by 69.0% C_4H_{10} and 31.0% H_2O in mass and the initial bulk temperature (i.e., the inlet temperature in the real tube in industry application) is 909.15 K in both S38 and R38. However, the initial bulk pressures (inlet pressure in the real tube) are chosen different, at 235.68 kPa (2.33 atm) in the case S38 and 260.63 kPa (2.57 atm) in R38, to get the same final pressure (outlet pressure in the real tube) of 218.69 kPa (2.16 atm), at the end of a residence time 0.14 s (according to data from TOTAL).

The initial fields of velocity and temperature were first established in non-reacting condition and with the same mixture composition.

Boundary conditions

The boundary condition at the wall is no-slip for the velocity, and a wall heat flux $q_{wall,imposed}(t)$ depending on time is imposed, deduced from the data (provided by TOTAL) of the cumulative heat along the cracking tubes in the real industrial case. As shown in Fig. 6.2.3, the heat flux $q_{wall,imposed}(t)$ imposed in AVBP is in good agreement with the TOTAL data. Note a small discrepancy between the S38 and R38 cases, which is however ignored in the AVBP calculation as the same $q_{wall,imposed}(t)$ is applied for both cases. This will not have any significant impact on the results.

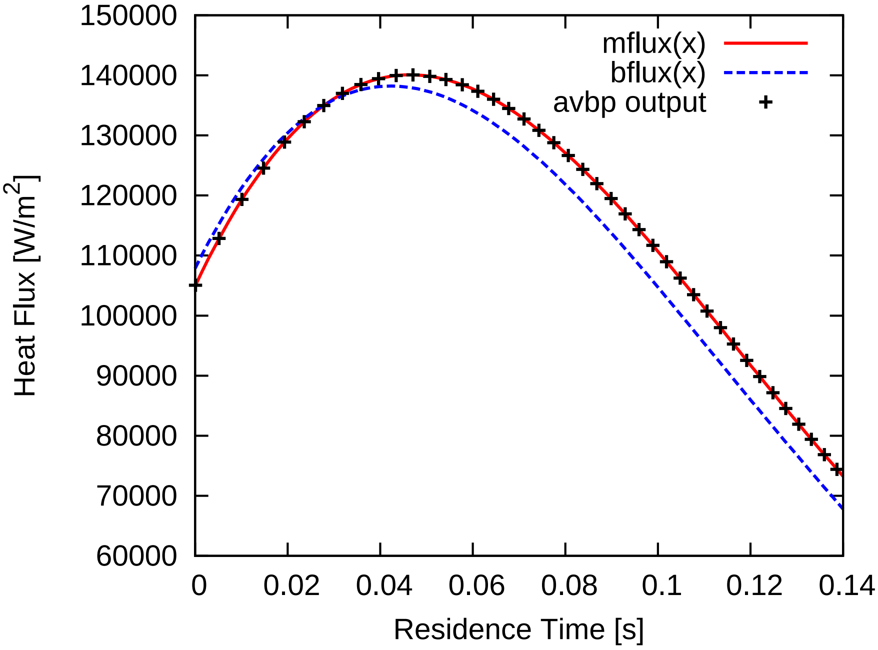

Figure 6.2.3: Imposed heat flux at the wall: in AVBP (crosses), and from the data provided by TOTAL (solid line for R38 and dashed line for S38).

6.2.4 Variation of density in a periodic configuration

As the periodic configuration used for 3D smooth and ribbed tube simulations leads to constant-volume evolutions, there is no temporal variation of the spatially-averaged mass density in the system due to mass conservation. Indeed it was observed from the previous results of cases S51 and R51 that pressure increases instead of decreasing in the real industrial process. This is due to the constant volume constraint, which does not allow flow expansion due to the change of temperature T and the specific gas constant r. This may have a strong impact on the chemical process and must be corrected. Considering the equation of state $P/rT = \rho$, T is controlled by the heat flux imposed at wall, and r is controlled by the reacting system. Therefore, in order to mimic the decreasing pressure in the real system, a source term S_ρ in unit kg/(m^3 s) is introduced in the mass conservation equation, and the momentum and energy equations are modified accordingly:

$$\frac{\partial \rho}{\partial t} + \frac{\partial (\rho u_i)}{\partial x_i} = S_\rho, \tag{6.2.1}$$

$$\frac{\partial (\rho u_i)}{\partial t} + \frac{\partial (\rho u_i u_j)}{\partial x_j} = -\frac{\partial p}{\partial x_i} + \frac{\partial \tau_{ij}}{\partial x_j} + S_{qdm,i} + u_i S_\rho, \tag{6.2.2}$$

$$\rho \frac{DE}{Dt} = -\frac{\partial q_i}{\partial x_i} + \frac{\partial}{\partial x_j}(\tau_{ij} u_i) - \frac{\partial}{\partial x_i}(p u_i) + \dot{w}_T + u_i S_{qdm,i} + E S_\rho, \tag{6.2.3}$$

The source term S_ρ is defined as follows:

$$\begin{aligned} S_\rho &= \frac{\mathrm{d}\langle \rho \rangle}{\mathrm{d}t} \\ &= \frac{\mathrm{d}}{\mathrm{d}t}(\langle P/rT \rangle) \\ &= \frac{1}{\langle r \rangle \langle T \rangle} \frac{\mathrm{d}\langle P \rangle}{\mathrm{d}t} + \langle P \rangle \frac{\mathrm{d}}{\mathrm{d}t}\left(\frac{1}{\langle r \rangle \langle T \rangle} \right), \end{aligned} \tag{6.2.4}$$

where $\langle\ \rangle$ refers to the spatial averaging.

This methodology was newly implemented in the code AVBP, with three options to set the source term S_ρ:

1) Constant S_ρ: $\mathrm{d}\langle \rho \rangle/\mathrm{d}t$ keeps constant during the simulation and the pressure varies with the specific gas constant r and the temperature T to achieve a linear variation of mass density ρ;

2) Dynamic S_ρ - 1: this option is designed to maintain a linear variation of pressure. The value of $\mathrm{d}\langle P \rangle/\mathrm{d}t$ should be given as an input parameter, and S_ρ is dynamically calculated at each time step following Eq. 6.2.4, using the current values of r and T.

3) Dynamic S_ρ - 2: this option allows the pressure to vary with time following a cubic polynomial function:

   $$P(t) = \frac{a}{3}t^3 + \frac{b}{2}t^2 + ct + P_0, \tag{6.2.5}$$

   so that,

   $$\frac{\mathrm{d}\langle P(t) \rangle}{\mathrm{d}t} = at^2 + bt + c, \tag{6.2.6}$$

   where the three parameters a, b, c are fixed in an input file by the user.

Non-reacting 2D test cases

Preliminary tests are performed with a 2D non-reacting isothermal laminar flow through a channel. The reference case uses a source term S_{qdm} in the momentum equation to maintain a laminar flow at Re $\sim$ 20 in a periodic domain as shown in Fig. 6.2.4a. No-slip boundary conditions are used at walls. The axial velocity field is shown in Fig. 6.2.4a after a stable

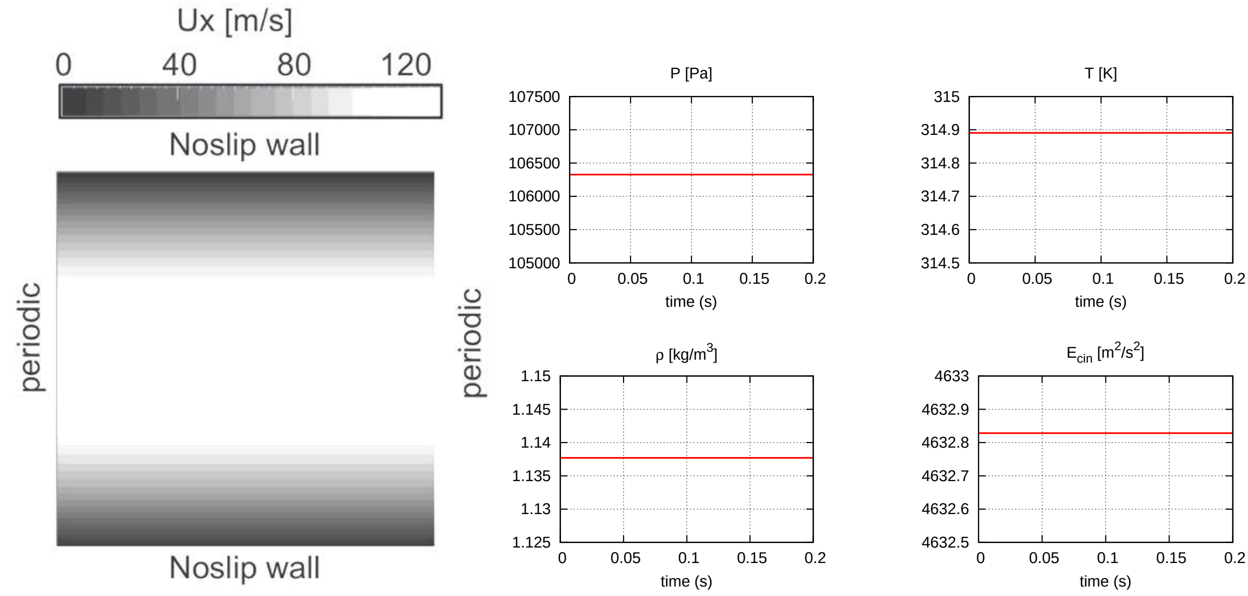

(a) Configuration.

(b) Stable regime.

Figure 6.2.4: Configuration (a) and stable regime (b) of the 2D non-reacting isothermal laminar flow through a channel.

regime has been established: the spatial-averaged pressure, temperature, mass density and kinetic energy all keep constant, as shown in Fig. 6.2.4b.

By taking this stable regime as the initial condition, the three options for setting the source term S_ρ are used. As for the non-reacting isothermal flow there will be no variation of temperature and specific gas constant, so that the same results should be obtained with the three options:

- Option 1: imposing a constant $\mathrm{d}\langle\rho\rangle/\mathrm{d}t = S_\rho = -1.07$;
- Option 2: setting $\mathrm{d}\langle P\rangle/\mathrm{d}t = -1{\times}10^5$;
- Option 3: fixing $a = 0, b = 0, c = -1{\times}10^5$

In all cases, the same linear decrease of ρ and P should be observed:

$$P(t) = P_0 + S_\rho r_0 T_0 t \tag{6.2.7}$$

$$\rho(t) = \rho_0 + S_\rho t \tag{6.2.8}$$

$$T(t) = T_0 \tag{6.2.9}$$

$$E_{cin}(t) = E_{cin,0} \tag{6.2.10}$$

Results are shown in Fig. 6.2.5. The simulation recovers well the theoretical curves, and only small errors are observed for T and E_{din}, not exceeding 0.03% and 0.006% respectively.

To be more complete, another test case is conducted using option 3 by setting $a = -1{\times}10^6, b = 0, c = -1{\times}10^5$. Fig. 6.2.6 shows that the pressure and mass density are in good agreement with the analytical results $P(t) = (a/3)t^3 + (b/2)t^2 + ct + P_0$ and $\rho(t) =$

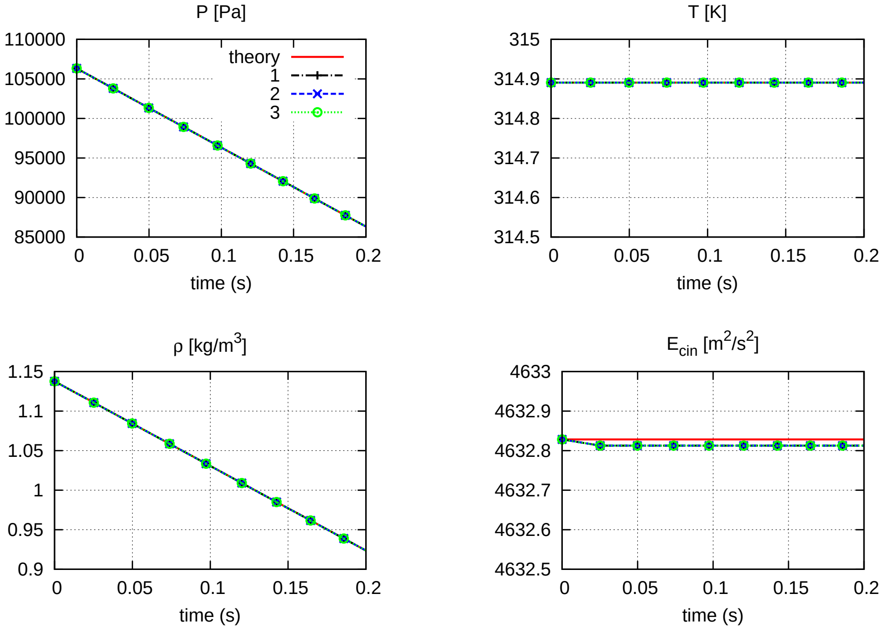

Figure 6.2.5: Temporal evolutions of P, T, ρ and E_{cin} for the 3 options of density source term, compared to the theoretical results.

$(1/r_0T_0)(a/3)t^3 + (b/2)t^2 + ct + \rho_0$, while the temperature and the kinetic energy still do not change.

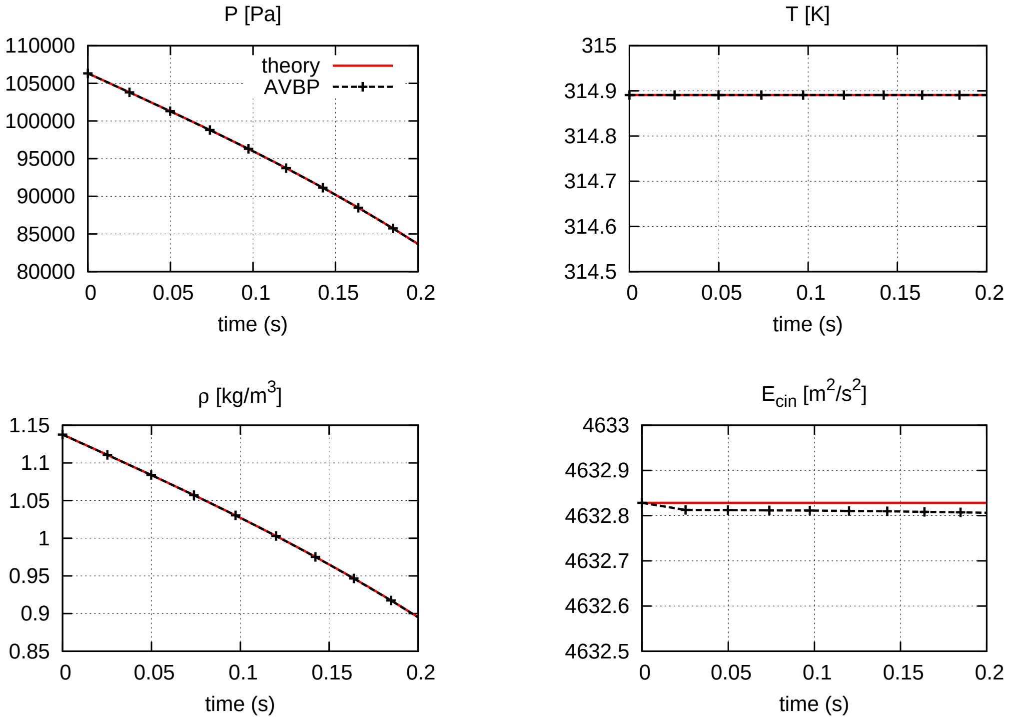

Figure 6.2.6: Comparison between option 3 and the theoretical results.

Reacting 0D test cases

In this section, the methodology to account for density variation is validated with the reacting case presented in Sec.6.1.2. Contrary to the non-reacting cases, the temperature and the specific gas constant now vary significantly. The three options of source term S_ρ are here used to differently impose a pressure decrease (instead of pressure increase in Fig. 6.1.4), and the temperature evolution as $T_{noS_\rho}(t)$ should be kept. The input parameters and the analytical results are given in Table. 6.2.2. For option 1, the density is directly controlled, and the pressure variation can be obtained using the equation of state, while for options 2 and 3 using a dynamic source term S_ρ, the pressure is directly controlled and the density is obtained from the equation of state.

Option	Input parameters	Value	Analytical results
1	$\mathrm{d}\langle\rho\rangle/\mathrm{d}t$	-0.376	$\rho(t) = \rho_0 - 0.376t$
2	$\mathrm{d}\langle P\rangle/\mathrm{d}t$	-1×10^5	$P(t) = P_0 - 1\times10^5 t$
3	a, b, c	-1×10^6, 0, -1×10^5	$P(t) = P_0 - (1\times10^6/3)t^3 - 1\times10^5 t$

Table 6.2.2: Input parameters and expected results for reacting case using the three options of density source term.

The temperature is not affected and varies as in Fig. 6.1.4 in Sec.6.1.2, as expected. Figs. 6.2.7a, 6.2.7b and 6.2.7c illustrate the temporal evolution of the spatially-averaged pressure, temperature and mass density respectively for options 1, 2 and 3, corresponding well to the analytical ones.

Pressure decrease in tubes

In the present work, the pressure temporal evolution is known from the data of TOTAL, and should be directly controlled. Considering the variation on T and r in the reacting flow in tubes, the option 2 of density source term is used. Parameters in the input file are set to obtain a pressure decrease corresponding to the data (especially to the initial and final pressures) in S38 and R38. Figs. 6.2.8a and 6.2.8b show the data of TOTAL and the pressure decrease imposed in AVBP (“curve fitting”).

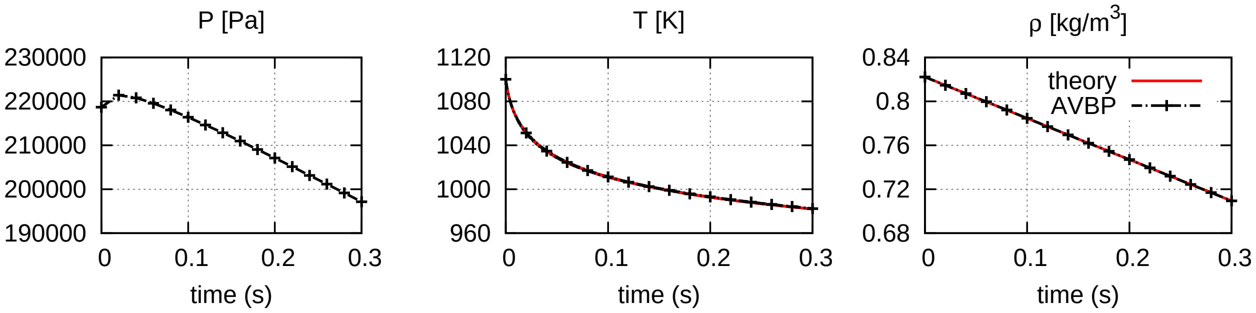

(a) Option 1.

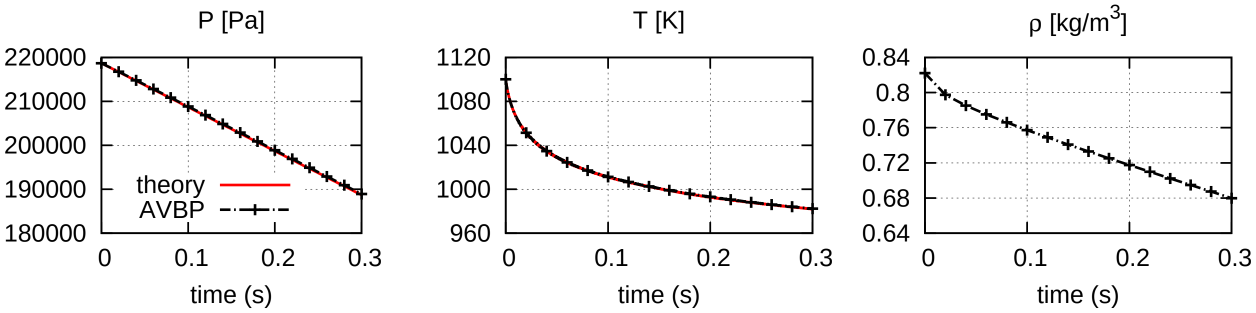

(b) Option 2.

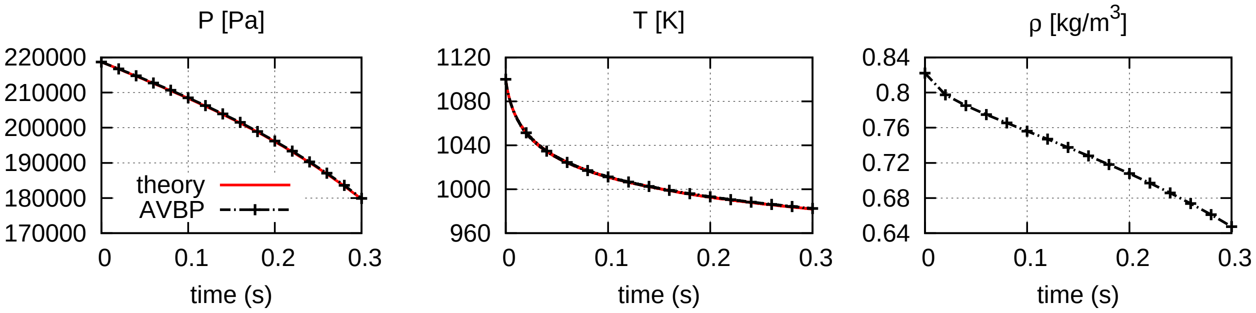

(c) Option 3.

Figure 6.2.7: Temporal evolutions of the spatially-averaged pressure, temperature and mass density using the 3 options, compared to the theoretical results.

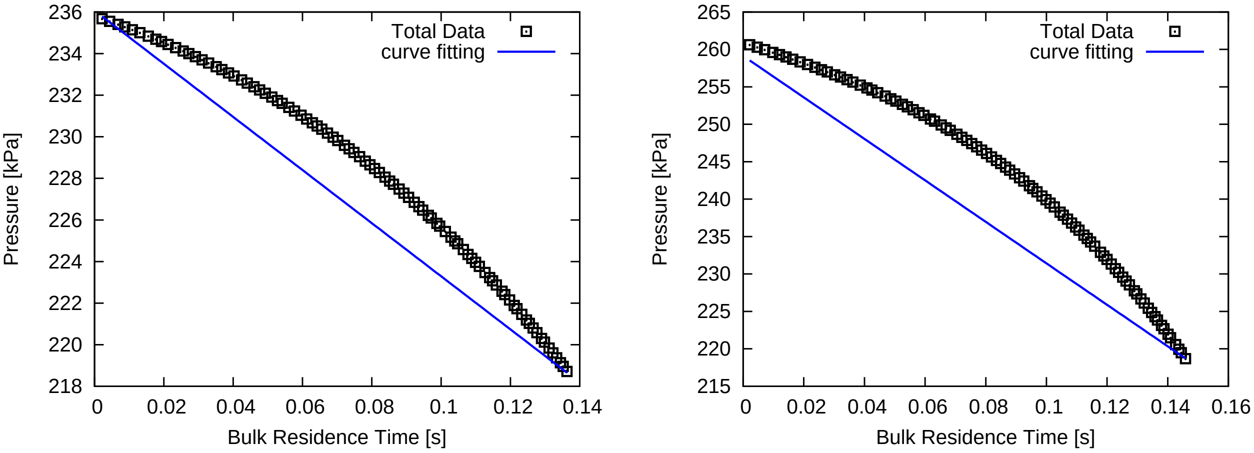

(a) S38. (b) R38.

Figure 6.2.8: Pressure decrease imposed in AVBP (solid line) and the data from TOTAL (symbols: squares) in both S38 and R38 tubes.

6.3 Preliminary PSR tests at different pressures

To simulate the industrial application, the initial pressures in case S38 and R38 are different, and vary from the final pressure, as mentioned above. Adiabatic PSR tests with constant volume have been conducted with Cantera to show the impact of the pressure on the butane cracking process. The two extreme of pressure, respectively 2.57 atm and 2.16 atm in tubes, and three different temperatures 909 K, 1000 K and 1200 K are used. The operating points are listed in Table. 6.3.1.

PSR	T [K]	Pressure [atm]
T9PI	909	2.57
T10PI	1000	
T12PI	1200	
T9PO	909	2.16
T10PO	1000	
T12PO	1200	

Table 6.3.1: Preliminary PSR tests at different pressures and temperatures with Cantera.

Results in Fig. 6.3.1 show the temporal evolutions of temperature, pressure, mole fraction of reactants and two mains products. Almost the same evolutions are observed between two series of tests at different pressures, so the pressure has little impact on the butane cracking chemistry. Note that these tests are with constant volume, i.e., constant density. For the simulations in tubes, the density varies a lot and can have a significant impact on the chemistry.

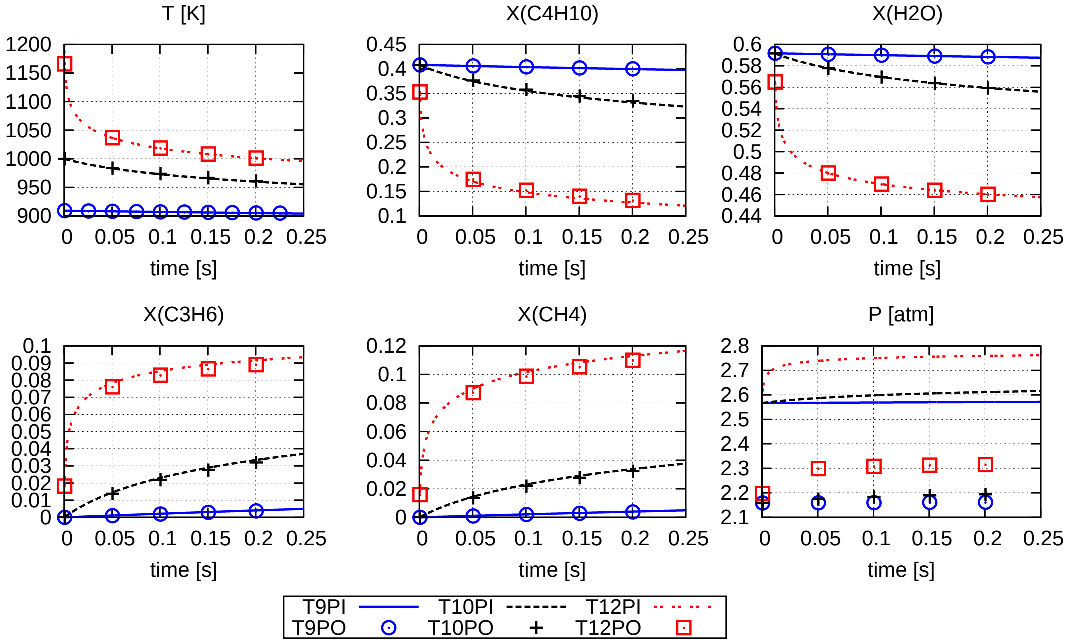

Figure 6.3.1: Preliminary PSR tests at different pressures and temperatures with Cantera: temporal evolutions of the temperature, pressure, mole fraction of reactants and two mains products.

6.4 LES results of reacting heated flow in tubes S38 and R38

6.4.1 Temporal evolution of spatially-averaged quantities

The temporal evolutions of the spatially-averaged temperature, pressure, mole fraction of the two main products C_3H_6, C_2H_4 and the two reactants H_2O and C_4H_{10} are plotted in Fig. 6.4.1 for both tubes S38 and R38, compared with the temperature data from TOTAL.

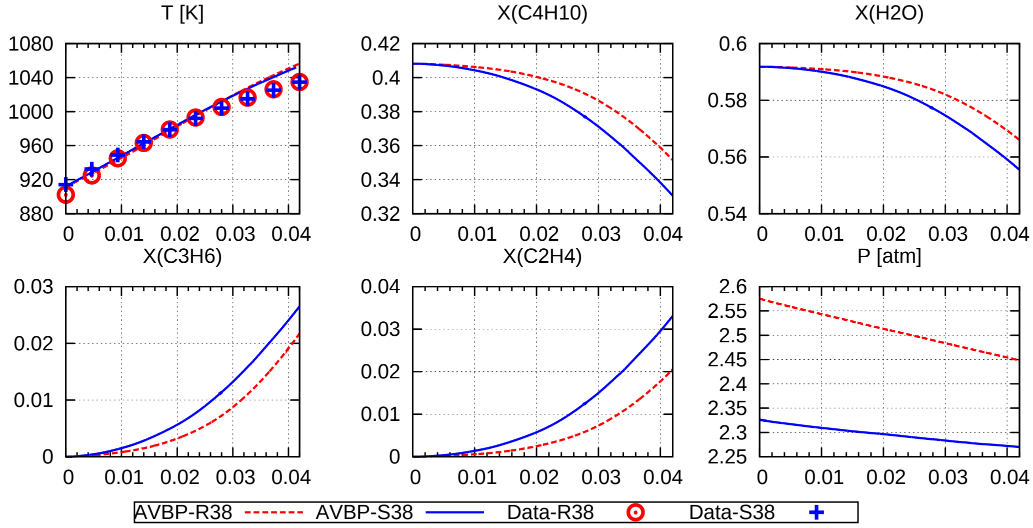

Figure 6.4.1: Temporal evolutions of the spatially-averaged temperature, pressure, mole fraction of the two main products and the two reactants for both tubes S38 and R38, compared with the data from TOTAL. The x-axis is "Time [S]". TOTLAL source: symbols. AVBP results: lines.

The simulations are still running and the results are shown till 42 ms. The temperature evolutions are well predicted by AVBP simulations, and no significant difference is observed between S38 and R38 (note that the same heat flux is imposed on the wall in both cases). The butane in the smooth tube S38 is consumed more rapidly, leading to more productions of C_3H_6 and C_2H_4. More analysis will be conducted in the next sections.

The temporal evolution of the spatially-averaged (global) reaction rate of the main decomposition reaction $C_4H_{10} \rightarrow 2C_2H_5$ in the butane cracking chemistry, and the relations between the reaction rate, the temperature and the mass fraction of the reactant C_4H_{10}, are plotted in Fig. 6.4.2. Higher reaction rate is observed in S38, leading to a faster consumption of C_4H_{10} and higher production, as observed in Fig. 6.4.1. These different relations in Figs. 6.4.2b-c between S38 and R38 show a mixing effect. At the same spatially-averaged temperature, the global reaction rate is higher in S38, leading to a higher consumption of C_4H_{10}, thus lower mass fraction.

6.4.2 Instantaneous fields

Instantaneous fields at 1 ms, 10 ms and 40 ms, of axial velocity, temperature, reaction rate of $C_4H_{10} \rightarrow 2C_2H_5$ and mass fraction of the main product C_3H_6, are investigated and compared

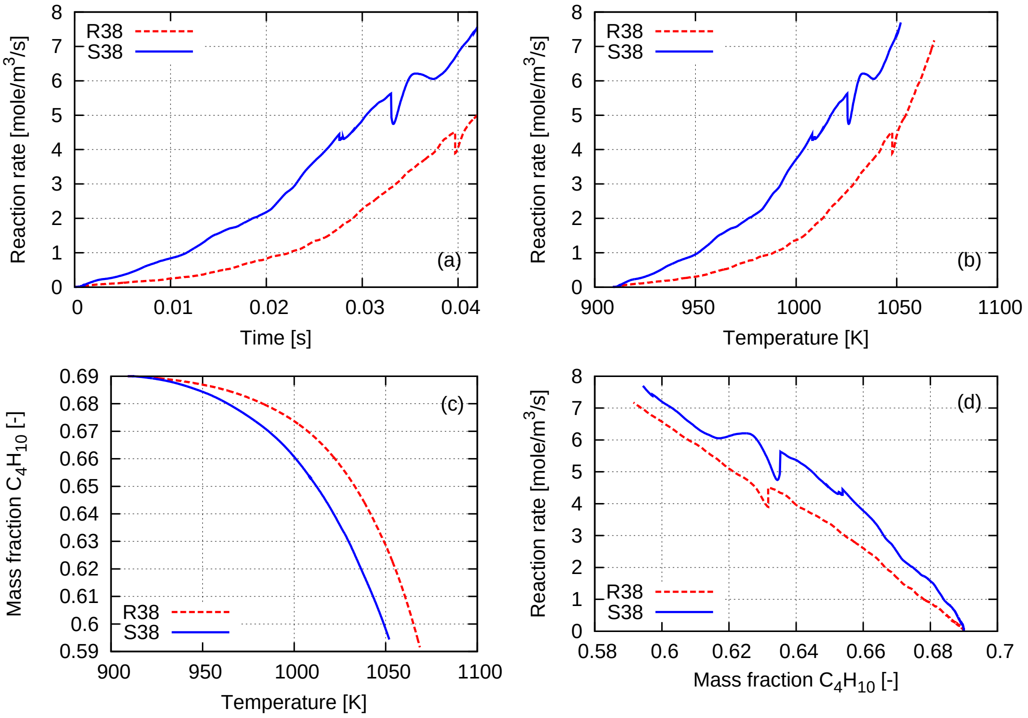

Figure 6.4.2: (a)Temporal evolution of spatially-averaged reaction rate of the reaction $C_4H_{10} \rightarrow 2C_2H_5$; (b)-(c) relations between reaction rate, temperature and mass fraction of C_4H_{10} in both S38 and R38 tubes.

between the cases S38 and R38.

Axial velocity

Instantaneous fields of axial velocity in both S38 and R38 tubes are shown in Fig. 6.4.3. The

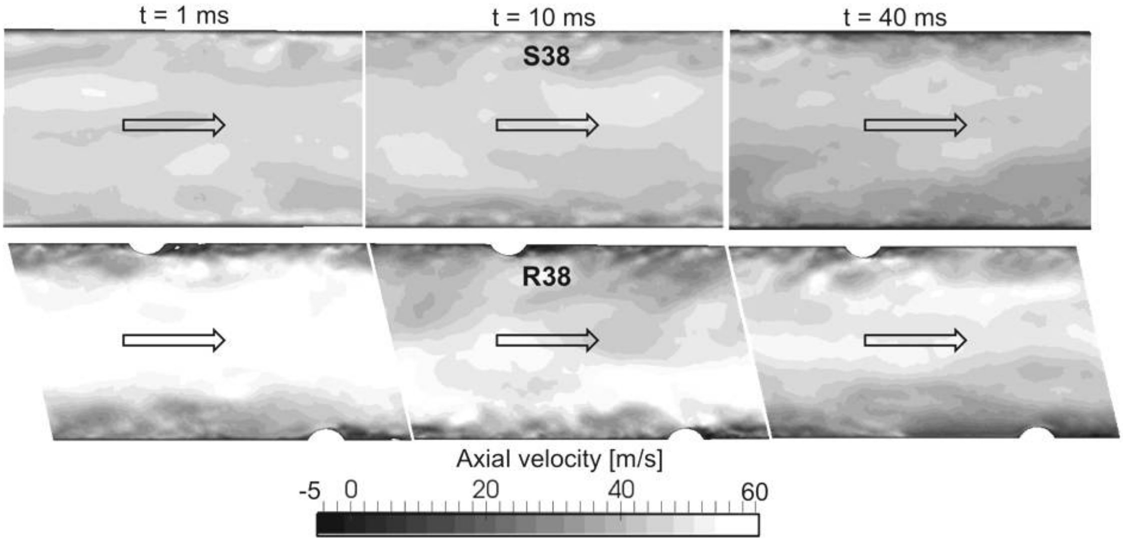

Figure 6.4.3: Instantaneous fields of axial velocity in both S38 and R38 tubes at 1 ms, 10 ms and 40 ms.

bulk velocity is kept at around 45 m/s. As expected, stronger turbulence is observed in R38.

Temperature

Fig. 6.4.4 shows the instantaneous fields of temperature.

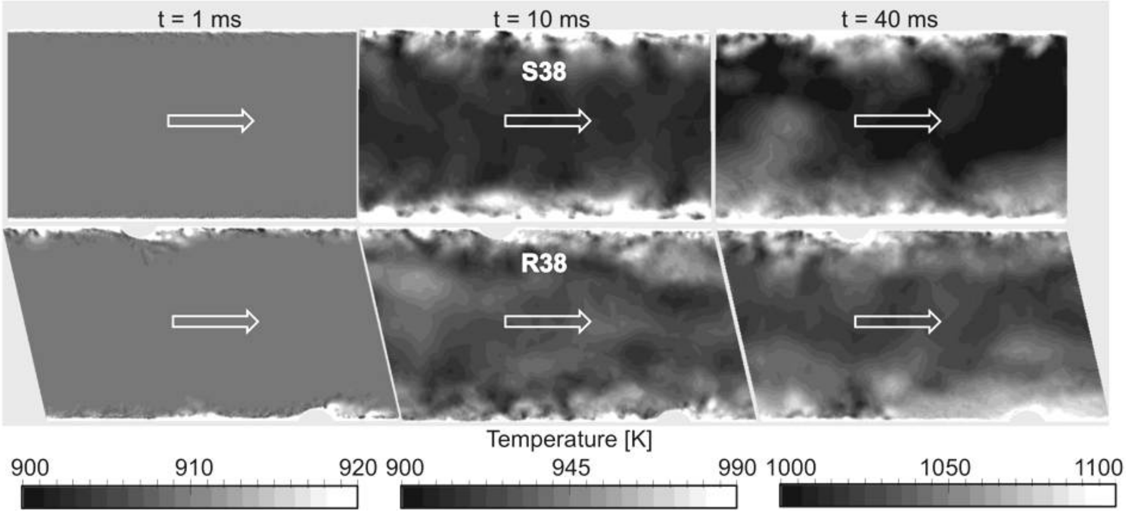

Figure 6.4.4: Instantaneous fields of temperature in both S38 and R38 tubes at 1 ms, 10 ms and 40 ms.

First, comparing the fields at 1 ms, 10 ms and 40 ms, the heating process from the wall towards the center of tubes is significant. Note that the same heat flux is imposed on the wall of both tubes, so the heat flux entering the two tubes are the same. Second, more homogeneous temperature distribution is observed in the tube R38, at 10 ms and 40 ms respectively, thanks to better mixing and faster heat transfer. In S38, the temperature is especially high in the near wall region (from the wall to almost 1/4 radius), and is higher than in R38, because the heat transfer at wall in S38 is less efficient than in R38, leading to a higher skin temperature, as shown in Fig. 6.4.5. As expected, globally lower skin temperature in the tube R38 is obtained, which is desirable because it can reduce the coking phenomena in tubes of thermal cracking. Note that high temperature appears in the rib corners, where the coke formation is the most.

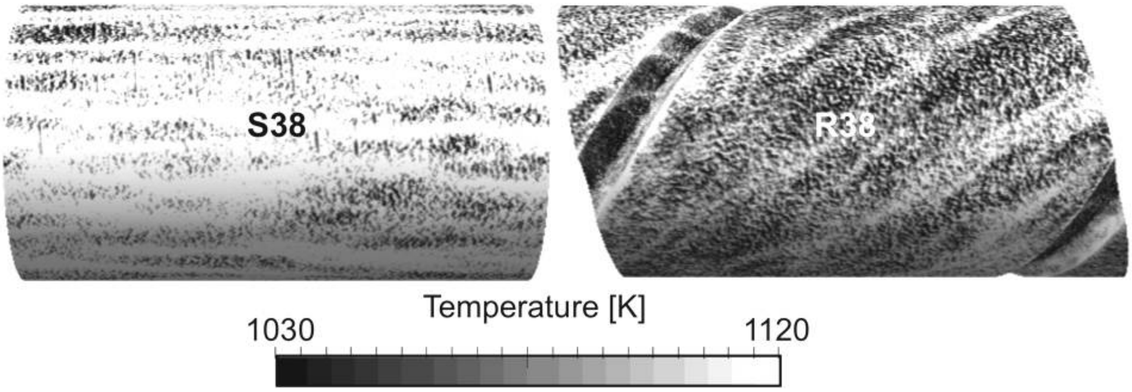

Figure 6.4.5: Instantaneous skin temperature distribution at the wall in both S38 and R38 tubes at 10 ms.

Reaction rate of $C_4H_{10} \rightarrow 2C_2H_5$

The temperature distribution in both tubes has a direct impact on the reaction rate of the main decomposition reaction $C_4H_{10} \rightarrow 2C_2H_5$ in butane cracking chemistry. In Fig. 6.4.6, high reaction rate is observed in a larger region near the wall in S38 than in R38, thanks to larger region of high temperature. In addition, more homogeneous distribution of reaction rate and slightly higher reaction rate towards the tube center is observed in R38.

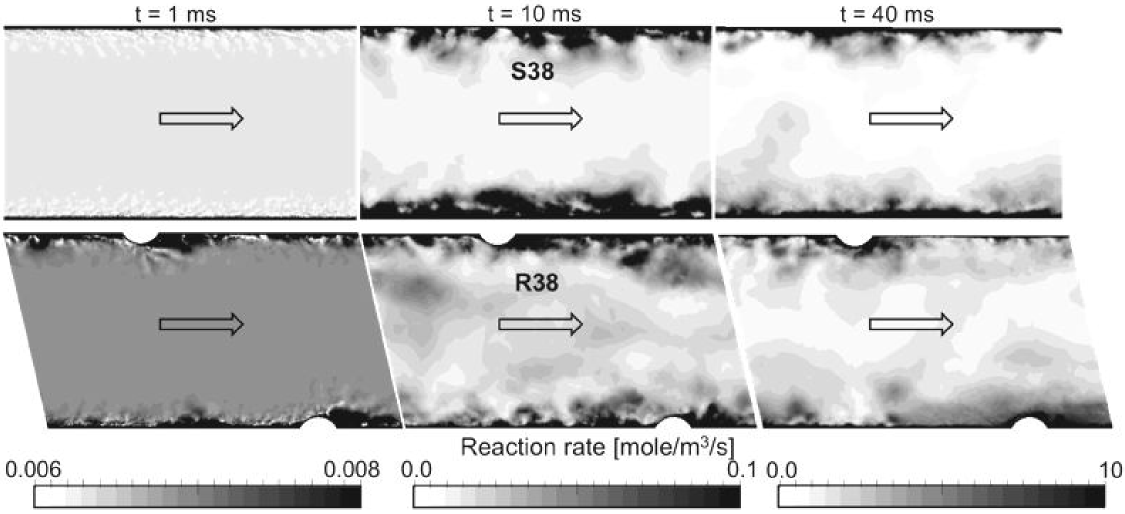

Figure 6.4.6: Instantaneous fields of the reaction rate of $C_4H_{10} \rightarrow 2C_2H_5$ in both S38 and R38 tubes at 1 ms, 10 ms and 40 ms.

Mass fraction of C_4H_{10}

The instantaneous fields of mass fraction of C_4H_{10} are given in Fig. 6.4.8. More C_4H_{10} is consumed in the near wall region in S38, leading to a stronger gradient of mass fraction of

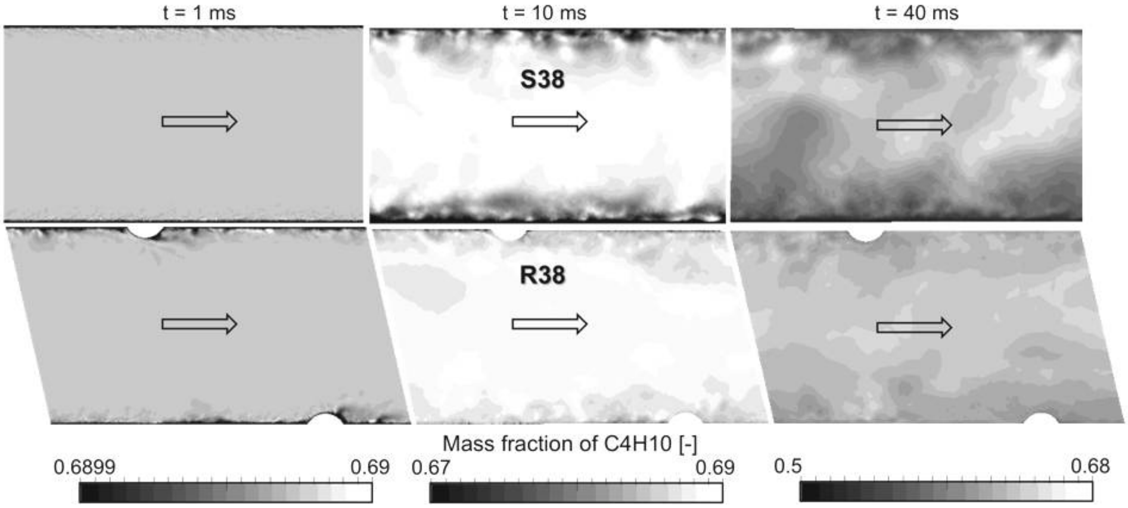

Figure 6.4.7: Instantaneous fields of mass fraction of C_4H_{10} in both S38 and R38 tubes at 1 ms, 10 ms and 40 ms.

C_4H_{10}. More homogeneous field in R38 is due to less consumption of C_4H_{10} near the wall and better mixing.

Mass fraction of C_3H_6

The observations above explain the higher productions of C_3H_6 in the tube S38. Higher reaction rate of $C_4H_{10} \rightarrow 2C_2H_5$ in the near wall region in S38 leads to higher production of C_3H_6, as shown in Fig. 6.4.8. Although the production of C_3H_6 in the center of R38 is higher, the global production is still lower.

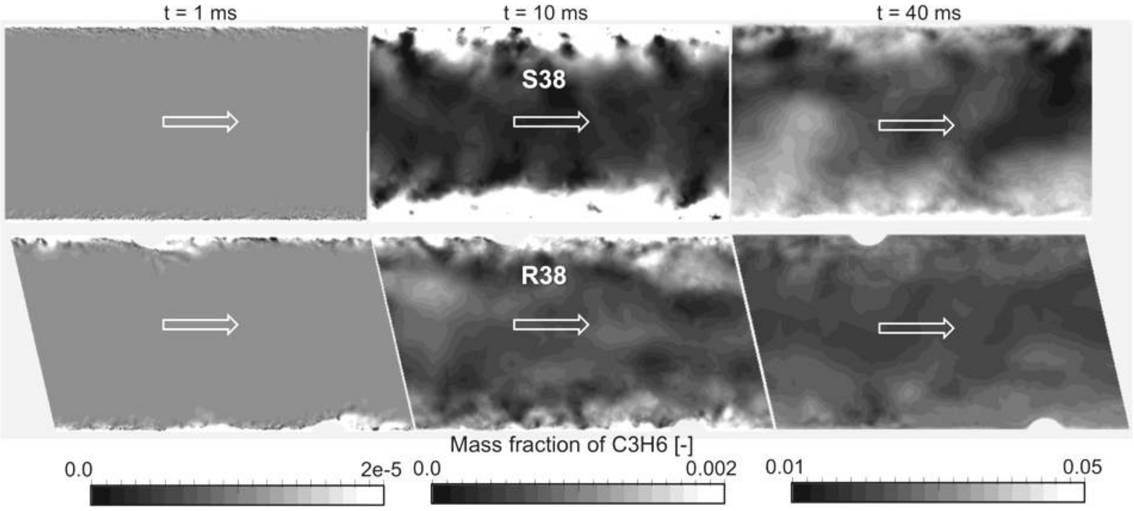

Figure 6.4.8: Instantaneous fields of mass fraction of C_3H_6 in both S38 and R38 tubes at 1 ms, 10 ms and 40 ms.

6.4.3 Probability distribution and contribution

Difference of geometry between ribbed and smooth tubes leads to different probability distribution of temperature although their spatially averaged temperatures are the same, having impact on chemistry. Results are here compared between R38 and S38 using instantaneous solutions at 10 ms and 40 ms.

Probability distribution of temperature

The probability distribution of temperature $PDF(T)$ is calculated as the percentage of the volume of tubes having the same temperature. The temperature range from 850 K to 1250 K is divided into 100 regular intervals and values of temperature higher than 1250 are counted into the last interval topped by 1250 to facilitate the illustration, as shown in Fig. 6.4.9. From 10 ms to 40 ms, temperature distribution moves from lower region to higher one, in agreement with the higher mean temperature at 40 ms. Note that the instantaneous global temperature in R38 and S38 is the same (refer to Fig. 6.4.1), while the distributions are different.The smooth tube S38 has a higher temperature probability distribution in the lowest and highest regions, consistent with the low temperature in the tube center and high temperature at wall as observed in Fig. 6.4.4, leading to a less homogeneous temperature field than in R38.

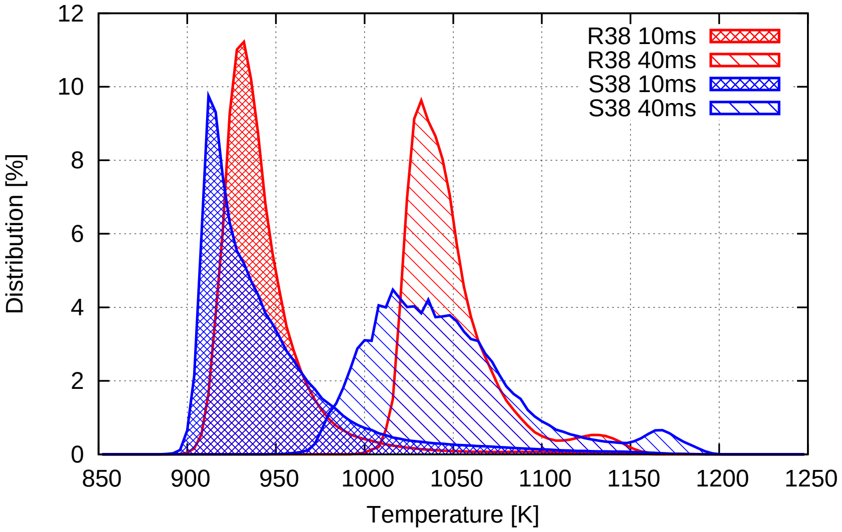

Figure 6.4.9: Probability distribution of temperature at 10 ms and 40 ms in both S38 and R38 tubes.

Different distribution of temperature leads to different distribution of reaction rate, showing an impact on chemistry.

Probability distribution of reaction rate of $C_4H_{10} \rightarrow 2C_2H_5$

The reaction rate of $C_4H_{10} \rightarrow 2C_2H_5$ is taken as an example to show the impact on chemistry. The probability distribution of reaction rate $PDF(r)$ is given in Fig. 6.4.10, 100 regular intervals are used from 0 to 200 mol/m^3/s, and values higher than 200 are counted into the last interval topped by 200 to facilitate the illustration. Fig. 6.4.10a is zoomed into the intervals from 0 to 20 mol/m^3/s, and Fig. 6.4.10b is zoomed on the values of distribution from 0 to 1% for all intervals. Most values of reaction rate are inferior to 5, as shown in Table. 6.4.1.

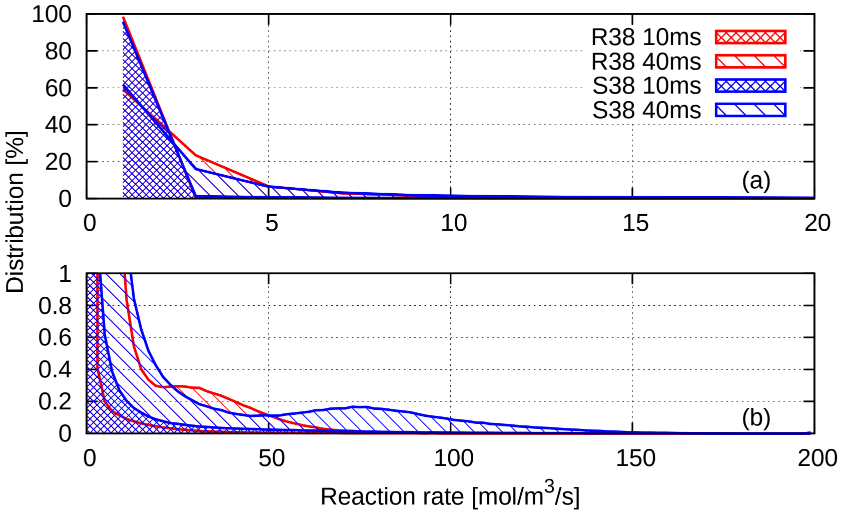

Figure 6.4.10: Probability distribution of reaction rate for $C_4H_{10} \rightarrow 2C_2H_5$ at 10 ms and 40 ms in both S38 and R38 tubes.

	$PDF(r<5)$		$PDF(r>50)$	
	10 ms	40 ms	10 ms	40 ms
R38	99%	87%	0.05%	0.75%
S38	97%	82%	0.4%	4.4%

Table 6.4.1: Probability distribution of reaction rate for $C_4H_{10} \rightarrow 2C_2H_5$ at 10 ms and 40 ms in both S38 and R38 tubes.

Due to the more homogeneous distribution of temperature in the ribbed tube R38, the distribution of reaction rate in R38 is more concentrated in the range [0, 5 mol/m^3/s] than in S38.

On the other hand, for $r > 50\,\text{mol/m}^3/\text{s}$, related to the high temperature in the near wall region, $PDF(r)$ in the smooth tube S38 is higher. Although this proportion is very small compared to $PDF(r < 5\,\text{mol/m}^3/\text{s})$, its contribution is quite important thanks to the high value of reaction rate. The contribution $C(r)$ is defined as:

$$C(r) = PDF(r) \cdot r, \tag{6.4.1}$$

and is illustrated in Fig. 6.4.11. It is observed that at 40 ms, the form of contribution area is similar in both smooth and ribbed tubes: high contribution is found in the lowest range thanks to high distribution, then it decreases and re-increases because of the high reaction rate r. The contribution of $r > 50\,\text{mol/m}^3/\text{s}$ in the smooth tube S38 is much more important than in R38, leading to a higher spatially averaged reaction rate, thus a faster consumption of C_4H_{10}. But this effect may change: since the reacting flow becomes more homogeneous with longer simulation time in both S38 and R38 (which can be already observed in the instantaneous fields at 40 ms in Figs. 6.4.4 and 6.4.6), the advantage of the high temperature (i.e. high reaction rate) in the near wall region of S38 may be limited, at the same time, less and less C_4H_{10} appears in the wall region, especially in S38, which limits the consumption rate of C_4H_{10}. It can be investigated with further results.

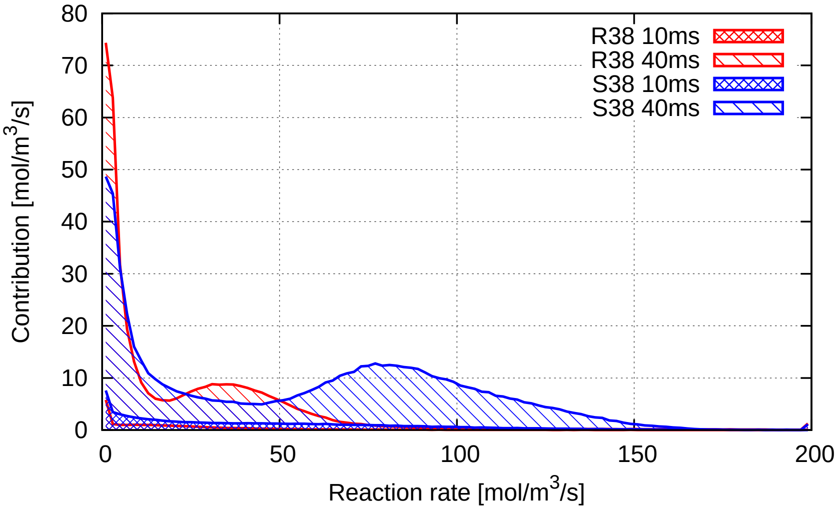

Figure 6.4.11: Contribution of reaction rate for $C_4H_{10} \rightarrow 2C_2H_5$ at 10 ms and 40 ms in both S38 and R38 tubes.

6.4.4 Selectivity of products

Different distributions of quantities as temperature and reaction rate in ribbed and smooth tubes have impact on the selectivity of products, which has an economic impact in petrochemical industry. The selectivity is defined as the amount of a specific product formed per mole of reactant consumed till time t:

$$Slc_{\text{prod}} = -\frac{\Delta n_{\text{prod}}(t)}{\Delta n_{\text{C}_4\text{H}_{10}}(t)} = -\frac{n_{\text{prod}}(t) - n_{\text{prod}}(0)}{n_{\text{C}_4\text{H}_{10}}(t) - n_{\text{C}_4\text{H}_{10}}(0)} \tag{6.4.2}$$

In the present work, the selectivities of CH_4, C_2H_4 and C_3H_6 are compared, at the moments when the same conversion of C_4H_{10} ($\Delta n_{\text{C}_4\text{H}_{10}}(t)/n_{\text{C}_4\text{H}_{10}}(0) = 13.9\%$) is achieved: $t = 47\,\text{ms}$ in R38 and $t = 42\,\text{ms}$ in S38. The selectivities of products are listed in Table. 6.4.2.

Selectivity	CH_4	C_2H_4	C_3H_6
R38	53.9%	54.9%	54.7%
S38	49.0%	62.9%	50.3%

Table 6.4.2: Selectivity of products CH_4, C_2H_4 and C_3H_6 in both S38 and R38 tubes.

It is observed that for the current results, the selectivity of CH_4 and C_3H_6 increase while the one of C_2H_4 decreases in the ribbed tube R38 compared to the smooth tube S38.

6.5 Conclusions and perspectives

In this chapter, butane cracking chemistry has been implemented in the code AVBP and validated against 0D PSR calculations, obtained with Cantera and Senkin. Simulations of butane cracking process within the configurations S38 and R38, with an imposed heat flux at the wall and the density variation model are conducted. The present results is run till 40 ms (the typical residence time 140 ms). Higher skin temperature, faster conversion of butane and higher selectivity of ethylene are observed in the tube S38. The advantage of the tube R38 is the lower skin temperature which reduces the coking phenomena, thanks to better mixing and faster heat transfer. Analysis shows that the higher temperature in the near wall region of the tube S38 is responsible for the faster conversion of butane. However, when the reacting flow becomes more homogeneous as time, this effect may be no longer dominant and higher conversion may appear in the tube R38 after some time. Further investigations will be conducted when the total simulation time increases.

Chapter 7

Conclusions and perspectives

In the present work, LES of non-reacting and reacting turbulent flows are performed in both smooth and ribbed tubes with the LES code AVBP and the results are analyzed in details. After introducing the industrial context, a literature review summarizes the experimental and numerical studies on wall flows over smooth and rough surfaces. Many experimental and numerical studies have been published for turbulent flows in smooth tubes. Wall models have been proposed for these flows, leading to a correct estimation of both the wall friction and the heat flux. For ribbed tubes however, experimental studies show very different results, with no clear conclusions about the nature of the wall flow. Examples of numerical simulations of ribbed tubes, especially of helically ribbed tubes, are scarce in the literature. For these reasons, high-fidelity numerical simulation appears as an interesting tool to investigate turbulent flows in ribbed tubes.

In Chaps 3 and 4, the non-reacting isothermal/non-isothermal turbulent flows in both smooth (S51) and ribbed (R51) tubes are investigated. The impact of the mesh and the numerical scheme is evaluated. The smooth tube reference cases are validated against theoretical/empirical results. The methodology of using a periodic configuration with a computational domain $L < D$, combined with a source term S_{qdm} (and S_e) in the flow equations solved on a hybrid mesh having $y^+ = 1$ at the wall, with the numerical scheme TTGC, is found to give accurate results and is applied to ribbed tube R51.

Comparisons between different meshes and numerical schemes on R51 show that mesh Y10t with scheme TTGC or LW can well capture both the dynamics and the thermal behavior of the turbulent flow, allowing to reduce significantly the computational cost of the LES. Comparisons between smooth and ribbed tubes show that, contrary to the smooth tube where the pressure loss is mainly due to friction drag, the pressure drag is dominant in ribbed tubes (where the pressure loss increases by a factor of 6), and can be well predicted on a coarse mesh with $y^+ = 10$ at the wall. As it is an effect of pressure, classical wall laws for smooth pipes do not work and WRLES is therefore used. The impact of ribs on the thermal behavior is also shown as a thicker thermal boundary layer, and enhanced heat transfer by a factor of 3.

Ethane cracking chemistry in the same configurations of smooth and ribbed tubes are studied in Chap. 5. Ethane cracking chemistry has been implemented in the code AVBP and validated against 0D PSR calculations, obtained with Cantera and Senkin. Simulations of ethane cracking within the configurations S51 and R51 show better performances of the ribbed tube R51 on ethylene production, thanks to the stronger heat transfer, turbulent fluctuations and mixing.

Finally the industrial applications from TOTAL are studied in Chap. 6. Butane cracking chemistry has been implemented in the code AVBP and also validated against 0D PSR calculations, obtained with Cantera and Senkin. Simulations of butane cracking process within the industrial configurations S38 (smooth tube) and R38 (ribbed tube), with an imposed heat flux at the wall and the density variation model are performed. Higher skin temperature, faster conversion of butane and higher selectivity of ethylene are observed in the tube S38. Lower skin temperature which reduces the coking phenomena is found in R38, as expected, thanks to better mixing and faster heat transfer. First analysis shows that during the time today simulated, the higher temperature in the near wall region of S38 is responsible for the faster conversion of butane. However, when the reacting flow becomes more homogeneous as time increases, this effect may no longer dominate and higher conversion of butane may appear in R38. Further investigations will be conducted in the simulations increasing the total simulation time.

This work has demonstrated the feasibility of LES of steam-cracking processes in realistic conditions at a reasonable CPU cost, thanks to periodic boundary conditions. The methodology that has been developed, based on specific source terms to reproduce the correct thermodynamic conditions, allows to accurately describe the involved phenomena and their interactions. Results demonstrate the significant and important information brought by the simulations, which are able to describe and explain the complexity of such system behaviors.

Bibliography

[1] Charles E Baukal Jr. *The John Zink Hamworthy Combustion Handbook: Volume 1-Fundamentals*. CRC Press, 2012.

[2] IHRDC. Overview of petrochemicals. `http://www.petroleumonline.com/content/overview.asp?mod=11`, 2015.

[3] Office of Industrial Technology U.S. Department of Energy. *Petroleum - Industry of the Future: Energy and Environmental Profile of the U.S. Petroleum Refining Industry*. U.S. Department of Energy, Washington, DC, December 1998.

[4] Psrinteractive. Fired heater - cabin design 03. `https://www.flickr.com/photos/44768056@N05/4147728536/in/photostream/`, 2009.

[5] Psrinteractive. Fired heater - cabin design 04. `https://www.flickr.com/photos/44768056@N05/4146970941/in/photostream/`, 2009.

[6] theleftcoast. Furnace efficiency. `http://www.cheresources.com/invision/topic/10604-furnace-efficiency/`, 2010.

[7] Charles E Baukal Jr. *Industrial combustion testing*. CRC Press, 2010.

[8] Marcello Picciotti. Novel ethylene technologies developing, but steam cracking remains king. *Oil and Gas Journal*, 95(25), 1997.

[9] C.Nithiyesh Kumar and P.Murugesan. Review on twisted tapes heat transfer enhancement. *International Journal Of Scientific & Engineering Research*, 3(4), 2012.

[10] Pedro G Vicente, Alberto García, and Antonio Viedma. Heat transfer and pressure drop for low reynolds turbulent flow in helically dimpled tubes. *International Journal of Heat and Mass Transfer*, 45(3):543–553, 2002.

[11] James G Withers. Tube-side heat transfer and pressure drop for tubes having helical internal ridging with turbulent/transitional flow of single-phase fluid. part 1. single-helix ridging. *Heat Transfer Engineering*, 2(1):48–58, 1980.

[12] J. Nikuradse. *Laws of flow in rough pipes*. National Advisory Committee for Aeronautics Washington, 1950.

[13] A. García, J.P. Solano, P.G. Vicente, and A. Viedma. The influence of artificial roughness shape on heat transfer enhancement: Corrugated tubes, dimpled tubes and wire coils. *Applied Thermal Engineering*, 35(0):196 – 201, 2012.

[14] R.L Webb, E.R.G Eckert, and R.J Goldstein. Heat transfer and friction in tubes with repeated-rib roughness. *International Journal of Heat and Mass Transfer*, 14(4):601 – 617, 1971.

[15] D.L. Gee and RL Webb. Forced convection heat transfer in helically rib-roughened tubes. *International Journal of Heat and Mass Transfer*, 23(8):1127–1136, 1980.

[16] Pedro G Vicente, Alberto García, and Antonio Viedma. Experimental investigation on heat transfer and frictional characteristics of spirally corrugated tubes in turbulent flow at different Prandtl numbers. *International journal of heat and mass transfer*, 47(4):671–681, 2004.

[17] R. Sethumadhavan and M. Raja Rao. Turbulent flow heat transfer and fluid friction in helical-wire-coil-inserted tubes. *International journal of heat and mass transfer*, 26(12):1833–1845, 1983.

[18] S.K. Saha. Thermal and friction characteristics of turbulent flow through rectangular and square ducts with transverse ribs and wire-coil inserts. *Experimental Thermal and Fluid Science*, 34(5):575–589, 2010.

[19] A. E. Perry, W. H. Schofield, and P. N. Joubert. Rough wall turbulent boundary layers. *Journal of Fluid Mechanics*, 37, 1969.

[20] J. Tani. *Turbulent boundary layer development over rough surfaces. In: Perspectives in Turbulence Studies*. Springer, 1987.

[21] Jie Cui, Virendra C Patel, and Ching-Long Lin. Large-eddy simulation of turbulent flow in a channel with rib roughness. *International Journal of Heat and Fluid Flow*, 24(3):372–388, 2003. Contains Selected Keynote Lectures from the 12th International Heat Transfer Conference.

[22] M. Inui, K. Hamada, and K. Otsubo. Cracking tube having helical fins, July 9 2009. US Patent App. 12/379,845.

[23] D. Viennet and E. Platvoet. Process for quenching the effluent gas of a furnace, November 10 2010. EP Patent App. EP20,090,159,742.

[24] M. Inui, K. Hamada, and K. Otsubo. Cracking tube having helical fins, September 21 2010. US Patent 7,799,963.

[25] K. Hashimoto. Thermal cracking tube, June 10 2010. US Patent App. 12/593,867.

[26] K. Hashimoto. Thermal cracking tube, July 31 2012. US Patent 8,231,837.

[27] Kubota Corporation. Kubota steel castings. `http://caststeel.kubota.co.jp/e/emc/emc-a.html`, 2004-2015.

[28] Stephen B Pope. *Turbulent flows*. Cambridge university press, 2000.

[29] Th Von Karman. Mechanical similitude and turbulence. 1931.

[30] Garbis Hovannes Keulegan. *Laws of turbulent flow in open channels*, volume 21. National Bureau of Standards US, 1938.

[31] Cyril Frank Colebrook. Turbulent flow in pipes, with particular reference to the transition region between the smooth and rough pipe laws. *Journal of the ICE*, 11(4):133–156, 1939.

[32] L.F. Moody. Friction factors for pipe flow. *Trans. Asme*, 66(8):671–684, 1944.

[33] Robert G Deissler. *Analytical and experimental investigation of adiabatic turbulent flow in smooth tubes.* National Advisory Committee for Aeronautics, 1950.

[34] John Laufer. The structure of turbulence in fully developed pipe flow. 1954.

[35] BS Petukhov and VN Popov. Theoretical calculation of heat exchange and frictional resistance in turbulent flow in tubes of an incompressible fluid with variable physical properties(heat exchange and frictional resistance in turbulent flow of liquids with variable physical properties through tubes). *High Temperature*, 1:69–83, 1963.

[36] Stuart W Churchill. Comprehensive correlating equations for heat, mass and momentum transfer in fully developed flow in smooth tubes. *Industrial & Engineering Chemistry Fundamentals*, 16(1):109–116, 1977.

[37] B.A. Kader. Temperature and concentration profiles in fully turbulent boundary layers. *International Journal of Heat and Mass Transfer*, 24(9):1541 – 1544, 1981.

[38] John Kim, Parviz Moin, and Robert Moser. Turbulence statistics in fully developed channel flow at low reynolds number. *Journal of fluid mechanics*, 177:133–166, 1987.

[39] JGM Eggels, F Unger, MH Weiss, J Westerweel, RJ Adrian, R Friedrich, and FTM Nieuwstadt. Fully developed turbulent pipe flow: a comparison between direct numerical simulation and experiment. *Journal of Fluid Mechanics*, 268:175–210, 1994.

[40] E. Choi and YI Cho. Local friction and heat transfer behavior of water in a turbulent pipe flow with a large heat flux at the wall. *Journal of heat transfer*, 117(2), 1995.

[41] Robert D Moser, John Kim, and Nagi N Mansour. Direct numerical simulation of turbulent channel flow up to Re= 590. *Phys. Fluids*, 11(4):943–945, 1999.

[42] M Piller. Direct numerical simulation of turbulent forced convection in a pipe. *International journal for numerical methods in fluids*, 49(6):583–602, 2005.

[43] L Redjem-Saad, M Ould-Rouiss, and G Lauriat. Direct numerical simulation of turbulent heat transfer in pipe flows: Effect of Prandtl number. *International Journal of Heat and Fluid Flow*, 28(5):847–861, 2007.

[44] D. Veynante T. Poinsot. *Theoretical and Numerical Combustion.* Third Edition (www.cerfacs.fr/elearning), 2011.

[45] Frank P Incropera. *Fundamentals of heat and mass transfer.* John Wiley & Sons, 2011.

[46] George Gabriel Stokes. On the effect of the internal friction of fluids on the motion of pendulums. *Transactions of the Cambridge Philosophical Society*, 9:8, 1851.

[47] Osborne Reynolds. An experimental investigation of the circumstances which determine whether the motion of water shall be direct or sinuous, and of the law of resistance in parallel channels. *Proceedings of the royal society of London*, 35(224-226):84–99, 1883.

[48] N Rott. Note on the history of the Reynolds number. *Annual review of fluid mechanics*, 22(1):1–12, 1990.

[49] Gregory Falkovich. *Fluid mechanics: A short course for physicists*. Cambridge University Press, 2011.

[50] JP Holman. Heat transfer, 9th, 2002.

[51] Rémy Fransen. *LES based aerothermal modeling of turbine blade cooling systems*. PhD thesis, Institut National Polytechnique de Toulouse-INPT, 2013.

[52] Robert S Rogallo and Parviz Moin. Numerical simulation of turbulent flows. *Annual Review of Fluid Mechanics*, 16(1):99–137, 1984.

[53] Haecheon Choi and Parviz Moin. Grid-point requirements for large eddy simulation: Chapman's estimates revisited. *Physics of Fluids (1994-present)*, 24(1):011702, 2012.

[54] Parviz Moin and Krishnan Mahesh. Direct numerical simulation: a tool in turbulence research. *Annual review of fluid mechanics*, 30(1):539–578, 1998.

[55] AJ Favre. The equations of compressible turbulent gases. Technical report, DTIC Document, 1965.

[56] Guillaume Boudier, LYM Gicquel, Thierry Poinsot, D Bissieres, and C Bérat. Comparison of LES, RANS and experiments in an aeronautical gas turbine combustion chamber. *Proceedings of the Combustion Institute*, 31(2):3075–3082, 2007.

[57] David Corson, Rajeev Jaiman, and Farzin Shakib. Industrial application of rans modelling: capabilities and needs. *International Journal of Computational Fluid Dynamics*, 23(4):337–347, 2009.

[58] Ugo Piomelli and Elias Balaras. Wall-layer models for large-eddy simulations. *Annual review of fluid mechanics*, 34(1):349–374, 2002.

[59] Paul J Mason. Large-eddy simulation: A critical review of the technique. *Quarterly Journal of the Royal Meteorological Society*, 120(515):1–26, 1994.

[60] Marcel Lesieur and Olivier Metais. New trends in large-eddy simulations of turbulence. *Annual Review of Fluid Mechanics*, 28(1):45–82, 1996.

[61] Ugo Piomelli. Large-eddy simulation: achievements and challenges. *Progress in Aerospace Sciences*, 35(4):335–362, 1999.

[62] Charles Meneveau and Joseph Katz. Scale-invariance and turbulence models for large-eddy simulation. *Annual Review of Fluid Mechanics*, 32(1):1–32, 2000.

[63] L Prandtl. Verhandlungen des dritten internationalen mathematiker-kongresses. *Heidelberg, Leipeizig*, pages 484–491, 1904.

[64] BC Sakiadis. Boundary-layer behavior on continuous solid surfaces: I. boundary-layer equations for two-dimensional and axisymmetric flow. *AIChE Journal*, 7(1):26–28, 1961.

[65] MJ Lighthill. Boundary layer theory, 1963.

[66] Stephen K Robinson. Coherent motions in the turbulent boundary layer. *Annual Review of Fluid Mechanics*, 23(1):601–639, 1991.

[67] Herrmann Schlichting, Klaus Gersten, and Klaus Gersten. *Boundary-layer theory*. Springer Science & Business Media, 2000.

[68] Symscape. Boundary layer. `http://www.symscape.com/node/447`, 2007.

[69] Heinrich Blasius. *Das Ähnlichkeitsgesetz bei Reibungsvorgängen in Flüssigkeiten*. Springer, 1913.

[70] L Fulachier and R Dumas. Spectral analogy between temperature and velocity fluctuations in a turbulent boundary layer. *Journal of Fluid Mechanics*, 77(02):257–277, 1976.

[71] Yoichiro Iritani, Nobuhide Kasagi, and Masaru Hirata. Heat transfer mechanism and associated turbulence structure in the near-wall region of a turbulent boundary layer. In *Turbulent Shear Flows 4*, pages 223–234. Springer, 1985.

[72] RA Antonia, LV Krishnamoorthy, and L Fulachier. Correlation between the longitudinal velocity fluctuation and temperature fluctuation in the near-wall region of a turbulent boundary layer. *International journal of heat and mass transfer*, 31(4):723–730, 1988.

[73] L Fulachier and RA Antonia. Spectral analogy between temperature and velocity fluctuations in several turbulent flows. *International journal of heat and mass transfer*, 27(7):987–997, 1984.

[74] Hojin Kong, Haecheon Choi, and Joon Sik Lee. Direct numerical simulation of turbulent thermal boundary layers. *Physics of Fluids (1994-present)*, 12(10):2555–2568, 2000.

[75] William Morrow Kays, Michael E Crawford, and Bernhard Weigand. *Convective heat and mass transfer*, volume 3. McGraw-Hill New York, 1993.

[76] Jin Lee, Seo Yoon Jung, Hyung Jin Sung, and Tamer A Zaki. Effect of wall heating on turbulent boundary layers with temperature-dependent viscosity. *Journal of Fluid Mechanics*, 726:196–225, 2013.

[77] Y.A. Çengel and J.M. Cimbala. *Fluid Mechanics: Fundamentals and Applications*. McGraw-Hill series in mechanical engineering. McGraw-HillHigher Education, 2006.

[78] Hiroshi Kawamura, Kouichi Ohsaka, Hiroyuki Abe, and Kiyoshi Yamamoto. DNS of turbulent heat transfer in channel flow with low to medium-high prandtl number fluid. *International Journal of Heat and Fluid Flow*, 19(5):482–491, 1998.

[79] Shin-ichi Satake and Tomoaki Kunugi. Direct numerical simulation of turbulent heat transfer in an axially rotating pipe flow: Reynolds shear stress and scalar flux budgets. *International Journal of Numerical Methods for Heat & Fluid Flow*, 12(8):958–1008, 2002.

[80] Th Von Karman. Turbulence and skin friction. *Journal of the Aeronautical Sciences (Institute of the Aeronautical Sciences)*, 1(1), 1934.

[81] Khanh Tuoc Trinh. On the Blasius correlation for friction factors. *arXiv preprint arXiv:1007.2466*, 2010.

[82] RA Gowen and JW Smith. The effect of the Prandtl number on temperature profiles for heat transfer in turbulent pipe flow. *Chemical Engineering Science*, 22(12):1701–1711, 1967.

[83] Volker Gnielinski. New equations for heat and mass transfer in the turbulent flow in pipes and channels. *NASA STI/Recon Technical Report A*, 75:22028, 1975.

[84] FW Dittus and LMK Boelter. University of california publications on engineering. *University of California publications in Engineering*, 2:371, 1930.

[85] RHS Winterton. Where did the Dittus and Boelter equation come from? *International Journal of Heat and Mass Transfer*, 41(4):809–810, 1998.

[86] WH McAdams and TH Frost. Heat transfer by conduction and convection II: Liquids flowing through pipes. *Industrial & Engineering Chemistry*, 14(12):1101–1104, 1922.

[87] WH McAdams and TH Frost. Heat transfer for water flowing inside pipes. *Refrigerating Engineering*, 10(9):323–334, 1924.

[88] FH Morris and Walter G Whitman. Heat transfer for oils and water in pipes 1. *Industrial & Engineering Chemistry*, 20(3):234–240, 1928.

[89] E Nn Sieder and Go E Tate. Heat transfer and pressure drop of liquids in tubes. *Industrial & Engineering Chemistry*, 28(12):1429–1435, 1936.

[90] L. N. Il'in. *Kotloturbostroenie*, 1, 1951.

[91] CA Sleicher and MW Rouse. A convenient correlation for heat transfer to constant and variable property fluids in turbulent pipe flow. *International Journal of Heat and Mass Transfer*, 18(5):677–683, 1975.

[92] Olivier Cabrit. *Modélisation des flux pariétaux sur les tuyères des moteurs à propergol solide*. PhD thesis, Montpellier 2, 2009.

[93] Khosrow Nourmohammadi, PK Hopke, and JJ Stukel. Turbulent air flow over rough surfaces: II. turbulent flow parameters. *Journal of Fluids Engineering*, 107(1):55–60, 1985.

[94] A Palikaras, K Yakinthos, and A Goulas. The effect of negative shear on the transitional separated flow around a semi-circular leading edge. *International Journal of Heat and Fluid Flow*, 24(3):421 – 430, 2003. Contains Selected Keynote Lectures from the 12th International Heat Transfer Conference.

[95] Luca Casarsa, Murat Çakan, and Tony Arts. Characterization of the velocity and heat transfer fields in an internal cooling channel with high blockage ratio. In *ASME Turbo Expo 2002: Power for Land, Sea, and Air*, pages 451–458. American Society of Mechanical Engineers, 2002.

[96] Luca Casarsa and Tony Arts. Experimental investigation of the aerothermal performance of a high blockage rib-roughened cooling channel. *Journal of turbomachinery*, 127(3):580–588, 2005.

[97] Seung-Hyun Lee, Jung Hun Kim, and Hyung Jin Sung. PIV measurements of turbulent boundary layer over a rod-roughened wall. *International Journal of Heat and Fluid Flow*, 29(6):1679 – 1687, 2008.

[98] Lei Wang, Mirko Salewski, and Bengt Sundén. Turbulent flow in a ribbed channel: Flow structures in the vicinity of a rib. *Experimental Thermal and Fluid Science*, 34(2):165 – 176, 2010.

[99] J.M. Tsikata and M.F. Tachie. Adverse pressure gradient turbulent flows over rough walls. *International Journal of Heat and Fluid Flow*, 39(0):127 – 145, 2013.

[100] Y.Z. Liu, F. Ke, and H.J. Sung. Unsteady separated and reattaching turbulent flow over a two-dimensional square rib. *Journal of Fluids and Structures*, 24(3):366 – 381, 2008.

[101] Tong-Miin Liou, Jenn-Jiang Hwang, and Shih-Hui Chen. Simulation and measurement of enhanced turbulent heat transfer in a channel with periodic ribs on one principal wall. *International Journal of Heat and Mass Transfer*, 36(2):507 – 517, 1993.

[102] S. Lorenz, D. Mukomilow, and W. Leiner. Distribution of the heat transfer coefficient in a channel with periodic transverse grooves. *Experimental Thermal and Fluid Science*, 11(3):234 – 242, 1995. Generation and Structure of Vortical Flows for Heat Transfer Enhancement.

[103] B Arman and TJ Rabas. The influence of the rib width on the performance of tubes with the separation and reattachment enhancement mechanism. Technical report, Argonne National Lab., IL (United States), 1992.

[104] Wei Peng, Pei-Xue Jiang, Yang-Ping Wang, and Bing-Yuan Wei. Experimental and numerical investigation of convection heat transfer in channels with different types of ribs. *Applied Thermal Engineering*, 31(14):2702–2708, 2011.

[105] John R Thome. Engineering data book III. *Wolverine Tube Inc*, 2004.

[106] P. L. Mantle. A new type of roughened heat transfer surface selected by flow visualization techniques. In *Proc. Third Int. Heat-Transfer Conf.*, volume 1, pages 44–45, 1966.

[107] Md Shafiqul Islam, M Monde, K Haga, M Kaminaga, and R Hino. Turbulent flow structure in fully developed narrow rib-roughened channel with PIV technique.

[108] DA Aliaga, JP Lamb, and DE Klein. Convection heat transfer distributions over plates with square ribs from infrared thermography measurements. *International journal of heat and mass transfer*, 37(3):363–374, 1994.

[109] Shafiqul M Islam, K Haga, M Kaminaga, R Hino, and M Monde. Experimental analysis of turbulent flow structure in a fully developed rib-roughened rectangular channel with PIV. *Experiments in Fluids*, 33(2):296–306, 2002.

[110] Javier Jimenez. Turbulent Flows Over Rough Walls. *Annual Review of Fluid Mechanics*, 36(1991):173–196, 2004.

[111] Jae Hwa Lee, Seung-Hyun Lee, Kyoungyoun Kim, and Hyung Jin Sung. Structure of the turbulent boundary layer over a rod-roughened wall. *International Journal of Heat and Fluid Flow*, 30(6):1087 – 1098, 2009.

[112] O. Labbé. Large-eddy-simulation of flow and heat transfer in a ribbed duct. *Computers & Fluids*, 76(0):23 – 32, 2013.

[113] S. Leonardi, P. Orlandi, L. Djenidi, and R.A. Antonia. Structure of turbulent channel flow with square bars on one wall. *International Journal of Heat and Fluid Flow*, 25(3):384 – 392, 2004. Turbulence and Shear Flow Phenomena (TSFP-3).

[114] Yasutaka Nagano, Hirofumi Hattori, and Tomoya Houra. DNS of velocity and thermal fields in turbulent channel flow with transverse-rib roughness. *International Journal of Heat and Fluid Flow*, 25(3):393 – 403, 2004. Turbulence and Shear Flow Phenomena (TSFP-3).

[115] P-Å Krogstadt and RA Antonia. Surface roughness effects in turbulent boundary layers. *Experiments in Fluids*, 27(5):450–460, 1999.

[116] M. Agelinchaab and M.F. Tachie. Open channel turbulent flow over hemispherical ribs. *International Journal of Heat and Fluid Flow*, 27(6):1010 – 1027, 2006.

[117] Seung-Hyun Lee and Hyung Jin Sung. Direct numerical simulation of the turbulent boundary layer over a rod-roughened wall. *Journal of Fluid Mechanics*, 584:125–146, 2007.

[118] M Cakan. *Aero-thermal investigation of fixed rib-roughened internal cooling passages.* PhD thesis, von Karman Institute & Université Catholique de Louvain (Belgique), 2000.

[119] R. V. Mises. Elemente der technischen hydrodynamik. *Teubner, Leipzig*, 1914.

[120] T. E. Stanton. The mechanical viscosity of fluids. *Proceedings of the Royal Society A*, pages 366–376, 1911.

[121] Y.F. Zhang, F.Y. Li, and Z.M. Liang. Heat transfer in spiral-coil-inserted tubes and its application. In *Advances in Heat Transfer Augmention, MA Ebadin, DW Pepper and T. Diller, Eds., ASME Symp. Vol. HTD*, volume 169, pages 31–36, 1991.

[122] TS Ravigururajan and AE Bergles. Development and verification of general correlations for pressure drop and heat transfer in single-phase turbulent flow in enhanced tubes. *Experimental Thermal and Fluid Science*, 13(1):55 – 70, 1996.

[123] A. García, P.G. Vicente, and A. Viedma. Experimental study of heat transfer enhancement with wire coil inserts in laminar-transition-turbulent regimes at different Prandtl numbers. *International Journal of Heat and Mass Transfer*, 48(21):4640–4651, 2005.

[124] W. Nakayama, K. Takahashi, and T. Daikoku. Spiral ribbing to enhance single-phase heat transfer inside tubes. In *Proceedings of the ASME–JSME Thermal Engineering Joint Conference, Honolulu*, 1983.

[125] HM Li, KS Ye, YK Tan, and SJ Deng. Investigation on tube-side flow visualization, friction factors and heat transfer characteristics of helical-ridging tubes. In *Proceedings of the 7th International Heat Transfer Conference*, volume 3, pages 75–80. Grigull, 1982.

[126] D.F. Dipprey and R.H. Sabersky. Heat and momentum transfer in smooth and rough tubes at various Prandtl numbers. *International Journal of Heat and Mass Transfer*, 6(5):329 – 353, 1963.

[127] AE Bergles, AR Blumenkrantz, and J. Taborek. Performance evaluation criteria for enhanced heat transfer surfaces. *J. Heat Transfer*, 2:239 – 243, 1974.

[128] P.R. Chandra, M.L. Fontenot, and J.C. Han. Effect of rib profiles on turbulent channel flow heat transfer. *Journal of thermophysics and heat transfer*, 12(1):116–118, 1998.

[129] Je-Hoon Kim, Kenneth E. Jansen, and Michael K. Jensen. Analysis of heat transfer characteristics in internally finned tubes. *Numerical Heat Transfer, Part A: Applications*, 46(1):1–21, 2004.

[130] Alireza Ashrafian, Helge I. Andersson, and Michael Manhart. DNS of turbulent flow in a rod-roughened channel. *International Journal of Heat and Fluid Flow*, 25(3):373 – 383, 2004. Turbulence and Shear Flow Phenomena (TSFP-3).

[131] H. Braun, H. Neumann, and N.K. Mitra. Experimental and numerical investigation of turbulent heat transfer in a channel with periodically arranged rib roughness elements. *Experimental Thermal and Fluid Science*, 19(2):67 – 76, 1999.

[132] Kyung-Soo Yang. Large eddy simulation of turbulent flows in periodically grooved channel. *Journal of Wind Engineering and Industrial Aerodynamics*, 84(1):47 – 64, 2000.

[133] Lionel Temmerman and Michael A Leschziner. Large-eddy simulation of separated flow in a streamwise periodic channel constriction. In *Second international symposium turbulence and shear flow phenomena*, pages 399–404, 2001.

[134] Lionel Temmerman, Michael A. Leschziner, Christopher P. Mellen, and Jochen FrÃűhlich. Investigation of wall-function approximations and subgrid-scale models in large eddy simulation of separated flow in a channel with streamwise periodic constrictions. *International Journal of Heat and Fluid Flow*, 24(2):157 – 180, 2003.

[135] Jochen Fröhlich, Christopher. P. Mellen, Wolfgang Rodi, Lionel Temmerman, and Michael a. Leschziner. Highly resolved large-eddy simulation of separated flow in a channel with streamwise periodic constrictions. *Journal of Fluid Mechanics*, 526:19–66, 2005.

[136] M. M. Lohász, P. Rambaud, and C. Benocci. Flow features in a fully developed ribbed duct flow as a result of LES. *Engineering Turbulence Modelling and Experiments 6*, pages 267–276, 2005.

[137] P Vass Xcifb, P Rambaud, and M M Loh. Large eddy simulation of a ribbed duct flow with FLUENT: Effect of rib inclination. (May), 2005.

[138] Evan A. Sewall, Danesh K. Tafti, Andrew B. Graham, and Karen A. Thole. Experimental validation of large eddy simulations of flow and heat transfer in a stationary ribbed duct. *International Journal of Heat and Fluid Flow*, 27(2):243 – 258, 2006.

[139] Joon Ahn, Haecheon Choi, and Joon Sik Lee. Large eddy simulation of flow and heat transfer in a rotating ribbed channel. *International Journal of Heat and Mass Transfer*, 50(25):4937–4947, 2007.

[140] Zhenhua Xia, Yipeng Shi, Renkai Hong, Zuoli Xiao, and Shiyi Chen. Constrained large-eddy simulation of separated flow in a channel with streamwise-periodic constrictions. *Journal of Turbulence*, 14(1):1–21, 2013.

[141] A. Ooi, G. Iaccarino, P.A. Durbin, and M. Behnia. Reynolds averaged simulation of flow and heat transfer in ribbed ducts. *International Journal of Heat and Fluid Flow*, 23(6):750 – 757, 2002.

[142] G. Iaccarino, A. Ooi, P.A. Durbin, and M. Behnia. Conjugate heat transfer predictions in two-dimensional ribbed passages. *International Journal of Heat and Fluid Flow*, 23(3):340 – 345, 2002.

[143] Tong-Miin Liou, Shih-Hui Chen, and Kuan-Chen Shih. Numerical simulation of turbulent flow field and heat transfer in a two-dimensional channel with periodic slit ribs. *International Journal of Heat and Mass Transfer*, 45(22):4493 – 4505, 2002.

[144] Hong-Min Kim and Kwang-Yong Kim. Design optimization of rib-roughened channel to enhance turbulent heat transfer. *International Journal of Heat and Mass Transfer*, 47(23):5159 – 5168, 2004.

[145] D.N. Ryu, D.H. Choi, and V.C. Patel. Analysis of turbulent flow in channels roughened by two-dimensional ribs and three-dimensional blocks. part ii: Heat transfer. *International Journal of Heat and Fluid Flow*, 28(5):1112 – 1124, 2007.

[146] R. Kamali and Ali Reza Binesh. The importance of rib shape effects on the local heat transfer and flow friction characteristics of square ducts with ribbed internal surfaces. *International Communications in Heat and Mass Transfer*, 35:1032–1040, 2008.

[147] Smith Eiamsa-ard and Pongjet Promvonge. Numerical study on heat transfer of turbulent channel flow over periodic grooves. *International Communications in Heat and Mass Transfer*, 35(7):844–852, 2008.

[148] Ting Ma, Qiu-wang Wang, Min Zeng, Yi-tung Chen, Yang Liu, and Vijaisri Nagarajan. Study on heat transfer and pressure drop performances of ribbed channel in the high temperature heat exchanger. *Applied Energy*, 99:393–401, 2012.

[149] Stephen A. Jordan. The turbulent character and pressure loss produced by periodic symmetric ribs in a circular duct. *International Journal of Heat and Fluid Flow*, 24(6):795 – 806, 2003.

[150] Sowjanya Vijiapurapu and Jie Cui. Simulation of turbulent flow in a ribbed pipe using large eddy simulation. *Numerical Heat Transfer, Part A: Applications*, 51(12):1137–1165, 2007.

[151] Sowjanya Vijiapurapu and Jie Cui. Performance of turbulence models for flows through rough pipes. *Applied Mathematical Modelling*, 34(6):1458 – 1466, 2010.

[152] L.I. Shub. Calculation of turbulent flow and heat transfer in a tube with a periodically varying cross-section. *International Journal of Heat and Mass Transfer*, 36(4):1085–1095, 1993.

[153] Xiaoyue Liu and Michael K Jensen. Geometry effects on turbulent flow and heat transfer in internally finned tubes. *Journal of heat transfer*, 123(6):1035–1044, 2001.

[154] Je-Hoon Kim, Kenneth E Jansen, and Michael K Jensen. Simulation of three-dimensional incompressible turbulent flow inside tubes with helical fins. *Numerical Heat Transfer, Part B*, 46(3):195–221, 2004.

[155] Özden Ağra, Hakan Demir, Ş Özgür Atayılmaz, Fatih Kantaş, and Ahmet Selim Dalkılıç. Numerical investigation of heat transfer and pressure drop in enhanced tubes. *International Communications in Heat and Mass Transfer*, 38(10):1384–1391, 2011.

[156] S Hossainpour and R Hassanzadeh. Numerical investigation of tub side heat transfer and pressure drop in helically corrugated tubes. *International Journal of Energy and Environmental Engineering*, 2(2):65–75, 2011.

[157] Suhas Patankar. *Numerical heat transfer and fluid flow.* CRC Press, 1980.

[158] JO Hinze. Turbulence (2nd edn). *McGraw-Hiil, New York*, 1975.

[159] Eunjung Joo, Kihong Lee, Moonyong Lee, and Sunwon Park. CRACKER–a PC based simulator for industrial cracking furnaces. *Computers & Chemical Engineering*, 24(2):1523–1528, 2000.

[160] Geraldine J Heynderickx, Arno JM Oprins, Guy B Marin, and Erik Dick. Three-dimensional flow patterns in cracking furnaces with long-flame burners. *AIChE journal*, 47(2):388–400, 2001.

[161] Arno JM Oprins, Geraldine J Heynderickx, and Guy B Marin. Three-dimensional asymmetric flow and temperature fields in cracking furnaces. *Industrial & engineering chemistry research*, 40(23):5087–5094, 2001.

[162] AJM Oprins and GJ Heynderickx. Calculation of three-dimensional flow and pressure fields in cracking furnaces. *Chemical engineering science*, 58(21):4883–4893, 2003.

[163] A Niaei, J Towfighi, SM Sadrameli, and R Karimzadeh. The combined simulation of heat transfer and pyrolysis reactions in industrial cracking furnaces. *Applied Thermal Engineering*, 24(14):2251–2265, 2004.

[164] Hu Guihua, Wang Honggang, and Qian Feng. Numerical simulation on flow, combustion and heat transfer of ethylene cracking furnaces. *Chemical engineering science*, 66(8):1600–1611, 2011.

[165] Nan Zheng, Qui Tong, and Chen Bingzhen. CFD simulation of propane cracking tube using detailed radical kinetic mechanism. *Chinese Journal of Chemical Engineering*, 21(12):1319–1331, 2013.

[166] Carl M Schietekat, David J Cauwenberge, Kevin M Geem, and Guy B Marin. Computational fluid dynamics-based design of finned steam cracking reactors. *AIChE Journal*, 60(2):794–808, 2014.

[167] Dean Khalil Chapman. Computatisnal aerodynamics development and outlook. *AIAA journal*, 17(12):1293–1313, 1979.

[168] Pierre Sagaut, Eric Garnier, Eric Tromeur, Lionel Larcheveque, and Emmanuel Labourasse. Turbulent inflow conditions for large-eddy-simulation of compressible wall-bounded flows. *AIAA journal*, 42(3):469–477, 2004.

[169] Lars Davidson. Large eddy simulations: how to evaluate resolution. *International Journal of Heat and Fluid Flow*, 30(5):1016–1025, 2009.

[170] J Dombard and G Iaccarino. Sensitivity analysis to the normal grid-resolution in a turbulent channel flow using large-eddy simulations.

[171] T. Schönfeld and M. Rudgyard. Steady and unsteady flow simulations using the hybrid flow solver AVBP. *AIAA journal*, 37(11):1378–1385, 1999.

[172] V Moureau, G Lartigue, Y Sommerer, C Angelberger, O Colin, and Thierry Poinsot. Numerical methods for unsteady compressible multi-component reacting flows on fixed and moving grids. *Journal of Computational Physics*, 202(2):710–736, 2005.

[173] CERFACS. AVBP handbook. `http://www.cerfacs.fr/~avbp/AVBP_V6.X/HANDBOOK/AVBP/`, 2011.

[174] Joseph Smagorinsky. General circulation experiments with the primitive equations: I. the basic experiment*. *Monthly weather review*, 91(3):99–164, 1963.

[175] Franck Nicoud and Frédéric Ducros. Subgrid-scale stress modelling based on the square of the velocity gradient tensor. *Flow, turbulence and Combustion*, 62(3):183–200, 1999.

[176] Olivier Colin and Michael Rudgyard. Development of high-order Taylor-Galerkin schemes for LES. *J. Comput. Phys.*, 162(2):338–371, August 2000.

[177] Peter Lax and Burton Wendroff. Systems of conservation laws. *Communications on Pure and Applied mathematics*, 13(2):217–237, 1960.

[178] O. Colin. A finite element operator for diffusion terms in AVBP. `http://www.cerfacs.fr/~avbp/AVBP_V6.X/DOC/DIFF/op_diffusion.pdf`, 2003.

[179] O. Colin. Simulations aux grandes échelles de la combustion turbulente premelangée dans les statoreacteurs. *Ph.D Thesis, INP Toulouse*, 2000.

[180] Edward R Van Driest. Turbulent boundary layer in compressible fluids. *Journal of spacecraft and rockets*, 40(6):1012–1028, 2003.

[181] Xi Jiang and Choi-Hong Lai. *Numerical techniques for direct and large-eddy simulations*. CRC Press, 2009.

[182] JMJ Den Toonder and FTM Nieuwstadt. Reynolds number effects in a turbulent pipe flow for low to moderate Re. *Physics of Fluids (1994-present)*, 9(11):3398–3409, 1997.

[183] Xiaohua Wu and Parviz Moin. A direct numerical simulation study on the mean velocity characteristics in turbulent pipe flow. *Journal of Fluid Mechanics*, 608:81–112, 2008.

[184] Yaser Khalighi, Joseph W Nichols, S Lele, Frank Ham, and Parviz Moin. Unstructured large eddy simulation for prediction of noise issued from turbulent jets in various configurations. *AIAA paper*, 2886, 2011.

[185] Iván Bermejo-Moreno, Laura Campo, Johan Larsson, Julien Bodart, David Helmer, and John K Eaton. Confinement effects in shock wave/turbulent boundary layer interactions through wall-modelled large-eddy simulations. *Journal of Fluid Mechanics*, 758:5–62, 2014.

[186] Johan Larsson, Stuart Laurence, Iván Bermejo-Moreno, Julien Bodart, Sebastian Karl, and Ronan Vicquelin. Incipient thermal choking and stable shock-train formation in the heat-release region of a scramjet combustor. Part II: Large eddy simulations. *Combustion and Flame*, 2014.

[187] Massimo Germano, Ugo Piomelli, Parviz Moin, and William H Cabot. A dynamic subgrid-scale eddy viscosity model. *Physics of Fluids A: Fluid Dynamics (1989-1993)*, 3(7):1760–1765, 1991.

[188] Douglas K Lilly. A proposed modification of the Germano subgrid-scale closure method. *Physics of Fluids A: Fluid Dynamics (1989-1993)*, 4(3):633–635, 1992.

[189] Pet al Moin, K Squires, W Cabot, and Sangsan Lee. A dynamic subgrid-scale model for compressible turbulence and scalar transport. *Physics of Fluids A: Fluid Dynamics (1989-1993)*, 3(11):2746–2757, 1991.

[190] AW Vreman. An eddy-viscosity subgrid-scale model for turbulent shear flow: Algebraic theory and applications. *Physics of Fluids (1994-present)*, 16(10):3670–3681, 2004.

[191] Donghyun You and Parviz Moin. A dynamic global-coefficient subgrid-scale eddy-viscosity model for large-eddy simulation in complex geometries. *Physics of Fluids (1994-present)*, 19(6):065110, 2007.

[192] Maarten K Sabbe, Kevin M Van Geem, Marie-Françoise Reyniers, and Guy B Marin. First principle-based simulation of ethane steam cracking. *AIChE journal*, 57(2):482–496, 2011.

[193] KM Sundaram and GF Froment. Modeling of thermal cracking kinetics - I: Thermal cracking of ethane, propane and their mixtures. *Chemical Engineering Science*, 32(6):601–608, 1977.

[194] DG Goodwin. Cantera user's guide. *Division of Engineering and Applied Science, California Institute of Technology, Pasadena, CA*, 2001.

[195] RJ Kee. Senkin manual. *Chemkin Collection, Release*, 3, 2001.

[196] Robert J Kee, Fran M Rupley, and James A Miller. The chemkin thermodynamic data base. *Unknown*, 1, 1990.

[197] Stephen R Turns. *Thermodynamics: concepts and applications*, volume 1. Cambridge University Press, 2006.

[198] Michael J Zehe. Nasa thermo build. `http://www.grc.nasa.gov/WWW/CEAWeb/ceaThermoBuild.htm`, 2006.

Appendix A

Impact of numerical schemes on PDE for a simple case

A.1 Isothermal 2D case

The grid is on quad $\Delta y \times \Delta y$, as shown in Fig. A.1.1. The boundary condition used at walls is “NO_BOUNDARY” [173].

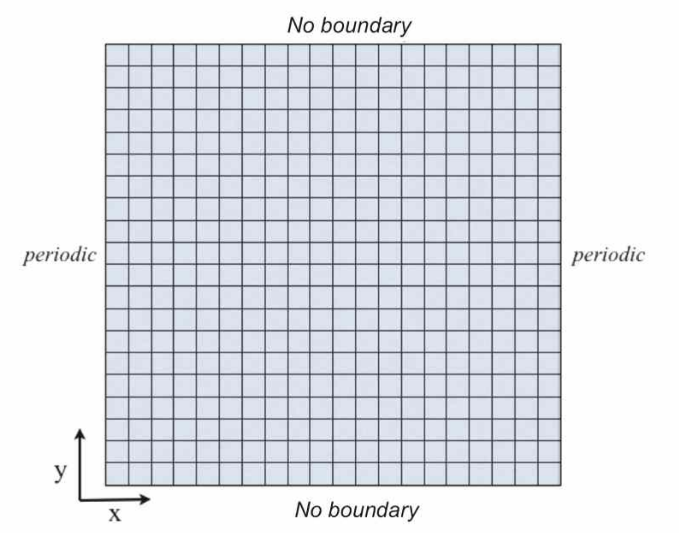

Figure A.1.1: Computational domain

Initial solution
The temperature T and the pressure P are constant, and the velocity in y direction is zero in the whole domain.
The axial velocity u has a parabolic profile: $u = Cy^2$ where C is a constant.

Equation:

$$\frac{\partial U}{\partial t} + \vec{\nabla}\vec{F} = 0 \tag{A.1.1}$$

In $\vec{\nabla}\vec{F}$, it appears the term $\vec{\nabla}(U, \vec{\nabla}U)$. For the viscous flux, $\partial U/\partial t \propto \vec{\nabla}(\vec{\nabla}U)$, and it can be calculated with:

$$\frac{\partial \rho u}{\partial t} \propto \frac{\partial^2 \rho u}{\partial y^2} \propto \frac{\partial^2 u}{\partial y^2} \tag{A.1.2}$$

$$\frac{\partial \rho E}{\partial t} \propto \frac{\partial^2 \rho E}{\partial y^2} \propto \frac{\partial^2 E}{\partial y^2} \propto \frac{\partial^2 \left(\frac{1}{2}u^2\right)}{\partial y^2} \propto \frac{\partial^2 (u^2)}{\partial y^2} \tag{A.1.3}$$

The numerical calculation of $\partial^2 u/\partial y^2$ and $\partial^2(u^2)/\partial y^2$ in the code AVBP with the diffusion operators 4Δ et 2Δ are compared in Table. A.3.1, together with the analytical results.

A.2 Non-isothermal 2D case

The same computational domain and boundary conditions as in the isothermal case are considered.

Initial solution
The pressure P, the velocities u and v are constant in the domain with $P = 1\,\mathrm{atm}, u = 10\,\mathrm{m/s}, v = 0\,\mathrm{m/s}$.
The temperature T has a parabolic profile: $T = 300 + Cy^2$ with a constant C.

Equation:

$$\frac{\partial U}{\partial t} + \vec{\nabla}\vec{F} = 0 \tag{A.2.1}$$

Still for the viscous flux where appears the term $\partial U/\partial t \propto \vec{\nabla}(\vec{\nabla}U)$, the temperature is used to calculate the heat flux $q_y = -\lambda(\partial T/\partial y)$. In the present case, at a node i we have:

$$\left(\frac{\partial \rho E}{\partial t}\right)_i \propto \frac{\partial}{\partial y}\left(\lambda \frac{\partial T}{\partial y}\right)_i \tag{A.2.2}$$

For the RHS, analytical result and the numerical calculations with two diffusion operators 4Δ et 2Δ are written:

Analytical

$$\begin{aligned}\frac{\partial}{\partial y}\left(\lambda\frac{\partial T}{\partial y}\right)_i &= \left(\lambda\frac{\partial^2 T}{\partial y^2}\right)_i + \left(\frac{\partial\lambda}{\partial y}\frac{\partial T}{\partial y}\right)_i \\ &= 2C\lambda_i + 2C\left(\frac{\partial\lambda}{\partial y}\right)_i y_i\end{aligned} \tag{A.2.3}$$

Using 4Δ, at a central node

$$\begin{aligned}\frac{\partial}{\partial y}\left(\lambda\frac{\partial T}{\partial y}\right)_i &= \frac{\left(\lambda\frac{\partial T}{\partial y}\right)_{i+1} - \left(\lambda\frac{\partial T}{\partial y}\right)_{i-1}}{2\Delta y} \\ &= \frac{\lambda_{i+1}\left(\frac{\partial T}{\partial y}\right)_{i+1} - \lambda_{i-1}\left(\frac{\partial T}{\partial y}\right)_{i-1}}{2\Delta y} \\ &= \frac{\lambda_{i+1}\left(\frac{T_{i+2}-T_i}{2\Delta y}\right) - \lambda_{i-1}\left(\frac{T_i - T_{i-2}}{2\Delta y}\right)}{2\Delta y} \\ &= \frac{\lambda_{i+1}T_{i+2} - \lambda_{i+1}T_i - \lambda_{i-1}T_i + \lambda_{i-1}T_{i-2}}{4\Delta y^4} \\ &= \frac{\lambda_{i+1}\left(T_{i+2} - T_{i+1} + T_{i-1} - T_i\right) + \lambda_{i-1}\left(T_{i+1} - T_{i-1} - T_i + T_{i-2}\right)}{4\Delta y^2} \\ &\quad + \frac{(\lambda_{i+1} - \lambda_{i-1})}{2\Delta y}\frac{(T_{i+1} - T_{i-1})}{2\Delta y}(\text{replace } y_{i+k} \text{ by } y_i + k\Delta y) \\ &= 2C\frac{(\lambda_{i+1} + \lambda_{i-1})}{2} + 2C\frac{(\lambda_{i+1} - \lambda_{i-1})}{2\Delta y}y_i\end{aligned} \tag{A.2.4}$$

Using 4Δ, at a node at the wall

$$\begin{aligned}
\frac{\partial}{\partial y}\left(\lambda\frac{\partial T}{\partial y}\right)_i &= \frac{\left(\lambda\dfrac{\partial T}{\partial y}\right)_{i+1}-\left(\lambda\dfrac{\partial T}{\partial y}\right)_i}{\Delta y}\\
&= \frac{\lambda_{i+1}\left(\dfrac{\partial T}{\partial y}\right)_{i+1}-\lambda_i\left(\dfrac{\partial T}{\partial y}\right)_i}{\Delta y}\\
&= \frac{\lambda_{i+1}\left(\dfrac{T_{i+2}-T_i}{2\Delta y}\right)-\lambda_i\left(\dfrac{T_{i+1}-T_i}{\Delta y}\right)}{\Delta y}\\
&= \frac{\lambda_{i+1}T_{i+2}-\lambda_{i+1}T_i-2\lambda_iT_{i+1}+2\lambda_iT_i}{2\Delta y^4}\\
&= \frac{\lambda_{i+1}\left(T_{i+2}-2T_{i+1}+T_i\right)}{2\Delta y^2}+\frac{\left(\lambda_{i+1}-\lambda_i\right)}{\Delta y}\frac{\left(T_{i+1}-T_i\right)}{\Delta y}\\
&\left(\text{replace } y_{i+k} \text{ by } y_i+k\Delta y\right)\\
&= C\lambda_{i+1}+2C\frac{\left(\lambda_{i+1}-\lambda_i\right)}{\Delta y}y_i+C\frac{\left(\lambda_{i+1}-\lambda_i\right)}{\Delta y}\Delta y\\
&\left(y_i \text{ is } 0 \text{ at walls}\right)\\
&= C\lambda_{i+1}+C\left(\lambda_{i+1}-\lambda_i\right)
\end{aligned} \tag{A.2.5}$$

Using 2Δ, at a central node

$$\begin{aligned}
\frac{\partial}{\partial y}\left(\lambda\frac{\partial T}{\partial y}\right)_i &= \frac{\left(\lambda\dfrac{\partial T}{\partial y}\right)_{i+\frac{1}{2}}-\left(\lambda\dfrac{\partial T}{\partial y}\right)_{i-\frac{1}{2}}}{\Delta y}\\
&= \frac{\dfrac{\left(\lambda_{i+1}+\lambda_i\right)}{2}\dfrac{\left(T_{i+1}-T_i\right)}{\Delta y}-\dfrac{\left(\lambda_i+\lambda_{i-1}\right)}{2}\dfrac{\left(T_i-T_{i-1}\right)}{\Delta y}}{\dfrac{1}{2}\Delta y}\\
&= \frac{\lambda_{i+1}(T_{i+1}-T_i)+\lambda_i(T_{i+1}-2T_i+T_{i-1})+\lambda_{i-1}(-T_i+T_{i-1})}{2\Delta y^2}\\
&= \frac{(\lambda_{i+1}+2\lambda_i+\lambda_{i-1})(T_{i+1}-2T_i+T_{i-1})}{4\Delta y^2}+\frac{\left(\lambda_{i+1}-\lambda_{i-1}\right)}{2\Delta y}\frac{\left(T_{i+1}-T_{i-1}\right)}{2\Delta y}\\
&\left(\text{replace } y_{i+k} \text{ by } y_i+k\Delta y\right)\\
&= 2C\frac{\left(\lambda_{i+1}+2\lambda_i+\lambda_{i-1}\right)}{4}+2C\frac{\left(\lambda_{i+1}-\lambda_{i-1}\right)}{2\Delta y}y_i
\end{aligned} \tag{A.2.6}$$

Using 2Δ, at a node at the wall

$$\begin{aligned}
\frac{\partial}{\partial y}\left(\lambda\frac{\partial T}{\partial y}\right)_i &= \frac{\left(\lambda\frac{\partial T}{\partial y}\right)_{i+\frac{1}{2}} - 0}{\frac{1}{2}\Delta y} \\
&= \frac{\frac{(\lambda_{i+1}+\lambda_i)}{2}\frac{(T_{i+1}-T_i)}{\Delta y}}{\frac{1}{2}\Delta y} \\
&= \frac{(\lambda_{i+1}+\lambda_i)(T_{i+1}-T_i)}{\Delta y^2} \\
&= \frac{2\lambda_i(T_{i+1}-T_i)}{\Delta y^2} + \frac{(\lambda_{i+1}-\lambda_i)}{\Delta y}\frac{(T_{i+1}-T_i)}{\Delta y} \\
&\text{(replace } y_{i+k} \text{ by } y_i + k\Delta y) \\
&= 2C\lambda_i(2y_i+1) + 2C\frac{(\lambda_{i+1}-\lambda_i)}{\Delta y}y_i + C\frac{(\lambda_{i+1}-\lambda_i)}{\Delta y}\Delta y \\
&(y_i \text{ is } 0 \text{ at walls}) \\
&= 2C\lambda_i + C\left(\lambda_{i+1}-\lambda_i\right)
\end{aligned} \tag{A.2.7}$$

A.3 Comparison

The results by developing the second derivative are given for:
In the isothermal case:

$$\frac{\partial^2 u}{\partial y^2} \tag{A.3.1}$$

$$\frac{\partial^2 u^2}{\partial y^2} = \frac{\partial}{y}\left(2u\frac{\partial u}{\partial y}\right) \tag{A.3.2}$$

In the non-isothermal case:

$$\frac{\partial}{\partial y}\left(\lambda\frac{\partial T}{\partial y}\right) \tag{A.3.3}$$

A constant error using 4Δ is observed at the wall, which will not decrease with a refined mesh.

All these results are checked using AVBP_V6.2 with the numerical scheme LW after 1 iteration, and $C = 1/0.002^2 = 250000$ for the isothermal case and $1/10 \times 0.002^2 = 25000$ for the non-isothermal case.

		Theorie	ivisc=1 (4Δ)	ivisc=2 (2Δ)
center	$\left(\frac{\partial^2 u}{\partial y^2}\right)_i$	$2C$	$2C$	$2C$
	$\frac{\partial}{y}\left(2u\frac{\partial u}{\partial y}\right)_i$	$12C^2y_i^2$	$12C^2y_i^2 + 4C^2\Delta y^2$	$12C^2y_i^2 + 2C^2\Delta y^2$
	$\frac{\partial}{\partial y}\left(\lambda\frac{\partial T}{\partial y}\right)_i$	$2C\lambda_i + 2C\left(\frac{\partial \lambda}{\partial y}\right)_i y_i$	$2C\frac{(\lambda_{i+1}+\lambda_{i-1})}{2} +$ $2C\frac{(\lambda_{i+1}-\lambda_{i-1})}{2\Delta y}y_i$	$2C\frac{(\lambda_{i+1}+2\lambda_i+\lambda_{i-1})}{4} +$ $2C\frac{(\lambda_{i+1}-\lambda_{i-1})}{2\Delta y}y_i$
wall	$\left(\frac{\partial^2 u}{\partial y^2}\right)_i$	$2C$	C	$2C$
	$\frac{\partial}{y}\left(2u\frac{\partial u}{\partial y}\right)_i$	0	$4C^2\Delta y^2$	$2C^2\Delta y^2$
	$\frac{\partial}{\partial y}\left(\lambda\frac{\partial T}{\partial y}\right)_i$	$2C\lambda_i$	$C\lambda_{i+1} + C\left(\lambda_{i+1}-\lambda_i\right)$	$2C\lambda_i + C\left(\lambda_{i+1}-\lambda_i\right)$

Table A.3.1: Comparison of the numerical methods in AVBP using two diffusion operators 4Δ and 2Δ, together with the analytical resutls for the second derivative terms in PDE.

Appendix B

Stress vector

In ribbed tubes, where the mean flow does not only follow one direction as in smooth tube, the wall shear stress and friction coefficient (factor) should be redefined carefully.

Let us begin with the definition of the stress tensor:

$$\textit{stress tensor}: \boldsymbol{\tau} = \begin{pmatrix} \tau_{xx} & \tau_{xy} & \tau_{xz} \\ \tau_{yx} & \tau_{yy} & \tau_{yz} \\ \tau_{zx} & \tau_{zy} & \tau_{zz} \end{pmatrix}$$

$$\textit{stress vector}^{*}: \vec{\tau} = \boldsymbol{\tau} \cdot \vec{n} = \begin{pmatrix} \tau_{xj}\, n_j \\ \tau_{yj}\, n_j \\ \tau_{zj}\, n_j \end{pmatrix}$$

**Using summation convention.*

In the axial cut plane $z = 0$ in tubes, the wall normal is $\vec{n} = (0,\ 1,\ 0)$, so that the axial component of the stress vector $\vec{\tau}(x) = \tau_{xy}$. In a smooth tube, τ_{xy} (Eq. 2.1.5) is the wall shear stress τ_w (Eq. 2.1.28). On the contrary, for ribbed tubes, the wall shear stress τ_w is taken as the norm of the stress vector (it is also the output of τ_w by AVBP), thus:

$$\tau_w = |\vec{\tau}| = \sqrt{\vec{\tau}(x)^2 + \vec{\tau}(y)^2 + \vec{\tau}(z)^2}, \tag{B.0.1}$$

which allows τ_w keeping a positive value and being used for the definition of the friction velocity $u_\tau = \sqrt{(\tau_w/\rho)}$ (Eq. 2.1.30).

In fact, in the ribbed tube, the relation between the friction factor and the wall shear stress in Eq. 2.1.44 is no longer directly available. As a consequence, in the current work, the wall shear stress τ_w, which is always positive, is used for u_τ; and the global quantities, as the global friction factor f_g, the global wall shear stress $\tau_{w,g}$ and the global friction velocity $u_{\tau,g}$, are all obtained with the global pressure loss dP/dx, using Eqs. 2.1.48 and 2.1.49; finally, the local friction coefficient C_f is defined by the axial component of the stress vector $\vec{\tau}(x)$ (Eq. 2.3.1), which allows a negative value showing the recirculation of velocity.

Appendix C

Reduced chemical kinetic schema for ethane cracking process

```
!  This chemkin file was generated by RMG  Reaction Mechanism Generator (http://rmg.mit.edu
   )
!  The java code was compiled by ant at:
!    2012 08 09T12:04:51
!  The git repository was on the branch:
!    master
!  And at the commit with the hash:
!    1340a83f79b8bc9110decba6c27124b98f19bc2d
!
!  For details visit:
!   http://github.com/GreenGroup/RMG Java/tree/1340a8
!To see changes since then visit:
!   http://github.com/GreenGroup/RMG Java/compare/1340a8...master

ELEMENTS H C O N Ne Ar He Si S Cl END
SPECIES
    H2(23)
        CH4(11)
        C2H4(10) !C2H4
        C2H6(8) !C2H6
        C3H6(15) !C3H6
        C3H8(12) !C3H8
        C4H8(28) !1C4H8
        C4H8(29) !2C4H8
        C4H6(173) !13C4H6
        C4H10(1) !C4H10
    HJ(5) !H
        CH3J(2) !CH3
        C2H5J(6) !C2H5
        C3H7J(3) !1C3H7
    C3H7J(18) !2C3H7
        C4H9J(4) !1C4H9
        C4H9J(7) !2C4H9
        C4H7J(136) !1C4H7_4
        C4H7J(99) !1C4H7_3
        H2O
END
THERMO ALL
   300.000   1000.000   5000.000
! The first four sets of polynomial coefficients (Ar, N2, Ne, He) are from
! THIRD MILLENIUM IDEAL GAS AND CONDENSED PHASE THERMOCHEMICAL DATABASE FOR
! COMBUSTION WITH UPDATES FROM ACTIVE THERMOCHENICAL TABLES
! Authors: Alexander Burcat and Branko Ruscic
!
! The rest of the species are estimated by RMG (http://rmg.mit.edu/)
```

```
H2O                     C   0H   2O   1     G      300.       5000.     1000.        1
 0.28617966E+01 0.27417880E 02 0.69903300E 06 0.83739816E 10 0.38747362E 14    2
 0.29983447E+05 0.57924369E+01 0.39643913E+01 0.36069624E 03 0.19731396E 05    3
 0.36343313E 09 0.22898504E 12 0.30268709E+05 0.14771534E+00                   4

!Estimated by RMG using Group Additivity
C4H7J(99)               C   4H   7          G   250.000   5000.000    995.043    1
 9.30587932E+00 1.81664497E 02 6.26407184E 06 9.84132901E 10 5.79132700E 14    2
 1.20666362E+04 2.48404295E+01 3.57920944E+00 1.22166230E 02 4.63775625E 05    3
 6.35451306E 08 2.35062160E 11 1.46404979E+04 9.96573631E+00                   4

!Estimated by RMG using Group Additivity
C4H7J(136)              C   4H   7          G   250.000   5000.000    995.043    1
 9.06813694E+00 1.79475749E 02 6.17736805E 06 9.71267356E 10 5.72193042E 14    2
 2.02377598E+04 2.01308330E+01 3.60805455E+00 1.19094581E 02 4.51149543E 05    3
 6.16607785E 08 2.27807069E 11 2.27098861E+04 1.31459027E+01                   4

!Estimated by RMG using Group Additivity
C4H6(173)               C   4H   6          G   250.000   5000.000    995.043    1
 1.10283952E+01 1.28920777E 02 3.95448678E 06 5.66446112E 10 3.10025524E 14    2
 8.15102140E+03 3.56754561E+01 3.22147962E+00 1.05227964E 02 5.04981450E 05    3
 7.00058205E 08 2.62648333E 11 1.13755999E+04 1.03459015E+01                   4

!Estimated by RMG using Group Additivity
C4H10(1)                C   4H  10          G   250.000   5000.000    995.043    1
 9.55894461E+00 2.51112690E 02 8.70980376E 06 1.37678114E 09 8.14311852E 14    2
 2.01848471E+04 2.68629891E+01 3.59442147E+00 1.60364012E 02 5.47950347E 05    3
 7.45526578E 08 2.73825644E 11 1.73616090E+04 1.01047398E+01                   4

!Primary Thermo Library: GRIMech3.0 (Species ID: s00002703)
C2H5J(6)                C   2H   5          G   250.000   5000.000    995.043    1
 4.59320890E+00 1.18436237E 02 4.07290481E 06 6.40369771E 10 3.77359054E 14    2
 1.19693206E+04 8.17949459E 01 3.93585841E+00 1.41361383E 03 3.98804465E 05    3
 4.48664018E 08 1.54302743E 11 1.28872636E+04 6.30535006E+00                   4

!Primary Thermo Library: GRIMech3.0 (Species ID: s00009089)
CH3J(2)                 C   1H   3          G   250.000   5000.000    995.043    1
 3.29357244E+00 5.17342537E 03 1.59469094E 06 2.30721655E 10 1.27839589E 14    2
 1.64213935E+04 2.99099001E+00 3.95487471E+00 8.01537496E 05 1.02371184E 05    3
 1.03175622E 08 3.29596781E 12 1.64182649E+04 4.49456912E 01                   4

!Estimated by RMG using Group Additivity
C3H7J(3)                C   3H   7          G   250.000   5000.000    995.043    1
 6.95424497E+00 1.72816380E 02 5.92405012E 06 9.28115810E 10 5.45380465E 14    2
 8.39537670E+03 1.13350131E+01 3.74143322E+00 6.63085674E 03 4.56568982E 05    3
 5.74319432E 08 2.05881685E 11 1.02014031E+04 1.00112877E+01                   4

!Estimated by RMG using Group Additivity
C3H7J(18)               C   3H   7          G   250.000   5000.000    995.043    1
 5.33679302E+00 1.93426330E 02 6.91306521E 06 1.11583350E 09 6.69780006E 14    2
 7.64649051E+03 2.39416512E+00 4.00224620E+00 5.82500229E 03 4.19291210E 05    3
 5.06788648E 08 1.77377140E 11 8.84686013E+03 8.73482173E+00                   4

!Primary Thermo Library: GRIMech3.0 (Species ID: s00002577)
C2H4(10)                C   2H   4          G   250.000   5000.000    995.043    1
 4.53370569E+00 9.57308713E 03 3.23408854E 06 5.01623403E 10 2.92495620E 14    2
 4.05240745E+03 3.34571790E+00 3.90849430E+00 6.61973360E 03 4.93751261E 05    3
 5.36388906E 08 1.83200843E 11 5.10288607E+03 4.32080737E+00                   4

!Primary Thermo Library: GRIMech3.0 (Species ID: s00009800)
HJ(5)                   C   0H   1          G   250.000   5000.000    995.043    1
 2.50000000E+00 3.49466136E 16 1.88320877E 19 4.06176413E 23 3.19728232E 27    2
 2.54706576E+04 4.49305799E 01 2.50000000E+00 1.69371698E 15 4.40846916E 18    3
 4.33783649E 21 1.45212725E 24 2.54706576E+04 4.49305799E 01                   4

!Primary Thermo Library: GRIMech3.0 (Species ID: s00009809)
H2(23)                  C   0H   2          G   250.000   5000.000    995.043    1
```

```
 3.23597865E+00 3.41872004E 04  1.23407858E 07 4.57800734E 11  3.78637707E 15    2
 9.64700069E+02 2.79075150E+00  3.40255781E+00 1.01721558E 04 1.62009963E 07     3
 5.79222153E 10 2.62226797E 13 1.01911266E+03 3.70041102E+00                      4

!Estimated by RMG using Group Additivity
C4H9J(7)                C   4H   9          G    250.000   5000.000    995.043    1
 6.76177826E+00 2.59093186E 02 9.15278708E 06  1.46363455E 09 8.72805066E 14      2
 4.35496751E+03 6.90031400E+00 3.86622761E+00  1.63496182E 02  3.72160310E 05     3
5.10142749E 08  1.84770645E 11  5.98070403E+03 1.23282829E+01                     4

!Estimated by RMG using Group Additivity
C3H6(15)                C   3H   6          G    250.000   5000.000    995.043    1
 6.43968377E+00  1.54389014E 02 5.30972083E 06  8.34510743E 10 4.91522454E 14     2
 9.10049185E+02 1.05529198E+01 3.79616984E+00 3.13592835E 03  4.78025900E 05      3
 5.79088422E 08  2.05283796E 11  7.51179506E+02 7.89137976E+00                    4

!Estimated by RMG using Group Additivity
C4H9J(4)                C   4H   9          G    250.000   5000.000    995.043    1
 9.30384551E+00 2.28213487E 02 7.94275649E 06  1.25861444E 09 7.45754905E 14      2
 4.76859908E+03 2.20613609E+01 3.62888761E+00 1.69600053E 02  4.41187344E 05      3
 6.25826380E 08  2.32414908E 11  7.31749820E+03 1.24218583E+01                    4

!Primary Thermo Library: GRIMech3.0 (Species ID: s00009193)
CH4(11)                 C   1H   4          G    250.000   5000.000    995.043    1
 1.30383064E+00  1.06312170E 02 3.63140341E 06  5.65079843E 10 3.30334874E 14     2
 9.84472024E+03 1.18953866E+01 4.13429347E+00 5.99159306E 03  2.93330551E 05      3
 2.68176503E 08  8.17758596E 12 1.01483723E+04 4.41255344E 01                     4

!Primary Thermo Library: GRIMech3.0 (Species ID: s00002784)
C2H6(8)                 C   2H   6          G    250.000   5000.000    995.043    1
 4.31432931E+00  1.47965141E 02 5.13777267E 06  8.13192623E 10 4.81447582E 14     2
 1.25000423E+04 2.38870767E+00  3.97360158E+00 3.06302033E 03  5.07725418E 05     3
 5.60673537E 08  1.91223516E 11 1.14802815E+04  4.03689134E+00                    4

!Estimated by RMG using Group Additivity
C4H8(28)                C   4H   8          G    250.000   5000.000    995.043    1
 9.32323605E+00  2.02374952E 02 6.94441532E 06  1.08943405E 09 6.40749989E 14     2
 4.71568639E+03 2.42393839E+01  3.57358840E+00 1.09858540E 02  5.57912545E 05     3
 7.36307984E 08  2.69217805E 11 1.96922106E+03  1.15218616E+01                    4

!Estimated by RMG using Group Additivity
C4H8(29)                C   4H   8          G    250.000   5000.000    995.043    1
 8.03147951E+00  2.18298992E 02 7.70855002E 06  1.23496273E 09 7.37535387E 14     2
 5.73117481E+03 1.80898889E+01  3.78420755E+00  1.33482456E 02  4.36013543E 05    3
 5.89526982E 08  2.15329317E 11 3.62079935E+03  8.73680911E+00                    4

!Primary Thermo Library: GRIMech3.0 (Species ID: s00003749)
C3H8(12)                C   3H   8          G    250.000   5000.000    995.043    1
 7.39040044E+00  1.93494966E 02 6.81221609E 06  1.09026926E 09 6.50630141E 14     2
 1.63822386E+04 1.71504126E+01  3.81651685E+00  4.45590583E 03  5.97486434E 05    3
 7.30573201E 08  2.59891448E 11 1.42224570E+04  7.35257278E+00                    4

END

REACTIONS       KCAL/MOL        MOLES
!! Kinetics Genesys
!! recombinations
C2H5J(6)+C2H5J(6)=C4H10(1)                        8.730e+14    0.699   0.0031
CH3J(2)+C3H7J(3)=C4H10(1)                         1.230e+15    0.562    0.02
C4H9J(7)+HJ(5)=C4H10(1)                           1.660e+13    0.22     0.00
C4H9J(4)+HJ(5)=C4H10(1)                           5.440e+13    0.16     0.00

!! h abstractions
C4H10(1)+CH3J(2)=C4H9J(4)+CH4(11)                 2.280E+13    0.00     17.7    !4.560E13
      0.00     17.7 preexp halved CMS
C4H10(1)+CH3J(2)=C4H9J(7)+CH4(11)                 1.630E+13    0.00     15.4    !3.260E13
      0.00     15.4 preexp halved CMS
```

```
C4H10(1)+HJ(5)=C4H9J(4)+H2(23)                      3.515E+14    0.00     12.8    !7.030E14
        0.00     12.8 preexp halved CMS
C4H10(1)+HJ(5)=C4H9J(7)+H2(23)                      2.440E+14    0.00     10.14   !4.880E14
        0.00     10.14 preexp halved CMS
HJ(5)+CH4(11)=H2(23)+CH3J(2)                        4.270E14     0.00     15.87
C4H8(28)+CH3J(2)=C4H7J(99)+CH4(11)                  1.220E13     0.00     12.16
C4H8(28)+HJ(5)=C4H7J(99)+H2(23)                     1.590E14     0.00     7.29

!! additions
C2H4(10)+CH3J(2)=C3H7J(3)                           7.430E15     0.00     10.31
C2H4(10)+HJ(5)=C2H5J(6)                             2.130E13     0.00     4.43 !preexp /10
   CMS
C3H6(15)+HJ(5)=C3H7J(3)                             9.690E13     0.00     5.38
C2H4(10)+C2H5J(6)=C4H9J(4)                          7.430E15     0.00     10.31
C4H6(173)+HJ(5)=C4H7J(99)                           2.010E14     0.00     2.75
C4H8(28)+HJ(5)=C4H9J(7)                             3.340E14     0.00     3.85

!! Kinetics RMG

HJ(5)+HJ(5)=H2(23)                                  1.090e+11    0.00     1.50   !
    R_Recombination exact:   [ H_rad , H_rad ]
HJ(5)+C2H5J(6)=H2(23)+C2H4(10)                      1.083e+13    0.00     0.00   !
    Disproportionation exact:   [ H_rad , Cmethyl_Csrad ]
C2H5J(6)+C4H9J(7)=C2H4(10)+C4H10(1)                 6.330e+14    0.70     0.00   !
    Disproportionation exact:   [ Cmethyl_Csrad , C_rad/H/NonDeC ]
HJ(5)+C3H7J(3)=H2(23)+C3H6(15)                      3.620e+12    0.00     0.00   !
    Disproportionation exact:   [ H_rad , C/H2/Nd_Csrad ]
C3H6(15)+CH3J(2)=C4H9J(7)                           3.100e+12    0.00     8.50   !
    R_Addition_MultipleBond exact:   [ Cd/H2_Cd/H/Nd , C_methyl ]
C4H9J(7)+C3H7J(3)=C4H10(1)+C3H6(15)                 1.026e+14    0.35     0.00   !
    Disproportionation exact:   [ C_rad/H/NonDeC , C/H2/Nd_Csrad ]
C2H5J(6)+C4H9J(4)=C2H4(10)+C4H10(1)                 6.900e+13    0.35     0.00   !
    Disproportionation exact:   [ Cmethyl_Csrad , C_rad/H2/Cs ]
C4H9J(4)+C4H10(1)=C4H10(1)+C4H9J(7)                 6.160e+03    2.66     10.10          !
    H_Abstraction exact:   [ C_rad/H2/Cs , C/H2/NonDeC ]
C4H9J(4)=C4H9J(7)                                   2.360e+10    0.82     35.10          !
    intra_H_migration exact:   [ Others R3H_SS , C_rad_out_2H , Cs_H_out_H/NonDeC ] pre exp
    doubled to account for duplicate (CMS)
C3H7J(3)+C4H9J(4)=C3H6(15)+C4H10(1)                 2.900e+12    0.00     0.00   !
    Disproportionation exact:   [ C/H2/Nd_Csrad , C_rad/H2/Cs ]
CH3J(2)+C2H5J(6)=CH4(11)+C2H4(10)                   6.570e+14    0.68     0.00   !
    Disproportionation exact:   [ C_methyl , Cmethyl_Csrad ]
CH3J(2)+C3H7J(3)=CH4(11)+C3H6(15)                   2.300e+13    0.32     0.00   !
    Disproportionation exact:   [ C_methyl , C/H2/Nd_Csrad ]
HJ(5)+CH3J(2)=CH4(11)                               1.930e+14    0.00     0.27   !
    R_Recombination exact:   [ H_rad , C_methyl ]
C4H9J(4)+C2H6(8)=C4H10(1)+C2H5J(6)                  1.926e 05    5.28     7.78   !
    H_Abstraction exact:   [ C_rad/H2/Cs , InChI=1/C2H6/c1 2/h1 2H3 ]
C4H10(1)+C2H5J(6)=C4H9J(7)+C2H6(8)                  6.160e+03    2.66     10.10          !
    H_Abstraction estimate: (Average:)   [ C/H2/NonDeC , InChI=1/C2H5/c1 2/h1H2,2H3 ]
C2H5J(6)+C2H5J(6)=C2H6(8)+C2H4(10)                  6.900e+13    0.35     0.00   !
    Disproportionation exact:   [ C_rad/H2/Cs , Cmethyl_Csrad ]
CH3J(2)+CH3J(2)=C2H6(8)                             8.260e+17    1.40     1.00   !
    R_Recombination exact:   [ C_methyl , C_methyl ]
C2H5J(6)+C3H7J(3)=C2H6(8)+C3H6(15)                  2.900e+12    0.00     0.00   !
    Disproportionation exact:   [ C_rad/H2/Cs , C/H2/Nd_Csrad ]
HJ(5)+C2H5J(6)=C2H6(8)                              1.000e+14    0.00     0.00   !
    R_Recombination exact:   [ H_rad , C_rad/H2/Cs ]
HJ(5)+C2H6(8)=H2(23)+C2H5J(6)                       3.768e+08    1.75     7.51   !
    H_Abstraction estimate: (Average:)   [ H_rad , InChI=1/C2H6/c1 2/h1 2H3 ]
CH3J(2)+C2H6(8)=CH4(11)+C2H5J(6)                    1.668e+06    1.90     11.05          !
    H_Abstraction estimate: (Average:)   [ C_methyl , InChI=1/C2H6/c1 2/h1 2H3 ]
C2H5J(6)+C4H9J(7)=C2H6(8)+C4H8(28)                  6.900e+13    0.35     0.00   !
    Disproportionation exact:   [ C_rad/H2/Cs , Cmethyl_Csrad ]
CH3J(2)+C4H9J(7)=CH4(11)+C4H8(28)                   6.570e+14    0.68     0.00   !
    Disproportionation exact:   [ C_methyl , Cmethyl_Csrad ]
HJ(5)+C4H9J(7)=H2(23)+C4H8(28)                      1.083e+13    0.00     0.00   !
```

```
    Disproportionation exact:  [ H_rad , Cmethyl_Csrad ]
C4H9J(7)+C4H9J(7)=C4H10(1)+C4H8(28)               6.330e+14    0.70    0.00   !
    Disproportionation exact:  [ C_rad/H/NonDeC , Cmethyl_Csrad ]
C4H8(28)+HJ(5)=C4H9J(4)                           1.180e+13    0.00    3.80   !
    R_Addition_MultipleBond exact:  [ Cd/H/Nd_Cd/H2 , H_rad ]
C2H5J(6)+C4H9J(4)=C2H6(8)+C4H8(28)                2.900e+12    0.00    0.00   !
    Disproportionation exact:  [ C_rad/H2/Cs , C/H2/Nd_Csrad ]
CH3J(2)+C4H9J(4)=CH4(11)+C4H8(28)                 2.300e+13    0.32    0.00   !
    Disproportionation exact:  [ C_methyl , C/H2/Nd_Csrad ]
HJ(5)+C4H9J(4)=H2(23)+C4H8(28)                    3.620e+12    0.00    0.00   !
    Disproportionation exact:  [ H_rad , C/H2/Nd_Csrad ]
C4H9J(4)+C4H9J(7)=C4H10(1)+C4H8(28)               6.900e+13    0.35    0.00   !
    Disproportionation exact:  [ C_rad/H2/Cs , Cmethyl_Csrad ]
C4H9J(4)+C4H9J(4)=C4H10(1)+C4H8(28)               2.900e+12    0.00    0.00   !
    Disproportionation exact:  [ C_rad/H2/Cs , C/H2/Nd_Csrad ]
C4H7J(136)+C2H6(8)=C4H8(28)+C2H5J(6)              1.926e 05    5.28    7.78   !
    H_Abstraction exact:  [ C_rad/H2/Cs , InChI=1/C2H6/c1 2/h1 2H3 ]
C4H8(28)+CH3J(2)=C4H7J(136)+CH4(11)               8.340e+05    1.90    11.05          !
    H_Abstraction exact:  [ C/H3/Cs , C_methyl ]
C4H8(28)+HJ(5)=C4H7J(136)+H2(23)                  1.884e+08    1.75    7.51   !
    H_Abstraction exact:  [ C/H3/Cs , H_rad ]
C4H7J(136)+C4H10(1)=C4H8(28)+C4H9J(7)             6.160e+03    2.66    10.10          !
    H_Abstraction exact:  [ C_rad/H2/Cs , C/H2/NonDeC ]
C4H7J(136)+C4H10(1)=C4H8(28)+C4H9J(4)             3.954e+03    2.71    12.92          !
    H_Abstraction exact:  [ C_rad/H2/Cs , C/H3/Cs ]
C4H7J(136)+HJ(5)=C4H8(28)                         1.000e+14    0.00    0.00   !
    R_Recombination exact:  [ C_rad/H2/Cs , H_rad ]
C2H5J(6)+C4H7J(136)=C2H4(10)+C4H8(28)             6.900e+13    0.35    0.00   !
    Disproportionation exact:  [ Cmethyl_Csrad , C_rad/H2/Cs ]
C3H7J(3)+C4H7J(136)=C3H6(15)+C4H8(28)             2.900e+12    0.00    0.00   !
    Disproportionation exact:  [ C/H2/Nd_Csrad , C_rad/H2/Cs ]
C4H9J(7)+C4H7J(136)=C4H8(28)+C4H8(28)             6.900e+13    0.35    0.00   !
    Disproportionation exact:  [ Cmethyl_Csrad , C_rad/H2/Cs ]
C4H9J(4)+C4H7J(136)=C4H8(28)+C4H8(28)             2.900e+12    0.00    0.00   !
    Disproportionation exact:  [ C/H2/Nd_Csrad , C_rad/H2/Cs ]
C4H8(28)+C2H5J(6)=C4H7J(99)+C2H6(8)               3.120e 04    4.31    3.39   !
    H_Abstraction estimate: (Average:)  [ InChI=1/C4H8/c1 3 4 2/h3H,1,4H2,2H3 , InChI=1/C2H5
    /c1 2/h1H2,2H3 ]
C4H8(28)+C4H9J(7)=C4H7J(99)+C4H10(1)              1.936e+02    2.96    6.79   !
    H_Abstraction estimate: (Average:)  [ InChI=1/C4H8/c1 3 4 2/h3H,1,4H2,2H3 , C_rad/H/
    NonDeC ]
C4H8(28)+C4H9J(4)=C4H7J(99)+C4H10(1)              3.120e 04    4.31    3.39   !
    H_Abstraction estimate: (Average:)  [ InChI=1/C4H8/c1 3 4 2/h3H,1,4H2,2H3 , C_rad/H2/Cs
    ]
C4H7J(99)+HJ(5)=C4H8(28)                          5.000e+13    0.00    0.00   !
    R_Recombination estimate: (Average:)  [ C_rad/H/OneDeC , H_rad ]
C2H5J(6)+C4H7J(99)=C2H4(10)+C4H8(28)              6.330e+14    0.70    0.00   !
    Disproportionation estimate: (Average:)  [ Cmethyl_Csrad , C_rad/H/OneDeC ]
C3H7J(3)+C4H7J(99)=C3H6(15)+C4H8(28)              1.026e+14    0.35    0.00   !
    Disproportionation estimate: (Average:)  [ C/H2/Nd_Csrad , C_rad/H/OneDeC ]
C4H9J(7)+C4H7J(99)=C4H8(28)+C4H8(28)              6.330e+14    0.70    0.00   !
    Disproportionation estimate: (Average:)  [ Cmethyl_Csrad , C_rad/H/OneDeC ]
C4H9J(4)+C4H7J(99)=C4H8(28)+C4H8(28)              1.026e+14    0.35    0.00   !
    Disproportionation estimate: (Average:)  [ C/H2/Nd_Csrad , C_rad/H/OneDeC ]
C4H8(28)+C4H7J(136)=C4H7J(99)+C4H8(28)            3.120e 04    4.31    3.39   !
    H_Abstraction estimate: (Average:)  [ InChI=1/C4H8/c1 3 4 2/h3H,1,4H2,2H3 , C_rad/H2/Cs
    ]
C4H7J(136)=C4H7J(99)                              2.820e+08    1.28    27.90          !
    intra_H_migration exact:  [ Others R2H_S , C_rad_out_2H , Cs_H_out_H/OneDe ]
C4H6(173)+HJ(5)=C4H7J(136)                        5.700e+13    0.00    4.30   !
    R_Addition_MultipleBond exact:  [ Cd/H/De_Cd/H2 , H_rad ]
C2H5J(6)+C4H7J(136)=C2H6(8)+C4H6(173)             1.099e+13    0.06    2.47   !
    Disproportionation estimate: (Average:)  [ C_rad/H2/Cs , C/H2/De_Csrad ]
CH3J(2)+C4H7J(136)=CH4(11)+C4H6(173)              1.099e+13    0.06    2.47   !
    Disproportionation estimate: (Average:)  [ C_methyl , C/H2/De_Csrad ]
HJ(5)+C4H7J(136)=H2(23)+C4H6(173)                 1.099e+13    0.06    2.47   !
    Disproportionation estimate: (Average:)  [ H_rad , C/H2/De_Csrad ]
```

```
C4H9J(7)+C4H7J(136)=C4H10(1)+C4H6(173)                 1.099e+13    0.06     2.47   !
    Disproportionation estimate: (Average:)  [ C_rad/H/NonDeC , C/H2/De_Csrad ]
C4H9J(4)+C4H7J(136)=C4H10(1)+C4H6(173)                 1.099e+13    0.06     2.47   !
    Disproportionation estimate: (Average:)  [ C_rad/H2/Cs , C/H2/De_Csrad ]
C4H7J(136)+C4H7J(136)=C4H8(28)+C4H6(173)               1.099e+13    0.06     2.47   !
    Disproportionation estimate: (Average:)  [ C_rad/H2/Cs , C/H2/De_Csrad ]
C2H5J(6)+C4H7J(99)=C2H6(8)+C4H6(173)                   6.900e+13    0.35     0.00   !
    Disproportionation exact:   [ C_rad/H2/Cs , Cmethyl_Csrad ]
CH3J(2)+C4H7J(99)=CH4(11)+C4H6(173)                    6.570e+14    0.68     0.00   !
    Disproportionation exact:   [ C_methyl , Cmethyl_Csrad ]
HJ(5)+C4H7J(99)=H2(23)+C4H6(173)                       1.083e+13    0.00     0.00   !
    Disproportionation exact:   [ H_rad , Cmethyl_Csrad ]
C4H9J(7)+C4H7J(99)=C4H10(1)+C4H6(173)                  6.330e+14    0.70     0.00   !
    Disproportionation exact:   [ C_rad/H/NonDeC , Cmethyl_Csrad ]
C4H9J(4)+C4H7J(99)=C4H10(1)+C4H6(173)                  6.900e+13    0.35     0.00   !
    Disproportionation exact:   [ C_rad/H2/Cs , Cmethyl_Csrad ]
C4H7J(99)+C4H7J(136)=C4H8(28)+C4H6(173)                1.099e+13    0.06     2.47   !
    Disproportionation estimate: (Average:)  [ C_rad/H/OneDeC , C/H2/De_Csrad ]
C4H7J(99)+C4H7J(99)=C4H8(28)+C4H6(173)                 6.330e+14    0.70     0.00   !
    Disproportionation estimate: (Average:)  [ C_rad/H/OneDeC , Cmethyl_Csrad ]
C3H7J(3)=C3H7J(18)                                     1.938e+10    0.89     35.80          !
    intra_H_migration exact:   [ Others R2H_S , C_rad_out_2H , Cs_H_out_H/NonDeC ]
C3H6(15)+HJ(5)=C3H7J(18)                               2.010e+13    0.00     2.10   !
    R_Addition_MultipleBond exact:   [ Cd/H2_Cd/H/Nd , H_rad ]
C3H7J(18)+C4H9J(4)=C3H6(15)+C4H10(1)                   1.380e+14    0.35     0.00   !
    Disproportionation exact:   [ Cmethyl_Csrad , C_rad/H2/Cs ]
C3H7J(18)+C4H9J(7)=C3H6(15)+C4H10(1)                   1.266e+15    0.70     0.00   !
    Disproportionation exact:   [ Cmethyl_Csrad , C_rad/H/NonDeC ]
C3H7J(18)+HJ(5)=C3H6(15)+H2(23)                        2.166e+13    0.00     0.00   !
    Disproportionation exact:   [ Cmethyl_Csrad , H_rad ]
C3H7J(18)+CH3J(2)=C3H6(15)+CH4(11)                     1.314e+15    0.68     0.00   !
    Disproportionation exact:   [ Cmethyl_Csrad , C_methyl ]
C3H7J(18)+C2H5J(6)=C3H6(15)+C2H6(8)                    1.380e+14    0.35     0.00   !
    Disproportionation exact:   [ Cmethyl_Csrad , C_rad/H2/Cs ]
C3H7J(18)+C4H7J(99)=C3H6(15)+C4H8(28)                  1.266e+15    0.70     0.00   !
    Disproportionation estimate: (Average:)  [ Cmethyl_Csrad , C_rad/H/OneDeC ]
C3H7J(18)+C4H7J(136)=C3H6(15)+C4H8(28)                 1.380e+14    0.35     0.00   !
    Disproportionation exact:   [ Cmethyl_Csrad , C_rad/H2/Cs ]
C4H8(29)+HJ(5)=C4H9J(7)                                2.000e+13    0.00     2.90   !
    R_Addition_MultipleBond estimate: (Average:)  [ Cd/H/Nd_Cd/H/Nd , H_rad ]
C2H5J(6)+C4H9J(7)=C2H6(8)+C4H8(29)                     2.900e+12    0.00     0.00   !
    Disproportionation exact:   [ C_rad/H2/Cs , C/H2/Nd_Csrad ]
CH3J(2)+C4H9J(7)=CH4(11)+C4H8(29)                      2.300e+13    0.32     0.00   !
    Disproportionation exact:   [ C_methyl , C/H2/Nd_Csrad ]
HJ(5)+C4H9J(7)=H2(23)+C4H8(29)                         3.620e+12    0.00     0.00   !
    Disproportionation exact:   [ H_rad , C/H2/Nd_Csrad ]
C4H9J(7)+C4H9J(7)=C4H10(1)+C4H8(29)                    1.026e+14    0.35     0.00   !
    Disproportionation exact:   [ C_rad/H/NonDeC , C/H2/Nd_Csrad ]
C4H9J(4)+C4H9J(7)=C4H10(1)+C4H8(29)                    2.900e+12    0.00     0.00   !
    Disproportionation exact:   [ C_rad/H2/Cs , C/H2/Nd_Csrad ]
C4H7J(136)+C4H9J(7)=C4H8(28)+C4H8(29)                  2.900e+12    0.00     0.00   !
    Disproportionation exact:   [ C_rad/H2/Cs , C/H2/Nd_Csrad ]
C4H9J(4)+C4H8(29)=C4H10(1)+C4H7J(99)                   3.360e+12    0.00     12.40          !
    H_Abstraction estimate: (Average:)  [ C_rad/H2/Cs , InChI=1/C4H8/c1 3 4 2/h3 4H,1 2H3/b4
    3+ ]
C4H9J(7)+C4H8(29)=C4H10(1)+C4H7J(99)                   1.722e+12    0.00     12.30          !
    H_Abstraction estimate: (Average:)  [ C_rad/H/NonDeC , InChI=1/C4H8/c1 3 4 2/h3 4H,1 2H3
    /b4 3+ ]
HJ(5)+C4H8(29)=H2(23)+C4H7J(99)                        2.598e+06    2.38     2.80   !
    H_Abstraction estimate: (Average:)  [ H_rad , InChI=1/C4H8/c1 3 4 2/h3 4H,1 2H3/b4 3+ ]
CH3J(2)+C4H8(29)=CH4(11)+C4H7J(99)                     4.824e+02    2.92     7.16   !
    H_Abstraction estimate: (Average:)  [ C_methyl , InChI=1/C4H8/c1 3 4 2/h3 4H,1 2H3/b4 3+
     ]
C2H5J(6)+C4H8(29)=C2H6(8)+C4H7J(99)                    3.360e+12    0.00     12.40          !
    H_Abstraction estimate: (Average:)  [ InChI=1/C2H5/c1 2/h1H2,2H3 , InChI=1/C4H8/c1
     3 4 2/h3 4H,1 2H3/b4 3+ ]
C4H8(28)+C4H7J(99)=C4H7J(99)+C4H8(29)                  3.120e 04    4.31     3.39   !
```

```
    H_Abstraction estimate: (Average:)  [ InChI=1/C4H8/c1 3 4 2/h3H,1,4H2,2H3 , InChI=1/C3H5
    /c1 3 2/h3H,1 2H2 ]
C4H7J(136)+C4H8(29)=C4H8(28)+C4H7J(99)              3.360e+12    0.00    12.40         !
    H_Abstraction estimate: (Average:)  [ C_rad/H2/Cs , InChI=1/C4H8/c1 3 4 2/h3 4H,1 2H3/b4
    3+ ]
C4H7J(99)+HJ(5)=C4H8(29)                            5.000e+13    0.00    0.00    !
    R_Recombination estimate: (Average:)  [ C_rad/H2/Cd , H_rad ]
C4H7J(99)+C2H5J(6)=C4H8(29)+C2H4(10)                6.870e+13    0.35    0.13    !
    Disproportionation exact:  [ C_rad/H2/Cd , Cmethyl_Csrad ]
C4H7J(99)+C3H7J(3)=C4H8(29)+C3H6(15)                2.900e+12    0.00    0.13    !
    Disproportionation exact:  [ C_rad/H2/Cd , C/H2/Nd_Csrad ]
C4H7J(99)+C4H9J(7)=C4H8(29)+C4H8(28)                6.870e+13    0.35    0.13    !
    Disproportionation exact:  [ C_rad/H2/Cd , Cmethyl_Csrad ]
C4H7J(99)+C4H9J(7)=C4H8(29)+C4H8(29)                2.900e+12    0.00    0.13    !
    Disproportionation exact:  [ C_rad/H2/Cd , C/H2/Nd_Csrad ]
C4H7J(99)+C4H9J(4)=C4H8(29)+C4H8(28)                2.900e+12    0.00    0.13    !
    Disproportionation exact:  [ C_rad/H2/Cd , C/H2/Nd_Csrad ]
C4H7J(99)+C4H7J(136)=C4H8(29)+C4H6(173)             1.099e+13    0.06    2.47    !
    Disproportionation estimate: (Average:)  [ C_rad/H2/Cd , C/H2/De_Csrad ]
C4H7J(99)+C4H7J(99)=C4H8(29)+C4H6(173)              6.870e+13    0.35    0.13    !
    Disproportionation exact:  [ C_rad/H2/Cd , Cmethyl_Csrad ]
C4H7J(99)+C3H7J(18)=C4H8(29)+C3H6(15)               1.374e+14    0.35    0.13    !
    Disproportionation exact:  [ C_rad/H2/Cd , Cmethyl_Csrad ]
CH3J(2)+C2H5J(6)=C3H8(12)                           3.370e+13    0.00    0.00    !
    R_Recombination exact:  [ C_methyl , C_rad/H2/Cs ]
C4H9J(4)+C3H8(12)=C4H10(1)+C3H7J(3)                 3.954e+03    2.71    12.92         !
    H_Abstraction exact:  [ C_rad/H2/Cs , C/H3/Cs ]
C4H10(1)+C3H7J(3)=C4H9J(7)+C3H8(12)                 6.160e+03    2.66    10.10         !
    H_Abstraction exact:  [ C/H2/NonDeC , C_rad/H2/Cs ]
C3H7J(3)+C2H5J(6)=C3H8(12)+C2H4(10)                 6.900e+13    0.35    0.00    !
    Disproportionation exact:  [ C_rad/H2/Cs , Cmethyl_Csrad ]
C3H7J(3)+C3H7J(3)=C3H8(12)+C3H6(15)                 2.900e+12    0.00    0.00    !
    Disproportionation exact:  [ C_rad/H2/Cs , C/H2/Nd_Csrad ]
HJ(5)+C3H7J(3)=C3H8(12)                             1.000e+14    0.00    0.00    !
    R_Recombination exact:  [ H_rad , C_rad/H2/Cs ]
HJ(5)+C3H8(12)=H2(23)+C3H7J(3)                      3.768e+08    1.75    7.51    !
    H_Abstraction exact:  [ H_rad , C/H3/Cs ]
C3H7J(3)+C4H9J(7)=C3H8(12)+C4H8(28)                 6.900e+13    0.35    0.00    !
    Disproportionation exact:  [ C_rad/H2/Cs , Cmethyl_Csrad ]
C3H7J(3)+C4H9J(7)=C3H8(12)+C4H8(29)                 2.900e+12    0.00    0.00    !
    Disproportionation exact:  [ C_rad/H2/Cs , C/H2/Nd_Csrad ]
C3H7J(3)+C4H9J(4)=C3H8(12)+C4H8(28)                 2.900e+12    0.00    0.00    !
    Disproportionation exact:  [ C_rad/H2/Cs , C/H2/Nd_Csrad ]
CH3J(2)+C3H8(12)=CH4(11)+C3H7J(3)                   1.668e+06    1.90    11.05         !
    H_Abstraction exact:  [ C_methyl , C/H3/Cs ]
C2H5J(6)+C3H8(12)=C2H6(8)+C3H7J(3)                  3.954e+03    2.71    12.92         !
    H_Abstraction estimate: (Average:)  [ InChI=1/C2H5/c1 2/h1H2,2H3 , C/H3/Cs ]
C4H8(28)+C3H7J(3)=C4H7J(99)+C3H8(12)                3.120e 04    4.31    3.39    !
    H_Abstraction estimate: (Average:)  [ InChI=1/C4H8/c1 3 4 2/h3H,1,4H2,2H3 , C_rad/H2/Cs
    ]
C4H7J(136)+C3H8(12)=C4H8(28)+C3H7J(3)               3.954e+03    2.71    12.92         !
    H_Abstraction exact:  [ C_rad/H2/Cs , C/H3/Cs ]
C3H7J(3)+C4H7J(136)=C3H8(12)+C4H6(173)              1.099e+13    0.06    2.47    !
    Disproportionation estimate: (Average:)  [ C_rad/H2/Cs , C/H2/De_Csrad ]
C3H7J(3)+C4H7J(99)=C3H8(12)+C4H6(173)               6.900e+13    0.35    0.00    !
    Disproportionation exact:  [ C_rad/H2/Cs , Cmethyl_Csrad ]
C4H9J(4)+C3H8(12)=C4H10(1)+C3H7J(18)                3.080e+03    2.66    10.10         !
    H_Abstraction estimate: (Average:)  [ C_rad/H2/Cs , InChI=1/C3H8/c1 3 2/h3H2,1 2H3 ]
C4H10(1)+C3H7J(18)=C4H9J(7)+C3H8(12)                6.080e+01    3.19    10.31         !
    H_Abstraction estimate: (Average:)  [ C/H2/NonDeC , InChI=1/C3H7/c1 3 2/h3H,1 2H3 ]
HJ(5)+C3H8(12)=H2(23)+C3H7J(18)                     2.600e+08    1.69    4.78    !
    H_Abstraction estimate: (Average:)  [ H_rad , InChI=1/C3H8/c1 3 2/h3H2,1 2H3 ]
CH3J(2)+C3H8(12)=CH4(11)+C3H7J(18)                  2.900e+06    1.77    8.53    !
    H_Abstraction estimate: (Average:)  [ C_methyl , InChI=1/C3H8/c1 3 2/h3H2,1 2H3 ]
C2H5J(6)+C3H8(12)=C2H6(8)+C3H7J(18)                 3.080e+03    2.66    10.10         !
    H_Abstraction estimate: (Average:)  [ InChI=1/C2H5/c1 2/h1H2,2H3 , InChI=1/C3H8/c1 3 2/
    h3H2,1 2H3 ]
```

```
C4H8(28)+C3H7J(18)=C4H7J(99)+C3H8(12)                    1.936e+02    2.96    6.79   !
    H_Abstraction estimate: (Average:)  [ InChI=1/C4H8/c1 3 4 2/h3H,1,4H2,2H3 , InChI=1/C3H7
    /c1 3 2/h3H,1 2H3 ]
C4H7J(136)+C3H8(12)=C4H8(28)+C3H7J(18)                   3.080e+03    2.66    10.10          !
    H_Abstraction estimate: (Average:)  [ C_rad/H2/Cs , InChI=1/C3H8/c1 3 2/h3H2,1 2H3 ]
C3H7J(18)+HJ(5)=C3H8(12)                                 2.000e+13    0.00    0.00   !
    R_Recombination exact:   [ C_rad/H/NonDeC , H_rad ]
C3H7J(18)+C2H5J(6)=C3H8(12)+C2H4(10)                     6.330e+14    0.70    0.00   !
    Disproportionation exact:   [ C_rad/H/NonDeC , Cmethyl_Csrad ]
C3H7J(18)+C3H7J(3)=C3H8(12)+C3H6(15)                     1.026e+14    0.35    0.00   !
    Disproportionation exact:   [ C_rad/H/NonDeC , C/H2/Nd_Csrad ]
C3H7J(18)+C4H9J(7)=C3H8(12)+C4H8(28)                     6.330e+14    0.70    0.00   !
    Disproportionation exact:   [ C_rad/H/NonDeC , Cmethyl_Csrad ]
C3H7J(18)+C4H9J(7)=C3H8(12)+C4H8(29)                     1.026e+14    0.35    0.00   !
    Disproportionation exact:   [ C_rad/H/NonDeC , C/H2/Nd_Csrad ]
C3H7J(18)+C4H9J(4)=C3H8(12)+C4H8(28)                     1.026e+14    0.35    0.00   !
    Disproportionation exact:   [ C_rad/H/NonDeC , C/H2/Nd_Csrad ]
C3H7J(18)+C4H7J(136)=C3H8(12)+C4H6(173)                  1.099e+13    0.06    2.47   !
    Disproportionation estimate: (Average:)  [ C_rad/H/NonDeC , C/H2/De_Csrad ]
C3H7J(18)+C4H7J(99)=C3H8(12)+C4H6(173)                   6.330e+14    0.70    0.00   !
    Disproportionation exact:   [ C_rad/H/NonDeC , Cmethyl_Csrad ]
C3H7J(18)+C3H7J(18)=C3H8(12)+C3H6(15)                    1.266e+15    0.70    0.00   !
    Disproportionation exact:   [ C_rad/H/NonDeC , Cmethyl_Csrad ]
C4H8(29)+C3H7J(3)=C4H7J(99)+C3H8(12)                     3.360e+12    0.00    12.40          !
    H_Abstraction estimate: (Average:)  [ InChI=1/C4H8/c1 3 4 2/h3 4H,1 2H3/b4 3+ , C_rad/H2
    /Cs ]
C4H8(29)+C3H7J(18)=C4H7J(99)+C3H8(12)                    1.722e+12    0.00    12.30          !
    H_Abstraction estimate: (Average:)  [ InChI=1/C4H8/c1 3 4 2/h3 4H,1 2H3/b4 3+ , InChI=1/
    C3H7/c1 3 2/h3H,1 2H3 ]
C3H8(12)+C3H7J(3)=C3H7J(18)+C3H8(12)                     3.080e+03    2.66    10.10          !
    H_Abstraction estimate: (Average:)  [ InChI=1/C3H8/c1 3 2/h3H2,1 2H3 , C_rad/H2/Cs ]
END
```

Appendix D

Reduced chemical kinetic schema for butane cracking process

```
ELEMENTS H C O      END
SPECIES
aH2
aCH4
aC2H2
aC2H4
aC2H6
aC3H6
a1C4H8
a1,3C4H6
anC4H10
aH.
aCH3.
aC2H3.
aC2H5.
a1C3H7.
a1C4H9.
a2C4H9.
a1C4 4.
aC3H5.
H2O
        END
THERMO ALL
 300             1000             1500
aH2                     TPIS78H   2                G    200.000    3500.000    1000.000      1
  3.33727920E+00 4.94024731E 05  4.99456778E 07 1.79566394E 10  2.00255376E 14    2
 9.50158922E+02 3.20502331E+00  2.34433112E+00  7.98052075E 03 1.94781510E 05    3
  2.01572094E 08 7.37611761E 12 9.17935173E+02  6.83010238E 01                    4
aH.                     L  7/88H   1               G    200.000    3500.000    1000.000      1
  2.50000001E+00 2.30842973E 11  1.61561948E 14 4.73515235E 18  4.98197357E 22    2
  2.54736599E+04 4.46682914E 01  2.50000000E+00  7.05332819E 13 1.99591964E 15    3
  2.30081632E 18 9.27732332E 22  2.54736599E+04 4.46682853E 01                    4
aCH4                    L  8/88C    1H    4        G    200.000    3500.000    1000.000      1
  7.48514950E 02  1.33909467E 02 5.73285809E 06  1.22292535E 09 1.01815230E 13    2
 9.46834459E+03  1.84373180E+01  5.14987613E+00 1.36709788E 02  4.91800599E 05    3
 4.84743026E 08  1.66693956E 11 1.02466476E+04 4.64130376E+00                     4
aCH3.                   L11/89C    1H    3        G    200.000    3500.000    1000.000      1
  2.28571772E+00  7.23990037E 03 2.98714348E 06  5.95684644E 10 4.67154394E 14    2
  1.67755843E+04  8.48007179E+00  3.67359040E+00  2.01095175E 03  5.73021856E 06   3
 6.87117425E 09  2.54385734E 12  1.64449988E+04  1.60456433E+00                    4
aC2H4                   L  1/91C    2H    4        G    200.000    3500.000    1000.000      1
  2.03611116E+00  1.46454151E 02 6.71077915E 06  1.47222923E 09 1.25706061E 13    2
  4.93988614E+03  1.03053693E+01  3.95920148E+00 7.57052247E 03  5.70990292E 05    3
 6.91588753E 08  2.69884373E 11  5.08977593E+03  4.09733096E+00                    4
aC2H3.                  L  2/92C    2H    3        G    200.000    3500.000    1000.000      1
```

```
 3.01672400E+00 1.03302292E 02 4.68082349E 06 1.01763288E 09 8.62607041E 14    2
 3.46128739E+04 7.78732378E+00 3.21246645E+00 1.51479162E 03 2.59209412E 05    3
 3.57657847E 08 1.47150873E 11 3.48598468E+04 8.51054025E+00                   4
aC2H6             L 8/88C   2H   6          G    200.000   3500.000   1000.000    1
 1.07188150E+00 2.16852677E 02 1.00256067E 05 2.21412001E 09 1.90002890E 13    2
 1.14263932E+04 1.51156107E+01 4.29142492E+00 5.50154270E 03 5.99438288E 05    3
 7.08466285E 08 2.68685771E 11 1.15222055E+04 2.66682316E+00                   4
aC2H5.            L12/92C   2H   5          G    200.000   3500.000   1000.000    1
 1.95465642E+00 1.73972722E 02 7.98206668E 06 1.75217689E 09 1.49641576E 13    2
 1.28575200E+04 1.34624343E+01 4.30646568E+00 4.18658892E 03 4.97142807E 05    3
 5.99126606E 08 2.30509004E 11 1.28416265E+04 4.70720924E+00                   4
aC3H6                    C   3H   6O   0    G    300.000   5000.000    995.043    1
 5.42559783E+00 1.75791067E 02 6.56311899E 06 1.03199697E 09 5.99721148E 14    2
 6.08798934E+02 5.16515272E+00 3.64255985E+00 3.89757558E 03 4.54910439E 05    3
 5.49011352E 08 1.92835688E 11 7.78191818E+02 8.61457909E+00                   4
H2O               L 8/89H   2O   1          G    200.000   3500.000   1000.000    1
 3.03399249E+00 2.17691804E 03 1.64072518E 07 9.70419870E 11 1.68200992E 14    2
 3.00042971E+04 4.96677010E+00 4.19864056E+00 2.03643410E 03 6.52040211E 06    3
 5.48797062E 09 1.77197817E 12 3.02937267E+04 8.49032208E 01                   4
a1C4H8                   C   4H   8O   0    G    300.000   5000.000    995.043    1
 8.06996009E+00 2.30144195E 02 8.63501686E 06 1.36143870E 09 7.92542991E 14    2
 4.35738469E+03 1.76345584E+01 3.38887348E+00 1.16753402E 02 5.39187583E 05    3
 7.10067706E 08 2.57553494E 11 1.93288526E+03 1.24275196E+01                   4
anC4H10                  C   4H  10O   0    G    300.000   5000.000    995.043    1
 8.14175944E+00 2.81601588E 02 1.04914204E 05 1.64919250E 09 9.58548867E 14    2
 1.98023414E+04 1.86858146E+01 3.30538686E+00 1.69397004E 02 5.26457415E 05    3
 7.16205466E 08 2.60935571E 11 1.73219078E+04 1.22504344E+01                   4
a1,3C4H6                 C   4H   6         g   0300.00   4000.00   1000.00      1
 1.09677803E+01 1.29510755E 02 3.97761193E 06 5.74948089E 10 3.17795241E 14    2
 8.19411540E+03 3.52875277E+01 2.73144721E+00 1.39063890E 02 4.30537876E 05    3
 6.34108493E 08 2.42036418E 11 1.14250236E+04 1.24057762E+01                   4
!a1,3C4H6                 C   4H   6         G        300        1500             1
!     0.88865930 4.36173119E 02 0.30531615E 02 0.00814646E 06      0.00000000     2
!     13.13101113     33.53241339     0.88865930 4.36173119E 02 0.30531615E 04    3
! 0.00814646E 06     0.00000000     13.13101113     33.53241339                   4
a1C4H9.                  C   4H   9O   0    G    300.000   5000.000    995.043    1
 8.01071857E+00 2.56389459E 02 9.61171963E 06 1.51622055E 09 8.83434947E 14    2
 5.10907933E+03 1.52614715E+01 3.37009523E+00 1.75812457E 02 4.28036708E 05    3
 6.05809533E 08 2.22917667E 11 7.35502735E+03 1.37488542E+01                   4
a1C3H7.             mar97C   3H   7    0   0g    300.       5000.      1390.      1
 9.43799350e 00 1.47160681e 02 5.03338420e 06 7.81317497e 10 4.35209260e 14    2
 7.27396508e 03 2.60136738e 01 1.13366571e 01 3.54171389e 02 2.28073697e 05    3
 7.88746806e 09 1.16856961e 12 1.06821595e 04 2.45520758e 01                   4
aC2H2             L 1/91C   2H   2          G    200.000   3500.000   1000.000    1
 4.14756964E+00 5.96166664E 03 2.37294852E 06 4.67412171E 10 3.61235213E 14    2
 2.59359992E+04 1.23028121E+00 8.08681094E 01 2.33615629E 02 3.55171815E 05    3
 2.80152437E 08 8.50072974E 12 2.64289807E+04 1.39397051E+01                   4
a2C4H9.                  C   4H   9O   0    G    300.000   5000.000    995.043    1
 5.49903935E+00 2.86742945E 02 1.07982839E 05 1.71698889E 09 1.00774201E 13    2
 4.70679917E+03 2.82131411E 01 3.60287439E+00 1.68404053E 02 3.63708807E 05    3
 4.95364606E 08 1.77135673E 11 6.04734795E+03 1.36963168E+01                   4
a1C4 4.                  C   4H   7         G        300        1500            1
     1.10163544 3.75603309E 02 0.22133407E 04 0.51658042E 08      0.00000000    2
    23.01954865     37.67109864     1.10163544 3.75603309E 02 0.22133407E 04    3
 0.51658042E 08      0.00000000     23.01954865     37.67109864                 4
aC3H5.                   C   3H   5         G        300        1500            1
     0.04917080 3.04661612E 02 0.19510226E 04 0.49211082E 08      0.00000000    2
    20.44168144     31.39258220     0.04917080 3.04661612E 02 0.19510226E 04    3
 0.49211082E 08      0.00000000     20.44168144     31.39258220                 4
END

REACTIONS          JOULES/MOLE

      1aC2H6=>1aCH3.+1aCH3.                       5.73E+16    0.0    368305.0
      1aH2+1aCH3.=>1aH.+1aCH4                     1.23E+12    0.0     38800.0
      1aH2+1aC2H3.=>1aH.+1aC2H4                   7.43E+11    0.0     22900.0
      1aH2+1aC2H5.=>1aH.+1aC2H6                   2.20E+12    0.0     62682.0
```

```
    1aCH4+1aH.=>1aCH3.+1aH2                   4.25E+13     0.0     41572.0
    1aC2H4+1aH.=>1aC2H3.+1aH2                 3.05E+13     0.0     39593.0
    1aC2H4+1aC2H5.=>1aC2H3.+1aC2H6            1.98E+12     0.0     75965.0
    1aC2H6+1aH.=>1aC2H5.+1aH2                 7.91E+13     0.0     37550.0
    1aC2H6+1aCH3.=>1aC2H5.+1aCH4              2.87E+12     0.0     50040.0
    1aC2H6+1aC2H3.=>1aC2H5.+1aC2H4            1.73E+12     0.0     34140.0
    1anC4H10+1aH.=>1a1C4H9.+1aH2              7.91E+13     0.0     37550.0
    1anC4H10+1aH.=>1a2C4H9.+1aH2              5.65E+13     0.0     30660.0
    1anC4H10+1aC2H5.=>1a2C4H9.+1aC2H6         5.27E+11     0.0     52610.0
    1aC2H4+1aH.=>1aC2H5.                      4.38E+13     0.0     12660.0
    1aC2H4+1aCH3.=>1a1C3H7.                   2.19E+12     0.0     40360.0
    1aC2H4+1aC2H5.=>1a1C4H9.                  3.81E+10     0.0     43970.0
    1aC2H3.=>1aC2H2+1aH.                      2.83E+13     0.0    178725.0
    1aC2H5.=>1aC2H4+1aH.                      4.90E+13     0.0    173636.0
    1a1C3H7.=>1aC2H4+1aCH3.                   5.85E+13     0.0    139750.0
    1a2C4H9.=>1aC3H6+1aCH3.                   3.84E+13     0.0    134606.0
    1a1C4H9.=>1aC2H4+1aC2H5.                  1.32E+12     0.0    120974.0
    1a1C4H9.=>1a1C4H8+1aH.                    4.20E+13     0.0    157860.0
    1aH.+1aC2H5.=>1aC2H6                      9.77E+13     0.0         0.0
    1aC2H5.+1aC2H5.=>1anC4H10                 2.00E+12     0.0         0.0
    1aC2H3.+1aC2H3.=>1a1,3C4H6                2.00E+12     0.0         0.0
    1aC2H4+1aC2H3.=>1a1C4 4.                  1383.7E+09   0   37500.0
    1aC2H2+1aH.=>1aC2H3.                      28908.8E+09   0   20560.0
    1a1C4 4.=>1a1,3C4H6 +    1aH.             22958718.3E+06   0  149671.8
      1a1C4H8    =>  1aC2H3.    +    1aC2H5.                          5811674283.5E+06
          0  384871.9
    1aC2H6+1aC3H5.=>1aC2H5.+1aC3H6            333.2E+09   0   82437.8
      1aCH4      +   1aC2H5.    =>  1aCH3.     +  1aC2H6                   2751.6E+09
          0   77944.4
1aH2       +    1aC3H5.    =>  1aH.        +  1aC3H6                  993.1E+09   0
    85620.2
END
```

Appendix E

Thermodynamic database of butane cracking chemistry

The thermal database used to obtain the enthalpies of each species plays an important role in the reversible reactions, because the chemical equilibrium constant $K_{eq}^0(T)$ at a certain temperature T of a reversible reaction is linked to the standard Gibbs free energy $\Delta G^0 = \Delta H^0 - T\Delta S^0$:

$$K_{eq}^0(T) = exp\left(-\frac{\Delta G^0}{RT}\right)\left(\frac{P_0}{RT}\right)^{\sum \nu_k}, \tag{E.0.1}$$

where the ^{0} indicates the standard state at pressure $P_0 = 1\,\text{bar}$. ΔH^0 and ΔS^0 are respectively the enthalpy (sensible + chemical) and the entropy changes through the reaction, and ν_k is the stoichiometric coefficient for species k in this reaction.

The steps to obtain the reaction rates differ a little between Cantera and AVBP, but they both lead to the same final results. Table E.0.1 explains and compares the difference between Cantera and AVBP.

Different from Cantera where the thermodynamic database is in polynomial form [196], AVBP uses a block of 51 data storing every 100 K the sensible enthalpy changes of the species from 0 K to 5 000 K, and a second block storing their entropies in the same way for the calculation of the total enthalpy and entropy for each species at a given temperature. The standard-state temperature T_{ref} in AVBP for the reference enthalpy (of formation) is 0 K, instead of the conventional standard-state temperature 298 K used in Chemkin. Therefore, the total enthalpy of the species $h(T)$ by summing the enthalpy of formation at the standard reference state and the sensible enthalpy change from T_{ref} to T [197] is calculated inCantera and AVBP using different formulas:

$$h_{Cantera}(T) = \Delta H_f(298\,\text{K})_{Cantera} + \int_{298\,\text{K}}^{T} C_{p,Cantera}\text{d}T, \tag{E.0.2}$$

$$h_{AVBP}(T) = \Delta H_f(0\,\text{K})_{AVBP} + \int_{0\,\text{K}}^{T} C_{p,AVBP}\text{d}T \tag{E.0.3}$$

where $\Delta H_f(0\,\text{K})$ in AVBP has to be determined. To keep the same total standardized

Steps	**Cantera**	**AVBP**	Relation between Cantera and AVBP
enthalpy change	$\Delta H(T)$	$\Delta H^0(T)$	$\Delta H(T) = \Delta H^0(T)$
entropy change	$\Delta S(T,P)$	$\Delta S(T,P_0)$	$\Delta S(T,P) = \Delta S(T,P_0) - R\ln\left(\frac{P_0}{P}\right)^{\sum\nu_k}$
Gibbs free energy	$\Delta G(T,P) = \Delta H(T) - T\Delta S(T,P)$	$\Delta G^0(T) = \Delta H^0(T) - T\Delta S^0(T)$	$\Delta G(T,P) = \Delta G^0(T) + RT\ln\left(\frac{P_0}{P}\right)^{\sum\nu_k}$
equilibrium constant in terms of partial pressure	$K_p(T,P) = \exp\left(\frac{-\Delta G(T,P)}{RT}\right)$	$K_p^0(T) = \exp\left(-\frac{\Delta G^0(T)}{RT}\right)$	$K_p(T,P) = K_p^0(T)\left(\frac{P}{P_0}\right)^{\sum\nu_k}$
equilibrium constant in terms of concentration	$K_{eq}(T,P) = K_p(T,P)\left(\frac{P_0}{RT}\right)^{\sum\nu_k}$	$K_{eq}^0(T) = K_p^0(T)\left(\frac{P_0}{RT}\right)^{\sum\nu_k}$	$K_{eq}(T,P) = K_{eq}^0(T)\left(\frac{P}{P_0}\right)^{\sum\nu_k}$
reverse rate coefficient	$k_{rev}(T,P) = \frac{k_{fwd}}{K_{eq}(T,P)}$	$k_{rev}^0(T) = \frac{k_{fwd}}{K_{eq}^0(T)}$	$k_{rev}(T,P) = k_{rev}^0(T)\left(\frac{P}{P_0}\right)^{-\sum\nu_k}$
reverse rate	$r_{rev,Cantera} = k_{rev}(T,P)\cdot\prod_{k=1}^{N}\left(\frac{\rho Y_k}{W_k}\right)^{\nu_k}\left(\frac{P}{P_0}\right)^{\sum\nu_k}$	$r_{rev,AVBP} = k_{rev}(T)\prod_{k=1}^{N}\left(\frac{\rho Y_k}{W_k}\right)^{\nu_k}$	$r_{rev,Cantera} = r_{rev,AVBP}$

Table E.0.1: Difference in the calculation method of the reverse rate of a given reaction in Cantera and in AVBP.

enthalpy at the temperature T between Cantera and AVBP $h_{Cantera}(T) = h_{AVBP}(T)$, it is required that:

$$\Delta H_f(298\,\mathrm{K})_{Cantera} + \int_{298\,\mathrm{K}}^{T} C_{p,Cantera}\mathrm{d}T = \Delta H_f(0\,\mathrm{K})_{AVBP} + \int_{0\,\mathrm{K}}^{T} C_{p,AVBP}\mathrm{d}T \tag{E.0.4}$$

Since the difference between $C_{p,Cantera}$ and $C_{p,AVBP}$ can be neglected, by using $C_{p,Cantera} = C_{p,AVBP}$, Eq. E.0.4 leads to:

$$\Delta H_f(0\,\mathrm{K})_{AVBP} = \Delta H_f(298\,\mathrm{K})_{Cantera} - \int_{0\,\mathrm{K}}^{298\,\mathrm{K}} C_{p,AVBP}\mathrm{d}T, \tag{E.0.5}$$

In AVBP, the heat capacity at constant pressure is considered constant in each interval range $[T, T + 100\,\mathrm{K}]$:

$$C_p = \frac{h_s(T + 100\,\mathrm{K}) - h_s(T)}{100\,\mathrm{K}} \tag{E.0.6}$$

Therefore, it is possible to write:

$$\int_{0\,\mathrm{K}}^{298\,\mathrm{K}} C_{p,AVBP}\mathrm{d}T = h_s(298\,\mathrm{K})_{AVBP} - h_s(0\,\mathrm{K})_{AVBP}, \tag{E.0.7}$$

and Eq. E.0.5 turns to:

$$\Delta H_f(0\,\mathrm{K})_{AVBP} = \Delta H_f(298\,\mathrm{K})_{Cantera} - h_s(298\,\mathrm{K})_{AVBP} + h_s(0\,\mathrm{K})_{AVBP}, \tag{E.0.8}$$

where h_s is the sensible enthalpy tabulated in AVBP. The enthalpy of formation at 298K (the standard-state reference enthalpy in Cantera) can be directly calculated with the 7 polynomial coefficients, and it is found that $\Delta H_f(298\,\mathrm{K}) = h(298\,\mathrm{K}_{AVBP})$ (which is confirmed by checking the thermo database for species on the site NASA Thermo Build [198]). Finally, Eq. E.0.8 turns to be:

$$\Delta H_f(0\,\mathrm{K})_{AVBP} = h_s(0\,\mathrm{K})_{AVBP}. \tag{E.0.9}$$

In fact, as the polynomial coefficients of Cantera are only validated for two temperature ranges which do not contain 0 K, there are different ways to estimate $h_s(0\,\mathrm{K})$, but this will not affect the final results in the current study. In this study, the polynomies are used to get $h_s(0\,\mathrm{K})_{AVBP}$:

$$h(T) = RT\left(a_1 + \frac{a_2}{2}T + \frac{a_3}{3}T^2 + \frac{a_4}{4}T^3 + \frac{a_5}{5}T^4 + \frac{a_6}{T}\right) \tag{E.0.10}$$